Imperial College London

Centre of Research Excellence
British Heart Foundation
Imperial College London

The development of a platform to manipulate cardiomyocyte structure and function

by

Worrapong Kit-Anan

A thesis submitted in partial fulfilment for the Degree of Doctor of Philosophy

in the

Department of Materials

Imperial College London

January 2019

Declaration

I, Worrapong Kit-Anan, declare that the work presented in this thesis is entirely my own work, unless specifically referenced and acknowledged.

Worrapong Kit-Anan
January 2019

Acknowledgements

I would like to extend my sincere gratitude to my colleagues, friends and family. Without their help and support I received, this PhD would not be successfully achievable. I would like to thank Professor Molly M. Stevens for her great opportunities given since I did my master's degree, excellent guidance and incredible support throughout my PhD, Professor Sian E. Harding for her great academic supervision. I would also like to express my genuine thanks to Professor Cesare M. N. Terracciano for being great supervisor, mentor, friend and amazing source of constructive comments and joy during my PhD.

I would like to specially say thank you to my post-doc mentor, Dr Manuel Maria Mazo Vega for being such a great mentor and friend who always on hand to provide scientific, emotional and life-guiding supports. A very special thanks to Dr Anika Nagelkerke for her help, fun and accompany. Their idea, motivation, dedication and enthusiasm were crucial to my success. I would like to thank Mr Oisín King, Mr Brian Wang, Mr Jerome Fourre and Mr Barrett Downing for their great scientific discussion and spending time proof reading my thesis.

This PhD would have been impossible without great contributions of my colleagues and collaborators. Particularly, Dr Muzamir Mahat, Dr Paresh Parmar, Ms Ye Wang, Ms Chia-Chen Hsu, Dr Arbel Artzy-Schnirman, Dr Filippo Perbellini, Ms Ifigeneia Bardi, Mr Charlie Winter, Dr Sahana Gopal, Mr Chunching Li. Mr Jelle Penders, Dr Axel Moore, Dr Eleanor Humphrey, Dr Michael B. Albro and Dr Amy Gelmi for their scientific help and great moments at Imperial College London. I would like to thank Dr Anna Regoutz, Dr David Payne, Mr Stephen Rothery, Dr Ciro Chiappini, Mr Michele Becce and Dr Andreas Bruckbauer for great scientific collaborations and supports. To Ms Sabrina Skeete, Dr Benjamin Pierce, Ms Jinata Subba and Ms Melisse Chee who helped me in lab and various applications. I thank Dr Wirat Lerdprom and his family for their support. To all of you whose name has not been mentioned, sincerely, thank you.

I would like to thank British Heart Foundation for their scholarship.

I am also grateful to all my wonderful extended family in the UK who are always there to cheer me up; especially, Ms Kate Teh, Mr Christopher Chew, Mr David Chew and Dr Duncan Garrood. I am extremely fortunate to have a big and wonderful people who always have been a source of happiness and support. Importantly, I owe a debt of gratitude to Dr Amanda You, not only for supporting me, but also tirelessly cheer me up. I could not be more grateful for the great

partnership I have been afforded and the experience of the most challenging, rewarding and enjoyable years of my life to date.

Finally and most importantly, I would like to deeply pay my gratitude to my father (Wisit), mother (Jarassri), sister (Waratchaya) and brother (Wachirawit) who have wholeheartedly supported my decision and journey and have been always at my side. The great support provided since my day 1. Thank you for always believing in me.

Abstract

Cardiac tissue engineering to replace damaged areas of the postmitotic heart is still presented with significant challenges, due to the complex and dynamic interplay of electrical, mechanical and biochemical signals involved in the myocardium. The advancement of regenerative approaches is focussed on understanding the underlying regulatory mechanisms involved throughout cardiac development. However, current knowledge of how biophysical cues in the stem cell niche can modulate cell behaviour is limited.

Firstly, polyacrylamide-*co*-acrylic acid was used as an *in vitro* stiffness-tuneable platform to test the effect of substrate mechanics on human induced pluripotent stem cell (hiPSC) differentiation into cardiomyocytes (CM). The results showed that the optimum differentiation efficiency level peaked at the embryonic-like stiffness of 560 Pa, with increased upregulation of cardiac genes. Functionally, hiPSC-CMs showed a biphasic relationship with a faster calcium transient and higher force generation at cardiac physiological stiffness. Next, shape was incorporated into the experimental design via CardioArray, a custom-built platform which mimics both the stiffness and shape of an adult human CM. This system can accommodate individual hiPSC-CMs to adopt the 3D geometry of an adult CM, while at the same time providing the relevant stiffness cues from the underlying substrate. The results highlighted the specific contribution of stiffness and 3D shape to α-sarcomeric structure, cell membrane stiffness, single cell gene expression and intracellular calcium cycling. Finally, the electrical microenvironment was investigated as a third influencing factor on hiPSC-CM development. A hybrid conductive polyaniline-Scl2 scaffold was fabricated, showing long term electronic stability and no cell toxicity when interfaced with electrosensitive hiPSC-CMs. This could provide electromechanical stability in model studies. Improvement of conduction velocity was observed in an *in vitro* myocardial slice model. As a whole, this thesis demonstrates the differential effects of substrate mechanics on hiPSC cardiac differentiation, providing a novel crucial understanding of how biophysical cues modulate the stem cell niche during differentiation and *in vitro* culture.

Scope of the thesis

The synergy between pluripotent stem cell biology and biomaterial technology holds promises to have a profound influence on both cardiac regenerative medicine and drug discovery. Building on the pedestal of knowledge in hiPSC and cardiac differentiation, researchers have been able to achieve immense developments in cardiovascular research. Furthermore, biomaterial development is rapidly advancing towards engineered material properties that, in a precise and physiological manner, can drive stem-cell fate. Investigations in this field could potentially unleash an unlimited source of clinically useful cells for cellular therapy, and a highly relevant means to reveal the accurate insight into healthy and diseased heart physiology. This would enable them to be used for cell therapy and precision medicine with sufficient guarantee of success. The major challenge currently blocking any potential translation of this technology is the developmental immaturity of hiPSC-CMs. Moreover, this degree of maturation must be homogenous enough to ensure safety upon application. Despite promising early results, nobody has produced an adult human cardiac phenotype in the hiPSC-CMs yet. The main culprit behind this is the use of only a single cue to induce this maturation, thus leading to an intermediate state. Finally, where improvements in the function of neonatal-like cardiomyocytes have been achieved, the mechanisms remain unclear.

This thesis focusses on the development of two different biomaterials and their application for *in vitro* study of hiPSC-CMs' fate and cardiac tissue engineering. The biomaterials will be designed to encourage cell activities, such as proliferation, adhesion, migration and differentiation of hiPSC and hiPSC-CMs. ECM proteins will be incorporated to recreate instructive microenvironments for the cells. The ability to manipulate properties *in vitro*, such as topological and mechanical control, is essential since they can dictate the cell fates. Therefore, the ideal biomaterial would mimic the native myocardium exactly and hence the construct should combine all the individual parameters considered in the introduction.

This project aims to study how novel materials, able to supply multiple cues – physical and biochemical factors - drive hiPSC-CM phenotype and functionality towards that of healthy, adult CMs. The resulting information will improve the understanding of hiPSC-CM-matrix interactions, leading to the design of advanced platforms for novel and significant applications. Based on this premise, this thesis focusses on achieving four milestones described below in each chapter.

1. Optimisation of *in vitro* biomaterials to study the static mechanical regulation involved throughout cardiac embryogenesis using hiPSC
2. Design, development and optimisation of a three-dimensional (3D) microwell device, CardioArray, to recapitulate the microenvironment of the human adult myocardium, focusing mainly on static mechanical and topographical interaction to hiPSC-CMs
3. Fabrication of a novel cardiac patch that mimics physiological stiffness and provides conductivity

Chapter 1 introduces the challenges currently impeding the full use of hiPSC-CM. This reviews the current state-of-the-art on stem cell technologies, focusing on the use in cardiovascular research for regenerative medicine and drug testing platform. This chapter will highlight the attempts of maturation strategies used in various ways, such as differentiation protocol, small molecules and external cues. The biomaterials-based strategy will be thoroughly reviewed, and each cue identified, in order to understand its relationship with specific features reported in the literature. The scoring method will be used to reveal the most influential stimulation and/or combinations. The final part will introduce the key challenges and obstacles that impede the major development in the field.

Chapter 2 includes all methods and statistical analyses that have been used in this thesis.

Chapter 3 ***(The Role of Matrix Stiffness in Modulating Cardiac Specification of Human Pluripotent Stem Cells)*** shows a new approach centred on understanding the mechanical regulation involved throughout embryogenesis. The optimised polymer from Chapter 1 is used to study the effect of substrate mechanics on hiPSC-CM differentiation, as a model of cardiac development. The differentiation protocol will be optimised on the new substrate of tunable stiffness. Signalling pathway modulation will be investigated by merging results from functional (i.e. force and calcium cycling) and molecular (i.e. gene/protein expression, proteomic profiler) assays. The consequent analysis will identify the mechanisms priming hiPSC to undergo cardiac lineage differentiation on the more physiologically relevant stiffness substrate. These findings will aid the development of the next-generation cell-biomaterial therapies for the heart.

Chapter 4 ***(CardioArrays: a novel platform for the multidimensional in vitro manipulation of myocyte niche)*** focuses on hiPSC modification using CRISPR to insert a GFP (green fluorescent protein) intracellular marker for live and long-term observations. The hiPSC differentiation into CMs will be optimized using relevant markers as a key observer. Recapitulating the microenvironment of adult CMs *in vitro* will be achieved using microfabrication, which allows the creation of a 3D geometrical boundary with high precision. A physical properties-tunable

polymer is optimized to match physiological stiffness of the healthy heart before microprinting this boundary. The polymer is conjugated with adhesive molecules to allow hiPSC-CM attachment for long-term studies. Consequent stimuli will be applied on the optimized device in a controlled manner to obtain insight on how hiPSC-CMs respond. Results will improve the understanding of cardiac development and the key regulators provided by this novel platform. This will highlight the vital factors dictating hiPSC-CMs development to more clinically relevent phenotypes.

Chapter 5 ***(Conductive collagen–mimetic foams for cardiac tissue regeneration)*** is centred on the next generation of cardiac patches. A streptococcal collagen-like 2 (Scl2) construct of physiologically-relevant elasticity will be fabricated. The electrically-active “dopant” polyaniline will be immobilized in Scl2, generating a hybrid scaffold. The materials will be characterised to observe morphology, chelation activity of crosslink, stiffness and conductivity. The hiPSC-CM will be plated on the scaffold to study the interactions between materials and hiPSC-CMs. This material-based strategy aims to induce mature features into hiPSC-CMs by matching the physical and electrical properties of the scaffold with those of the tissue. The goal is to improve function but also potentially repair damaged areas of the heart. These findings will provide a major advancement for the application of conductive patch.

Finally, **Chapter 6** summarises the major findings of this thesis and discusses the potential future expansions worth pursuing. It highlights the contribution made by this research by placing it in the wider context of the field.

Table of Contents

List of Figures

List of Tables

List of Abbreviations

AFM	Atomic Force Microscopy
APS	Ammonium persulfate
AVN	Atrioventricular node
BDM	2,3-butanedione monoxime
Bis	N,N'-methylenebisacrylamide
BrS	Brugada syndrome
CCS	Cardiac conduction system
ChR2	Channelrhodopsin2
CICR	Ca^{2+}-induced Ca^{2+} release
CP	Conductive polymers
CPCs	Cardiac progenitors
CPVT	Catecholaminergic polymorphic ventricular tachycardia
CMs	Cardiomyocytes
CV	Conduction velocity
Cx-40	Connexin-40
Cx-43	Connexin-43
Cx-45	Connexin-45
DIC	Doxorubicin-induced cardiotoxicity
DMSO	Dimethyl sulfoxide
EB	Embryoid body
ECs	Endothelial cells
ECM	Extracellular Matrix
EDC	1-ethyl-3-(3-dimethylaminopropyl)carbodiimide hydrochloride
EDTA	Ethylenediaminetetraacetic acid
ESCs	Embryonic stem cells
FFR	Force-frequency response
HBBS	Hanks' Balanced Salt solution
HCN	Hyperpolarization-activated cyclic nucleotide-gated potassium
HEPES	(4-(2-hydroxyethyl)-1-piperazineethanesulfonic acid

hESCs	Human embryonic stem cells
hESC-CMs	Human embryonic stem cells derived cardiomyocytes
HF	Heart failure
HGPS	Hutchison-Gilford progeria syndrome
hiPSCs	Human induced pluripotent stem cells
hiPSC-CMs	Human induced pluripotent stem cells derived cardiomyocytes
I_{CaL}	L-type current
I_{CaT}	T-type current
I_f	Funny current
I_{k1}	Inward rectifier current
I_{kr}	Rapid delayed rectifier K + current
I_{ks}	Slow delayed rectifier K + current
I_{TO1}	Cardiac transient outward potassium current
iPSCs	Induced pluripotent stem cells
LTCC	Voltage-sensitive L-type Ca^{2+} channels
LQTS	Long-QT syndrome
LV	Left ventricular
MES	2-(N-morpholino)ethanesulfonic acid
MFS	Marfan syndrome
MHC	Myosin heavy chain
MI	Myocardial infarction
MLC	Myosin light chain
NCX	Na^{+}-Ca^{2+} exchanger
NRVMs	Neonatal rat ventricular myocytes
PAAm	Polyacrylamide
PANI	Polyaniline
PBS	Phosphate saline buffer
PDL	Poly-D-lysine hydrobromide
PDMS	Polydimethylsiloxane
PEDOT	Poly(3,4-ethylenedioxythiophene)
PVDF	Polyvinylidene fluoride
RBC	Red blood cell

RYR	Ryanodine receptor
SAN	Sinoatrial node
Scl2	Streptococcus collagen–like 2
SERCA	Sarco-endoplasmic reticulum ATPase
SMCs	Smooth muscle cells
SR	Sarcoplasmic reticulum
sulfo-SANPAH	N-sulfosuccinimidyl-6-(4'-azino-2'-nitrophenylamino)hexanoate
T3	triiodothyronine
T-tubules	Transverse tubules
TBS	Tris-Buffered Saline
TEMED	N,N,N′,N′-Tetramethylethylenediamine
TFM	Traction force microscopy
TH	Thyroid hormone
TNNI1	Slow skeleton isoform
TNNI3	Fast skeleton isoform

1. Introduction

Cardiovascular diseases are the biggest cause of mortality worldwide. Although medical advancement and interventions have improved survival rates, these diseases still account for over 30% of all deaths worldwide and are increasingly prevalent (***Figure 1***). This number is even higher in developed countries, with a 5-year mortality rate over 50%[1,2]. These diseases include, but are not limited to, myocardial infarction (MI), dilated cardiomyopathy, arrhythmias and heart valve disease. Cardiac dysfunction frequently ensues and culminates in heart failure (HF), a pathological state characterised by a reduction or a preservation of ejection fraction. Specifically, left ventricular (LV) failure are typically the result of impaired filling, increased end-diastolic pressure and pulmonary capillary pressure. The consequences of the loss of cardiac functionality are exacerbated by poor regeneration in the adult mammalian heart, leading to a progressive but persistent deterioration of the patient[3]. The hypothesis that cardiomyocytes (CMs) irreversibly exit the cell cycle shortly postpartum, making the heart a post-mitotic organ, was first established in early 1900s[4,5]. The Lee group extensively showed mechanisms of cardiac regeneration in vertebrates and mammalian rodents. The authors demonstrated that, unlike regeneration-competent vertebrates such as zebrafish or axolotls, mammalian rodents lose their ability to regenerate in adult life. In a severe myocardial infarction case involving a newborn child due to coronary artery occlusion, the report observed clinically functional recovery which resulted in long-term normal heart function and ejection fraction[6]. In 2009, Bergmann *et al.* proved that the human heart has a limited regenerative capacity, using carbon-14 integration generated by the atmospheric nuclear bomb tests during the Cold War, suggesting it is therefore unable to repair itself following damage[3]. Human adult CMs have been reported to renew about 1% annually, which progressively decreases with age to approximately 0.45% by age of 75[3]. This study, however, did not compare healthy aging individuals to patients of acute myocardial infarction, and raises doubts over the appropriate breadth of the myocardial samples examined for the carbon dating protocol[7]. Later in 2015, Bergmann *et al.* published further findings that reported a constant number of CMs throughout a lifespan with a low turnover rate, using carbon-14 datng plus stereology. Therefore, while recent improvements in medical technologies and treatments have become acutely effective in saving a patient´s life immediately after primary insults, such as MI, there remains the challenge of preventing the subsequent chronic burden arising from cell loss.

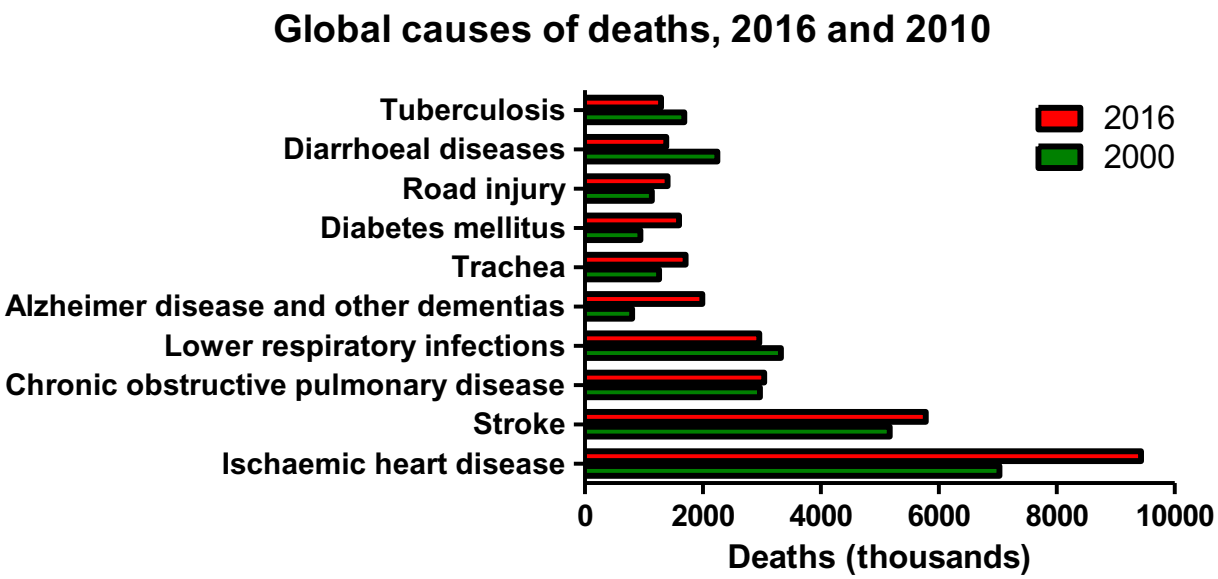

***Figure 1: Estimates of mortality from WHO Global Health Estimates (GHE)**. This graph has been plotted from data available on WHO statistic information at the beginning of 2018[8].*

1.1 Cardiac development

The heart is the first organ to form during human embryogenesis, and quickly matures in function and structure, establishing a circulatory system that is crucial for subsequent foetal development. This section summarizes the developmental signals created during embryogenesis, highlighting the changes in mechanical properties of the myocardium. Cardiogenesis starts three weeks after fertilisation when gastrulation occurs, and three germs layers known as the endoderm, mesoderm, and ectoderm are formed. This process is governed by antecedent spatial asymmetries laid down in the blastula. At a fundamental level, this process is recognised to arise from multiple sources in the embryo. Part of the mesodermal layer differentiates forming the heart. The splanchnic mesoderm differentiates into the myocardium, responsible for the early contractility of the heart, whereas the epicardium develops from the mesodermal lining[9]. Mesodermal cardiac progenitors (CPCs) differentiate into several cell types, such as CMs, endothelial cells (ECs), fibroblast and smooth muscle cells (SMCs). The somatic mesoderm develops into the body wall lining and dermis. Biochemical, physical and electrical stimuli drive the differential growth in CPCs, which entail neighbouring or distant signals from morphogens such as bone morphogenetic proteins[10], WNTs[11,12], fibroblast growth factors, Notch, Nodal, Activin[13], Insulin-like growth factor[14] and many members of the transforming growth factor family[13], amongst others, leading to formation of the endocardial tube[15]. Before the fusion of the

endocardial tubes, CMs initiate their rhythmic electrical activity, starting in close proximity to the pacemaker. The initiation of contraction creates diverse mechanical changes beat-to-beat. This dynamic mechanical environment from myocardial contractions influences cardiac development by generating a range of mechanical forces on the tissue microenvironment of up to 16 kPa in each heartbeat. This results in an increase of tissue elasticity from 0.5 to >10 kPa in the physiological myocardium measured by Atomic Force Microscopy (AFM)[16]. The difference in elasticity during contraction-relaxation of the myocardium varies between species: 3:1 in mouse[17], 2:1 in rat[18] and 20:1 in zebrafish[19]. This highlights the importance of mechanical factors experienced by CMs during embryogenesis. Postnatally, cardiac development continues, with dynamic and increased electrical, humoral and mechanical stimuli[19]. However, much about the heart's developmental mechanisms remains to be discovered.

1.2 Structure and function of the heart

Structurally, human adult CMs have a cylindrical shape, with a length-to-width ratio of ≈ 5-7, an unloaded sarcomeric length of 1.8 μm, an extensive network of t-tubules, large cell volume with a high mitochondrial density, and individual cell contractility on the μN scale[20]. This highly organised structure is a result of strictly regulated distribution and compartmentalisation of ultrastructural domains, thus enabling the ordered molecular events required to allow the heart to beat synchronously and to generate enough force to pump blood throughout the body[21]. The beating is preserved by a hierarchy of control mechanisms, ensuring the function of myocardium is maintained. These control mechanisms require coordination of metabolic, electrical, humoral and mechanical events that are coordinated by transmembrane integrin receptors, the cytoskeleton of CMs and non-myocytes, and extracellular matrix (ECM). These dynamic components operate in an interdependent manner, and as such are functionally connected and capable of processing events simultaneously.

ECM provides physical cues to cells as well as initiate, regulate and store biochemical and biomechanical signals, which are required for cellular morphogenesis, differentiation and homeostasis. The most abundant ECM molecules found in the human heart are hyaluronan, laminin and collagen (type I in the healthy heart and type III in the damaged heart). These components steer the anisotropic alignment of CMs, influence the cell mechanical microenvironment, and affect the stress-strain relationship in the heart. Thus ECM has a profound influence on cardiac development and function[22]. Under healthy conditions, ECM fibres store energy during systole, which is spent in diastole for re-lengthening of CMs. Initially in HF, adequate cardiac output is maintained. However, further increase in collagen deposition during

cardiac remodelling leads to ventricular dysfunction and conduction abnormalities as the disease progresses[23–25].

Transmembrane integrins are heterodimeric receptors that are expressed in all cells, including those in the heart as shown in ***Figure 2***. Integrins are instrumental in multiple critical cellular process including cell adhesion, migration, ECM organisation, signalling, survival and proliferation, amongst others (e.g. dystrophin[26] and sarcoglycans[27]). In CMs, the integrin heterodimers that are the most highly expressed are α1β1, α5β1 and α7β1, which are predominantly collagen, fibronectin and laminin binding receptors, respectively. A study by Wang *et al.* showed that focal adhesion protein formation, actin polymerisation and actin-myosin stress fibre formation form a mechanosensitive link between the extra- and intracellular environments[28]. This means integrins and their multi-molecular complex can convert events outside the cell, mechanical information, to intracellular signals, biochemical signals, and vice versa[29]. Additionally, mutations in dystrophin and sarcoglycans have been shown to cause cardiovascular diseases[26,27].

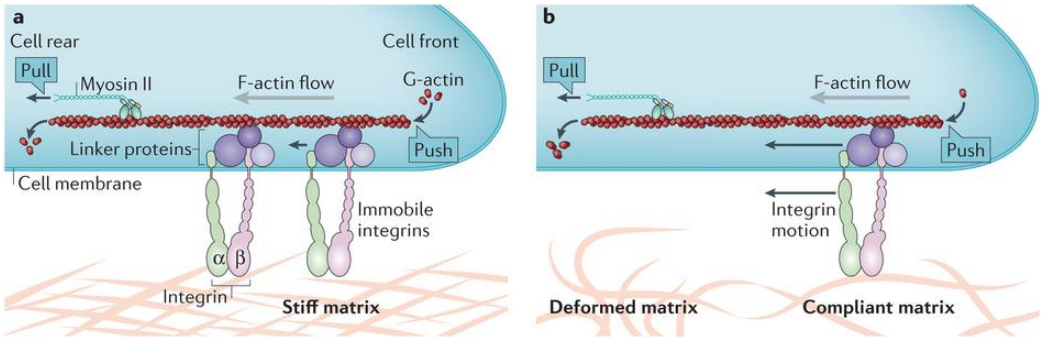

***Figure 2**: **Transmembrane receptor interactions with the extracellular environment.** (a) Static integrin adhesion to ECM, (b) conformational change of integrin allows different cellular processes, such as migration, proliferation and apoptosis. Reproduced from Nature Reviews[30].*

The **cytoskeleton** is an essential structure that provides transitional signals between integrins and the nucleus, while also providing mechanical support for cellular integrity. It allows cells to carry out essential functions, such as division and movement. In CMs, sarcomeres form the contractile unit of the cell and consist of thick and thin filaments of proteins, connecting myofibrils to the sarcolemma and ECM. It can utilise the physical signals sensed through the ECM connection via linker proteins, such as focal adhesion kinase and paxillin. A distinctive striated pattern is formed by the overlap of thin actin filaments from adjacent sarcomeres at the Z-disk,

cross-linked by tight interactions with α-actinin. The distance between each striation, termed sarcomeric length, determines tension development and the degree of muscle shortening[31–33]. At an ultrastructural level in CM, there is a direct relationship between sarcomeric length and myofilament sensitivity to Ca^{2+} and force generation[34]. At the organ level, the ability of the heart to adjust the contraction force in response to changes in ventricular volume/expansion forms the fundamental basis of the Frank-Starling relationship[35]. This relationship explains the myocardium's intrinsic property by which increased sarcomere length results in enhanced performance during subsequent contraction[35,36]. Two processes contribute to this length-dependence of activation; Ca^{2+} sensitivity and [Ca^{2+}]. Impaired length-dependent activation, a reduced Frank-Starling relationship, has been observed in hypertrophic cardiomyopathy. The study by Tobacman *et al.* showed that the disruption of the thin filament in cardiac hypertrophy causes abnormal thin filament Ca^{2+}-activation, and, hence, a reduction in force[37]. Other examples of cytoskeletal modulation in CMs are the Z-disc anchors, the thin filaments that maintain stable force propagation and titin, which serves as a length-dependent sensor, providing myocardial elasticity. These modulations form part of the ultrastructural changes that tightly regulate heart function.

1.3 Heterocellularity: diversity in the heart

This section has been partly published in Wang, B., Kit-Anan, W. & Terracciano, C. Many Cells Make Life Work—Multicellularity in Stem Cell-Based Cardiac Disease Modelling. Int. J. Mol. Sci. 19, 3361 (2018).

CMs are the contractile cells of the myocardium, but the adult human myocardium is composed of a variety of cell types. The most abundant myocardial cells are hypothesised to be CMs, fibroblasts, endothelial cells, neurons, resident lymphocytes and perivascular cells. CMs constitute 70-80% of the adult myocardium by volume, and 30-40% by number[38]. Although estimates for the frequency of the non-myocyte component of the heart vary substantially, it is widely agreed that they are vital for normal homeostasis in healthy and pathological remodelling in diseases. Non-myocyte cell types and ECM provide the biochemical, electrical and mechanical stimulations for the CMs, and form structures essential for the vascular supply and optimal shape/support required for efficient cardiac contraction and long-term survival (***Table 1***). This close interplay between other cells via biochemical, electrical and physical communication suggests they are essential to cardiac development. This section will discuss non-myocyte components and their functions.

Table 1: Summary of non-cardiomyocyte roles in healthy and diseased myocardium. *This table has been reproduced from B. Wang and W. Kit-Anan et al.*[39]*.*

Cell	Healthy	Disease	Refs.
Fibroblasts	• ECM turnover, maintaining balance between synthesis and degradation of matrix	• Scar formation (fibrosis) • Deposit excessive ECM protein • Crosstalk to EC and macrophage for angiogenesis and matrix synthesis	23,40–42
ECM	• Periostin, laminin, vimentin, fibronectin, and collagen types I (90%), III, V, and VI • Alignment • Mechanical support	• Increase in collagen I, III, IV, V, and VI • laminin, fibronectin, thrombospondin, and tenascin	23–25,43,44
Endothelial cells	• Structural support • Vasculature homeostasis • Biochemical factors, such as nitric oxide, endothelin-1, IL-6 • Progenitor of cardiac pericytes and vascular smooth muscle cells	• Inflammation (hypertrophy, inotropy, apoptosis, mitosis) • Neovascularisation increase the density of peri-infarct vessels • Paracrine	45–47
Smooth muscle cells	• Mechanical support of vasculature: contractile or synthetic (proliferative) mode	• Loss of elasticity • Reduced contractility • Increased proliferation	48,49
conductive cardiomyocytes	• Conduction fibre and pacemaker	• Block, slow down conduction	50–53

	(Atrioventricular node, Sinoatrial node, Purkinje) • Control rhythmic beating	• Essential component for embryo development	
Leukocytes	• Few residents • Mast cells act as inflammation mediator storage and activating the local renin-angiotensin system • Macrophage performs a janitorial homeostasis and facilitate electrical conduction	• Macrophage has a role in ECM turnover/cell death, scar formation, neutrophil recruitment and vascularisation support	[54–57]

Endothelial cells (ECs) are the most abundant cell type in the heart and form the vascular system, an essential part of the nutrient supply of CMs[58]. They consist of different subtypes including arterial, venous, and lymphatic populations[59]. During development, the arterial and venous populations express various factors such as vascular endothelial growth factor, Notch signalling and Sox18. The vascular endothelium is a single-cell layer that lines the entire circulatory system. It forms an interface that displays remarkable phenotypic plasticity for vascular homeostasis. ECs play important roles in initiating inflammatory response, triggering thrombosis, regulating vasomotor tone, and controlling vascular permeability. During endothelial dysfunction, the transition between EC function and dysfunction are not always clear. The dysfunction often arises from initially adaptive responses to heterogenous physiopathological stimuli[60]. The ECs demonstrate either atheroprotective or atheroprone phenotypes, depending on vascular flow.

Fibroblasts are crudely defined based on their capacity to secrete ECM, and on their interstitial location. Although no precisely specific markers have been recognised to date, there are some markers used commonly, from RNA-seq and other methods, such as CME+, THY-1, PDGFRA, PECAM1, ECM-encoding genes (e.g. Col1a2 and Col1a1), and CD45[61–63]. They form 20% of the non-myocyte component of the myocardium and increasingly accumulate in disease. Fibroblasts are highly connected with other cell types and form extensive interactions with CMs. During mouse development, fibroblast-enriched cell populations were not identified initially but increase overtime as CM populations decreases[62]. They become highly active and play an

essential role after MI in fibrotic formation and cardiac decompensation[23,40–42]. Due to the lack of suitably specific markers, cardiac fibroblasts, their molecular properties, sub-populations, compartmentalisation, and temporal function during development, homeostasis, injury, and repair are not well-understood.

Vascular smooth muscle cells (SMCs) play an important role in remodelling the arterial, venous, and lymphatic vasculature. Their ability to switch between contractile and proliferative phenotypes regulates vessel tone and blood pressure in response to environmental stimuli. SMCs directly control contraction of the vascular wall, regulating the diameter of the blood vessel lumen. During disease, changes in their microenvironment, initiate acute, ligand/receptor-dependent signalling pathways within SMCs, as well as chronic nuclear signalling pathways, resulting in reduction of contractility and elasticity, altering their phenotype[48,49].

Leukocytes are part of the immune system that essentially acts following onset of heart disease[64]. They respond as part of the acquired immune system to autoantigens and play an important role in pathogenesis by orchestrating an adaptive immune response and modulating cytokine secretion. This mechanism protects the heart from further injury through fibrotic formation. In humans, macrophages have been shown to be a key player in fibrotic formation by increasing ECM production and turnover. Recently, they were also found to facilitate impulse conduction in the heart[57]. Additionally, a state of chronic inflammation found in HF is characterised by increase in circulation of myocardial pro-inflammatory cytokines has been shown to promote pathological left ventricular remodelling[54–57]. For T and B lymphocytes, they activate and play essential roles during myocardial remodelling[54]. Inhibition of T_{Reg} can induce suppression of the postinfarction inflammatory responses[65]. The population of dendritic cells shifted from day 3 to day 7 postinfarction, indicating its role as an early adaptive immune response[66].

Sympathetic neurons modulate the functions of vital organs as part of the autonomous nervous system including the heart. Responding to stressors, the autonomous system that has tonic control over cardiac function changes the contractions of the myocardium. The dynamic crosstalk between the heart and the neuronal system are bidirectional, and mutually advantageous[67]. Equally, myocardial injury can also cause neuronal dysfunction. For example cardiac ischemia scar tissues can result in reduced conduction velocity and induce cardiac arrhythmia, leading to HF[53], as well as hyperactivity observed, causing decreased neuronal density and function[68].

In summary, non-myocytes play essential roles in myocardium from development to remodelling in diseases. Understanding their role could reveal underlying mechanisms (***Figure 3***), expanding hiPSC-CMs applications to more complex diseases and advanced treatments.

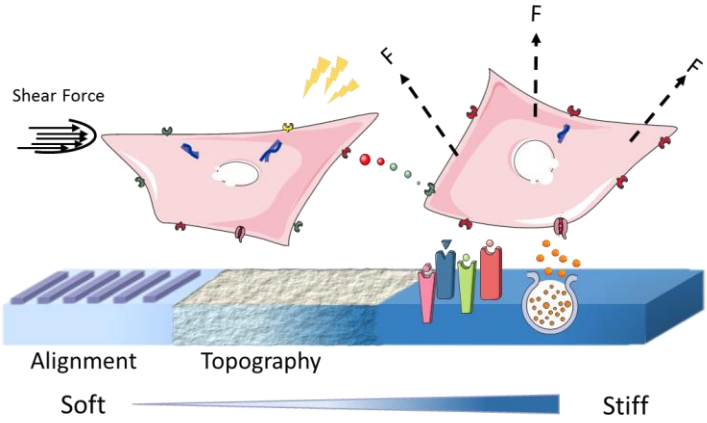

Figure 3: Cardiomyocyte microenvironment. *Neighbouring factors that directly and/or indirectly affect cell fates on cell behaviour via biophysical*[69] *(alignment*[70]*, topography*[71]*, stiffness*[72] *and shear*[73]*), biochemical (cytokines*[74]*, integrin*[75] *and extracellular vesicles*[76]*) and other routes, such as electrical signals and cell crosstalk.*

1.4 Stem cells and cardiomyocyte derivation

Stem cells are undifferentiated cells that have a self-renewal capacity through mitotic division, but retain the ability to give rise to more committed derivatives[77,78]. They can be classified according to their potency, indicating their ability to differentiate to more specialised cell types, ranging from unipotent, multipotent, pluripotent and totipotent stem cells. As this thesis focuses on the use of pluripotent stem cells in medical applications, this introduction outlines their history, subtypes and current uses in research.

Pluripotent stem cells include embryonic stem cells (ESCs) and induced pluripotent stem cells (iPSCs), which are both pluripotent and can be differentiated into any adult cell type[77–79]. The successful isolation of human ESCs in 1998 led to efforts to differentiate these cells into different cell types, including CMs[80]. Human ESCs (hESCs) represent a promising candidate as a source of CMs thanks to their unlimited capacity for *in vitro* expansion with high scalability and accepted cardiac potential. Undifferentiated hESCs retain their phenotype and potency through as many as one hundred population doublings. After differentiation, hESC-derived CMs (hESC-CMs) demonstrate robust proliferative capacity both *in vitro* and *in vivo* although this capacity diminishes after a few passages[81]. hESCs can also be differentiated into the non-myocyte cell types present

in myocardium. This opens up an avenue for repopulating all myocardial cellular elements. However, techniques for the isolation of hESCs from blastocyst-stage human embryos have raised ethical concerns due to the necessity of the destruction of human embryos[82].

Human iPSCs (hiPSCs) are generated via direct reprogramming of somatic cells, and thus have become an attractive source of stem cells by eliminating the ethical issues associated with embryonic tissue[79]. Additionally, they offer the unique potential of the generation of patient specific, autologous pluripotent stem cells. Since hiPSCs are reprogrammed from somatic cells, the cell source is an important factor to be considered for their accessibility, availability, and good reprogramming efficiency, of which fibroblasts have been the most common cell source. Reprogramming tools, such as miRNA, small molecules and plasmids, can regulate the genes involved in pluripotency, reverting somatic cells to iPSCs[83], Yamanaka *et al.* demonstrated that OCT3/4, SOX2, KLF4 and C-MYC are important transcription factors in the repression of the genes associated with differentiation and specialisation hence the cocktail can reset gene expression to an embryonic-like profile. However, while the reprogramming mechanism has not yet been fully explained[79], hiPSC-CMs exhibit contractile apparatus, intercellular communication via gap channels and various ion channels similar to the adult CM[84]. As a result, hiPSC-CMs open up many avenues for medical applications, such as toxicology safety, drug discovery, disease models and cardiac regeneration.

Initial studies used the embryoid body (EB) method, which aims to recapitulate the early environment during embryogenesis, to induce spontaneous CM differentiation. In EB, hiPSCs spontaneously differentiated to derivatives of the three primary germ layers, resulting in only a fraction of CMs and large proportion of other unwanted cell types[85]. This is due to the variable size and density of the EB created, which can significantly alter cell yield and quality. Complexity in hiPSC differentiation has slowed down the advancement of the field. Therefore, an efficient and consistent differentiation methodology is vital to produce the desired cardiac lineages. In 2012, Lian *et al.* and Burridge *et al.* showed an alternative approach using hiPSCs grown as monolayer[86,87]. Relatively uniform monolayers of hiPSCs enable more readily controlled and reproducible application of biochemical factors and other interventions, improving CM differentiation efficiency to > 80%. As a consequence, hiPSC-CMs have been increasingly explored and expanded. ***Table 2*** compares key features between hiPSC-CMs and native adult CMs.

Table 2: Comparison of hiPSC-CMs cultured in 2D tissue culture vessels and adult CMs. *Note: Action potential has been showed by the Terracciano group to be dependent on cell density[88]. Adapted from Worrapong Kit-Anan's master's thesis 2014 and reproduced from B. Wang and W. Kit-Anan et al.[39].*

Structure			
	hiPSC-CM	**Atrial**	**Ventricular**
Shape	Any, not defined	Cylindrical	Cylindrical and bifurcated
Volume	Small (8 – 15 μm^3)	Large (100 – 130 μm^3)	Very large (110 – 150 μm^3)
Sarcomere Organization	Random	Orderly and aligned	Orderly and aligned
Mitochondria population	Few (~2% of cell volume)	Abundant (~30% of cell volume)	Abundant (~30% of cell volume)
T-tubule organization	Absent	Scarce	Abundant
Glucose Metabolism	High	Low	Low
Nucleus morphology	Mono	Mono, bi, multi	Mono, bi, multi
Electrophysiology			
Spontaneous activity	Very frequent	Absent	Absent
Maximum diastolic potential	- 60 mV	- 70 mV	- 80 mV
Maximum upstroke velocity	44 – 187 V/s	200 V/s	200 V/s
Action potential amplitude	94 – 113 mV	80 – 130 mV	100 mV

***Action potential duration at 50%**		See comments	200 ms	200 – 300 ms
***Action potential duration at 90%**			200 – 400 ms	250 – 400 ms
Force Generation		100 - 150 Pa for a single cell	Myocardium tensile force ≈ 56 kPa	Myocardium tensile force ≈ 56 kPa
Elastic modulus		466 Pa	22 – 55 kPa	22 – 55 kPa
Molecular Marker				
Gap junction	Cx40	-	+	-
	Cx43	+	+	+
	Cx45	+	-	-
Ion channel	KCNA5	+	+	-
	Na^{+}-Ca^{2+} exchangers 1 (NCX1)	+	+	+
	SERCA2a	+	+	+
	RYR2	+	+	+
	Ca_v 1.2	+	+	+
	K_{ir} 2.1	+	+	+
	K_v 4.3	+	+	+
	KChip 2	+	+	+

	KCNH2 (HERG)	+	+	+
Structural protein	TNNT2	+	+	+
	ACTN2	+	+	+
	MLC2A	+	+	+
	MLC2V	+	-	+
	MYL2	+	+	+
	MYH6	+	+	+
Master gene	NKX2.5	+	±	±

hiPSC-CMs present a much-improved *in vitro* model compared to that generated from non-human cells as a preclinical human validation model. However, there remain critical differences between hiPSC-CMs and native adult CMs, an issue which will need to be resolved for hiPSC-CMs to realise their full potential. Briefly, the structure of hiPSC-CMs is significantly different from that of adult CMs, particularly in volume, shape, cytoskeletal organisation and mitochondrial density. For example, CM shape is an essential contributor to force generation which dictates ejection fraction of the heart. Equally important, hiPSC-CMs beat spontaneously due to the immature nature of their ion channels (i.e. potassium channels) and high presence of funny current (I_f), while adult CMs only beat when stimulated either by electrical or biochemical cues. As such hiPSC-CMs exhibit a relatively neonatal-like phenotype. Detailed comparisons will be discussed in the next section.

1.5 Structure, function and gene expression of hiPSC-CMs

hiPSC-CMs have characteristic, spontaneous beating, that can be visually observed during *in vitro* differentiation and culture. However, this is a characteristic that only exists in neonatal CMs and selectively in the adult myocardium in pacemaker cells, a fact which reasserts the similarity between hiPSC-CMs and neonatal CMs. Overall, by displaying several substantial differences in comparison to most adult CMs, the full realisation of the potential of hiPSC-CMs in cardiovascular research is hampered. Many characterisation studies have been performed to understand the structure, function and gene expression of hiPSC-CMs. Therefore, the term "maturation" is commonly used to compare morphological and/or functional properties of hiPSC-CMs to those residing in the native adult heart. In this chapter, structure, function and gene expression will be discussed.

1.5.1 Structure

The **shape and size** of hiPSC-CMs are dependent on their density and local environment but they are significantly smaller than adult CMs, having flattened irregular shapes (< 10 μm thickness) and forming a disorganised monolayer, even after prolonged *in vitro* culture[89]. These characteristics recapitulate the phenotype observed during early cardiogenesis, before the transition from hyperplastic to hypertrophic myocardial growth occurs. During physiological hypertrophy, neonatal CMs form an anisotropic alignment of elongated, rod-like shaped cells, which increases conduction velocity via unidirectional gap junctions, enabling them to contract efficiently. This does not occur in hiPSC-CMs *in vitro.*

To be able to perform high **energy**-consuming activities, maturation of the foetal heart to the adult phenotype is also accompanied by a pronounced increase in mitochondrial content via mitochondrial biogenesis. **Mitochondria** in hiPSC-CMs were found to be lower in number and activity. Mitochondria account for up to ~ 30% of total cell volume in the adult ventricular myocyte, compared to only 2% of the cell volume in hiPSC-CMs, while also showing immature structure of cristae on the inner membrane[90]. At the same time, the source of energy production also switches from glycolysis in the foetal heart and hiPSC-CMs, to predominantly fatty acid oxidation in the adult CMs[91]. Additionally, the number of nuclei per CM can also differ between hiPSC- and adult CMs. Postnatal CM development results in nuclear division without cell division. Therefore, adult CM populations demonstrated higher percentages of bi- and multi- nucleation (25 - 30%)[20] than hiPSC-CMs which are often mono-nucleated, only occasionally demonstrating binucleation. This

is comparable to developing CMs in late foetal and early postnatal stages, having single oval nuclei that occupied 10 - 20% of the cell volume.

One of the common differences usually characterised in hiPSC-CMs is **sarcomere structure**. hiPSC-CMs demonstrate a short and disorganised sarcomere, similar to foetal CMs, with only the Z-disc and I-band formed. This results in a lower force production compared to adult CMs. Well- defined striations are observed in adult CMs with organised functional units: Z-discs delineate sarcomere borders, I-, H- and A-bands, different areas of thick, thin and overlapping filaments and M-bands form the central line. Sarcomeric length, or distance between two adjacent Z-lines, has been shown to be directly linked to force production. The optimal length of 2.2 μm under load and 1.8 μm unloaded produces the highest contraction force in the adult CM[92]. This length shortens to 1.6 μm in hiPSC-CMs, with consequently much less traction force capacity[93].

Another distinguishing feature is **transverse tubules** (T-tubules), which are regularly organised and arranged along the Z-lines in adult CMs. T-tubules are invaginations of the cell membrane, enabling rapid excitation, initiation and synchronous triggering of intracellular Ca^{2+} release from sarcoplasmic reticulum (SR). hiPSC-CMs, with their flat and thin morphology (~ 5 μm), reduces the need of T-tubules in comparison to thick (> 15 μm diameter) adult CMs. Numerous studies have shown that hiPSC-CMs lack T-tubules in both 2D and 3D culture with unsynchronised Ca^{2+} transients due to their non-uniform Ca^{2+} release (high number of Ca^{2+} sparks)[94–96]. This characteristic has been similarly observed in developing CMs until late embryogenesis.

Gap junctions consist of clusters of closely packed channels that link the cytoplasm of adjacent cells, allowing the exchange of ions and small molecules (< 1 kDa) in cell-cell communication. There are three main gap junctional connexins expressed in mammalian CMs: connexin-40 (Cx-40), connexin-43 (Cx-43), and connexin-45 (Cx-45). While Cx-40 and Cx-45 have predominantly been detected in the conducting tissue of developing mammalian hearts, Cx-43 is abundantly expressed in adult working myocardium (atrial and ventricular). In adult CMs, Cx-43 forms a gap junction between adjacent CMs around the periphery of the cell membrane along the longitudinal axis and are predominantly located in the intercalated discs. This allows a faster conduction velocity longitudinally compared to transverse conduction velocity to fibre direction and enables the syncytium of the heart[97]. In hiPSC-CMs, very few gap junctions have been observed. Gap junction proteins are distributed throughout the cytoplasm equally, resulting in isotropic electrical impulse conduction without control over direction, which reduces the maximum conduction velocity and efficiency of signal propagation[98].

The spontaneous beating observed in hiPSC-CMs is another sign of an immature electrophysiological phenotype. In spontaneous mode, the rate of depolarisation is much slower than in electrically paced mode, during both the triggering and upstroke phase of the action potential. There are two main ion currents widely hypothesised to be responsible for the spontaneous beating, I_{k1} and I_f. I_{k1} (inward rectifier current) is governed by the potassium voltage-gated channel subfamily J member 2 and is responsible for cardiac excitability and involved in arrhythmogenesis. A recent study by Gélinas *et al.* showed that an attenuation of the gene expression can maintain resting membrane potential in working hiPSC-CMs and antagonise spontaneous activity. A specific variant mutation can cause long-QT syndrome by altering channel cellular trafficking and fails to form a functional channel[99]. The funny current (I_f) conversely, is robustly present in the sinus node in the myocardium, flowing through hyperpolarisation-activated cyclic nucleotide-gated potassium (HCN) channel. During maturation, high expression of HCN4 has been detected in adult pacemaker cells whilst it is reduced in working adult CMs. However, a reduction of HCN4 expression does not occur in hiPSC-CMs, causing I_f levels to remain high[100–102]. Additionally, two types of Ca^{2+} channels are present in the human heart: L-type (I_{CaL}), which is found in adult CMs, and T-type (I_{CaT}) that is typically found in foetal CMs and the conductive system. These two Ca^{2+} channels have been detected in hiPSC-CMs but their expression and function are lower than in the adult heart[103–105]. Although these differences in ion channels and currents occur, a current drug proarrythmic potential assessment shows the utility of hiPSC-CMs in drug screening and toxicity studies[106].

1.5.2 Functional properties of hiPSC-CMs

CM function is closely linked to its uniquely well-defined structure. As mentioned previously, the structure of hiPSC-CMs is distinctively different from adult CMs, more resembling developing CMs. Hence, hiPSC-CMs functionally exhibit different qualities compared to adult CMs. hiPSC-CMs are able to form a functional syncytium with the evidence of gap junctional formation and the expression of essential ion channels, such as Na^+-Ca^{2+} exchangers (NCX) and potassium voltage-gated channel subfamily J member 2. However, the immature features of gap junctions and ion channels affect the electrophysiological properties, resulting in spontaneous beating with neonatal-like action potential and Ca^{2+} transient characteristics. This chapter reviews the functional differences between hiPSC-CMs, developing CMs and adult CMs in term of action potential, calcium handling, force generation and response to stimuli. This highlights areas that hiPSC-CMs lack and their potential in plasticity that can be utilised for understanding developmental processes and for medical applications.

1.5.2.1 Action potential

The adult heart contains different myocyte subpopulations: atrial, ventricular, pacemaker and Purkinje. Their action potential characteristics are unique for each subtype, governing the electrical behaviour of CMs, due to their different permeable membrane and ion channel expression. In adult working CMs, an equilibrium potential, known as the resting membrane potential, is set in -70 to -80 mV. The complex interplay between ion channels in combination with transport mechanisms allows the cell to maintain a stable negative electrical charge inside the cell, compared to outside the cell membrane. They remain inactive at resting membrane potential until depolarisation is initiated by the passage of ions from adjacent CMs, through transmembrane ion channels (i.e. sodium voltage-gated channel alpha subunit 5, LTCC and t-type calcium channel). Equilibrium maintenance at resting membrane potential, depolarisation mechanisms and action potential characteristics differs in adult, developing and hiPSC- CMs, due to the availability and maturity of ion channel permeability. hiPSC-CMs demonstrate heterogeneity in action potentials with reduced diastolic potential. They also demonstrate higher resting membrane potential at -60 mV (***Table 2***). hiPSC-CMs have a reduced expression of I_{K1} channels in combination with higher levels of I_f pacemaker current, contributing to the automaticity of their action potentials. During the repolarisation phase, early and late stage foetal CMs display I_{TO1} with an increased presence in atrial cells in comparison to ventricular CMs. In hiPSC-CMs, I_{TO1} is found to be inactivated; hence, more positive resting membrane potentials is observed. This reduces the repolarisation rate, prolongs action potential duration or prevents the maintenance of resting membrane potential. The other main repolarising currents, rapid delayed rectifier K+ current (I_{Kr}) and slow delayed rectifier K+ current (I_{Ks}), are present in hiPSC-CMs at similar levels to adult CMs.

Although each subpopulation in the human heart has a unique action potential characteristic, the action potential of hiPSC-CMs is mistakenly used to categorise the cells as ‘ventricular’, ‘atrial’ or ‘nodal’ (pacemaker) based on their resemblance to adult action potentials in the field. The Terracciano group demonstrated that differences in action potential profile is caused by cell density, and that cells exhibited a continuous range of characteristics instead of distinct properties assigned to chamber-specific CMs, found in adult heart[88]. Due to the heterogeneity, the source chamber of CMs cannot be accurately identified using a single property, such as action potential morphology. Rather, a fingerprint of multivariate properties collectively contribute to the characteristics of these functionally unique cells[20].

1.5.2.2 Excitation-contraction coupling

Myocardial contraction is coordinated on a beat-to-beat basis by the mechanism called Ca^{2+}-induced Ca^{2+} release (CICR) and is a unique characteristic that differentiates CMs from other muscle cells, serving as the crucial link between electrophysiological stimulation and the production of contraction force. Although absolute Ca^{2+} concentration has not been measured to date, hiPSC-CMs demonstrate a negative force-frequency response (FFR), suggesting inefficiency in utilising Ca^{2+} storage and a reduction in sarco-endoplasmic reticulum ATPase (SERCA) basal function[103,107]. hiPSC-CMs' transient kinetics show a substantial difference from those of adult CMs due to their ability to modulate [Ca^{2+}] during depolarisation and repolarisation. Depolarisation of CMs occurs when Ca^{2+} enters the cell via voltage-sensitive L-type Ca^{2+} channels (LTCC) and is quickly followed by a release of Ca^{2+} from SR via RYR, causing CMs contraction. Contraction occurs when raising [Ca^{2+}] directly stimulates the myofilament shortening, whereas relaxation is achieved by removal of intracellular Ca^{2+}. During repolarisation, three mechanisms are involved in Ca^{2+} removal: re-sequestering via the SERCA, extruding through NCX and slow mechanisms. In human ventricular CMs, 95% of the Ca^{2+} is removed via SERCA (85%) and NCX (10%) while the rest 5% via non-SR non-NCX slow mechanism extrusion which have been similarly observed in hiPSC-CMs. The major difference is the contribution of NCX, which in hiPSC-CMs accounts for around 30% of Ca^{2+} removal, compared to 10% in adult CMs[107]. Inefficient Ca^{2+} release and removal contribute to the longer rise time and slower Ca^{2+} decay assessed in hiPSC-CMs compared to adult CMs. Additionally, Ca^{2+} transients in hiPSC-CMs appear to be voltage dependent, similar to that of adult CMs. Transient amplitudes increase with the increase in magnitude of the depolarisation step used to activate I_{Ca}, however they are independent of direction of voltage change, which discriminates cardiac CICR from voltage-induced Ca^{2+} release specific to skeletal muscle[108]. Next, each compartment involved in Ca^{2+} regulation and excitation-contraction coupling in adult CMs compares to hiPSC-CMs will be discussed.

L-type Ca^{2+} channels are essential units in cardiac excitation-contraction coupling particularly $CaV_{1.2}$, the α-1C subunit of L-type Ca^{2+} channels. It has been shown to have similar expression level to adult heart[70]. Application of Ca^{2+} channel blocker has been observed in a similar manner to adult CMs. For example, the selective L-type Ca^{2+} channel antagonist, nifedipine, reduced hiPSC-CM transient amplitude[103]. This indicates that external Ca^{2+} is crucial to trigger a release of SR Ca^{2+} content in hiPSC-CMs. However, they respond unusually to Ca^{2+} channels agonist. Depending on the cell line, the Ca^{2+} channel activator FPL 64176 triggered an increase or decrease in calcium current[109].

RYRs are a high conductance Ca^{2+} sensitive channel on the SR membrane. In adult CMs, RYR closely connects $CaV_{1.2}$ to SR, contributing to CICR mechanism[110]. Activation of RYR2, the cardiac isoforms of RYR, through Ca^{2+} influx via L-type Ca^{2+} channels is key for inducing a mature calcium transient. In hiPSC-CMs, RYR expression is lower compared to adult CMs and diffuses throughout the cytoplasm. A large, rapid release of Ca^{2+} content from SR was assessed in response to caffeine[111], an antagonism to RYR, resulting in the reduction of whole cell Ca^{2+} transient amplitude. These characteristics observed in caffeine and RYR antagonism application are similar to that found in adult CMs.

Phospholamban (PLN) is a key regulator of SR function. The inhibition of SERCA by phospholamban is relieved by beta-adrenergic stimulated-phosphorylation.[112] Although PLN expression is comparable to adult CM, **SERCA2a** (the cardiac isoform of SERCA) expression is markedly lower in hiPSC-CMs[70]. This higher ratio of PLN:SERCA may be the cause of the low basal activity and the parallel ability of hiPSC-CMs to create a strong response to adrenergic stimulation[113,114].

Inositol-triphosphate receptors (IP_3R) are Ca^{2+} channels activated by inositol triphosphate. They act as dominant second messengers and are responsible for the induction of Ca^{2+} content release from intracellular storage. High IP_3 activity is a common feature of neonatal and failing adult human CMs[96]. In healthy adult CMs, Ca^{2+} storage mobilises on SR via IP_3R, which induces cardiac depolarisation and increases in intracellular Ca^{2+}. Hence, this mechanism promotes Ca^{2+} extrusion by forward mode NCX[115]. In hiPSC-CMs, U73122, an IP_3R antagonist, significantly reduced Ca^{2+} transient amplitude and diminishes at high concentration. The evidence shown in this study supports a complex role of IP_3-mediated Ca^{2+} release that subsequently propagate as Ca^{2+} waves in hiPSC-CMs[116]. However, full understanding of the IP_3R mechanism on intracellular Ca^{2+} regulation and a relation to other cellular components is lacking.

Sodium–Calcium Exchanger or NCX, NCX1 cardiac isoform, has a key role in maintaining Ca^{2+} homeostasis. NCX moves Ca^{2+} out across the membrane during systole in exchange for Na^+ at a ratio of 3:1 (Na^+:Ca^{2+}), generating a net positive inward current (I_{NCX}) and subsequently cellular depolarisation. Ca^{2+} cycling and cell membrane potential relationship is tightly regulated by NCX, creating an attractive source for therapeutic applications. A peak density current found in adult CMs (4.5 ± 0.5 pA/pF) is much higher compared to an average of < 0.5 pA/pF in developing CMs[117]. The Terracciano group showed that the NCX expression level in hiPSC-CMs is comparable to that of the adult human heart[70]. However, NCX contributes around 10% to Ca^{2+} extrusion in adult CMs compared to around 30% in hiPSC-CMs.[107] Low levels of SR

Ca^{2+} uptake and NCX-mediated Ca^{2+} extrusion in hiPSC-CMs result in the extremely slow Ca^{2+} decay rate.

Mitochondrial Ca^{2+} and its contributions are controversial whether the oscillation of mitochondrial Ca^{2+} is governed by active or passive calcium handling. Therefore, further investigation on mitochondrial Ca^{2+} is required.

Studies focussed on the CM specific phenomenon of CICR have given several insights into the regulation of Ca^{2+} handling in hiPSC-CMs, ultimately showing that hiPSC-CMs have immature intracellular Ca^{2+} regulation features and apparatus that more resemble neonatal CMs.

1.5.2.3 Contractile force

Force production is the key parameter of CM physiological function and is the essential purpose of the heart. Upon pacing, adult CMs presented positive force frequency responses (FFR), which means there is positive correlation between pacing rate, calcium transient and force of contraction. Negative FFR is observed in hiPSC-CMs. It is worth mentioning that there is no established gold standard for force measurement and is widely accepted that each technique cannot be directly compared. The ventricular myocardium generates isometric force of about 56 kPa, as measured by ultrasound[118]. In hiPSC-CMs, traction force microscopy (TFM), AFM and microarray pillar have been utilised to measure force production. This is due to the advantages each system offers. For example, TFM can be used in a long term observation of hiPSC-CMs in a tuneable stiffness substrate. AFM offers a higher flexibility as it measures the force directly from the cell contraction regardless of a substrate. However, it is a low throughput method. Studies in Engler *et al.* and Jacot *et al.* found that traction force generation in hESC-CMs depends on substrate stiffness, with the optimal stiffness that yielded the highest traction force being around 10 kPa, similar to native myocardium[118,119]. There is, however, a contradictory evidence as presented by Hesrch *et al*[120]. His group reported that force generation in CMs followed the Frank-Starling Law[121], which is that the force has a direct correlation to stiffness. Studies that were conducted on other species also showed a positive relationship between stiffness and force production. A study on single hiPSC-CMs, using a 2.5 MPa elastic modulus microarray needle substrate reported a traction force of 15 nN with a contraction rate of 1.46–1.74 μm/s[122,123]. A later study from Lui *et al.* used AFM to measure isolated single hiPSC- and hESC- CMs, showing 0.49 ± 0.45 nN and 0.23 ± 0.11 nN, respectively. A cluster of hiPSC-CMs produced higher force (average of 2.37 ± 0.16 nN) than an isolated hiPSC-CM, which could be partially explained by the collective movement of multiple hiPSC-CMs. Another study reported hESC-CM contractile force at an average axial force of 139 ± 29 nN and a total force of 144 ± 33 nN using TFM, showing

higher anisotropic contraction resembling that observed in adult CMs. Prolonged *in vitro* culture of up to 90 days on 4 kPa polyacrylamide (PAAm) hydrogels showed no sign of contractile force development[124]. Therefore, it is clear that there is a vast difference between the hiPSC-CM and the adult CM contractility, regardless of the fact that different techniques have been applied.

1.5.2.4 Response to stimuli

A response to external stimulation, including drugs, is the key monitoring factor clinicians use to predict the outcome of the treatments in patients. Using hiPSC-CMs in precision medicine could provide useful information on essential treatments and predict potential outcomes. Clinicians would be able to choose the optimal treatments based on patient-specific response. Therefore, this section will discuss drug response with changes in function and cell damage, compared to clinical data and adult CM response.

1.5.2.4.1 Drug response

In light of the previously discussed immature phenotype of hiPSC-CMs compared to adult CMs, it is expected that hiPSC-CMs also respond differently to pharmacological stimulation. Chronotropic responses have been observed in hiPSC-CMs and may be affected by time in culture. α, β1, and β2 adrenoceptor responses have been reported in hiPSC-CMs[125,126]. Isoprenaline, a β receptor agonist, is the most commonly used drug in studies on hiPSC-CMs. A positive response in beating rate has been observed irrespective of origin cell line and differentiation method, consistently demonstrating the presence of the β-receptor[84,85,114,126–128]. In the adult heart, isoprenaline not only increases contraction rate but also increases the amplitude of the calcium transient, force production and decrease relaxation time, exhibiting a positive FFR. Unlike adult CMs, force production in hiPSC-CMs is independent of isoprenaline concentration. The absence of inotropic reaction, even with an obvious chronotropic response upon β-adrenergic stimulation, points towards a neonatal-like SR. With increased time in culture, hiPSC-CMs demonstrated an increase to chronotropic β agonist response without any improvement in inotropic reaction[125,126]. In summary, a β adrenoceptor response is present in hiPSC-CMs and there are common characteristics with foetal CMs. Another drug used to study hiPSC-CM response is carbacholine, a cholinergic agonist. These studies demonstrated that carbacholine increases beating rate, described as a chronotropic response of muscarinic receptor activity[126,129,130]. This is similar to the immature β-adrenergic receptors present in foetal heart, the lack of G-proteins that couple receptors to adenylate cyclase, leads to a reduced response[131]. Finally, phosphodiesterase inhibitor, IBMX, and the adenylyl cyclase activator forskolin increase

the contraction rate of hiPSC-CMs by increasing intracellular cAMP[132]. In conclusion, hiPSC-CMs respond to adrenergic stimulation differently from adult CMs, resembling neonatal CM response.

1.5.2.4.2 Sensitivity to damage and apoptosis

hiPSC-CMs are viewed as a promising tool to study cardiotoxicity in pharmacological development and patient-specific responses from FDA-approved and in-trial drugs. There are many studies demonstrating their power as predictive tool for early stage drug screening prior to clinical trials. Direct application of oxidisers was reported to induce an apoptotic response in hiPSC-CMs[133–135]. The mechanism of this apoptotic induction has been shown to be modulated by opening of the mitochondrial permeability transition pore, which is reported to be inhibited by anaesthetic-mediated pre-conditioning using isoflurane. hiPSC-CMs derived from patients who suffer from doxorubicin-induced cardiotoxicity (DIC) can be clinically rescued from the prediction of DIC observed *in vitro*[136]. Cardiotoxic tyrosine kinase inhibitors, such as sunitinib and sorafenib demonstrate arrhythmogenicity and increase in induced cell death in hiPSC-CMs similarly to toxic doses of the drug shown in the clinic[137,138]. Additionally, ischemic models of hiPSC-CMs *in vitro* have been demonstrated to respond to human specific pharmacological post-conditioning drugs[139]. In summary, hiPSC-CMs are sensitive to oxidative stress, cardiotoxic agents and patient-specific responses similarly to clinical data. Additional studies are required to fully understand the mechanisms underlying these responses.

1.5.3 Gene expression

The structure and function of hiPSC-CMs are considered immature because they resemble foetal CMs more than adult CMs. These immature phenotypes may at least partly result from differences in gene expression. The transcriptional profile of hiPSC-CMs is significantly changed from their starting hiPSCs. Key differences include loss of pluripotency markers and upregulation of mesodermal, cardiac mesodermal and cardiac transcription factors. In this chapter, gene expression of human adult CMs will be compared with hiPSC-CMs.

Several myofibrillar protein isoforms undergo variation in expression during development, indicating changes in function of the human CM over time. Titin, which regulates sarcomere integrity and elasticity, shifts from the relatively elastic N2BA isoform to the stiffer N2B isoform, regulating the passive tension in CMs as they develop[140,141]. Troponin I switches from the slow skeleton isoform (TNNI1) to the cardiac troponin I (TNNI3) found in adult CMs, suggesting maturation of CMs[142]. This pair of genes has been demonstrated as a robust marker for cardiac maturation due to their stability and consistency over physiological and pathological conditions.

Myosin heavy chain (MHC) also switches isoform during development. MYH6 (α-MHC) expression levels have been shown to decrease during development, while the ratio of MYH7 (β-MHC) to MYH6 increases as maturation level improves. This change in expression *in vivo* correlates with a postnatal decrease in heart rate and cardiac hypertrophy[143]. In hiPSC-CMs, these cardiac structural markers have been shown to be similar to neonatal CMs, expressing a higher level of N2BA, lower ratio of TNNI3:TNNI1 and MYH7:MYH6 compared to adult CMs. This remains stable in prolonged culture[144]. Myosin light chain (MLC) has been demonstrated to be a chamber specific marker. MLC2a is predominantly found in atria but is also expressed in ventricles. It gradually decreases with development and is replaced with MLC2v, which is specifically expressed only in ventricular myocardium[20]. Additionally, electrophysiology related gene expression has been extensively characterised. It was mentioned previously that the expression levels of KCNJ2 and HCN4 found in hiPSC-CMs are much lower compared to adult CMs. This results in a unique characteristic of hiPSC-CMs, which is spontaneous beating. SERCA gene expression has been found to increase throughout development of the myocardium[145]. Phospholamban, RYR2 and calsequestrin have been observed at a lower expression level compared to adult CMs[70,146]. This correlates to immature SR and some mixed functional responses to caffeine, β-adrenergic activator, cholinergic agonist, adenylyl cyclase activator and thapsigargin mentioned previously. ADRA1A (α-adrenoceptor) has been detected in adult CMs whereas it is absent in hiPSC-CMs. Finally, many researchers speculate that maturation processes may be driven by genetic factors found in native tissue, shown in ***Figure 4***. In conclusion, cardiac gene expression related to both function and structure shows similarity to developing CMs, which correlates to immature function and structure. These ratios remain stable over time, suggesting that normal *in vitro* culture is not sufficient to induce a mature gene expression profile.

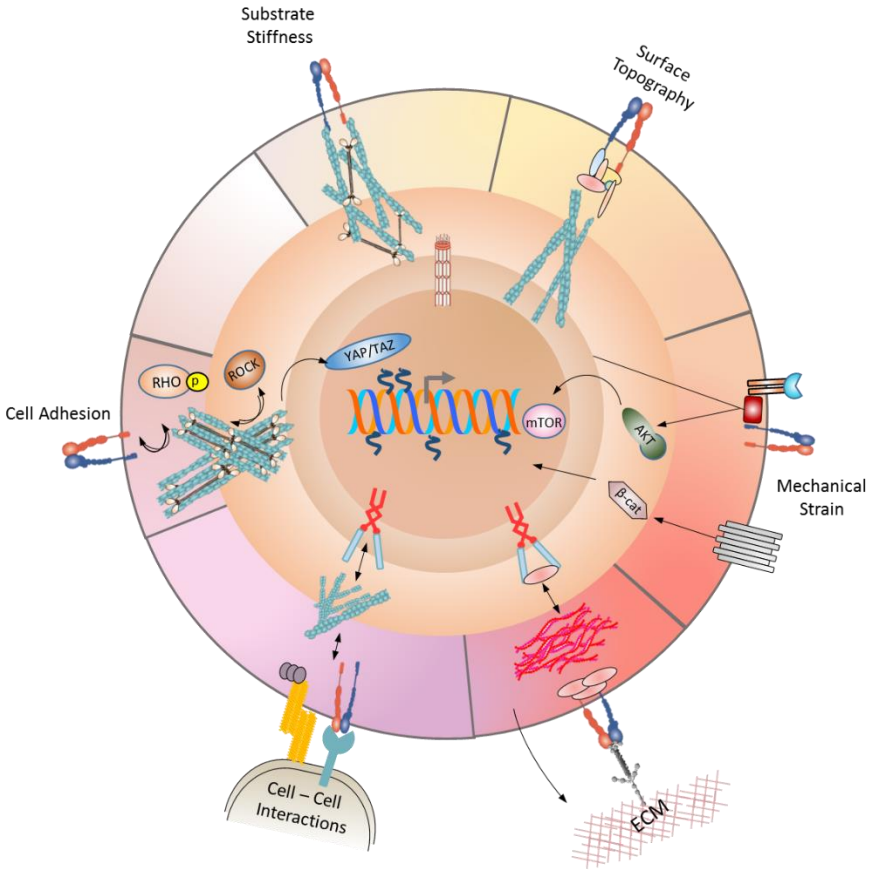

Figure 4: Selected Extracellular forces influence the CM's epigenetic status. *The mechanical manipulation involved in the CM's responses. This figure was illustrated based on findings from various sources: Cell adhesion*[147,148]*, Cell-Cell interaction*[149]*, ECM*[22,71]*, Mechanical strain*[25,94,150,151]*, Surface topography and stiffness*[71,119]*.*

1.6 *In vitro* manipulation of hiPSC-CMs

The immature features of hiPSC-CMs hamper the full realisation of their potential in medical applications. The comparable phenotype found in various laboratories suggests that the properties described are fundamental to hiPSC-CMs, raising the question whether hiPSC-CMs can develop adult CM-like function and ultrastructure *in vitro*. Therefore, the idea of *in vitro* maturation by using an engineered microenvironment mimicking *in vivo* stimulations has been widely explored. Numerous techniques have been used to encourage cell maturation, such as long-term culture, external stimulation and co-culture, amongst others. In this chapter, different maturation strategies will be discussed including incorporation of biomaterials.

1.6.1 *In vitro* long-term culture of hiPSC-CMs

The heart takes several years to fully develop and display adult, mature physiological structure and function. In most differentiation protocols, the current length of time for *in vitro* differentiation of hiPSCs to hiPSC-CMs varies from 7 - 15 days using monolayer-based culture; hence, an initial approach to produce more mature hiPSC-CMs is by a prolonged maintenance in culture. Studies showed that time in culture impacted the function and structure of hiPSC-CMs. When cultured for up to 30 days-, hiPSC-CMs demonstrated an improvement in sarcomeric organisation, expressing Z- and I- bands as compared to 15 days differentiation protocol. From 30 to 90 days in culture, hiPSC-CMs developed more matured sarcomeric organisation with visible Z-, I- and A- bands. However, after 360 days in culture, only some hiPSC-CMs displayed formation of M-bands.[152] Lundy *et al.* investigated the differences in function, structure and gene expression of hiPSC-CMs maintained for 20 - 40 days ('early stage') and 80 - 100 days ('late stage') in culture. The study observed in the late stages that hiPSC-CMs structure exhibited a higher percentage of multinucleation, increased sarcomeric organisation and cell size with elongated shape. Action potential and Ca^{2+} handling of late stage hiPSC-CMs were improved in both upstroke velocity and amplitude. Upregulation of MYH7, MYH6, GJA1 and SERCA2 expression was observed with increasing time in culture. This study concluded that hiPSC-CMs are capable of slowly maturating, but whether this process may continue to more closely resemble adult CMs is unknown[153]. Dias and his group developed customised software to monitor the structure of hiPSC-CMs in real-time in prolonged *in vitro* culture. The work showed that multinucleated hiPSC-CMs numbers peaked at day 90 (40%) while sarcomeric length increases to around 1.6 μm and remained unchanged. Cardiac contents of cTnT increased to 22% of adult CMs microtissue[89]. Electrophysiological improvements were reported, such as an increase of I_{to1}, I_{k1}, $I_{Ca,L}$ and I_{Na} density with an upregulation of GJA1, SCN5A, JCNK2 and CACNA1C gene expression. However, the hiPSC-CMs still beat spontaneously[88]. After unsuccessful attempts to mature hiPSC-CMs by long term *in vitro* culture, researchers speculated that *in vivo* maturation, providing relevant environments, could improve hiPSC-CMs' function and structure. Kadota *et al.* investigated hiPSC-CMs engraftment in neonatal and adult rat heart and monitored their functions. In neonatal hearts, hiPSC-CMs demonstrated a small improvement compared to native heart that reach adult size and structure in 3 months. The improvement was induced at a faster rate in adult heart. The mechanism of maturation remains unknown, speculations include the environmental mismatch from different species or cell-autonomous factors[154]. The *in vivo* studies showed hiPSC-CM plasticity and potential to improve their function, structure and gene expression towards that resembling adult CMs and its dependency on culture environment.

Hence, many laboratories have alternatively developed hiPSC-CM platforms by manipulating relevant factors, such as humoral, electrical, mechanical and co-culture environments.

1.6.2 Biochemical stimulation

Cardiovascular homeostasis as well as cardiovascular pathophysiology depends on neurohormonal systems. Activation of neurohormonal pathways is a crucial factor for cardiac development and disease onset and consequently target to accelerate maturation. Cardiovascular growth, for example, is regulated by vasoactive and growth hormones. This chapter will discuss the impact of hormones as a regulator of cardiac growth and development.

Recently, Chng *et al.* showed for the first time that a conserved hormone plays an essential early role during embryogenesis, effectively orchestrating the development of the heart. This hormone is a transcript from gene *ELABELA* (*ELA*). Together with the apelin receptor (*aplnr*), ELA forms a crucial signal for early cardiovascular development. Loss of *ELA* leads to abnormal heart formation[155]. Another of the most studied hormones in cardiology is the thyroid hormone (TH), triiodothyronine (T3), that has been shown to affect metabolism, growth and development in humans. It has been intensively studied for its role in physiological development and treatment of disease. TH actions are mediated by two TH receptors, TRα and TRβ that show differential patterns of expression in development and in adult tissues[156]. After birth, T3 concentration increases with liganded TRα increasing concomitantly with heart rate increase. Upregulation of phospho-mTOR, ANP, and SERCA2a in response to T3 promotes maturation and hypertrophy of foetal CMs[157]. *In vitro* studies showed evidence that elevated T3 accelerates the maturation rate of hiPSC-CMs. After a week of treatment, hiPSC-CMs increased in size, anisotropy and sarcomeric length. CMs increased 14% in width, 31% in binucleation and 500% in p21 protein while it reduced 39% in proliferation and 150% in cyclin D1 protein, indicating post-mitotic transition occurs in CMs. Functionally, contractile force increased nearly 2-fold per beat along with improved Ca^{2+} handling[158,159]. In disease modelling, a combination of T3, insulin-like growth factor 1 and dexamethasone induced a hypertrophic cardiomyopathy phenotype. These factors synergistically enhanced bioenergetics and contractile force generation[160]. Finally, sex hormones have been shown to induce cardiovascular diseases in humans, such as stroke and MI. However, underlying mechanisms involved in development of these diseases are under investigation.

1.6.3 Electrical stimulation

The heart starts beating very early during embryogenesis. From this point on, the heart can generate and propagate its own electrical impulse for effective beating. This suggests that continuous activation is important for CM development and could be used to mature foetal-like CMs. In the adult heart, electrical synchronicity is governed by the cardiac conduction system (CCS), consisting of various components that are dedicated to a specialised task. For instance, pacemaker myocytes, located in the sinoatrial node (SAN), generate the electrical impulse, which is then propagated throughout the atrial myocardium and decelerated in the atrioventricular node (AVN). This cascaded mechanism creates a pattern whereby the atria contract while the ventricles fill up, then the ventricles in turn contract and eject the blood to the body[161,162]. In two pivotal studies, Radisic *et al.* reported a relationship between electrical field stimulation and the enhancement of CMs alignment, synchronous contractions, and structure. By introducing carbon rods in a highly oxygenated atmosphere, hiPSC-CMs have been shown to beat synchronously with ordered sarcomeric development and improvement in the Ca^{2+} handling amplitude and upstroke/decay rate[163]. Further studies have shown that pacing frequency and starting point affect hiPSC-CM structure. Gradual increase of pacing frequency from 1 - 3 Hz or 1 - 6 Hz over time induced physiological hypertrophy, increased sarcomeric alignment and faster Ca^{2+} cycling and action potential[164]. Additional studies have implemented the effect of electrical stimulation on various starting points. Early stage electrical stimulation demonstrated a higher functional and structural improvement compared to later stage[94,165]. Early electrical stimulation also increased conduction velocity by increasing Cx-43, NCX, KCNH2 and KCND2 potassium channels function[166]. An alternative electrical stimulation method resulting in field stimulation is through conductive biomaterials that are versatile, as they are capable of conducting electrically and ionically, and can have tuneable mechanical, chemical and electrical properties to suit the desired applications[167]. The conductive polymer could establish a communication between cells *in vitro* or bridging the signal between interrupted cells in the damaged area of the heart. Numerous studies have been shown to support the utilisation of conductive biomaterials. CMs cultured on aligned composite nanofiber of polyaniline (PANI) and poly(lactic-co-glycolic acid) showed fully coupled behaviour as well as Cx-43 expression in each isolated cluster, appearing to beat synchronously. Electrical stimulation through the conductive polymer synchronised individual clusters, indicating a capability of a PANI cardiac patch to support cell development and differentiation[168–172]. Although it is clear that electrical stimulation produces more mature function and structure, the underlying mechanism remains unknown.

1.6.4 Mechanical stimulation

The role of mechanical forces in shaping the heart during cardiogenesis has been widely accepted. It is also acknowledged that the heart is subjected to dynamic mechanical changes since its formation. Biomechanics fundamentally affect early cardiac development, from looping to the development of chambers and valves as well as inducing and choreographing local and global molecular and cellular changes. Constant interactions between cardiac tissue motion and haemodynamic shape the development of the heart[173]. During cardiac contraction-relaxation cycles, each beat imposes large compressive and tensile mechanical forces, which differ to the shear force exerted by blood flow. Cardiac contraction generates a notable mechanical force on the myocardial wall (preload and afterload) and vessel. The fundamental principles are described by the Frank–Starling mechanism and Bowditch phenomenon[35,174]. At the molecular level, MYL2a knockout mice embryos have impaired contractility and, consequently, reduced blood flow. This cardiac defect leads to impaired yolk sac vessel remodelling where high-shear flow is needed[175,176]. Building the beating heart *in vitro* continues to be an arduous bioengineering challenge where hiPSC-CMs are the centre of mechanosensitive studies. Different mechanical loading schemes have been explored. A 2-week dynamic rocking culture of neonatal rat CMs significantly increased their size, contractile force, conduction velocity and expression of sarcomeric proteins, such that they approach those of adult CMs, compared to static *in vitro* culture. hiPSC-CMs cultured under the same condition increased around 2.5 times in contractile force and 1.4 times in conduction velocity. The study identified that mTOR signalling is essential to this improvement[151]. Applying 1 Hz of uniaxial cyclic stretch increased sarcomere alignment and gap junction density. Genes encoding for ion channels were upregulated, resulting in improved Ca^{2+} handling[177,178]. Gradual increase in static stretch, mimicking cardiac development, resulted in shortening of Ca^{2+} handling kinetics[178]. Additionally, engineered heart tissue with dynamic stretching to increase mechanical load enhanced hiPSC-CM contractile force. The level of improvement was different in isometric, isotonic or auxotonic loads, with auxotonic mode being superior to other less physiological loading regimes[179].

Besides dynamic contraction, static components of the myocardium, such as ECM, accumulates in the heart to provide structural support to facilitate the development. The mechanical properties of the ECM, especially stiffness and geometric boundary, have a profound effect on how CMs develop and perform[94,180–182]. The elasticity is dynamic and increases over time, reaching a plateau in adults. The optimum elasticity for a long-term CM *in vitro* culture vessel has been reported to be approximately 9 – 14 kPa. Neonatal rat ventricular myocytes (NRVMs)

cultured under this condition exhibited a recapitulation of regular beating at 1 Hz with well striated sarcomeres[119]. Furthermore, time-dependent stiffness hyaluronic hydrogels were fabricated by Young *et al.* The system was designed to increase its stiffness *in situ* over time in the culture from 0.5 to 10 kPa. Chicken embryonic CMs were cultured for 2 weeks, showing a 3-fold improvement of cardiac specific markers compared to a static stiffness system (PAAm hydrogel)[183]. In disease, the presence of a stiff ECM deposited after cardiac ischemia negatively affects the heart function and structure. Left ventricle biopsy of myocardial infarcted patients showed a direct relationship between an increased stiffness and a chance of developing heart failure[184]. This increase in stiffness has been shown to pathologically increase the magnitude of cell systolic forces[185–187], pushing CMs to adapt to excessive preload by abnormal enlargement or pathological hypertrophy of CMs, and thickening of the myocardium. This pathological change develops into cardiac dysfunction and eventually terminal heart failure.

1.6.5 Topographical influence

Geometry and isotropy are essential to achieve coordinated tissue contraction. During development, myofibrillogenesis is achieved by serial alignment and parallel bundling of CMs, guided by ECM remodelling from fibroblasts[149,188,189]. The importance of CM alignment is not only demonstrated within the native cardiac structure in the human heart, but also in several *in vitro* studies. The influence of synthetic 2D substrate patterning on cells was pioneered by Curtis *et al.* in 1964[190]. The researchers analysed the role of topographical patterning on various cell types, such as ECs, fibroblasts, and epithelial cells. The group demonstrated that cells effectively aligned and followed the directional grooves. Recently, the field has grown rapidly, and it is now widely accepted that 2D patterning in the range of micro- and nanometre scale influences different cellular processes, including proliferation and differentiation[191–193]. A study on NRVMs showed that changes in myofibrillar orientation and architecture were affected by both surface area and aspect ratio. The optimal aspect ratio was determined to be 7:1 and 5:1 as the result of the optimal formation of sarcomere organisation[72,194]. Therefore, CMs are plastic and can be modulated by ECM topography throughout an individual's life in development, healthy and disease. Delineating the mediators of the relationship between topography and CM function and structure would go some way to provide insights into therapeutic targets and improve on the accuracy of cardiac disease models.

Morphogenesis in a 3D microenvironment should occur in a similar way to the natural cardiac development. Kim *et al*. showed that aligned CMs on a 3D micro-grooved cantilever yielded a 67–88% increase in displacement compared to a flat surface, due to higher contractile

force generated[195]. Previous studies have attempted to provide grooved surfaces for CMs to mimic the native environment as a pseudo 3D platform. The results showed that the orientation and shape of the CMs were guided by micro-grooved surfaces[196–198]. The micropatterned surfaces have also been shown to alter gene expression, protein localisation, cell signalling, nuclear eccentricity and intracellular Ca^{2+} dynamics in CMs[199]. Rao *et al.* studied healthy hiPSC-CMs cultured on microgroove PDMS. After 2 weeks, Ca^{2+} handling properties of hiPSC-CMs were significantly abbreviated in time to peak. SR Ca^{2+} release improved in response to caffeine but these changes were not associated with gene expression[70]. Trantidou *et al.* have created an *in vitro* model using microgroove Paralene C on planar multi-electrode arrays. Aligned CMs showed a conduction velocity (CV) profile comparable to the myocardium. The fastest impulse propagation was observed along the long axis of the aligned CMs and the slowest propagation was found in perpendicular direction. This model provided a significant improvement, being more physiological than standard cultures where action potential propagates isotropically (CVL ≈ CVT)[200]. For cardiac regeneration using 3D engineered heart tissue, Zimmerman *et al.* studied freshly isolated cardiac cells from neonatal rats cultured on collagen I hydrogels, under dynamic mechanical load. The setup induced formation of interconnected and longitudinally orientated bundles of CMs, highly resembling adult native tissue[201]. Decellularised scaffolds have also been studied as the closest resembling matrix to recapitulate an *in vivo* system. The scaffold has been shown to maintain matrix components and structure in mouse[202], dog[203] and pig[204]. Recent work significantly improved the decellularised scaffold for engraftment of hiPSC-CMs. This was modelled as a scaffold with multiple complexities for functional human myocardial-like studies[205]. CMs are highly dynamic and variable in terms of their 3D structure, biomechanical, and biochemical microenvironments. To fully understand how cells form tissue and function, it is crucial to study how single cells behave as a part of the whole living heart.

1.6.6 Co-culture of stem cell derived CMs and non-myocyte cells

Synergy between CMs the contractile cells of the myocardium, and the non-myocyte components of the heart not only regulate cardiac development but also maintain healthy, adult CM function. Within the myocardium, each CM is surrounded by an intricate network of capillaries and is in close proximity to endothelial cells, as well as sympathetic neurons, vascular smooth muscle cells and resident lymphocytes. These cells are woven within ECM regulated by cardiac fibroblasts and form structures essential for the vascular supply required for efficient CM contraction and long-term survival.

Cardiac fibroblasts are one of the most studied cell types. They are responsible for cardiac ECM remodelling, guiding deposition and dynamic scar formation of infarcted heart tissue. This change directly affects CM function and structure, especially in pathological and physiological cardiac hypertrophy. Many studies have shown the importance of cardiac fibroblasts to CM function and structure in 2D format. A ratio of 3:1 (CM and fibroblast) *in vitro* co-culture improved sarcomere structure, demonstrating visible Z-band and H-disk. Conduction velocity increased to the level comparable to adult CMs. Gene expression exhibited an upregulation of atrial natriuretic factor, B-type natriuretic factor, MYL7, MYL2 and MYH7/MYH6[206]. Another study showed that a co-culture of primary CMs and fibroblasts produced phenotypes that more closely resembled adult CMs in both direct and indirect interactions on fibroblast-derived matrix[207]. Researchers looked into the electromechanical function of cardiac muscle and found that intercellular resistance increased with a maximal functional connectivity at 75% fibroblasts. They also showed that cardiac cell-cell junction is a function of cell density[208]. Additionally, co-culture of hESC-CMs and endothelial cells resulted in more uniform sarcomeres and Cx-43 localised at the longitudinal end of hESC-CMs located near the intercalated discs[209]. A demonstration of co-culture of neurons with CMs showed no significant increase in beating rate when propranolol was applied to the culture, indicating a formation of functional synapse between neurons and CMs[210]. Numerous studies using co-culture in 3D system to align CMs with non-myocytes, such as endothelial cells, showed that co-culture promoted cardiac function and prolonged cell survival in *in vivo* engraftments in an MI model, emphasising the importance of multicellular interactions within cardiac diseases[177,211]. These studies suggested the cross-talk between CMs and non-myocytes would recreate more *in vivo* like environment.

Finally, a combination of co-culture with primary fibroblasts and endothelial cells in conjunction with dynamic stretch and electrical stimulations demonstrated structural improvement on hiPSC-CMs, which included t-tubule-like structures, improved alignment and presence of Z-

,M-,I-line and A-band[94]. With these progress in stem cell-derived CM function and structure, great effort has been made to advance cardiovascular disease treatment, precision medicine and disease modelling. The next section will outline the progress of hiPSC-CMs and its medical applications created in the past decade.

1.7 Cardiac treatment: applications of biomaterials

1.7.1 Fundamental studies and *in vitro* disease modelling

Fundamental studies on stem cell fate within *in vitro* microenvironments expand knowledge in cardiac development and disease progression. This leads to the advancement in design of targeted therapeutics and regenerative treatment of complex cardiovascular diseases. Precise control of the microenvironment from the sub-cellular level is the most important component to study cell-microenvironment interactions *in vitro*. Over the last two decades, bio-functional materials have been successfully developed and utilised in biological and medical research. This establishes a diverse toolbox for dynamic and static generation, manipulation and stimulation of various extracellular interactions via biochemical, electrical and biomechanical signals for *in vitro* studies. As shown in ***Figure 5***, engineered biomaterials have revealed independent effects of individual stimuli on cell fate, such as cell shape[212] and geometry[72,213,214], ECM rigidity[215], topography[70], extracellular forces[94,151,216], dynamic culture[151,217] and electricity[164], in regulating cellular behaviours, such as cell adhesion, migration, proliferation, differentiation and apoptosis. These interactions between each cue on cell fates have previously mentioned in Section 1.5. Recent exploits with a clear goal on maturation of hiPSC-CMs in cellular mechanobiology have been generated from the accelerated development of engineered biomaterials accompanied by high-throughput characterisation techniques.

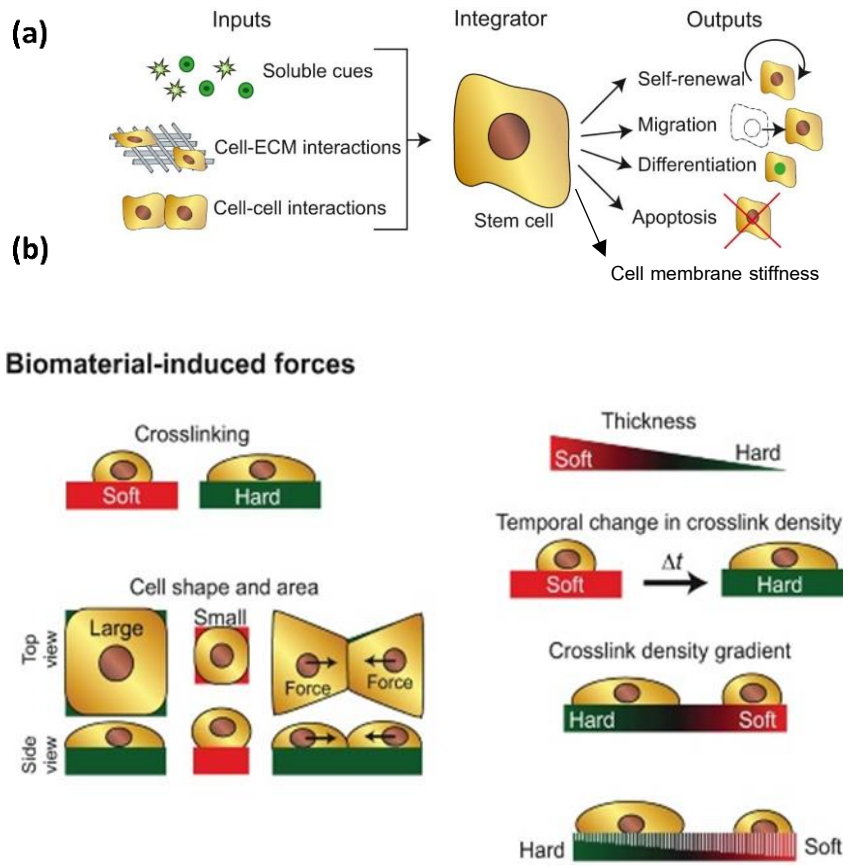

Figure 5: The stem cell as a biological integrator. *(a) A stem cell can integrate several input types to result in an output that is the often the amplified summation of all cues it received. (b) External stimulations provided by external force and biomaterials. Adapted from Kumar et al.*[218].

1.7.2 Cardiac Repair and regeneration

The current state-of-the-art treatment for MI patients is aimed at delaying disease progression, relieving symptoms, reducing morbidity and improving survival. The available options for treatment are cardiac reperfusion via coronary stents or surgical bypass to regain the blood supply. In addition, medication, such as β-blockers and anticoagulants are often used to manage associated problems, which prevents further heart attack, ultimately reducing mortality. Further progress of the disease with cardiac arrhythmias is often managed by a pacemaker to rectify the irregular heartbeat. As disease progresses from MI to end stage HF, heart transplant is the only treatment, leaving patients under a life-long regime of immunosuppressive drugs that can lead to many medical complications. Although these treatments ameliorate the disease and symptoms, they do not truly recuperate from the damage caused by cardiovascular diseases. As such, the use of stem cells is aimed towards realising the ambitious goal of cardiac regeneration.

Cardiac regeneration remains a common aim amongst scientists and clinicians. The first experimental cell-based therapy was conducted in 1992 by Marelli *et al.* The group isolated skeletal muscle cells and expanded these cells *in vitro*. At that time, these cells were hypothesised to be a neo-myocardium-pool. Cell suspension was injected into canine hearts and characterised between week 8^{th} – 14^{th}. Technically, the implantation was successful. Immunofluorescent staining showed muscle tissue surrounded by scar. However, isolating implanted cells from the host tissue, showed no transformation to myocytes[219]. In 2008, Menasche *et al.* conducted a multicentre, randomised, placebo-controlled, double-blind clinical study called The Myoblast Autologous Grafting in Ischemic Cardiomyopathy (MAGIC), following a successful phase I clinical study of autologous myoblast transplantation. This trial involved a treatment of cells grown from a skeletal muscle biopsy or a placebo solution injected in and around the scar. MAGIC demonstrated no significant difference between treated and placebo group[220]. hESC-derived cardiac progenitors were introduced into the clinic in 2014[221]. These cells derived from I6 hESCs embedded in fibrin were then sutured onto the epicardial surface of the infarcted region. Although the patch failed to integrate electrically with the host myocardium and to directly contribute to contractile force, the patient was symptomatically improved after 3 months. No implication from arrhythmias, teratoma formation or immunosuppression-related adverse events was clinically observed. The authors speculated paracrine effects to be the key mechanism for the observed improvements[222]. Currently there are two plans for Phase I clinical trials: Wu's group at Stanford University and Murry's group from University of Washington. Dr Wu focuses on treatment of end-stage heart failure by using a chemically defined culture system developed in his group[223]. hiPSC-CMs will be implanted to patients with a left ventricular assist device as a bridge for heart transplantation. Another study led by Dr Murry and Liu *et al.* showed successful remuscularisation of the infarcted macaque heart with hESC-CMs by directly injecting to the infarcted area. After a month, the injection fraction improved by 11% with an additional 12.4% after 3 months. The engraftment showed electromechanical integration and contained 99% ventricular CMs[224]. The authors proposed future plans consisting of extending the length of the animal trial and recruiting patients for clinical trial. Tabei *et al.* injected hiPSC-CM spheroids in farm pigs and observed no detrimental effects on cell viability and spheroid shape/size using a developed device containing multiple needles[225]. These findings have shown a promising therapeutic effect of stem cell-based treatment to regenerate diseased heart, although different delivery methods and routes of injection must be taken into account.

As the premise is that the transplanted cells need to engraft only transiently, the priority is to optimise their early retention using biomaterials, offering the potential to control cardiac

remodelling and redirect the adult heart to a regenerative state, and possibly to switch towards the sole administration of their secretome. Modification of the environment using engineered tissue is thought to improve cell survival and retention, while also promoting cell integration. Biomaterials have great potential in cardiac repair and regeneration, guiding the transplanted cells to perform the desired function in the native tissue, strengthening the tissue, supplying cells and/or growth factors and bridging electrical and/or mechanical stimulation across the infarcted region to regain cardiac function. Initially, natural (gelatin[226], collagen[227], alginate[183,228,229], chitosan[230–232], and fibrin glue[221]) and synthetic (poly(lactic-co-glycolic acid) or PLGA[233], carbon nanotubes[164,234], and polyurethane[235]) biomaterials have been investigated as candidates for cardiac regeneration[236]. Collagen hydrogels have many advantages over other natural polymers, such as being easy to obtain, offering mechanical support and playing a pivotal role in heart development[237,238]. Acellular collagen patches have been shown to support the infarcted heart's contractility and attract various native cells[239]. Collagen patches can be modified to slowly release vascular endothelial growth factor-16, promoting wall thickening with elevated angiogenesis in the defective heart[239]. The findings indicated that growth factor immobilisation promoted cell recruitment and proliferation. Further work from Rosca *et al.* showed that collagen scaffolds populated with endothelial progenitor cells induced vascularisation and preserved ventricular function after MI in a rat[240]. These studies showed beneficial effects of endothelial cells and its derivatives. Another widely used biomaterials is alginate, a derivation of seaweed. Injectable alginate delivered into the myocardium can be degraded and fully replaced by native ECM within 6 weeks, ameliorating the adverse effect of MI[228]. Finally, fibrin hydrogels, used to prevent cardiac rupture, were chemically modified as a scaffold delivering soluble factors and cells to the heart. *In vivo* studies demonstrated the preservation of the infarcted region's wall thickness and cardiac function[227,241]. A composite natural biomaterial of alginate-chitosan prevented adverse cardiac remodelling and promoted tissue repair in a rat model[242]. The current excitements highlight the development of synthetic biomaterials, such as conductive polymers. They hold the potential to regain electrical communication between cells separated by damaged area, whilst mechanically support myocardial wall. Recently, Stevens' group demonstrated the beneficial effects of first-generation and second-generation conductive polymers *in vivo* and *In vitro*, showing a beneficial effect in MI rat models. These preclinical trials in animals have demonstrated reduction in scar size, promotion of microvessel formation, cardiac remodelling and improved electrical communication between cardiac cells, which resulted in increased cardiac ejection fraction and function. However, hiPSC-CM interaction on conductive polymers have not yet been reported.

Clinically, the natural biomaterials (collagen, alginate and fibrin) have been recently studied as injectable hydrogels or patches. Alginate hydrogel, acting as a support to myocardium, preventing further enlargement, has been demonstrated in several clinical trials including Phase I and II studies in acute MI patients (NCT00557531, NCT01226563, NCT01311791). The alginate hydrogels were found to be a more effective treatment in advance chronic HF patients than the standard medical therapy alone[243,244]. Mann *et al.* administered Algisyl via limited anterior thoracotomy and demonstrated that the biomaterials could provide (sustained for 1-year) benefits in clinical status in patients, such as reduced cardiac-related mortality and re-hospitalisation rate[245]. An international, randomised, double-blind, controlled trial on 303 MI patients after a successful percutaneous coronary intervention with IK-5001 was conducted involving the injection of Algisyl. Although the study showed a reduction in mortality rate, presence of vascular thrombosis and significant arrhythmia rate, thus requiring further investigation before the definitive clinical application of this biomaterial.

Many questions on the interaction mechanism of biomaterials on myocardium remain to be answered. The major concern of stem cells and biomaterials in cardiac regeneration is the integrability of the biomaterials. Although there are limited studies that specifically focus on the risk of arrhythmia, a recent study showed that electronic properties of biomaterials dictate the degree of the electrophysiological changes[230,246]. The future of biomaterials and tissue engineering is moving toward optimising the cellular combination which is vital for the success of the engraftment and cardiac regeneration.

1.7.3 Drug screening

Cardiotoxicity accounted for at least 45% withdrawal of FDA-approved drugs from the market between 1953 – 2013[247–249]. Up until today, virtually all drug screenings paradigms heavily rely on the use of *in vitro* culture of a single cell type, grown in an artificial environment of very different biochemical, mechanical and electrical cues from the native organism, posting several challenges including their poor predictive capacity[70,250]. Moreover, employment of animal models also imposes severe limitations. Despite extensive testing with current models, cardiovascular toxicity can occur due to the species mismatch in factors, such as pharmacokinetic, mechanism of action and other physiology contributions, creating a major barrier in optimising a model for cardiac disease. These challenges are amplified by the difference in the pathologies between humans and animals. Human diseases are human-specific in terms of onset, progression and termination, affected by different behavioural factors and attributed to variation of pathologies. To ameliorate the aforementioned challenges associated with off-target effects and cardiotoxicity,

studies using human-specific tissue have been proposed. However, many difficulties limit the use of human tissue for drug screening, such as ethics around human sample collection, availability of specimens with end-stage symptoms, fast dedifferentiation and capability to recapitulate native environments.

Table 3 summarises the benefits and limitations of disease models currently available and used for drug screening. Currently, the main *in vitro* assay for standard testing is hERG assay. hERG channels are voltage-gated K^+ channels that, if blocked, would potentially lead to prolongation of the QT interval (acquired long QT syndrome)[251]. The industry standard is to use Chinese hamster ovary or human embryonic kidney cells expressing hERG proteins whose electrophysiological properties are substantially different in comparison to human CMs. Particularly, a single channel characteristic does not accurately represent CM electrophysiology of a disease that usually regulated by the concurrent activity of multiple ion channels.

Table 3: Status of physiological and pathological modelling. *Table summary benefits and limitations of currently available disease models. This table has been reproduced from W. Kit-Anan et al.*[39]*.*

Model type and description	Benefits	Limitations	Ref.
Animal: Animals with defined genetic background or subject to acute intervention (e.g. coronary obstruction) to mimic discrete time point.	• **Small animals**: delineate molecular pathways in early or late stage heart failure, aiding identification of biomarkers and therapeutic targets. • **Large animals**: preclinical proof of concept for novel therapies before clinical trial.	• Species mismatch • Differences in physiology, biochemical absorption, distribution, metabolism and immunoresponses.	252–258

Human-specific expression in Chinese hamster ovary (CHO) and human embryonic kidney (HEK) cells: Model protein force expression e.g. test off-target effects to ion channels prolonging QT interval.	• Expression of human ion channels. • Avoids the expense of whole animal studies. • Reproducibility	• Single ion channel does not recapitulate disease in humans. • Species mismatch.	259,260
Adult human CM: Isolated from diseased or non-diseased during surgery.	• Human genome so can map response in humans to cardiac disease.	• Limited quantities (e.g. ethical limitations). • Large variability in phenotype • Rapid dedifferentiation.	261–264
Organoids: 3D *in vitro* culture systems derived from self-organizing stem cells and ECM proteins secreted from the cells	• Higher complexity compared to 2D models	• Expensive • Technically challenging setup • Poor reproducibility	265,266
3D cardiac tissue: 3D *in vitro* culture systems with natural and/or synthetic ECM structural support	• Ease of manipulation • Decellularised scaffold for cell adhesion mimics naturally occurring macro- and micro-structures	• Limited information on cost, reproducibility and performance	94,267,268

The field is currently focused on the use of stem cell-derived CMs in drug screening. Since the advent of the iPSC technology[79], regenerative treatment and precision medicine are increasingly feasible[269]. Unlike other cells, iPSCs contain each individual's very own genetic fingerprint because they are derivatives of their own somatic cells. Several properties yield to hiPSCs being especially qualified as a model system for studying human diseases, namely, that they carry human genes, are pluripotent, and are stem cells. Functionally, hiPSC-CMs have been characterised and assessed with numerous known pharmacological agents. They have been shown to respond similarly to clinical data found in human CM[138,270–272]. For example, investigation of the pro-arrhythmic potential of 28 different compounds found compound-specific changes in beating rate similarly to what was observed in the clinic. hiPSC-CMs were induced to demonstrate a re-entrant arrhythmia model by using Na^+ channel blockers, such as lidocaine, TTX, together with manipulating time in culture and stimulation frequency. The application of drugs and culture manipulation resulted in different calcium wave form, monitoring by optical mapping[273]. Additionally, current anti-arrhythmic drugs (nifekalant, E-4031, sotalol and quinidine) can be administered to terminate the spiral waves in dose-dependent manner. Genetically modified hiPSC-CM-encoded voltage indicator, ArcLight, was used to study drug-induced TdP and electrically induced spiral waves. The researchers evaluated the mechanism of anti-arrhythmic drugs (carbenoxolone, lidocaine and quinidine) and their termination by electrical cardioversion and overdrive pacing[274]. Another classic drug response study is isoproterenol on catecholaminergic polymorphic ventricular tachycardia. The study showed the effect of isoproterenol caused inotropic and lusitropic effects[275]. Therefore, hiPSCs, which are genetically matched to the individual patient, offer the opportunity to model cardiovascular diseases in a similar manner to disease progression and response *in vivo*.

Early advancements have been made in using hiPSCs to better understand cardiomyopathies[276], rhythm disorders[277], valvular and vascular disorders[278], and metabolic risk factors for ischemic heart disease (***Table 4***)[279]. Although this promising work is still in its infancy due to the complexity of the *in vitro* culture and its multicellularity, the ability to recapitulate human pathophysiological conditions *in vitro* offers a potential advantage over animal models in addressing the issue of cross-species discrepancy. Cardiac channelopathies are one of the most studied topics since these phenotypes are readily detectable despite hiPSC-CM immaturity. Therefore, they gained major interests as disease models. Numerous channelopathies, including long-QT syndrome (LQTS), Brugada syndrome, Timothy syndrome (also called LQT8), and catecholaminergic polymorphic ventricular tachycardia (CPVT) have been modelled using hiPSC-CMs, with successfully recapitulation of cardiac phenotypes of the patients[280]. However,

cardiomyopathies are frequently triggered by mutations in the structural sarcomeric proteins, characterised by systolic and/or diastolic dysfunction, sarcomeric disorder, pathological hypertrophy, and interstitial fibrosis. These do not only result from CM dysfunctions but also from a finely orchestrated change of non-CM components in the heart. Hence, it is increasingly evident that crosstalk between multiple cardiac cell types are crucial in their survival, morphology, maturity, and function in the post-mitotic state of the heart. Therefore, beating hiPSC-CMs provide an exciting platform for studying cardiotoxicity and efficacy testing, offering the ability to recapitulate population genetic variations. This technology paves a powerful avenue for pharmacogenomics and personalised medicine.

Table 4: Summary of main available hiPSC derived cells used in disease modelling. *Note: SMC = Vascular smooth muscle cells, CM = cardiomyocyte, EC = Endothelial, RBC = Red blood cell. This table has been reproduced from B. Wang and W. Kit-Anan et al.*[39]*.*

Pathology	Cell type involved	Mutation	(Drug/Treatment) test	Ref.
Endothelial				
Healthy	EC	N/A	Flow induced disease and simvastatin	[281]
Hutchison-Gilford Progeria Syndrome (HGPS)	EC	Patient derived	N/A	[282]
Smooth muscle cells				
Supravalvular aortic stenosis	SMC	Elastin (ELN)	Elastin recombinant protein	[283]
Marfan syndrome (MFS)	SMC	FBN1	Gene editing and drugs	[284]
Lymphocytes				
Healthy	B-cell lymphoid lineage	N/A	N/A	[285]
Red Blood cell				
Healthy	CM and RBC	N/A	Toxicity of RBC	[286]
CM				
Hypoplastic left heart syndrome	CM	Patient derived (GM12601)	Isoproterenol	[287]
Dilated cardiomyopathy	CM	TTN, RBM20, cTnT and	N/A	[288–292]

Arrhythmogenic right ventricular dysplasia	CM	plakoglobin, plakophilin-2	Metabolism induced onset	[293]
Familial hypertrophic cardiomyopathy	CM	MYH7 Arg663His PRKAG2, E99K, β-myosin, β-myosin, MYL2, ACTC1, MT-RNR2, SCO2	Verapamil, Diltiazem, Mexiletine among 15 drugs	[294–297]
LEOPARD syndrome	CM and all three germ layers	PTPN11	N/A	[298]
Friedreich's ataxia	Neurons and CM	GAA triplet repeat expansion within the first intron of the frataxin gene	N/A	[299]
Catecholaminergic polymorphic ventricular tachycardia type 1	CM	RYR2	Isoproterenol	[300,301]
LQT1,2,3,5,8,14	CM	Patient derived	Common drugs	[272,302–306]
Barth syndrome	CM	tafazzin (TAZ)	Genetic rescue	[307]
Ischemic heart damage	CM	aldehyde dehydrogenase 2 (ALDH-2) deficiency	siRNA knockdown	[308]
Brugada syndrome (BrS)	CM	SCN5A-1795insD mutation	N/A	[277]

It is widely known that hiPSC-CMs cultured *in vitro* have a phenotype akin to developing CMs, such as ineffective EC coupling, and different pharmacological responses previously mentioned. The immaturity in structural and functional properties of hiPSC-CMs hampers the full realisation of their usage in disease modelling[98]. This immaturity of *in vitro* hiPSC-CMs could be partly affected by the different microenvironment and extracellular matrix found in developing and mature myocardium. Therefore, studying the effects of biochemical, mechanical and humoral cues on hiPSC-CM development may help us to answer the mechanisms that mediate healthy tissue homeostasis and disease remodelling.

1.8 Tools in a small world

1.8.1 Biomaterials

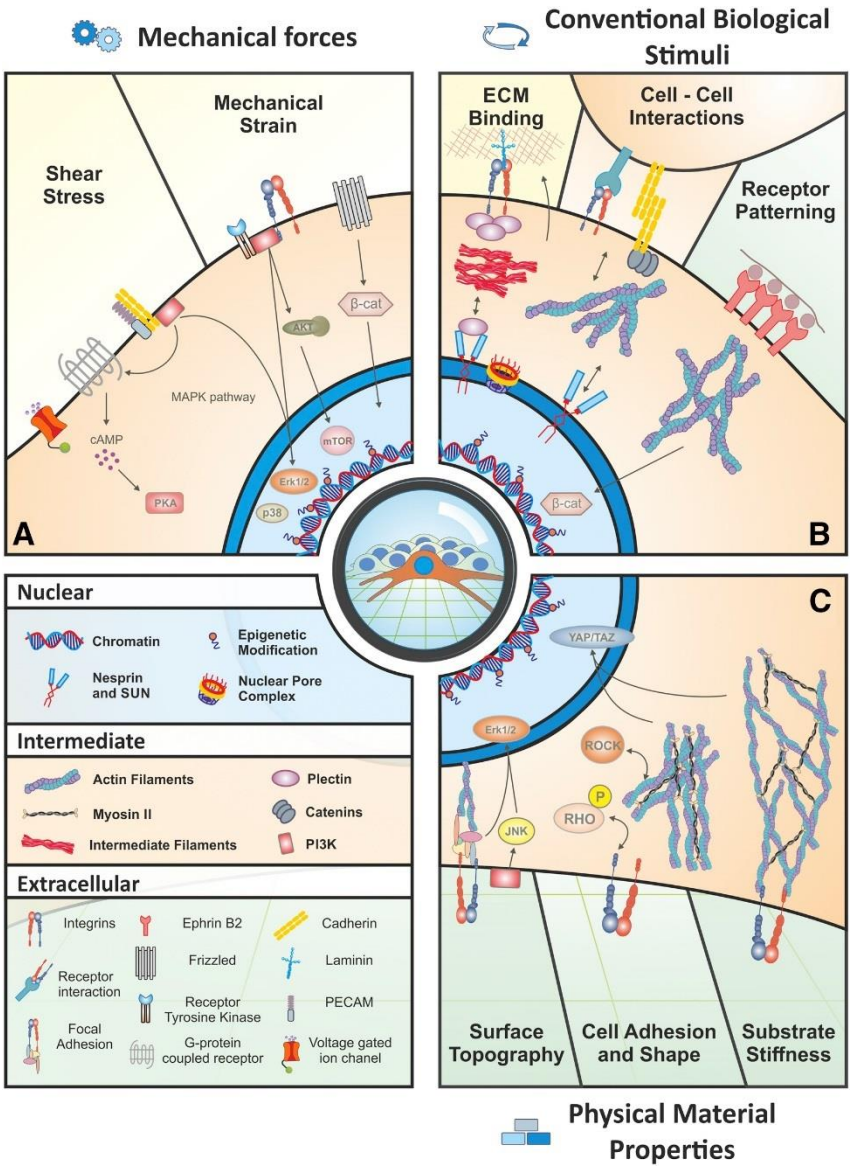

Figure 6: Biomaterials and their cues for stem cell fates. *Biomaterials have been designed to provide various stimuli either as a single or multiple cue. Physical stimuli and their possible interactions are presented, including mechanical force, several classes of biological stimuli, and physical material properties. Reproduced from Crowder et al.*[309].

Initial utilisation of hiPSC-CMs has partially realised their potential in drug screening and fundamental biomedicine. This is only partial, mainly due to the lack of direct similarity with adult CMs at the functional, structural and genetic levels. As shown in ***Figure 6***, designing an engineered platform of biomaterials would improve knowledge on hiPSC-CM interaction with biological cues, and broaden the applications of hiPSC-CMs for medical approaches. A biomaterial is broadly defined as any substance that has been engineered to interact with biological systems. Bioinert materials were initially designed to minimise the risk of reactions with biological tissues, such as titanium for hip transplants.

Biomaterials for cardiac application can be classified into two main groups: natural and synthetic biomaterials. Natural biomaterials are derived or isolated from native tissue of autogenic, allogenic or xenogeneic sources. Their strengths include biocompatibility and functionality, but they are inferior in terms of robustness and controllability. Next, synthetic biomaterials, such as metal, ceramics and polymers, possess high durability and strength but are disadvantaged in their biofunctionality. Both natural and synthetic biomaterials have limited mechanical durability and electrical conductivity and can produce immune responses. This thesis will focus on synthetic polymers with highly tuneable properties whether the need is strength, durability, biocompatibility, structures and conductivity.

Firstly, a material with robust tuneable elastic properties, explored in this thesis, is polyacrylamide-*co*-acrylic acid (PAAm). It has a wide range of mechanical properties[310], surface uniformity, minimal interaction with proteins and optical transparency[311]. Traditionally, proteins can be conjugated on the surface using N-sulfosuccinimidyl-6-(4'-azino-2'-nitrophenylamino)hexanoate (sulfo-SANPAH) under UV exposure. However, this chemical is difficult to handle, to store and is expensive[311–313]. Recently, Poellman *et al.* introduced acrylic acid as a co-monomer. Carboxylic group provides by the acid can be covalently linked to proteins via 1-ethyl-3-(3-dimethylaminopropyl)carbodiimide hydrochloride (EDC)[314].

Another type of natural material that will be explored in this thesis is collagen. It is found as the major component in cardiac ECM and has been fully sequenced. The result showed the presence of about 100 open reading frames of $(Gly\text{-}Xaa\text{-}Yaa)_n$. This sequence is widely known as collagen-like sequence, suggesting that the triple helical structure of collagen fibre is the result of physical constraints due to the presence of Gly at every third residue[315]. Recombinantly synthesised collagen, such as bacterial collagen, has shown promising applications in regenerative medicine[316]. In this thesis, streptococcus collagen–like 2 (Scl2) will be explored due to their physiologically relevant stiffness compared to native myocardium, cytocompatibility, and

ability to be manipulated via chemical functionalisation of amino acid residues. Scl2 protein contains collagen-like sequence (repeating (Gly-X_{aa}-Y_{aa})$_n$ residues), hence, self-assembles into a triple helical structure. Additionally, its production procedure minimises batch-to-batch variation in quality, as it requires no post-translational modification.

The synthetic biomaterial that will be exploited in this thesis is a type of conductive polymer (CP), which means it can carry electrical current, having conductivity greater than 10^3 S·cm^{-1}. Native mammalian myocardium has been reported to have electrical conductivity of around 10^{-4} S·cm^{-1}. Although no biomaterial with the ideal electrical conductivity for cardiac applications has yet been reported, creating CP with a conductivity within the physiological range is speculated to be beneficial for cardiac functions. CP used in medical applications are limited to a very select few, due to the dopants' toxicity. Polypyrrole was the first and most extensively studied CP. It shows excellent biocompatibility, but it is brittle and highly hydrophobic. These properties limit their use in a dynamic tissue like cardiac muscle[317]. Poly(3,4-ethylenedioxythiophene) (PEDOT) has drawn considerable attention due to its excellent electrical, physical and optical properties and stability. It has high electrical conductivity (>10^3 S·cm^{-1}), high optical transparency (>90%) and chemical stability[318]. As such, PEDOT is widely used in biomedical research. Peramo *et al.* demonstrated *in situ* polymerisation of PEDOT in biological tissue samples. Preliminary results suggested growth of myoblasts and fibroblasts immediately adjacent to PEDOT, providing an early indication of low cytotoxicity[319]. Recently, polyaniline (PANI) has been examined due to it's high conductivity around 10^2 S·cm^{-1} [230,320]. Cytocompatibility studies have shown conflicting reports with some constructs exhibiting significantly better cytocompatibility than others[321–323]. It is speculated that this major difference arises from various dopants and solvents used during polymerisation.

Composite biomaterials, such as a combination of Scl2 and conductive polymers, could prove to be a strategy which benefits from the advantages of both natural and synthetic biomaterials, thereby overcoming their individual weaknesses. This can be achieved by blending and multilayering. Composites of synthetic and natural polymers leads to a novel biomaterial, where the mechanical, electrical and chemical properties of the materials can be specifically designed, while maintaining their functionality. For example, the development of biocompatible conductive collagen represents an appealing approach in tissue engineering, since it is well known that electrical stimuli significantly affect important cardiac cell behaviours, such as proliferation, differentiation, and directional migration. Bonfrate *et al.* demonstrated a technique that co-precipitated paramagnetic nanoparticles coated by polyethylene-glycol, before being

sprayed into a collagen suspension, successfully creating the first conductive collagen via incorporation of metal. The 3T3 cell line was cultured on this material and no significant cellular toxicity compared to unmodified collagen was observed. Furthermore, they also demonstrated that addition of carbon nanotubes at subtoxic levels allowed the collagen to be strengthened and conductive. iPSC seeded on the construct showed minimal toxicity. However, the additions of conductive composite/metal to collagen increases the stiffness, creating a mechanical mismatch against the native myocardium. Young's modulus was reported in the MPa range, with reduction of maximum strain to around 10%. This compromise in mechanical properties makes the construct unsuitable for cardiac applications. Interestingly, a composite of collagen with conductive polymers, of which mechanical properties can be finely tuned, has not been demonstrated to date. This could potentially create an ideal biomaterial for cardiac applications.

1.8.1.1 Ideal biomaterials

Response to various cues have been used to explore the influence of biomaterials on hiPSC-CMs. Although multiple cues have been acknowledged for their importance during cardiac development, technical difficulties hinder the advancement of the field, including ease of providing cues and their manipulation. The primary aim of biomaterials is to provide these cues, to study cell fate upon stimulations and in tissue engineering. Ideally, the biomaterial should be able to precisely control each individual cue temporally and spatially, enabling us to individually understand a stimulus and its implication on cell fates. The essential assets for biomaterials that should be considered are listed below:

- **Degradability:** This property is often designed to increase integration of a graft to the native tissue. This allows time-dependent replacement and removal of biomaterial from the native ECM. However, many other medical applications require non-degradable materials, such as bone transplant and *in vitro* substrate.
- **Cytocompatibility:** This term is continuously redefined as the research field progresses. It generally refers to a biomaterial with properties that allow cells to behave healthily (i.e. proliferation, adhesion, migration, division and differentiation).
- **Mechanical properties:** A scaffold should provide suitable mechanical support for cells, which is specific to it's application. For cardiac biomaterials, these generally refer to physiological (0.5 – 50 kPa) and pathological (>50 kPa) stiffnesses. It should withstand cyclic stretching or fatigue, estimated to be around 1 billion cycles in an average lifetime after disease onset.

- **Topological cues:** Surfaces of biomaterials should provide an effective configuration for restructuring the niche found in the native microenvironment and aid individual factor analysis. It also directs cell behaviour at the host site, such as alignment and integration.
- **Biochemical cues:** Soluble cues can mediate cell fate by tethering to biomaterials. This could be designed such that their release would occur in a time-dependent manner, or could be induced by specific stimulation, enabling the material to mimic the paracrine effects found in the human heart.
- **Conductivity:** Adult CM contraction only occurs when they receive external stimulation, such as electrical signals. Passing of the electrical impulse could promote cell integration to native myocardium by synchronising beating.

Table 5 summarises important myocardium properties that should be taken into account in the design of cardiac biomaterials, according to the literature.

Table 5: Important parameters in biomaterial design for human cardiac applications.

Parameter	Range
Mechanical properties [324–326]	
Young's modulus – start of diastole	10 – 31 kPa
Young's modulus – end of diastole	200 – 500 kPa
Anisotropic ratio of Young's modulus	2 – 3 (E_{circ}/E_{long})
Matrix thickness	≤ 200 μm
Strain at failure	22 – 90%
Number of beats in an average lifetime (after disease onset)	2 billion cycles (0.5 – 1 billion cycles)
Topographical properties [327–329]	
Length of CM	134 – 141 μm
Diameter of CM	19 – 23 μm
Electrical properties [330–333]	
Conductivity	10^{-4}
Cell-to-cell conduction velocity	0.5 m/s
Purkinje fibre	2-4 m/s

It is worth noting that these parameters vary between different measurement settings and techniques. Both mechanical and topographical features have been shown to dictate stem cell fate. Properties matching the physiological environment of the heart have been shown to promote CM function and structure while pathological condition demotes CM function and structure, expressing disease-like phenotype.

1.8.2 Traction force microscopy (TFM)

Visualisation of hiPSC-CMs, reported in nN scale, is crucial to characterise hiPSC-CM development *in vitro*. TFM has become increasingly popular due to its high throughput nature and ease of image acquisition. Additionally, its resolution has improved significantly due to recent innovative progress in microscopy instruments and computational units. The TFM technique tracks movements of fluorescent microbeads embedded in a substrate of known mechanical properties. The analysis assumes that the tracked movements only occur in the same Z-plane. Further image reconstruction is calculated from known movement distance and mechanical properties. The result can reveal contractile direction and force generated by a single cell. This technique enables chronological monitoring of hiPSC-CM function *in vitro* in a high throughput manner.

1.8.3 Optogenetics

Optogenetics allow optical interrogation and control of light-sensitive channels in cells. It has many advantages over electrical or pharmacological stimulations, such as highly precise spatial and temporal excitation, even at a single cell level. There are two main optogenetic modifications utilised in cardiac fields: GCaMP and channelrhodopsin. Most studies are commonly focused on GCaMP to monitor intracellular Ca^{2+}. GCaMP binds to 2 free Ca^{2+} ions (a stimulated state) and, upon stimulation with blue light, emits green fluorescent signal. Initially, the GCaMP has many limitations, such as pH sensitivity and the requirement of folding at temperatures below 37°C. Recently, Sun *et al.* have improved the response rate and Ca^{2+} binding efficiency, supporting a rapid response in mammalian neurons with up to 20-fold increase in kinetics[334]. EC coupling studies on hiPSC-CMs hugely benefited from the employment of GCaMP over traditional toxic dyes for long term exposure, such as Flou-4 and Fura-2. This limits their uses especially in chronological repeated observation. This novel system allows long term observations and repeatable measurements of fluorescence-based cytosolic free Ca^{2+} imaging in cardiac cells.

Chapter 2

Methodology

2.1 Statistics

All statistical analysis was performed using GraphPad Prism 5. Prior statistical tests, all data were subjected to D'Agostino & Pearson omnibus normality test. For parametric distribution, statistical tests were performed using Student's t-Test (2 groups), one-way ANOVA (more than 2 groups) or two-way ANOVA followed by Bonferroni's post-hoc (when 2 multiple contributing factors are considered). For non-parametric distribution, statistical analysis was assessed using Mann-Whitney (2 groups) or Kruskal–Wallis (more than 2 groups). Multivariate analysis has been performed by Matlab® and ClustVis[335].Unless otherwise stated, the data are expressed as mean ± SEM, N = number of experiments in each independent replicate, n = number of technical replicates in each independent experiment. Statistical significance is highlighted by * indicates p-value < 0.05, ** indicates p-value < 0.01; *** p-value < 0.001.

2.2 Materials synthesis

2.2.1 Buffer preparation

- **50 mM (4-(2-hydroxyethyl)-1-piperazineethanesulfonic acid (HEPES) buffer** was prepared by dissolving 59.5753 g of HEPES (Sigma) in 800 mL dH_2O before adjusting pH to 8 with 10 M NaOH (Sigma). dH_2O was topped up to 1000 mL total volume.
- **100 mM 2-(N-morpholino)ethanesulfonic acid (MES) buffer** was prepared by dissolving 30.048 g of MES (Sigma) in 800 mL dH_2O before adjusting pH to 6 with 10 M NaOH (Sigma). dH_2O was topped up to 1000 mL total volume.
- **Slicing Tyrode's solution** contained 1 mM glucose, 10 mM HEPES, 6 mM KCl_2, 140 mM NaCl, 1 mM $MgCl_2$, 1 mM $CaCl_2$ (All from Sigma) and 30 mM 2,3-butanedione monoxime (BDM, Acros Organics).
- **Normal Tyrode's solution** contained 1 mM glucose, 10 mM HEPES, 4.5 mM KCl_2, 140 mM NaCl, 1 mM $MgCl_2$, 1.8 mM $CaCl_2$ (All from Sigma).
- **Loading Buffer:** 96.5%v/v SB20, 2.5% v/v 2-mercaptoethanol, 1% v/v bromophenol blue
- **Electrophoresis Running Buffer:** 0.192 mM glycine, 25 mM trizma base, 0.1% v/v SDS.
- **Transfer Buffer:** 192 mM glycine, 25 mM trizma base, 10 % methanol, 0.01% v/v SDS
- **Western Blot Blocking Solution:** 20 mM tris, 150 mM sodium chloride, 0.1%v/v tween20, 4% w/v non-fat dried milk; pH 7.6
- **Tris-Buffered Saline (TBS):** 20 mM tris, 150 mM sodium chloride; pH 7.6
- **Tris-Buffered Saline with Tween (TBS-Tween):** 20 mM tris, 150 mM sodium chloride, 0.1% v/v tween 20; pH 7.6

- **Alkaline Phosphatase Buffer:** 100 mM tris, 100 mM sodium chloride, 5 mM magnesium chloride; pH 9.5

2.2.2 Polyacrylamide-*co*-acrylic acid (PAAm) hydrogel

PAAm hydrogel was fabricated followed the recipe shown in ***Table 6*** of 40% w/v Acrylamide solution (BioRad), 2% w/v Bis-acrylamide solution (BioRad), and 0.4 % v/v Acrylic acid (Sigma). pH was adjusted to 7.4 using 50 mM HEPES buffer and 10 M NaOH. The polymer solution was degassed in vacuum chamber for 30 min. The monomers solution was then mixed with 10% w/v ammonium persulfate (APS, Sigma) and N,N,N′,N′-Tetramethylethylenediamine (TEMED, Sigma) to initiate the polymerisation in a humidified chamber at 37 °C for 30 min.

Table 6: Hydrogel composition and mechanical property. *(Volume stated in µL, Young's modulus was measured using indentation mode with 20 µm spherical in-house tip on atomic force microscopy).*

Young's Modulus	**0.565 kPa**	**9.673 kPa**	**45.91 kPa**	**112 kPa**
Total Volume	2000	2000	2000	2000
dH_2O	1510	1083	658	158
50 mM HEPES	200	200	200	200
40% w/v Acrylamide	150	375	700	800
2% w/v Bis-acrylamide	100	300	400	800
Acrylic Acid	8	8	8	8
10% w/v APS	20	20	20	20
TEMED	4	4	4	4
10 M NaOH	10	10	10	10

2.2.3 Protein conjugation

PAAm hydrogels were thoroughly washed with phosphate saline buffer pH 7.4 (PBS, Gibco), three times to remove unreacted monomers and kept in PBS. The hydrogels were transferred to a cell culture hood before exposed to a germicidal ultraviolet lamp for 15 min. The conjugation was performed in 2 steps by incubating the hydrogels with 15 mM 1-ehtyl-3-[3-dimentylaminopropyl] carbo- diimide hydrochloride (EDC, Thermofisher) and 25 mM N-hydroxysulfosuccinimide (Sulfo-NHS, Thermofisher) in 50 mM MES buffer pH 6 for 30 min at room temperature, shaking. The solution was removed, and the samples were washed three times using 50 mM MES buffer pH 6. Before adding the protein conjugation solution, the samples were quickly washed twice with 100 mM HEPES pH 8 to elevate the pH. The proteins, listed below, were individually prepared as appropriated at 0.2 mg/mL concentration with 100 mM HEPES buffer pH 8. The hydrogels were then incubated with the prepared protein solution overnight at 4 °C, shaking.

Protein solution was prepared by using proteins listed below.

- Collagen I, Rat Tail protein (ThermoFisher)
- Fibronectin from human plasma (Sigma)
- Laminin from Engelbreth-Holm-Swarm murine sarcoma basement membrane (Sigma)
- Poly-D-lysine hydrobromide, mol wt 70,000-150,000 (Sigma)
- BSA, Alexa Fluor® 680 (Invitrogen)

2.2.4 Polydimethylsiloxane (PDMS) fabrication

Two-part polymer Sylgard 184 (Dow Corning), base elastomer and curing agent were mixed at 1:10 wt ratio. The mixture was stirred vigorously until uniformly mixed. The mixture was placed in vacuum chamber for 30 min for degasification or until no gas buble observed. Degassed PDMS was casted onto the passivated mould. The mould was incubated in an oven at 60 °C overnight. PDMS was slowly removed from the mould and washed three times with PBS.

2.2.5 Agarose-Meth and Agarose synthesis

The following protocol has been calculated to synthesise 60%w/w of methacrylate-agarose to agarose ratio. 5 g of low melting point Agarose type VII (Sigma) was dissolved in 180 mL Dimethyl sulfoxide (DMSO, Sigma) at 90 °C. The following chemicals were then orderly added as stated, 10 mg of 4-(Dimethylamino)benzaldehyde (Sigma), 20 mg of Hydroquinone (Sigma) and 3mL of Methacrylic anhydride (Sigma). The temperature was changed to 60 °C, mixing for 1 h. The final product was precipitated using 900 mL of ice-cold acetone (Sigma) and palleted by 3000 rcf centrifugation. Repeated this step twice to ensure that the final product was precipitated. Methacrylate-agarose was then freeze dried overnight. This protocol has been conducted with assistance of Dr Michael B. Albro.

2.2.6 Scl2 purification and synthesis

This protocol has been published and performed by Dr Paresh Parmar[336]. Briefly, the fragment of the *Scl2.28 allele* (Q8RLX7) of *Streptococcus pyogenes* encoding the combined globular and collagen–like portions of the *Scl2.28* protein was used with removal of the N- and C-termini attachment domains[316,337–340]. Additional GGPCPPC sequence was inserted at C- and N-terminal of the DNA sequence using the QuikChange site–directed mutagenesis kit (Stratagene) according to the manufacturers' instructions. All DNA sequences were synthesised commercially with codon optimisation for expression in *E. coli* (GeneArt® Gene Synthesis).

pColdI (Takara Bio) vector systems for expression in *E.coli* was used to amplify the DNA construct. A selected positive clone was transformed, antibiotically selected and expanded in 2x yeast extract–tryptone media with ampicillin (100 µg/mL) at 37 °C, shaking at 200 rpm overnight. Isopropyl β–D–thiogalactopyranoside (1 mM) was added to induce protein expression and further incubated at 25 °C for 10 h. Harvesting was achieved by centrifugation at 12,000 rcf, 60 min and 4 °C. The Scl2 protein was extracted using sonication on ice. The lysate was palleted by centrifugation at 12,000 rcf for 30 min, 4 °C before adjusting pH to 2.2 and held at 4 °C for further 16 h. Scl2 proteins were concentrated using a 10 kDa cross–flow filtration membrane (Pall Life Sciences) before exchanging the buffer into 20 mM sodium phosphate buffer, pH 8.0.

2.2.7 Scl 2 foam fabrication

The purified Scl2 protein were dissolved in 100 mg/mL of 50 mM acetic acid at room temperature, and the pH was adjusted to 7.4 using 1 M NaOH. The solutions were sterile–filtered using 0.2 µm filter before casted in 8 mm diameter by 2 mm thickness custom–made PDMS moulds and subsequently frozen at – 20 °C for 24 h and – 80 °C for 4 h. The frozen samples were lyophilised. A dehydrothermal cross–linking treatment was performed under high vacuum condition at 121 °C for 24 h This created the formation of physical intermolecular crosslinks through condensation reactions via amide formation or esterification. Scl2 foams were sterilised with 70% v/v followed by PBS exchange. This fabrication has been performed by Dr Paresh Parmar.

2.2.8 Polyaniline (PANI)-Scl2 fabrication

PANI-Scl2 were fabricated following a protocol adapted from Mawad *et al*[230]. Briefly, the PANI-Scl2 foam were fabricated by the polymerisation of aniline on the Scl2 foam. Two solutions were prepared. Solution 1 contained 2.30 mL phytic acid (Sigma), and 1.15 mL aniline (Sigma) and 5 mL dH_2O. Solution 2 contained 1.34 g APS (Sigma) in 5 mL H_2O. The mixture of 73 µL of Solutions 1 and 23 µL of Solution 2 were vortexed. The solution was dropcasted onto Scl2 foam on one side at a time. The solution was allowed to polymerise on the foam for 3 h at room temperature. The scaffolds were rinsed with excess dH_2O thoroughly to quench the polymerisation and remove excess monomers. PANI-Scl2 was incubated in dH_2O overnight to wash out any excess phytic acid, uncrosslinked polymeric chains, and any side products, rocking. The scaffold was then incubated for 72 h prior to cell seeding.

2.2.9 Silicon master fabrication

Hard master moulds mimicking the shape and alignment of mature CMs in adult human myocardium were fabricated via UV photolithography. Patterns of aligned rectangles of 40 µm × 8 µm x 20 µm with gap distances 20 µm were made on a chrome-coated glass photomask (JD Photodata). Silicon wafers (Boron p-doped, resistivity 1-30 Ohm per cm, 4'' diameter, University Wafers, Inc.) were oxygen-plasma cleaned at 300 W for 5 min. The cleaned wafer then underwent a transition bake at 95 °C for 10 min prior to spin-casting photoresist SU-8 2010 (MicroChem Corp.) at 1000 RPM for 30 s followed soft-baked at 95 °C for 3 min. The pattern was transferred using to MA6 mask aligner (Suss). The photoresist was exposed to UV light for 70.8 s at 5.6 mW/cm^2. Post-exposure bake was then performed, at 95 °C for 4 min. This was followed by development in SU-8 developer (MicroChem Inc.) for 6 min, and finally washed with IPA. This

silicon master has been fabricated by Dr Ciro Chiappini and Mr Michele Becce. Following the fabrication, the passivation process was performed by activating micropatterned silicon master surfaces using oxygen plasma. trichloro(1H,1H,2H,2H-perfluorooctyl)silane (Sigma) was deposited on the surface using gas phase deposition.

2.3 Materials characterisations

2.3.1 Toluidine blue assay

Carboxylic groups in PAAm hydrogel were quantified using 0.5 mM Toluidine Blue O (Sigma). The Toluidine Blue O was dissolved in dH_2O, pH 10 and incubated with the PAAm scaffolds for 3 h at room temperature. The samples were washed three times with dH_2O, pH 10. The Toluidine Blue O dyes bound to carboxylic groups were incubated for 10 min at room temperature to desorb the dyes using 50 % w/v Acetic acid (Sigma). The solutions were read at 630 nm absorbance using a SpectraMax Paradigm Multi-Mode Microplate Reader.

2.3.2 Swelling ratio measurement

The swelling ratios were defined as the measured dimensions divided by the nominal dimensions (dimension of shape immediately after casted). PAAm hydrogel swell following polymerisation. Swelling depends on the polymer chain length which depends on the acrylamide concentration, the crosslinking density which depends on the bis-acrylamide concentration, pH of solution and salt content of the solvent. PAAm hydrogels were incubated and changed daily with RPMI1640 supplemented with B27 (Thermo Fischer) for 7 days in 37 ^{o}C, humidified chamber. Bright field images were taken using Nikon IX51 Inverted microscope (Olympus). The width and length measurements were performed using Fiji.

2.3.3 Matrigel thickness measurement

Polyacrylamide-*co*-acrylic acid solution was additionally mixed with FluoSpheres® Carboxylate-Modified Microspheres, 0.2 µm, red fluorescent (580/605), 2% solids (Thermo Fischer Scientific) at 1:100 wt, following the protocol previously mentioned in Materials Synthesis section 2.2.2. The hydrogel was covalently linked with PDL (Sigma) as described previously. The Matrigel Basement Membrane Matrix, LDEV-Free (Corning) was diluted 1:20 v/v with appropriate media before mixing with FluoSpheres™ Carboxylate-Modified Microspheres, 0.2 µm, yellow-green fluorescent (505/515), 2% solids. The matrix solution was transferred over the hydrogel, swirl and incubated overnight at 4 ^{o}C. Prior to imaging, the samples were incubated at 37 ^{o}C, in

a humidified chamber for 30 min.The Z-stack images were taken using Leica SP5 MP/FLIM inverted confocal microscope (Leica). The image reconstruction was performed using Fiji.

2.3.4 FTIR measurement

Before FTIR spectroscopy was performed, the samples were freeze dried and grounded using pestle and mortar. FTIR measurements were performed using the Perkin Elmer Spectrum 100 FTIR spectrometer with a single bounce germanium ATR crystal. After calibration, a background scan was measured averaging 32 scans. Spectra of the samples in powder form were collected in the range of 650 to 4000 $cm^{-1,}$ with a resolution of 4 cm^{-1}, 32 scans were performed on each sample. The data were analysed using MatLab® code and integrated toolboxs. This measurement has been performed and analysed by Dr Paresh Parmar.

2.3.5 Mechanical compression

PAAm hydrogels were equilibrated by immersing in PBS (Life technologies) overnight at room temperature. The hydrogels were punched into 9 mm diameter cylindrical shape using an in-house puncher made by the Dept. of Materials' workshop. The hydrogel thicknesses were recorded by using RS caliper (RS Components). The measurement was conducted while the hydrogels were immersed in PBS. The upper plate was slowly moved down to ensure a compression using Bose Electroforce 3200 Series III with 1000 g load cell equipped with parallel plates. Bose was directed to increase strain to 5%, 7.5%, 10%, 12.5%, 15%, 17.5%, and 20%, calculated from thickness, with 10 min intermission at 0.1% strain rate. Compressive Young's modulus was calculated as the slope of the linear region in the stress/strain curve using Regression model by Microsoft Excel 2010.

2.3.6 Dynamic mechanical analysis (DMA)

Prior to DMA all samples underwent a preconditioning protocol. Three specimens were placed in a 35 mm diameter petri dish with 1.5 mL of PBS and attached to a 250 g load cell. The upper platen was brought into contact with the samples under a tare load (0.25 N for PANI-Scl2 or 0.1 N for Scl2). From this reference condition the samples were then compressed by 1 mm at 1 Hz for 18,000 cycles (5 h).

Following preconditioning the length, width, and thickness of each sample was measured with digital callipers. A single sample was then placed in a 35 mm diameter petri dish with 1.5 mL of PBS. The loading platen approached the sample at 0.05 mm/s to detect the surface of the specimen and define the reference condition. The surface was determined by post fitting a bi-

linear function to the data. This fit was optimised by the least squares method and provided an objective method for determining contact.

Samples were then run through a frequency sweep from 0.1 to 10 Hz in a fixed random order (0.1, 0.5, 1, 1.5, 2, 3, 5, 10, 1, 0.1, 3, 0.5, 2, 5, 1.5, and 10 Hz) at 12.5 ± 7.5% strain. Samples were held at their mean strain (12.5%) for 30 s prior to each frequency tested. The number of cycles run at each frequency was determined by the DMA software. Raw data files were then imported into MatLab® 2016. The files were processed to determine the experimental frequency, complex modulus, storage modulus, loss modulus, phase shift, and tangent delta. This experiment has been performed with assistance of Dr Axel Moore.

2.3.7 Atomic force microscopy

In-house atomic force microscopy (AFM) tip was made by using tipless AFM cantilevers (Windsor Scientific) and 20 µm Polybead® Microspheres (Polyscience). One polystyrene bead was adhered to the tipless tip with epoxy adhesive (RS Components) and allowed to air dry overnight at room temperature. Contact mode AFM (Agilent) was used and analysed using Hertz model for 200-nm indentation in Agilent or AtomicJ software[341]. Both softwares have been chosen to ensure consistency of the analysis. The hydrogels were incubated with RPMI 1640 (Life Technologies) 24 h before and during measurement. This was done to equilibrate the hydrogel to *in vitro* environment.

2.3.8 Multiphoton second-harmonic imaging microscopy

Scl2 were incubated in PBS and imaged by multi–photon second harmonic generation (MP–SHG) in wet state using a Leica SP5 inverted microscope equipped with a MaiTai HP DeepSee multi–photon laser (Spectraphysics) on a 25x NA Nikon objective. Second harmonic signal was generated at 900 nm and detected on a photomultiplier tube (PMT) (435–465 nm). This technique has been performed by Dr Paresh Parmar.

2.3.9 X-ray photoelectron spectroscopy

Quantification of surface elements and level of doping were collected from K-Alpha spectrophotometer (Thermo Fisher) utilising a monochromatic Al-Kα X-ray source (Energy = 1486.71 eV). The spectra were calibrated to the adventitious C 1s signal (284.6 eV). Dehydrated samples were positioned at the electron take-off angle normal to the surface with respect to the analyser. Two scans were conducted, initiated by survey spectra in the range 0 - 1300 eV (pass energy = 200 eV) followed by high-resolution scans (pass energy = 50 eV) for C 1s, N 1s, S 2p, and O 1s core levels. Peak analysis and curve fitting were performed using Thermo Avantage

Software (v. 5.948) using a Shirley background. The quantification of the surface chemical elements and compositions was calculated using methods described by Seah[342]. This experiment was conducted by Dr Anna Regoutz.

2.3.10 Characterisation of current voltage characteristics

At different time points, the cell culture medium was removed, and the hydrogel was gently blotted and air dried before the I-V curves were recorded. The samples were then assembled into custom-made copper plates to ensure uniform conductance. In-house probe station made by custom-made Keysight was connected to the copper plates using two-probe setup. The current-voltage characteristics traces were recorded using Keysight EasyEXPERT Software©. The traces were plotted and analysed using Regression in Microsoft Excel 2017. The resistivity was calculated from the linear region of the plot.

2.3.11 Scanning electron microscopy

Scl2 and PANI-Scl2 were freeze dried to remove remaining liquid from the scaffolds. Samples were sputtered with Au using an Emitech K550 sputter coater. Morphological observation of Scl2 and PANI-Scl2 were imaged using scanning electron microscopy (SEM) using a JEOL 5610 (Herts, UK) at an accelerating voltage of 15 kV and a working distance of 150 mm.

2.4 Biological procedures

2.4.1 NRVM isolation

All work was carried out in accordance to the Animals (Scientific Procedures) Act 1986 and the EU Directive 2010/63/EU. Neonatal rat ventricular myocytes (NRVM) from P1 Sprague Dawley rats were isolated using a gentleMACS™ Dissociator (Miltenyl Biotec) and Neonatal Heart Dissociation Kit (Mouse and rat) (Miltenyl Biotec). Atria were removed, and the ventricles were dissected into 1 mm^3 pieces in HBSS (Life Technologies). The tissues were enzymatically digested as per gentleMACS™ kit's instructions. Dissociated tissues were re-suspended in complete medium containing Medium 199 (Sigma-Aldrich), 10% v/v New born calf serum (Labtech International), 100 U/mL-100 µM Penicillin-Streptomycin (Invitrogen), 700 µM L-Glutamine (Life Technologies), and 2 µg/mL Vitamin B12 (Sigma-Aldrich). The suspension was filtered with a 70 µm cell strainer. The heterogeneous cell suspension was plated at 37 ºC and 1% CO_2 for 1 h to remove fibroblasts. The preplated solution was filtered through a 70 µm mesh before collecting the NRVM.

2.4.2 Stem cell maintenance

Human Episomal iPSC line (Life Technologies), IMR90-4 (WiCell Research Institute, Inc.) or WTC GCaMP6f (Gladstone Institutes, Professor Bruce Conklin) were maintained on 1:200v/v dilution Matrigel (corning)-coated TCP with Essential 8™ Medium (Thermo Fischer). The dissociation was performed when the cells reached 70 - 90% confluency by washing the cells with 0.5 mM Ethylenediaminetetraacetic acid (EDTA) in PBS and incubating for 5 - 7 min at room temperature. The solution was removed and replaced vigorously by Essential 8™ Medium supplemented with 10 μM ROCK inhibitor (Y-27632, Tocris) to remove the cells from TCP. To increase cell survival, minimal pipetting was ensured to reduce cell cluster segregation. The cell solution was finally replated at appropriate density on Matrigel (corning)-coated TCP. The density varies from line to line. In general, cell splitting ratio was performed at 1:12 – 1:18 to reach confluency in 3 – 4 days. The cells were kept in Essential 8™ Medium supplemented with 10 μM ROCK inhibitor for the first 22 h before replacing with fresh Essential 8™ Medium daily.

2.4.3 Stem cell differentiation

The cells were differentiated into human induced pluripotent stem cell-derived cardiomyocytes (hiPSC-CMs) using an adapted protocol [87,223]. The optimisation was performed and the highest percentage of cTnT expression of the differentiated cells from the protocol was chosen. hiPSC was split at a 1:12 – 1:18 ratio to achieve 80 – 95% confluency on day 4 after splitting. Briefly, at 80 – 95% confluency, cells were treated with a 6 μM GSK-inhibitor (CHIR99021, MERCK Millipore) for 24 - 48 h, followed by washing with room temperature RPMI-1640 and replacing with 24 - 48 h in RPMI-1640 (Life Technologies) supplemented with B27 minus insulin (Life Technologies). The culture was then washed once using room temperature RPMI-1640 before incubating in a 2 μM Wnt-inhibitor (C-59, biorbyt) in RPMI-1640 supplemented with B27 minus insulin for 48 h. The media was replaced with RPMI-1640 (Life Technologies) supplemented with B27 minus insulin for additional 48 h before replacing with RPMI-1640 supplemented with B27 (Life Technologies). At this point, spontaneous beating of the hiPSC-CMs should be observed before starting metabolic selection. Optionally, metabolic selection was implemented to increase purity by replacing previous media with RPMI-1640 no glucose supplemented with 4 mM sodium L-lactate (Sigma) for 72 - 120 h. The duration depends on beating activity of the hiPSC-CMs. The selection was ceased if hiPSC-CMs showed a slower, irregular beating or 60 – 80% of non-myocytes death was observed. The metabolic selection was ceased when hiPSC-CMs' beating stopped.

2.4.4 Slice production

All work was carried out in accordance to the Animals (Scientific Procedures) Act 1986 and the EU Directive 2010/63/EU. This protocol has been previously described by Watson *et al.* [332]. Briefly, rats were sedated with isoflurane (4% isoflurane and 4 L/min O_2) and sacrificed using cervical dislocation and dissection of the carotid arteries. The heart was rapidly removed and placed in 37 °C heparinised Slicing Tyrode's solution for 5-10 s to remove remaining blood from the ventricle followed by being placed in 4 °C Slicing Tyrode's solution. A left ventricular tissue block was prepared as previously described[332]. The tissue block was then mounted with epicardial surface facing down on an agarose-coated specimen holder using Histoacryl surgical glue (Braun). The specimen holder was placed in the bath of a high-precision vibratome (7000smz-2, Campden Instruments) submerged in oxygenated 4 °C Slicing Tyrode's solution. The tissue block was sliced using a ceramic blade, longitudinal to myocardial fibre orientation and from endocardium down to the epicardium. The vibratome was set to vibrate at 80 Hz, with an amplitude of 2 mm and a Z-axis error < 0.7 µm. Slices were kept in oxygenated 4 °C Slicing Tyrode's solution under mesh holders until further experiments were performed. This procedure has been done with assistance of Dr Samuel Watson and Ms Ifigeneia Badi.

2.5 Biological characterisations

2.5.1 Viability – Calcein

A LIVE/DEAD™ Viability/Cytotoxicity kit (Life Technologies) was used according to manufacturer's instruction. Cells were washed three times with PBS and incubated with 2 µM calcein AM and 4 µM ethidium homodimer-1 diluted in no phenol red media for 45 min at 37 °C, humidified chamber. Following incubation, the media was refreshed, and the sample was visualised by an inverted Nikon Eclipse TE200 (Japan) microscope.

2.5.2 alamarBlue™ assay

1/10 v/v. alamarBlue™ solution (Life Technologies) was diluted in media. 2 mL of the mixture was added per 1 well of each 6-well plate dish. Cells were incubated with the mixture for 3 h at 37 °C, humidified chamber. The solution was mixed thoroughly until uniform colour was observed followed by the absorbance measured at 570 nm and 600 nm on a SpectraMax Paradigm Multi-Mode Microplate Reader (Molecular Devices).

2.5.3 PicoGreen™ DNA content assay

The samples were washed three times with PBS before freeze drying. 500 µL of papain mixture contained 19.8 mL PBS, 0.2 mL 0.5 M EDTA, 17.6 mg cysteine hydrochloride (Sigma) and 60 µL Papain solution (Sigma) adjusted pH to 7 was added to lyophilised samples and crush using pestle and mortar. Additional 500 µL of papain mixture was added before vigorously vortex. To ensure succeful lysation process, the solution was incubated at 60 °C for 16 hr prior to centrifugation at 14,000 rcf for 10 s. The precipitated particles were discarded. The supernatant was collected and analysed using Quant-iT™ PicoGreen® dsDNA Assay Kit (Thermo Fischer) as per manufacturer's instruction.

2.5.4 Primers' design

Primers were designed using BLAST (NIH). The primers were synthesised by Thermo Fischer. The primers were dissolved in dH_2O to 100 µM stock solution. Primer sequence showed below (***Table 7***). This has been performed collaboratively with Dr Manuel Mazo.

Table 7: Forward and reverse primers sequences.

Name	Encoding	Forward primer sequence	Reverse primer sequence
GAPDH	Glyceraldehyde-3-phosphate dehydrogenase	TGGTATCGTGGAAGGACTCATGA	ATGCCAGTGAGCTTCCCGTTCAG
KCNJ2	Potassium Voltage-Gated Channel Subfamily J Member 2	ACTCCATGTCCCCATGCTC	GGTCTGTCTACTGACATGCAGAGTT
RYR2	Ryanodine receptor 2	CGGCAGGGCTGGACTTAT	TGGATTTCTTGGTTCGGTCA
HCN4	Hyperpolarisation activated cyclic nucleotide gated potassium channel 4	CGGCCGGATTTTGGATTAT	AATCAGGTTTCCCACCATCA
MYL2	Ventricular Myosin Light Chain 2	CAACGTGTTCTCCATGTTCG	GTCAATGAAGCCATCCCTGT
MYL7	Myosin light chain 7	CCCATCAACTTCACCGTCTT	AGGCACTCAGGATGGCTTC
MYH6	Myosin heavy chain 6 (α-MHC)	GGAGGGAGGCAAGGTCAT	GGTTCTGCTGCAACACCTG
MYH7	Myosin heavy chain 7 (β-MHC)	ATGCATTCATCTCCCAAGGA	GAAGCCCAGCACATCAAAAG

2.5.5 Protein Extraction

Samples were placed on ice and washed three times with 4 °C PBS containing cOmplete™, Mini Protease Inhibitor Cocktail (Roche) and PhosSTOP™ (Roche). 100 µL of RIPA Lysis and Extraction Buffer (New England Biolabs) with cOmplete™ Mini Protease Inhibitor Cocktail and PhosSTOP™ was added to the sample. The sample was thenscraped under microscope to ensure all the cells were collected. The lysates were incubated at 4 °C, rocking for 30 min and were sonicated for 30 s using Ultrasonic Processor Stainless Steel Temperature Probe (Cole-Parmer) at 20% power to promote complete lysis. The lysates were centrifuged at 14,000 rcf for 15 min at 4 °C to pellet the cell debris and discarded. Protein concentration in the supernatants was quantified using the Pierce BCA Protein Assay Kit (Thermo Fisher Scientific) as per manufacturer's instruction.

2.5.6 RNA extraction and rt-qPCR

RNA was extracted and isolated using TRIzol® following manufacturer´s instructions. Briefly, samples were washed three times with PBS followed by 500 µL of TRIzol®. The solution was pipetted onto the sample to ensure total lysation. The RNA was then isolated using Direct-zol RNA Kits (Zymo, research) as per manufacturer's protocol. Quantification of RNA was performed using nanodrop (ThermoFischer) using 2 µL of final RNA product diluted in TE buffer. cDNA was produced using QuantiTect Reverse Transcription Kit (Qiagen) as per manufacturer's instruction. All primers were shown in

Table 7. RT-qPCR was conducted using ExpressSyBr Green Mastermix (Life Technologies). Samples were cycled 40 times using QuantStudio™ 6 Flex Real-Time PCR. All cycle conditions were as followed: 95 °C for 15 min followed 40 cycles of 94 °C for 15 s, primer-specific melting temperature for 30 s, and 72 °C for 30 s. Results were analysed using the comparative change in threshold cycle (∆Ct) method and are normalised to the gene expression of the cells collected on Day 0 unless stated otherwise.

2.5.7 Single Cell PCR

RNA were isolated using Single Cell Lysis Kit (Thermo Fischer Scientific), according to the manufacturer's protocol, without quantification. The total solution on this step was then added up to 11 µL. RNA was used to generate cDNA using SuperScript® VILO™ cDNA Synthesis Kit (Thermo Fischer Scientific), assuming a 1:1 conversion. cDNA was pre-amplified with 0.2X Taqman® probes, see below, and TaqMan® PreAmp Master Mix (Thermo Fischer Scientific). cDNA was diluted with TE buffer to 133 µL. Single Quantitative PCR was performed using 4 µL of cDNA with TaqMan® Fast Advanced Master Mix (Thermo Fischer Scientific) and QuantStudio™ 6 Flex Real-Time PCR (Thermo Fischer Scientific). The following Taqman® probes were used: GAPDH (Hs02758991_g1), MYL2 (Hs00166405_m1), MYL7 (Hs01085598_g1), MYH6 (Hs01101425_m1), MYH7 (Hs01110632_m1), TNNI1 (Hs00913333_m1) and TNNI3 (Hs00165957_m1). The ΔΔCt method was used to compare expression between single hiPSC-

CM cultured on 3D micropatterned substrate and flat control surface normalised to hiPSC-CMs before plating.

2.5.8 Flow cytometry

Cells were dissociated and transferred to cytometry tubes. The 100 µm filter was used to ensure that the cells were single. The samples were washed by 300 rcf centrifugation for 1 min before resuspending in PBS and replacing with FluoroFix buffer (BioLegend). Zombie Violet™ Fixable Viability Kit was used to stain dead cells and further exclude from analysis. The samples were fixed using Fix and Perm Cell Permeabilization Kit (Thermofisher) following manufacturer's protocol. 1:500 Troponin T Cardiac Isoform Antibody (13-11) (Thermofisher) was used and followed by secondary staining of 1:500 Alexa Fluor® 488 donkey anti-mouse IgG (H+L) (Life Technologies). Each of the antibody was incubated at 4 °C for 30 min, rotating. The analysis was performed using BD Fortessa (BD Bioscience). The data were analysed using FlowJo software. This experiment was performed by Dr Manuel Mazo.

2.5.9 Biological atomic force microscopy

Nanosensors AFM Prob qp-BioAC-10 (Windsor Scientific) was used. Contact mode AFM (Agilent) was used and analysed using Hertz model for 200-nm indentation. The samples were maintained in Leibovitz's L-15 Medium (no phenol red, Life Technologies) at 37 °C, atmospheric condition. The scan (Force-Distance curve) was identified to ensure that the probe did not breakthe cell membrane. The measurements were analysed using AtomicJ[341] at maximum plotting range of 0.5 nm.

2.5.10 Immunofluorescent staining

Samples were washed with PBS and fixed using 4% v/v paraformaldehyde (Sigma) at room temperature for 15 min. The samples were washed with PBS, three times. Samples were permeated with 0.1% v/v Triton X-100 (Sigma-Aldrich) in PBS for 15 min and washed three times with PBS, 15 min each. The samples were blocked in 10% v/v donkey serum (VWR International), 5% w/v bovine serum albumin (Sigma-Aldrich), and 0.3 M glycine (Sigma-Aldrich) for at least 1 h at room temperature. Samples were incubated with 1:200 v/v anti-α-actinin (Sigma), 1:200 v/v anti–cardiac troponin T (Abcam), 1:200 v/v anti-Connexin-40 (Abcam), 1:100 v/v anti-Connexin-43 (Abcam), 1:500 v/v anti-Connexin-45 (Abcam), 1:140 v/v anti-MYL2 (Abcam) and 1:140 v/v anti-MYL7 (Abcam) in 1:10 v/v dilution of blocking buffer and PBS. The incubation was performed overnight at 4 °C, shaking. The samples were thoroughly washed with PBS, 15 min each. The secondary antibodies were chosen and diluted 1:400 v/v donkey anti-mouse immunoglobulin G

(IgG) (H + L) (Thermo Fisher Scientific), donkey anti-rabbit IgG (H + L) (Thermo Fisher Scientific) and donkey anti-goat IgG (H + L) (Thermo Fisher Scientific) in PBS for 1 h at room temperature. The washes were conducted three times with PBS. The excitation wavelengths of secondary antibody were selected among 488 (Green), 555 (Red) and 647 (Far red) nm. Nuclei were visualised using 1:500 v/v DAPI (Thermo Fisher Scientific) in PBS for 1 min. Fluoromount Aqueous Mounting Medium (Sigma-Aldrich) were used to mount the samples and preserved fluorescent signals. The samples were imaged with using a Zeiss LSM-780 confocal microscope unless stated otherwise.

2.5.11 Optical mapping and caffeine application

Intracellular calcium sensitive dye was prepared from a mixture of 50 µg of Fluo-4 AM (Invitrogen) and 50 µL of 20% v/v Pluronic® F-127 in DMSO (Invitrogen). The constructs were mounted on a 35 mm glass bottom dish (MatTek). Samples were incubated with 4 µL in 1 mL RPMI-1640 (50 µM concentration) supplemented with B27 (Life Technologies) for 20 min at 37 °C, humidified chamber. The media was replaced with fresh RPMI-1640 supplemented with B27 and the samples were further incubated for 20 min at 37 °C, humidified chamber. Additionally, genetically engineered hiPSC line (WTC GCaMP6f) was used without Fluo-4 AM incubation. The fluorescent signals were recorded using an upright Nikon Eclipse TE2000-U microscope equipped with a 40X water immersion objective and Osca Flash 4 (Hamamatsu) (1024x256 pixels, 4 ms frame rate, bin 2). WinFluor software (University of Strathclyde) was used to record the images. During the experiment, the sample was perfused with 37 °C Normal Tyrode's solution and field stimulated at 1 Hz using a MyoPacer (IonOptix). Local caffeine application to hiPSC-CMs allowed assessment of CM Ca^{2+} SR content and calcium removal mechanisms. 40mM caffeine in normal Tyrodes was loaded into borosilicate glass micropipettes and mounted on a 3-axis micromanipulator. The tip was positioned near the surface of the cells. CMs were paced at 1 Hz for 3 calcium transients before the stimulus was ceased and caffeine was applied simultaneously with a syringe pump applying the positive pressure. The caffeine application has been performed with help of Mr Brian Wang and Dr Liam Couch.

The signal was analysed with custom MatLab® code (available upon request) or Axon™ pCLAMP™ Electrophysiology Data Acquisition & Analysis software (Molecular Devices) to determine four main parameters: normalised amplitude (f/f0), which is the peak transient amplitude divided by the baseline value of the signal; time to peak (Tp), which is the time taken to reach peak amplitude; time to 50% decay (T50) and 90% decay (T90), which are the time taken

for the transient to decrease from transient peak amplitude to 50% and 90% of the transient amplitude respectively, during the recovery phase of the transient.

2.5.12 Traction force microscopy

The samples were mounted on a glass bottom 35 mm MatTek dish No. 0, 14 mm diameter. Leibovitz's L-15 Medium was used during the experiment. time-lapse TFM acquisition and Live imaging of bead displacement were recorded using 63x Nikon Oil immersion objective mounted on Zeiss Axio Observer Inverted Widefield Microscope at 50 frames/s. The samples were kept in 37 °C and 5% CO_2 chamber, Leibovitz's L-15 Medium. All the acquired images were processed by ImageJ (NIH) comparing the area where the cell was before and after trypsinisation. Displacement and force field were analysed by a JAVA custom written plugin by Dr Qingzong Tseng (Institut Curie, France) (https://sites.google.com/site/qingzongtseng/).

2.5.13 Conduction Velocity measurement

The conduction velocity of myocardial ultrathin slices was recorded using multielectrode arrays setup (Multichannel Systems) and MC_Rack software. The samples were superfused with 37 °C oxygenated Normal Tyrode's solution. The samples were held in place using in-house washer. The changes in voltage were acquired with a 60-microelectrode plate with the microelectrodes arranged in an 8 × 8 matrix with a 700-µm interelectrode space. The sample was stimulated at 1 Hz, 1 – 3 V and 5 ms intervals. The stimulations were performed at two different directions according to fibre alignment. This was achieved to observe transversal and perpendicular conduction velocity. The results were analysed using a custom MatLab® code and Microsoft Excel. The code is available upon request.

2.5.14 Scanning ion conductance microscopy

The samples were mounted onto a 35 mm MatTek dish No. 1.5 and perfused with 37 °C Leibovitz's L-15 Medium, no phenol red during the experiment. A glass pipette probe was created from borosilicate glass (O.D. 1 mm, I.D. 0.5, Intracel) using a P-2000 laser puller (Sutter Instruments). The setup was optimised to create maximal inner diameter of the tip to be 100 nm. This was confirmed under a microscope before filling the tip with PBS. Ion current measurements (Molecular Devices) was measured using Axopatch 200B amplifiers with a bias potential of 200 mV during imaging. Three topographical images were analysed to generate stiffness maps at progressively increased set points using approach speed of 30 nm/ms as reported previously[343]. Cell stiffness maps were generated from each height map on the basis of stress and strain using custom-made software written by Dr P. Novak, Queen Mary University of London.

2.5.15 Western blot

4 – 20% Mini-PROTEAN TGX Precast Gel (BioRad) was used to pass the protein samples through a low density stacking layer before the high density. The individual gel was fitted in Mini Trans-Blot® Cell (BioRad). The system filled with electrophoresis running buffer. The protein sample was prepared by adding appropriate amount of 2x Laemmli Sample Buffer (BioRad) and heated at 95 °C for 5 min to ensure complete protein denaturation. 20 µg of protein sample was loaded into each well. Electrophoresis was initiated at 60 V for 30 min or until the dye front reached the separating gel when the voltage was increased to 120 V until the dye front was approximately 0.5 cm from the bottom of the precast gel.

After separation, proteins were transferred to polyvinylidene fluoride (PVDF) membranes (Bio-Rad Laboratories) electrophoretically using a wet transfer system (BioRad). The protein transfer was performed at 10 V/100 mA for 2 h at room temperature. After transferred, the PVDF was washed three times with TBS-Tween before blocking using 4% w/v skim milk (Sigma) or 4% v/v FBS (Gibco) for 1 h at room temperature. The membranes were subsequently incubated in primary antibody diluted to an appropriate concentration in blocking solution overnight at 4 °C. After incubation the membranes were washed three times for 45 min each with TBS-Tween. An appropriate secondary antibody was selected and diluted to a working concentration in blocking solution for 1 h at room temperature. The membranes were washed three times for 15 min each in TBS-Tween. The membrane was imaged using Odyssey® CLx Infrared Imaging System (Licor) and analysed using Image Studio Software (Licor).

2.5.16 Proteomic Profiler

The samples were analysed with Proteome Profiler Human Phospho-Kinase Array Kit (R&D System) according to the manufacturer's instruction. The membranes were washed with TBST for 30 min, three times. The membranes were then put onto a transparent plastic sheet for further development. The membrane was further developed using SuperSignal™ West Femto Maximum Sensitivity Substrate (Thermo Fischer). The signals were recorded using BioSpectrum Imaging System (UVP). The optical density of the bands was then measured using Fiji software (NIH).

2.5.17 Image analysis for sarcomere length

The samples were stained for sarcomeric α-actinin and imaged with confocal microscopy. The images were processed with Fiji (NIH). A line was drawn perpendicularly to several

consecutive sarcomeres, the sarcomeric α-actinin resulted in peaks on the fluorescence signal which corresponded to the consecutive sarcomeres. The distance between the first and last peaks was measured. The length of the line was then divided by the number of peaks. Three images per slice were acquired and the sarcomere lengths of at least five cells per image were measured.

2.5.18 PCR multivariate analysis

Statistical analysis was performed in MatLab® and R. Normalised relative fold change values for each gene of gene of interest was analysed. Principal Component Analysis (PCA) was performed using PLS toolbox (Version 8.2.1, Eigenvector Research Inc.) for data reduction and visualisation. Variable correlation was performed in MatLab® using a Spearman correlation. For feature selection and sample classification, the PCR data were imported into R (version 3.4.0) and incorporated into the analysis as both normalised relative fold change and the indicated ratio combinations. Each group (substrate-stiffness combination) was split into training and validation groups for a 5-fold cross-validation of optimal model sparsity based on LASSO ($\alpha = 1.0$) as implemented in the GLMnet package for multinomial regression. Following optimal parameter selection for winner features, the predicted probability for class membership was calculated for each sample based on a leave-one-sample-out cross-validation procedure. Predicted class membership was assigned for each sample to the class with the highest predicted probability. A resulting confusion matrix was generated based on known and predicted class membership. This analysis has been done by Dr Isaac J. Pence. Code is available upon request.

Chapter 3

The Role of Matrix Stiffness in Modulating the Cardiac Specification of Human Pluripotent Stem Cells

3.1 Abstract

The advancement of new regenerative therapies is centred on the understanding of the mechanisms involved throughout development. In particular, embryogenesis is influenced not only by a set of soluble factors and cell-cell interactions, but also by a variety of mechanical cues that play a role in a range of intracellular events. However, fundamental knowledge of how biophysical signals affect stem cell behaviour is lacking, thus slowing the progression of cellular therapy on MI. Tuneable stiffness substrates can be used to explore this effect and the underlying mechanisms. Here, the effect of substrate mechanics on the differentiation of CMs from hiPSCs was studied using mechanically tuneable hydrogel substrates.

The chapter describes the optimised functionalisation technique of polyacrylamide substrates for hiPSC cultures and CM differentiation. Two different hydrogels (agarose and polyacrylamide) were tested. Methacrylate modified agarose was shown to support culture of a muscle cell line (C2C12). However, the stiffness of the resulting hydrogel was not enough to serve as a model of disease-like myocardium (> 50 kPa). Next, acrylic acid was incorporated into polyacrylamide during polymerisation, resulting in superior protein conjugation uniformity and efficiency compared to current techniques. A carboxylic group and protein were quantitatively assayed to optimise the protein conjugation and to determine the amount of protein bound to the substrates. Mechanical characterisation was performed to determine the influence of acrylic acid on Young's modulus, and to identify the mixtures to be used in further experiments. Polyacrylamide-*co*-acrylic acid (PAAm) demonstrated adhesion of hiPSCs, with retention of pluripotent phenotype of hiPSCs. By using PAAm as an *in vitro* cell culture substrate, hiPSCs can be differentiated to CMs (hiPSC-CMs). Next, structural and functional properties of hiPSC-CMs were observed by characterising gene and protein expression, cardiac structure and EC coupling. Differentiation efficiency level (percentage of cTnT+ cells) demonstrated a peak at embryonic-like stiffness with an increase in upregulation of cardiac genes. Functionally, hiPSC-CMs showed a biphasic relationship with optimal calcium handling and force generation at adult cardiac physiological stiffness. In conclusion, this chapter highlights optimal substrate conditions for hiPSC-CM differentiation and *in vitro* culture.

3.2 Introduction

The process of cardiogenesis involves the development of a dynamic mechanical environment. CM contractility and ECM remodelling influence cardiac development by generating varied mechanical loads within the developing tissue, of up to 16 kPa in each heartbeat. The mechanical properties of the ECM, especially stiffness, have a profound effect on how CMs develop and perform. CMs are embedded in a highly structured microenvironment which consists of neighbouring cells and the ECM. This imposes specific boundary conditions that highly influences cell mechanics and architecture, providing not only essential physical cues for the cellular constituents, but which also initiates, regulates and stores biochemical and biomechanical signals. These signals are required for cellular morphogenesis, differentiation, and homeostasis. Many studies have demonstrated that ECM stiffness affects CM function and structure, showing optimal stiffness at ~ 10 kPa[118,119]. The presence of a stiff ECM in the scar tissue deposited after cardiac ischemia negatively affects the heart function and structure. For example, this increase in stiffness has been shown to pathologically increase the magnitude of cell tractile forces[185–187]. In a process known as hypertrophy, CMs adapt to this excessive load by abnormal enlargement of the cells and thickening of the myocardium. Over time, this pathological change leads to severe functional degradation and heart failure.

The development of hiPSCs generates enormous potential for regenerative medicine, drug screening, disease modelling, and personalised healthcare, by providing a theoretically unlimited source of pluripotent stem cells that can be differentiated to CMs. But despite this advancement in stem cell technology, the inability to recreate the adult CM phenotype remains a significant hurdle[344]. Generally, they are grown in a tissue culture plastic for which the stiffness of the substrate is much higher than their native environment (a few orders of magnitudes higher than fibrotic region found in MI).

This chapter shows a novel approach centred on understanding the mechanical conditions which regulate cardiogenesis. The polymer substrate was optimised to study the effect of substrate mechanics on hiPSC-CM differentiation, as a model of cardiac development. The differentiation protocol was developed on the new substrate of tuneable stiffness. Signalling pathway modulation was investigated by merging results from functional (e.g. force and calcium cycling) and molecular (e.g. gene/protein expression, proteomic profiler) assays. The consequent analysis identified the mechanisms priming hiPSC to undergo cardiac lineage differentiation on the more physiologically relevant stiffness substrate. The results described in this chapter highlight the role of mechanical signals, from varied cell culture substrate stiffness[215,345–347], on

hiPSC differentiation and hiPSC-CM fate. These insights will highly contribute to the field of cardiac research and regeneration and aid the development of the next-generation cell-biomaterial therapies for the heart.

3.3 Results

Agarose and PAAm have been widely used as a substrate to study cellular mechanoresponsive behaviour to varying stiffness. However, they are limited by either the range of potential stiffnesses they can generate, or by protein conjugation efficiency. Therefore, a system which allows easy modulation of stiffness with efficient and uniform surface protein conjugation would represent a valuable tool for the study of cellular mechanoresponsive behaviours.

Varying agarose concentration allows the tailoring of substrate mechanical properties, making this natural hydrogel a suitable platform to study the influence of the mechanical environment on cells. Given, however, that agarose is cell repellent, it must be modified using chemical derivatisation and radical crosslinking (as shown in ***Figure 7a***), to produce acrylate-activated agarose, which is spontaneously reactive to the primary amine on proteins, thus providing a cell adhesive ligand on agarose surface. Briefly, low melting point Agarose was dissolved in DMSO before adding 4-(Dimethylamino)benzaldehyde. The mixture was reacted to methacrylic anhydride to create an acrylate group. Acrylate-activated agarose was precipitated, freeze dried and powdered. Next, agarose gelation was performed by mixing different acrylate-activated agarose and non-modified low melting point agarose in dH_2O before autoclaving. Ratios of 0:100, 2.4:97.6, 7.1:92.9, 11.8:88,2 and 16.6:83.4% acrylate-activated agarose to non-modified low melting point agarose (in 2% w/w and 3% w/w total agarose solution) were produced and equilibrated in PBS for 24 h prior to mechanical test. The compressive Young's modulus was performed using an in-house force transducer assembled by Dr Michael B. Albro (Dept. of Materials, Imperial College London). ***Figure 7b*** showed that, at 2% w/v agarose hydrogel, the compressive Young's moduli were 18.15, 10.06, 0.92 kPa at a mixture ratio of 0:100, 2.4:97.6 and 7.1:92.9% w/v acrylate-activated agarose, respectively. Higher mixtures of acrylate-activated agarose did not form a hydrogel. At 3% w/w agarose hydrogel, the compressive Young's modulus was 45.43, 33.18, 10.29, 3.01 and 0.53 kPa at ratios of 0:100, 2.4:97.6, 7.1:92.9, 11.8:88,2 and 16.6:83.4% w/w respectively. The trend showed a decrease in the compressive Young's modulus, with an increase in the percentage of acrylate-activated agarose in the agarose hydrogel, showing a trade-off between the amount of protein the hydrogel can potentially conjugate, and the mechanical properties of the material.

Next, the C2C12 cell line was used to test whether the hydrogel can be used as a cell culture platform. The extracellular matrix (ECM) proteins collagen I, laminin and fibronectin were conjugated to acrylated-agarose to provide adhesive cues on the hydrogel surface. PBS and

collagen I coated tissue culture polystyrene (TCP) were used as a negative and positive controls, respectively. C2C12 were plated and cultured for 24 h. ***Figure 7c*** showed that C2C12 cells can adhere onto collagen I conjugated agarose hydrogel while laminin and fibronectin could not accommodate cell adhesion. Although C2C12 adhesion might differ depending on substrate, this result showed that the hydrogel is biocompatible and adhesive ligand conjugation was achieved. Therefore, a mixture of acrylate-activated agarose and non-modified agarose demonstrated its capability to serve as an *in vitro* cell culture platform.

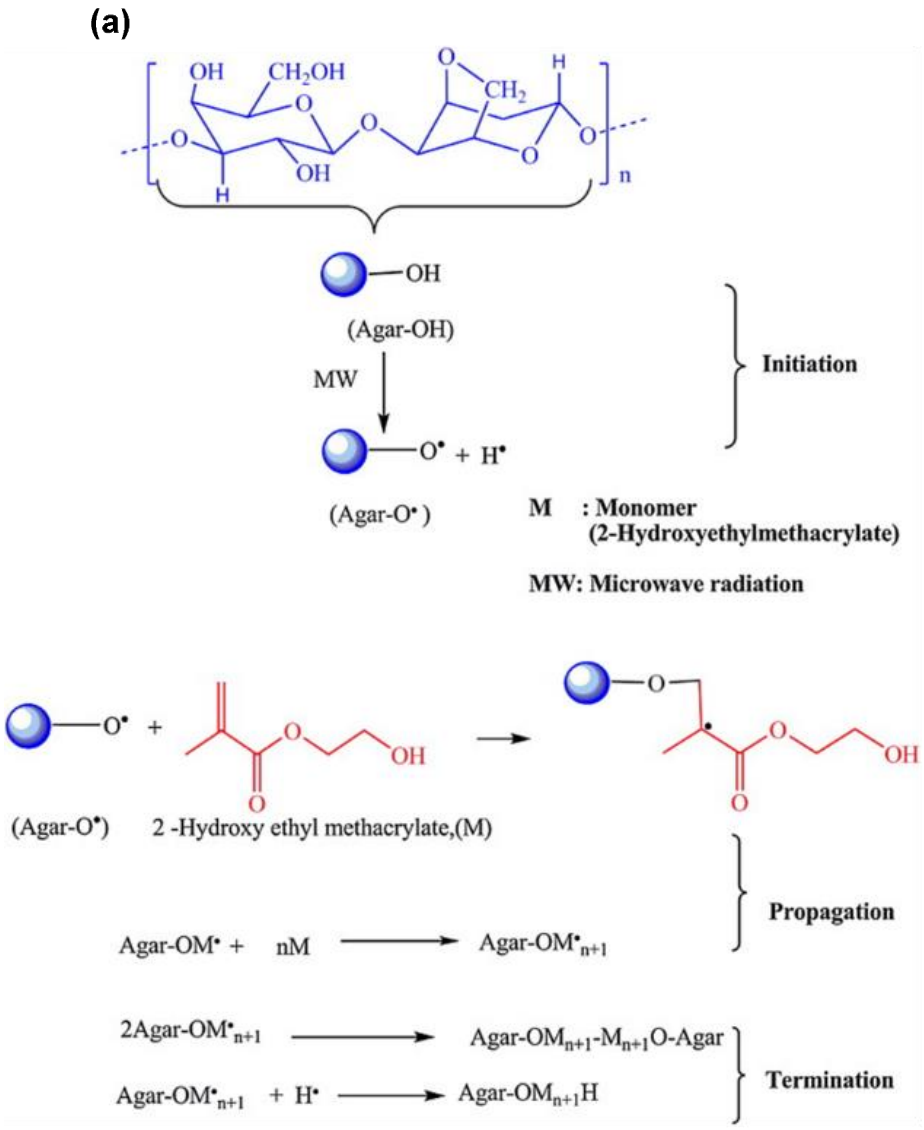

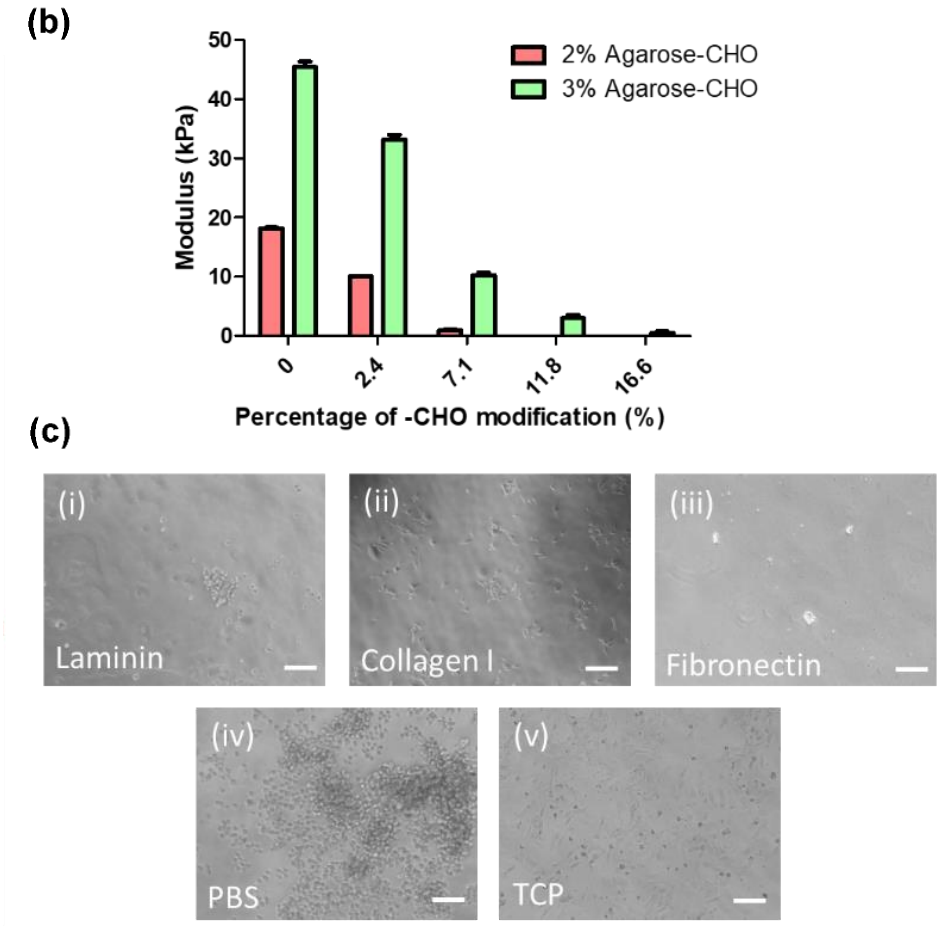

***Figure 7**: **Agarose hydrogel synthesis and optimisation.** (a) Schematic diagram of acrylate-activated agarose synthesis. Low melting point agarose was dissolved in DMSO and reacted with methacrylate anhydride. Reproduced from [348]. This synthesis was performed with the assistance of Dr Michael B. Albro. (b) Equilibrium compressive Young's modulus of 2-, 3-% wt agarose hydrogel with various mixture ratio between agarose and acrylate-activated agarose (N = 6), (c) Representative bright field images of C2C12 cultured on (i) Laminin, (ii) Collagen I, (iii) Fibronectin, (iv) PBS (negative control) conjugated agarose hydrogel and (v) Collagen I coated TCP. Data shows mean ± SEM. (Scale bar: 100 μm).*

While acrylated-agarose supports C2C12 adhesion and proliferation, the range of Young's modulus cannot exceed 50 kPa. This depends on the ratio between methacrylated agarose and non-modified agarose. Typically, agarose can exhibit stiffness of above 50 kPa. The addition of methacrylated agarose reduced the stiffness. This severely hinders the capacity of this platform to replicate the mechanical environment in cardiac tissue, where pathological remodelling raises its stiffness well beyond this point. Therefore, this chapter aimed to develop an *in vitro* system with a wider range of stiffnesses (0.5 - >50 kPa), covering both physiological and pathological stiffness of native myocardium.

Polyacrylamide (PAm) is a polymer consisting of acrylamide monomers and N,N'-methylenebisacrylamide (bis) cross-linker. It has a wide range of stiffness that can be tuned to match even the nervous system (the softest tissue of the body)[310]. It has been widely used as an *in vitro* cell culture platform, by using Sulfo-SANPAH as a crosslinker to ECM proteins. Sulfo-SANPAH provides an amine-reactive NHS ester and a photoactivatable nitrophenyl azide to covalently link proteins onto the hydrogel surface. Additionally, there are two main reported modifications of PAm: hydrazine[349] and acrylic acid[314]. Hydrazine hydrate was used as a reducing agent to modify an amide group to a hydrazide group which is highly reactive to aldehyde and ketone groups found in oxidised proteins. Oxidation of proteins however can cause structural changes, compromising protein functionality. Acrylic acid was speculated to provide a more robust conjugation by adding carboxylic groups to the PAm backbone that could be covalently linked with an amine group in proteins via 1-ethyl-3-(3-dimethylaminopropyl) carbodiimide (EDC). This simple conjugation method overcomes the frequently observed non-uniform coating due to variability in UV irradiation of previously used photoactivatable cross-linkers. To test this, PAm hydrogels were first immersed in a hydrazine hydrate solution. ECM proteins were oxidised before using EDC as a crosslinker to hydrazide PAm. Secondly, an equivalent amount of acrylamide monomer was substituted by 0.4% w/w acrylic acid monomer (pH was adjusted to 7.4 using 10 M NaOH). After modification, the conjugation of fibronectin on the hydrogel was performed using EDC and NHS. These three hydrogels (Sulfo-SANPAH, acrylic acid addition and hydrazine hydrate) were equally conjugated to the same concentration of fibronectin. The HL-1 cell line was used as a model for an *in vitro* cell culture test and cultured for 24 h on the 3 modifications of PAm substrates. This was switched due to the need of contractile cell type, which was previously not available. The results showed that polyacrylamide-*co*-acrylic acid (PAAm) was the optimal substrate, as a higher cell density was produced on these substrates, as compared with Sulfo-SANPAH or hydrazine hydrate conjugated hydrogels (***Figure 8*a**). The PAAm chemical structure is shown in ***Figure 8*b**(i). As shown in ***Figure 8*c**, Bovine Serum Albumin-Alexa Fluor® 680 (BSA-

AF680) were conjugated and relatively quantified the amount of proteins bound on each PAm modification. The result demonstrated that PAAm can conjugate the highest amount of BSA-AF680 compared to control, hydrazine hydrate and sulfo-SANPAH modification.

Mechanical characterisation was performed by measuring the Young's modulus of different monomer concentrations with fixed acrylic acid at 0.4% w/w using Atomic Force Microscopy (AFM) with in-house 20 µm tips on indentation mode (***Figure 8*b(ii)**). The result showed that modulating the acrylamide monomer to bis crosslinker ratio was able to significantly modify the hydrogel´s Young´s modulus, ranging from 0.56 to 112 kPa. Therefore, this system truly covers the full spectrum of stiffness, from embryonic to adult human myocardium[17,119,183], both physiological and diseased.

Finally, neonatal rat ventricular CMs (NRVMs) were seeded with different ECM proteins conjugation on 9.67 kPa PAAm hydrogel's surface to optimise ECM protein binding for cardiomyocyte adhesion and growth. Bright field images showed that collagen I proved the most optimal ECM protein for NRVMs culture at 24 h after seeding. Therefore, PAAm can serve as a superior cardiomyocyte culture substrate than PAm hydrogel modified with sulfo-SANPAH and hydrazine hydrate. Although the difference between cell types, especially NRVMs and hiPSCs has been acknowledged, the behaviours of NRVMs are broadly similar to hiPSC-CMs (e.g. growth as a syncticium in monolayer culture and spontaneous contractility).

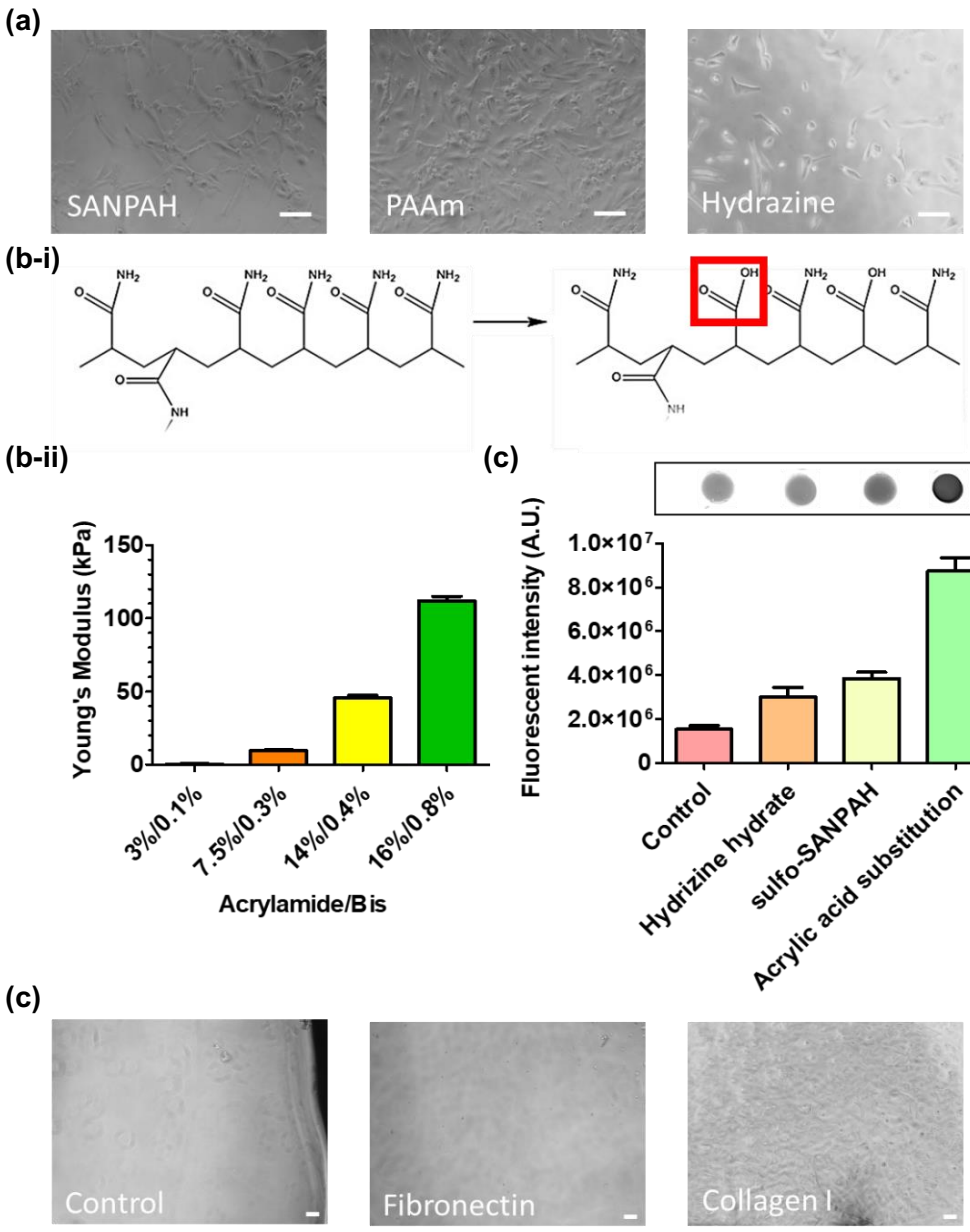

***Figure 8**: **Polyacrylamide hydrogel optimisation.** (a) Representative brightfield images of HL-1 cultured on different polyacrylamide modifications: SANPAH, Acrylic acid, Hydrazine hydrate. (Scale bars: 100 μm). (b) Polyacrylamide-co-acrylic acid (PAAm) (i) Chemical structure (the highlighted square shows a substitution of acrylic acid on acrylamide monomer), (ii) Young's modulus determination using AFM, (c) Fluorescent quantification of Bovine Serum Albumin (BSA), Alexa Fluor® 680 (BSA-AF-680) conjugated on PAm with sulfo-SANPAH, hydrazine hydrate and acrylic acid substitution (N = 6), (inset) representative images from Odyssey Licor infrared scanner, (d) representative brightfield images of neonatal rat ventricular cardiomyocytes*

(NRVMs) cultured on fibronectin and collagen I conjugated PAAm for 24 h (Scale bars: 100 µm). Data shows mean ± SEM.

Microfabrication, a set of techniques used to fabricate miniature structures with finely controlled size and organisation, has been utilising to create natural mimicking 3D microenvironment. It can create features at sub-micron resolution in a highly controllable manner. In this study, soft lithography was utilised to cast a 3D micropattern on PAAm. Since the silicon master that was used to form a micropattern is expensive and time consuming to produce, a sacrificial hydrophobic coating step was introduced to protect the silicon master and to facilitate the removal of PAAm after polymerisation. Trichloro(1H,1H,2H,2H-perfluorooctyl)silane was vaporised and deposited on the silicon master to create hydrophobic surfaces. However, this treatment might repel and/or reduce cell adhesion. Therefore, to study cell activity, NRVMs were plated on the PAm cast from a bare hydrophobic coated silicon master (***Figure 9a***). alamarBlue™ was used to quantify cell metabolic activity. As shown in ***Figure 9b***, the result showed insignificant differences between the hydrogel fabricated using a silicon master with or without hydrophobic sacrificial layer coated on both stiffnesses tested, 7.5%/0.3% v/v and 14%/0.4% v/v. ($p = 0.5415$ and $p = 0.0757$, respectively, Student's t-test).

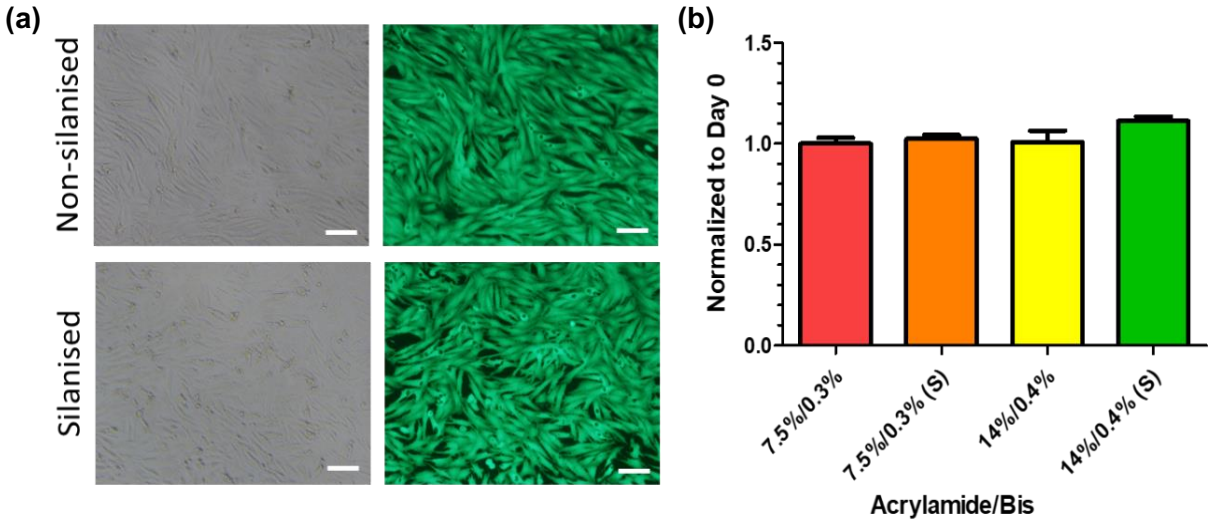

***Figure 9**: **Effect of hydrophobic coating on cellular metabolic activity.** The PAAm hydrogels were casted on the masters with (S) and without hydrophobic layer coating. (a) Representative image of bright field images and calcein (green) of NRVMs cultures on the hydrogels. Scale bars: 100 µm. (b) Measurement of cellular metabolic activity was assayed by alamarBlue™. Data shows mean ± SEM; n = 5 per experiment, N = 3 independent biological experiments. (one-way ANOVA, n.s, p>0.05).*

With the purpose of determining the thickness of the Matrigel layer, both the hydrogel and Matrigel were embedded with fluorescent microbeads (***Figure 10b***), to allow visualisation of the thickness of each component. Matrigel-coated hydrogel 3D images were reconstructed from z-stack pictures taken with a Leica SP5 MP/FLIM inverted confocal microscope. The 3D reconstructed image showed that Matrigel thickness was approximated to be 5 μm as shown in ***Figure 10c***. This is within the range of previously reported hydrogel thicknesses that stem cells can feel (≤ 50 μm) with a tactile range of ~ 5 μm[350].

Next, mesenchymal stem cells (MSC) were used as a mechanosensitive cell type to study the impact of Matrigel coating on the surface. MSC responses to mechanical changes on substrates have been widely established and reported, making them an ideal system to test our platform[148,350,351]. Yes-associated protein (YAP) has been recently shown to act as a sensor and a mediator of biomechanical signals affected by the ECM. Functionally, YAP expressions were required for MSC differentiation in responses to the external microenvironment. YAP responds to ECM rigidity by altering its subcellular localisation. Localisation of YAP protein is observed in the nucleus when the cells are cultured on a rigid substrate and cytoplasm, when the cells are cultured on a soft substrate. The localisation of YAP can thus be related to the mechanoresponse of cells on a substrate. Therefore, MSCs were seeded onto two widely different stiffnesses (560 Pa and 112 kPa) and maintained for 24 h. Next, immunofluorescent staining of mechanosensitive protein, YAP[147], on MSC was performed (***Figure 10d***). As shown in ***Figure 10e***, the nuclear/cytoplasm YAP protein intensity ratio was calculated using custom MatLab® code. The result demonstrated that mesenchymal stem cells can sense different PAAm hydrogel stiffnesses from 560 Pa (cytoplasmic YAP localisation), 112 kPa (nuclear YAP localisation) and TCP (nuclear localisation - control). Therefore, double coating steps do not affect the way MSC sense the underlying PAAm hydrogel stiffness.

Next, to determine the actual capacity of hiPSCs to sense the varying stiffness, hiPSCs were seeded onto different PAAm and immunofluorescently stained YAP was used to quantify the localisation of YAP in the nucleus and cytoplasm (***Figure 10g***). Results showed for the first time that YAP can be used as a mechanosensitive protein indicator in hiPSCs, with its localisation varying amongst the different PAAm samples (***Figure 10f***). Indeed, the significant elevated gene expression of YAP downstream genes, RHOF and SCARA3 was detected with increased stiffness. The softest stiffness of 560 Pa is in the range of stiffness found during early embryogenesis, which is optimally replicated in our system by the higher OCT4 levels as determined by RT-qPCR[215]. These results highlight the capacity of the developed PAAm system

to replicate the mechanical environment cells experience throughout development and disease, which is adequately accompanied by relevant changes in YAP downstream gene expression and protein colocalisation (***Figure 10h***). Therefore, hiPSC can sense the change in underlying stiffness from stiffness tuneable PAAm platform developed in this study. Additionally, proliferation capacity could be further explored due to the changes in the Hippo-YAP pathway[15].

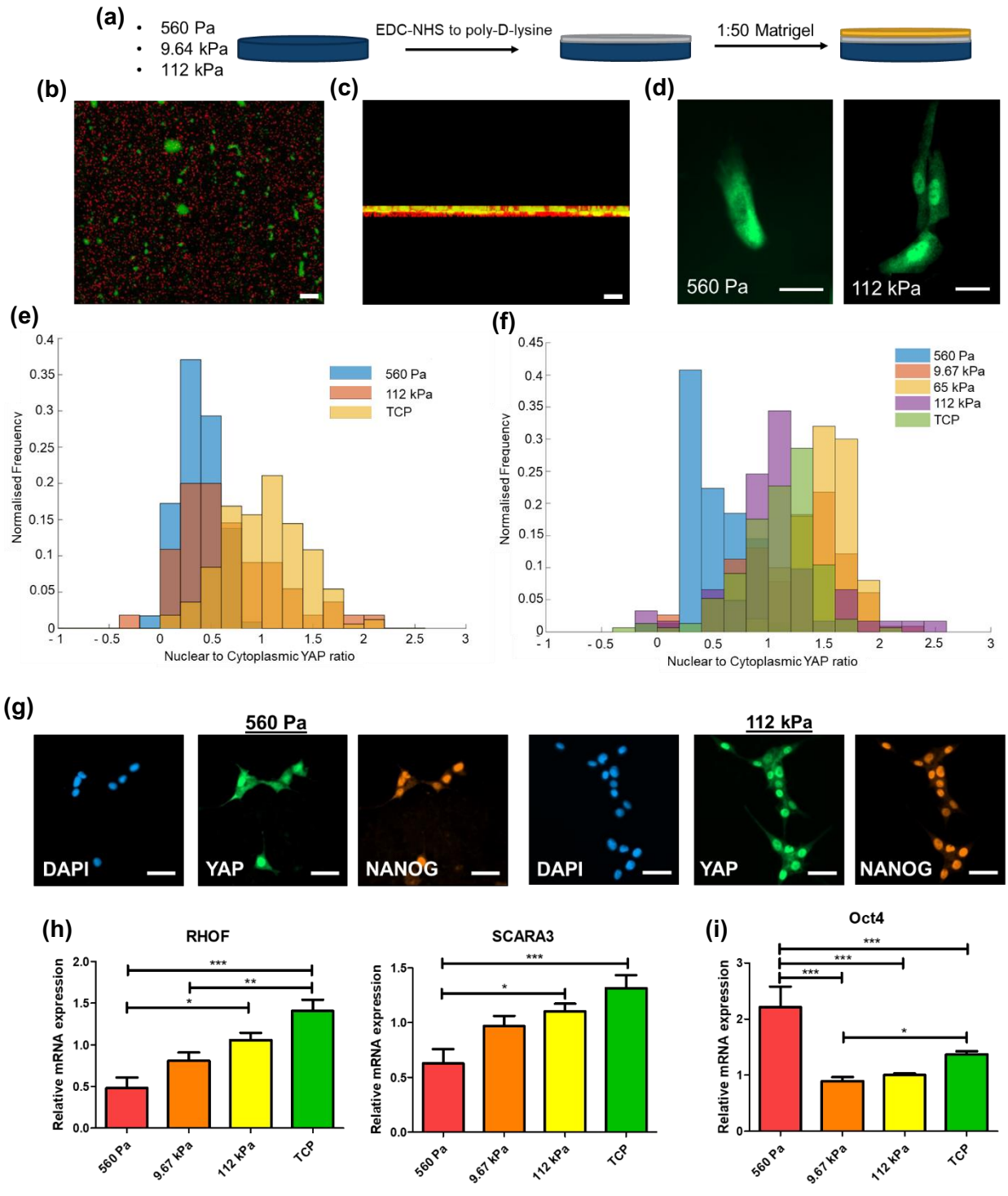

***Figure 10**: **MSC and hiPSC sense the underlying PAAm substrate.** (a) Conjugation strategy: schematic diagram of optimised PAAm substrate fabrication for in vitro cell culture. (b) Top view and (c) Side view of fluorescent image of red fluorescent beads embedded PAAm hydrogel with greed fluorescent beads Matrigel (Scale bars: 10 μm), (d) Representative confocal*

*immunofluorescent images of YAP protein localisation in MSC cultured on PAAm hydrogel (Scale bars: 20 µm), (e) Nuclear/cytoplasm YAP protein localization ratio in (MSC) plated on PAAm hydrogel (N = 3), (f) Bar graph of nuclear/cytoplasm YAP protein localization ratio in human induce pluripotent stem cell (hiPSC) plated on PAAm hydrogel (N = 5), (g) Representative confocal immunofluorescence images of YAP protein localisation in hiPSC grew on PAAm hydrogel (Scale bars: 50 µm), (h) real-time qPCR of hiPSC after 24 h in culture on PAAm hydrogel of YAP downstream genes, RHOF and SCARA3 (N ≥ 8) and (i) immunoblotting fluorescent intensity for OCT4 protein in hiPSC after 24 h in culture on PAAm hydrogel (N ≥ 6). (one-way ANOVA, *p < 0.05, **p < 0.01, ***p < 0.001)*

During embryogenesis, stem cell differentiation is guided by cell-cell and cell-matrix interactions, ultimately directing stem cell fate. Traditional *in vitro* culture uses non-physiological high stiffness tissue culture polystyrene (TCP) to generate stem cell derived-lineages, including CMs. This, however, does not represent the native setting and thus imposes a significant bias to any research conducted under these conditions, either aiming to shed light on the underlying mechanisms of stem cell commitment and differentiation or to direct stem cell fate for biomedical applications. Therefore, hiPSCs were used to investigate how biomechanical signals from the microenvironment could differentially modulate CM specification. ECM protein coating was optimised to provide the suitable adhesive cues for hiPSC growth and differentiation. As shown in ***Figure 11***, laminin (a), Matrigel (b), poly-d-lysine (PDL) (c) and fibronectin (d) were initially, individually conjugated to PAAm substrates through the previously optimised method. hiPSCs were plated at 32,000 cells per cm^2 and maintained in culture for 48 h. However, results showed that hiPSC formed clumps without proper cell adhesion and spreading. Therefore, these ECM proteins *per se* cannot serve as a suitable matrix on PAAm for hiPSCs.

Next, double coating steps were implemented. This was achieved by covalently conjugating PDL with PAAm, which provided positive charges as a fundamental building block for ECM proteins to later bind statically to the PDL. Two different molecular weight PDL were conjugated individually, 30,000 – 70,000 (low) and 70,000 – 150,000 (high), and Matrigel was used in the second step[87,223]. hiPSCs were then seeded and cultured for 48 h. hiPSCs on high molecular weight PDL demonstrated a pluripotent morphology and grew as colonies without spontaneous differentiation, demonstrating that double coating steps are suitable for supporting hiPSC adhesion and growth (***Figure 11g***).

After the double coating was developed for hiPSC culture, the Matrigel concentration was then further optimised for CM differentiation[87,223,352]. Therefore, different Matrigel dilutions were incubated with high molecular weight PDL conjugated PAAm hydrogel from 1:10 (~128 μg/cm^2), 1:20 (~64 μg/cm^2), 1:25 (~80 μg/cm^2), 1:50 (~40 μg/cm^2), 1:100 (~20 μg/cm^2). hiPSCs were maintained in culture for 48 h and images were taken. The bright field images as shown in ***Figure 11g*** demonstrated that, at 1:50 dilution or ~40 μg/cm^2, hiPSC grew to confluency without detaching and showed a healthy and pluripotent morphology, which is one of indicators to start CM differentiation[352]. In conclusion, PAAm coated with Matrigel can serve as an *in vitro* platform to investigate the effect of substrate stiffness on hiPSC differentiation into CM.

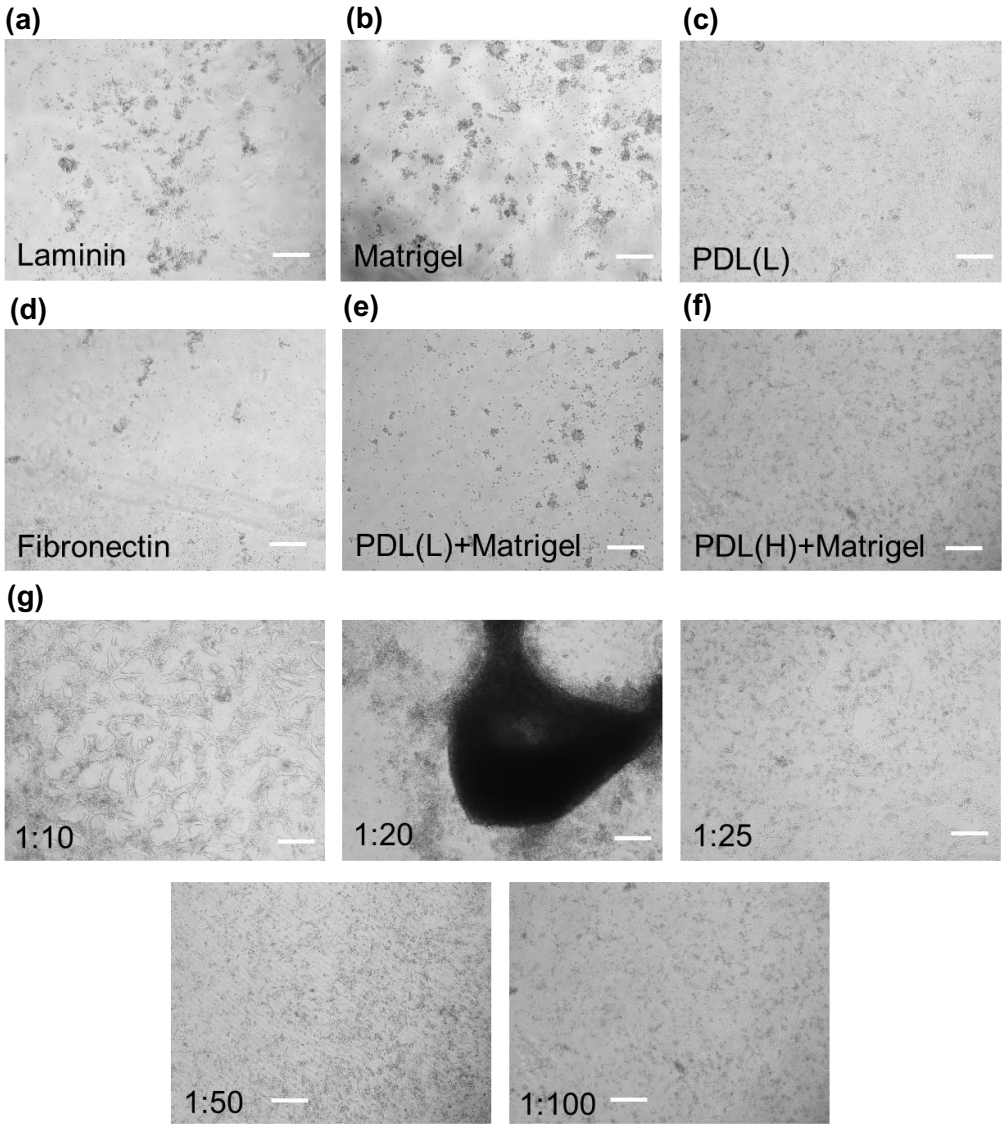

Figure 11: Protein coating optimization for hiPSC culture. *Representative bright field images of hiPSC plated at 32,000 cells per cm^2 and maintained in culture for 48 h on (a) laminin, (b) Matrigel, (c) Poly-d-lysine (PDL), (d) Fibronectin conjugated on PAAm substrate. Double step coating of different molecular weight PDL (e) 30,000 – 70,000 (low) and (f) 70,000 – 150,000 (high) covalently conjugated on PAAm as an initial layer, followed by incubation of Matrigel at 15 ug/cm^2. (Scale bars: 200 μm). (g) Representative brightfield images of hiPSC plated at 32,000 cells per cm^2 on high molecular weight PDL conjugated on PAAm with different dilution of Matrigel: 1:10 (~128 μg/cm^2), 1:20 (~64 μg/cm^2), 1:25 (~80 μg/cm^2), 1:50 (~40 μg/cm^2), 1:100 (~20 μg/cm^2) and maintained in culture for 48 h. (Scale bars: 100 μm).*

Here, the effect of substrate mechanics and how these signals integrate with soluble cues were studied using the novel functionalised PAAm hydrogels on the differentiation from hiPSCs towards CMs. Briefly, clean glass coverslips No.0 were activated using γ-methacryloxypropyltrimethoxysilane to create a reactive surface for PAAm adhesion (Binding coverslips) and using dichlorodimethylsilane to form a hydrophobic surface (Repelling coverslips) on a coverslip. Next, the desired concentration of PAAm monomers were mixed and vortexed. Polymerisation was initiated using ammonium persulfate and TEMED before dropping a solution onto a repelling coverslip. This was immediately followed by putting a binding coverslip on top, to form a uniform and flat surface. The setup was then incubated in a 37 °C humidified compartment for 30 min before the repelling coverslip was removed. The hydrogel was washed and equilibrated overnight at 4 °C with PBS. Hydrogels can be stored under this condition or conjugated with proteins for further experiments. For protein conjugation, EDC-NHS coupling to high molecular weight PDL followed by incubating with 1:50 v/v Matrigel was employed as previously described. hiPSCs were then seeded at the desired concentration before differentiation.

The effect of substrate stiffness on cell behaviour modulation and differentiation revolutionised the field just over a decade ago[185]. Therefore, this chapter aimed to explore the effect of gastrulation-, healthy heart- and diseased myocardium-like stiffnesses (approximately 0.56, 9.67 and 112 kPa)[183] on the capacity of hiPSCs to give rise to CMs, as compared to supra-physiological TCP (effective stiffness = infinite)[353].

To study the effect of substrate on hiPSCs, hiPSCs were plated on PAAm substrate and proteins were analysed at 24 h, using human proteomic profiler. This technique allows a prescreening observation of protein dynamics in hiPSCs. Next step would be analysis of phosphorylated proteins and total proteins using western blot. The array detected a significant increase in the phosphorylation state of many proteins. In *Error! Reference source not found.**a***, heatmap correlation, using Euclidean Clustering algorithm, showed a clustering of 9.64 kPa, 112 kPa and TCP together which distant further away from 560 Pa. Many phosphorylated proteins that were downregulated in 560 Pa in comparision to others (e.g. β-Catenin, GSK3a/b, TOR, Src) have been showed a link to cardiomyocyte differentiation such as inconsistency of differentiation and number of differentiated cells[354–356].Recent work from Przybyla *et al.* demonstrated the importance of b-catenin and E-cadherin that are required for compliance-driven mesoderm induction[215]. The PCA analysis on *Error! Reference source not found.**b*** demonstrated a cluster of 9.67 kPa and TCP, 112 kPa, 590 Pa as three separate group. This showed a prescreening of phosphorylated proteins in each difference condition can be clustered into three groups.

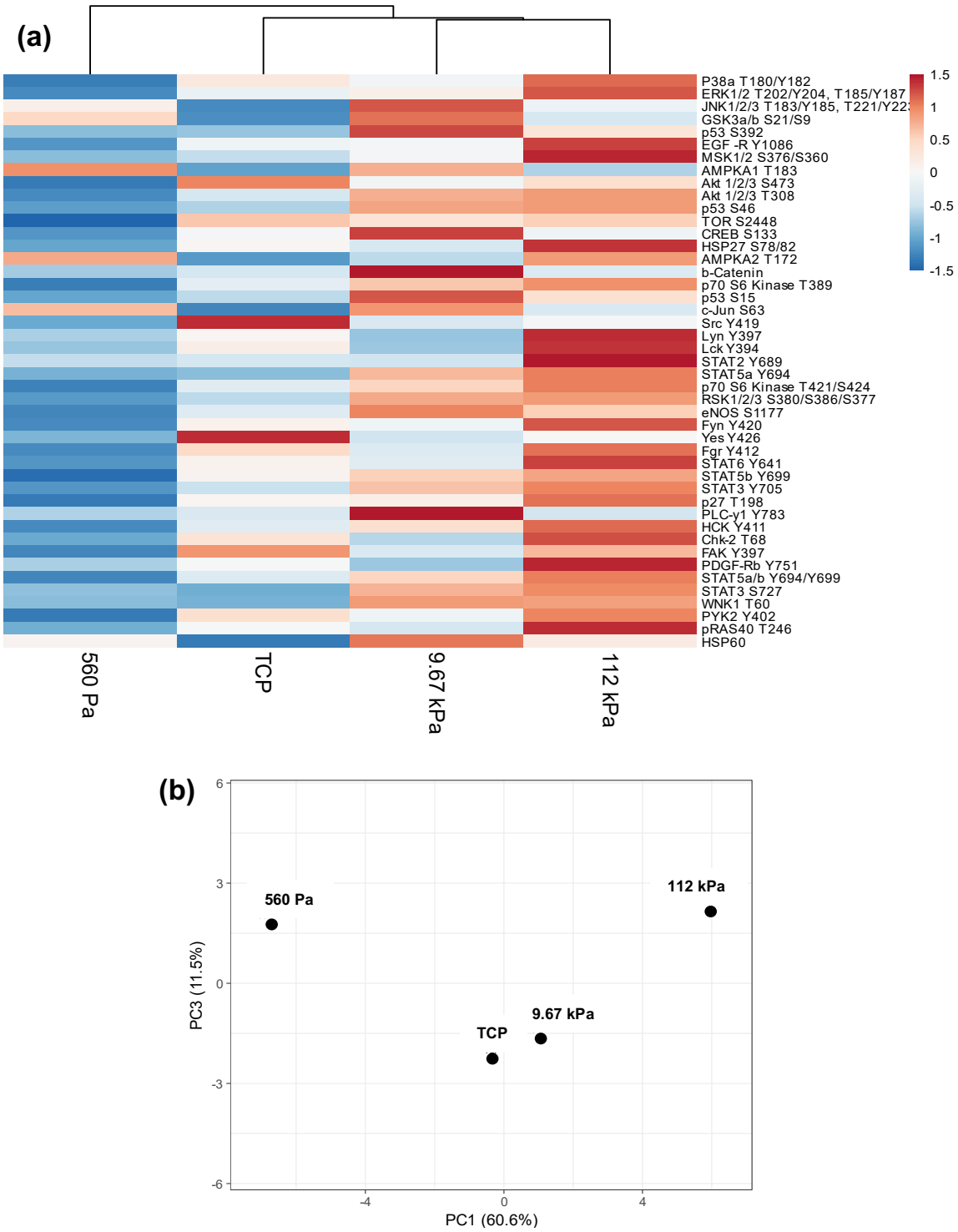

Figure 12: Human phosphorylated protein profiling. *Phosphorylated protein expression levels were quantified using Human proteomic profiler™ phosphor-kinase array. Representative image of blotting membrane detected using chemiluminescent method, Appendix* ***Table 10*** *shows*

targets and membrane coordinates. (a) Heatmap of listed phosphor-kinase proteins. Annotations on top of the heatmap show clustering of the samples, (b) PCA plot of each substrate condition the hiPSC-CMs were differentiated on. (N = 4). The analysis was performed using Matlab® and ClustVis[335]*.*

The simplistic differentiation protocol on directing hiPSC cultured on PAAm substrates to CMs depicted in ***Figure 13a***[87,223]. Briefly, at day 3 after seeding, the confluent monolayer of hiPSC was supplemented with a GSK-inhibitor for 48 h followed by Wnt-inhibitor for 48 h. Next, mRNA were collected at days 3, 7, 14 and 21 and analysed using RT-qPCR for pluripotency and mesodermal markers, and at day 7, 14, and 21 for cardiac structural markers. In ***Figure 13***, pluripotency marker (OCT4) showed a decrease over the differentiation time course as expected. Mesoderm (MESP1[223]) and cardiac mesodermal markers (NKX2.5[223]) peaked at day 14 before decreasing.Although Chan *et al.* demonstrated the heterogeneity of Mesp1+ mesoderm in single cell RNA-seq and suggested to use in conjunction with Kdr- Pdgfr+ for identification of cardiac mesoderm, MESP1 is one of the factors that could identify the transition from pluripotent stem cells to mesoderm in cardiomyocate differentitation. Finally, expression of cardiac structural markers (MYH6, MYH7, TNNI1 and TNNI3) was observed from day 7, and was maintained until day 21. These results demonstrate that in spite of the varying stiffness, the protocol successfully proceeded with beating hiPSC-CMs.

In order to characterise the differentiation efficiency at different substrate stiffnesses, FACS was performed by staining against cardiac troponin T (cTnT - *TNNT2*). Results showed 71.9%, 62.44%, 55.42% and 46.83% cTnT+ hiPSC-CMs on 560 Pa, 9.67 kPa, 112 kPa and TCP, respectively (***Figure 13b***). There were two noticeable cTnT+ fractions observed from flow cytometry as shown in ***Figure 13c***, namely cTnT+$_{high}$ and cTnT+$_{low}$, which were gated and further quantified. For cTnT+$_{high}$, hiPSC-CMs were cultured on 560 Pa, 9.67 kPa, 112 kPa and TCP represented 58.6%, 32.03%, 19.80% and 5.68% of total cTnT+ population, respectively, while the rest from cTnT+ total fraction accounted for cTnT+$_{low}$. These results therefore show that the gastrulation-like substrate (560 Pa) produced an increased percentage of hiPSC-CMs and that these had a higher fluorescent intensity of cTnT. To further investigate how this change affected hiPSC-CM protein expressions[357], the expression of MYL2a and MYL2v, the atrial and ventricular isoforms of myosin light chain respectively, on the cTnT+ fraction (***Figure 13e****)* was quantified. This is one of the markers that could be further analysed besides NR2F2, TBX5, HEY2, IRX4, GJA5 and sarcolipin, amongst others. However, it has been reported in many studies of their relevance to atrial-like and ventricular-like hiPSC-CMs[358,359]. Surprisingly, substrate stiffness did

impact subtype specification: MYL2a+ hiPSC-CMs represented 48.8%, 28.88%, 26.54% and 5.06% on 560 Pa, 9.67 kPa, 112 kPa and TCP, respectively, while MYL2v+ cells accounted for 8.76%, 30.79%, 24.47% and 51.32% on 560 Pa, 9.67 kPa, 112 kPa and TCP substrate. Therefore, substrate stiffness has a significant influence on the level of cTnT+ cells of cardiac differentiation on hiPSC[360]. Also, the MYL2V level increases with an increase in substrate stiffness.

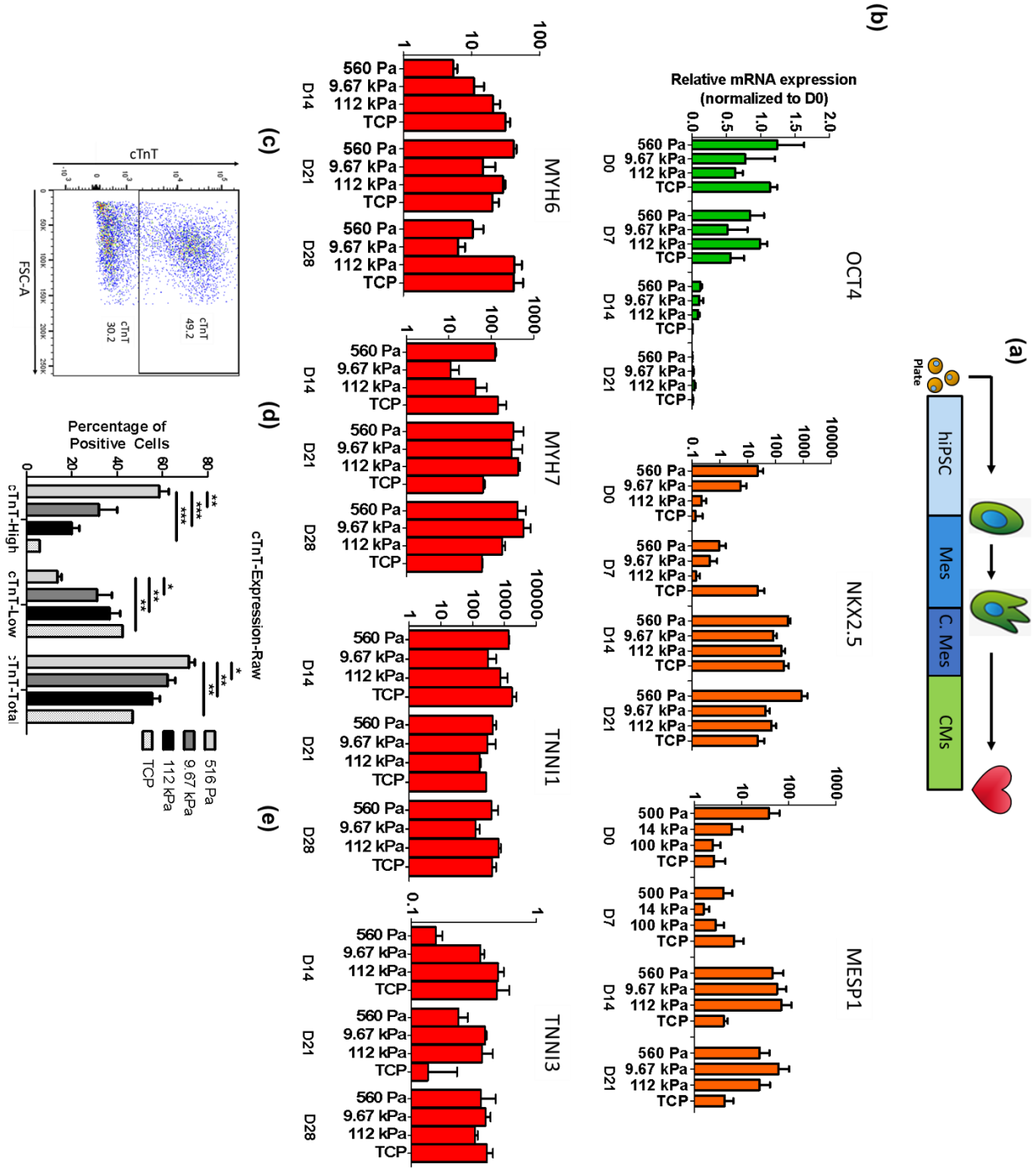

Figure 13: hiPSC-CM differentiation and efficiency characterization on PAAm gels. *(a) Schematic diagram of hiPSC differentiation protocol on different stiffness. (b) mRNA expression*

*levels of OCT4, NKX2.5, MESP1, MYH6, MYH7, TNNI1 and TNNI3 in differentitated hiPSC differentiated ubder the indicated conditions (N = 4), (c) Representative image of hiPSC-CMs' cTnT protein expression levels as analysed by FACS, (d) Percentage of cTnT+ cells as analysed by FACS in cells differentiated on stiffness varying hydrogels. cTnT+ cells were gated and cTnT+$_{high}$ and cTnT+$_{low}$ subpopulations quantified (N = 3), (e) Percentage of MYL2a and MYL2v positive hiPSC-CMs as analysed by FACS in cTnT+ cells on the indicated stiffness (N = 3). (one-way ANOVA, *p < 0.05, **p < 0.01, ***p < 0.001). This figure c, d and e were performed with the assistance of Mr Vincent Leonardo.*

ECM stiffness sensing is achieved through protein deformation caused by cell-generated force loading on transmembrane integrins adhered to the matrix[361,362]. This results in membrane stiffness changes in response to the extracellular stiffness. To confirm whether hiPSC-CM responds to matrix rigidity, membrane stiffness was measured using scanning ion conductance microscope[363]. This technique allows live cell imaging with minimal physical contact with the cell. To reduce the artefacts caused from cell contraction and response from external stimuli, a contraction inhibitor, Blebbistatin, was added to hiPSC-CMs culture. Results showed that hiPSC-CMs differentiated at 560 Pa, 9.67 kPa, 112 kPa and TCP exhibited increasing membrane stiffness (736.4 Pa, 1.61 kPa, 2.14 kPa, 2.41 kPa respectively). As previously mentioned, increase in membrane stiffness has been directly linked to the underlying substrate stiffness, whereas stronger adhesion points are established in higher stiffness, increasing cell membrane rigidity[364].

(a)

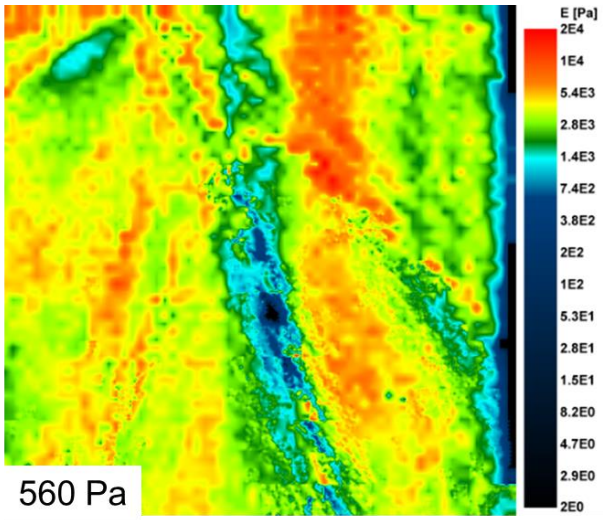
E [Pa]
2E4
1E4
5.4E3
2.8E3
1.4E3
7.4E2
3.8E2
2E2
1E2
5.3E1
2.8E1
1.5E1
8.2E0
4.7E0
2E0
560 Pa

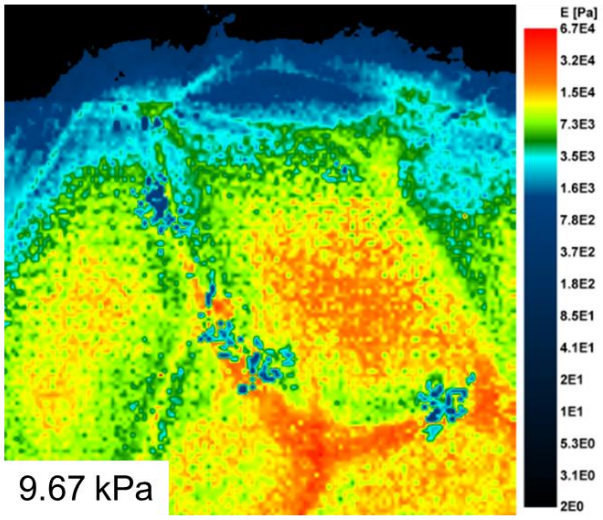
E [Pa]
6.7E4
3.2E4
1.5E4
7.3E3
3.5E3
1.6E3
7.8E2
3.7E2
1.8E2
8.5E1
4.1E1
2E1
1E1
5.3E0
3.1E0
2E0
9.67 kPa

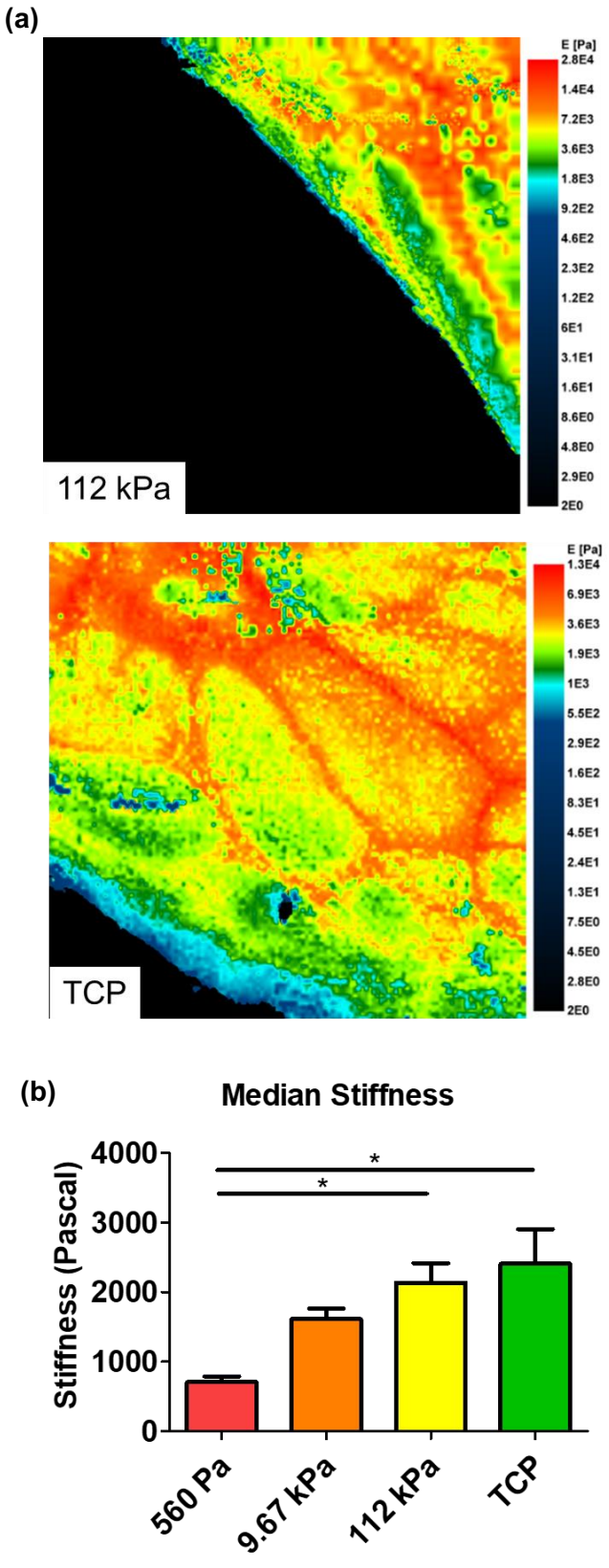

***Figure 14**: **hiPSC-CMs membrane rigidity quantified using scanning ion conductance microscope at day 21.** (a) Representative heatmap images generated from custom software to*

*visualize membrane stiffness of hiPSC-CMs, (b) A bar graph of the median membrane stiffness of hiPSC-CMs differentiated on indicated culture platform ($N \geq 4$). Data shows median ± Q_1. (one-way ANOVA, *$p < 0.05$). Performed with the assistance of Dr Sahana Gopal.*

In order to measure if these different extracellular stiffnesses had any impact on the functional capacity of hiPSC-CMs, calcium handling and force generation were measured using optical mapping and TFM, respectively. For optical mapping, hiPSC-CMs were incubated with Fluo-4AM dye, stimulated using electrical field stimulation at 1 Hz and fluorescent profiles recorded. ***Figure 15a-b*** *show* a representative trace extracted from fluorescent profiles and key parameters in calcium handling. In ***Figure 15c***, calcium handling kinetic characteristics (time-to-peak (Tp), time-to-50% decay (T50) and time-to-80% decay (T80)) were determined and showed that hiPSC-CMs exhibited the fastest kinetics at 9.67 kPa. This showed that transient change in stiffness occurring during cardiogenesis is an important factor to produce the highest percentage of CMs before increasing their stiffness to the adult myocardium stiffness to improve their calcium transient. hiPSC-CMs cultured on 9.67 kPa showed a shorter Tp (70.3 ms), T50 (153.6 ms) and T80 (208.4 ms) compared to Tp (99.75, 113.1 ms), T50 (225.9, 227.4 ms) and T80 (340.4, 252 ms) of hiPSC-CMs cultured on 560 Pa and 112 kPa, respectively. This suggests a faster calcium release and calcium re-uptake. Additionally, the amplitude of hiPSC-CMs cultured on 9.67 kPa, 112 kPa and TCP showed a significant reduction from those cultured on 560 Pa. Next, caffeine application was conducted by injecting 40 mM caffeine with a micropipette. This causes rapid opening of RyRs on the SR, leading to total Ca^{2+} release from the SR with fluorescence increasing proportionally to Ca^{2+} SR content. The result showed that hiPSC-CMs cultured on 560 Pa had a significant higher amplitude than those cultured on 9.67 kPa, 112 kPa and TCP (***Figure 15d***). However, the efficiency of calcium release, calculated by a ratio between amplitude over SR Ca^{2+} content, demonstrated the insignificant difference of the individual efficiency in spite of the varying underlying stiffness from 79.5 – 84.5% (***Figure 15e***), showing similar calcium handling efficiency.

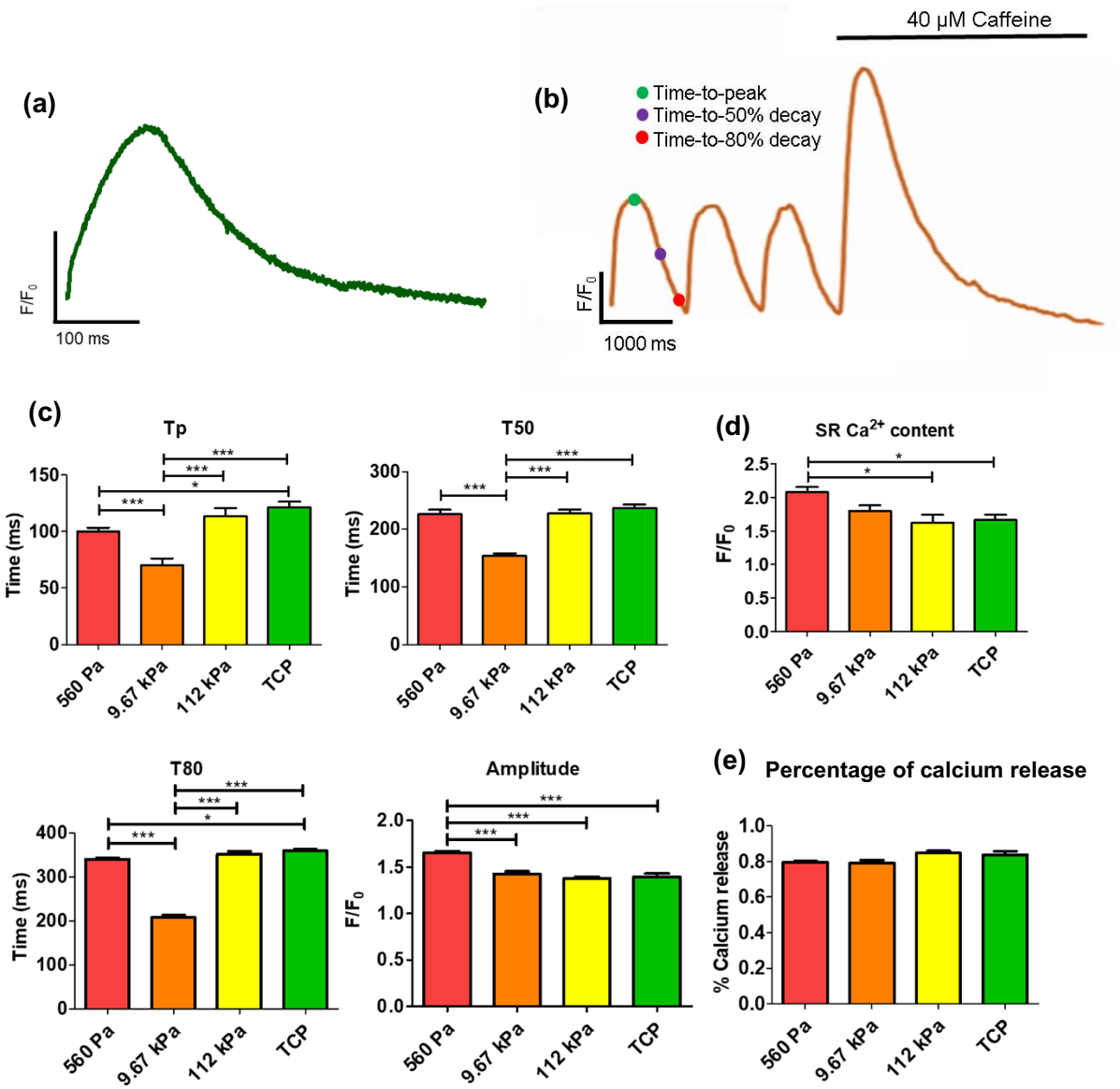

***Figure 15**: **Calcium transient with caffeine application.** Optical mapping of intracellular Ca^{2+} cycling in hiPSC-CMs field stimulated at 1 Hz. (a) Representative calcium trace, (b) Important calcium cycling parameters with caffeine application. (c) Representative trace of Ca^{2+} transients. Ca^{2+} transient parameters were as follows: Time to Ca^{2+} transient peak, time to 50% decay, time to 80% decay and amplitude. (d) Induction of 40mM micropipette caffeine application showing SR Ca^{2+} content (e) percentage release of intracellular Ca^{2+} from SR Ca^{2+} content. Data presented as mean ± SEM. (N ≥ 4). (one-way ANOVA, *p < 0.05, **p < 0.01, ***p < 0.001)*

As a second functional measurement, the generation of traction force was evaluated in collaboration with Dr Armando Del Rio Hernandez (Dept. of Bioengineering, Imperial College London). To do this, hiPSC-CMs were dissociated and replated at low density on their respective stiffness PAAm substrates, embedded with fluorescent beads and traction force was calculated by measuring bead displacement. This was achieved to observe single hiPSC-CM contraction, since cell-cell contact might interfere with the measurement. This displacement was calculated based on the characterised PAAm mechanical properties (***Figure 16a***). The total force was a sum of force generated in all directions corresponding to single hiPSC-CM area. All the calculations were performed using a custom MATLAB® code. Results from the optimization of the traction force setup (***Figure 16b***)[365] showed that single hiPSC-CMs differentiated and cultured on 9.67 kPa significantly exerted higher force (34.25 kPa) compared to single hiPSC-CMs cultured on 560 Pa and 112 kPa which produced a traction force at 0.25 and 22.86 kPa, respectively. This biphasic relationship showed that there is an optimal stiffness, at which it is similar to what has been reported on healthy myocardium, where single hiPSC-CMs can generate the highest force[118]. This finding confirmed that the relationship of calcium handling and traction force generation was as expected, demonstrating again that supplying a native- and healthy-like mechanical environment permits the most optimal functionality of CMs.

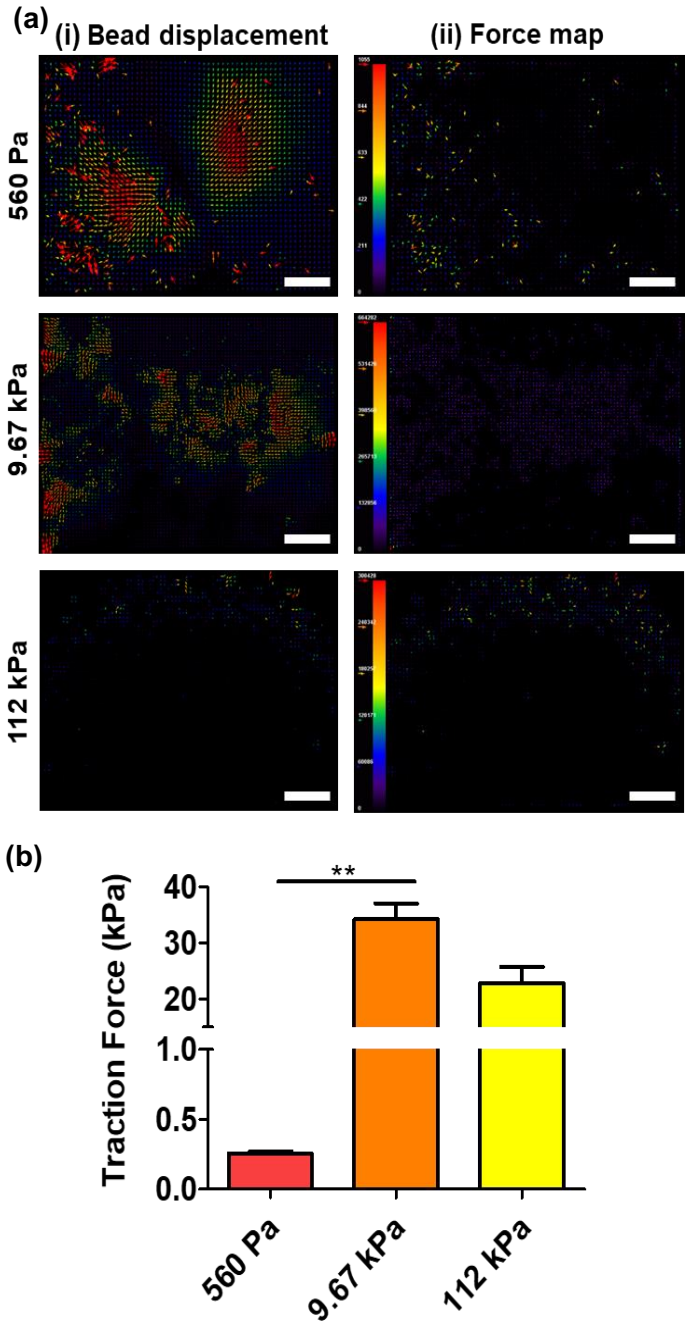

Figure 16: Traction Force Microscopy of single hiPSC-CMs on hydrogels of varying stiffness. *(a) Representative heatmaps indicating peak systolic displacement (i) and traction force generated by single hiPSC-CMs cultured on indicated stiffness (ii), (b) A bar graph of quantified total force generated from single hiPSC-CMs cultured on indicated stiffness. (N = 3). (one-way ANOVA, **p < 0.01). Performed with the assistance of Mr Darius Lachowski.*

3.4 Discussion and conclusion

The advancement of new regenerative approaches is centred on the understanding of the fundamental mechanisms involved throughout development. In particular, embryogenesis is influenced not only by a combination of biochemical factors and cell-cell interactions, but also by a variety of biomechanical cues that play a role in a range of intracellular events[309]. However, there is still a lack of knowledge on how these biophysical cues present in the stem cell can modulate their behaviour. This chapter demonstrated how a stiffness tuneable cell culture platform can be applied to understand the influence of these factors on hiPSC culture and differentiation. This approach offers superior uniformity and efficient protein conjugation with a wider range of stiffness that covers embryonic as well as adult physiological and pathological settings.

Optimisation of scaffold mechanical properties for stem cell culture is at the core of this thesis. This necessitates a precise temporal and spatial control of physical and chemical properties at cellular level. The hydrogel's mechanical properties and tethering biochemical molecules must be finely adjusted in order to fabricate a functional ECM-mimicking hydrogel. The design of biomaterials should be cytocompatible, reliable, reproducible and cost-effective. There are two promising options that were explored in this chapter, agarose and polyacrylamide hydrogels. These are mechanically tuneable, stable, optically transparent, inexpensive and naturally inert while allowing conjugation of adhesive ligands. These characteristics make these materials suitable for the long-term study of the role of stiffness in directing cell fate.

Although agarose has been known to be cell repellent and widely used to prevent cell adhesion to a surface, it stands superior to other hydrogels through its capacity to gel *in situ* at 37 °C and biocompatibility. There are various chemical modifications reported to provide reactive binding sites for ECM proteins on agarose[366]. However, it has been shown that these modifications significantly alter mechanical properties of the resulting substrate. Therefore, a novel modification through the insertion of acrylate groups onto the agarose backbone (by homogenous reaction of methacrylic anhydride with agarose[367]) was established. The selected ECM proteins were incubated with acrylate-agarose to allow a conjugation via Michael addition. This technique has been optimised, validated and characterised by Dr. Michael B. Albro and Dr. Christopher Spicer (Dept. Materials, Imperial College London). The hydrogel was formed by mixing two components, acrylate-activated and non-modified low melting point agarose, at different percentages, in order to better preserve the mechanical properties potentially altered during synthesis. The compressive Young's modulus was measured at different modification

percentages. At 3% w/w total agarose, it demonstrated that although this platform can reproduce the physiological stiffness range of myocardium (10 - 50 kPa), it does not do so for a disease-like environment (> 50 kPa)[368]. Here, a mixture agarose hydrogel was demonstrated that it can be used for cell culture and to study the stiffness-dependent response of cell fate by showing that cells grown on the substrate exhibit a healthy phenotype. However, the environment in disease-like myocardium possess higher stiffness than the agarose can support. Therefore, an alternative option, PAm, which has been previously reported to recreate the required high stiffness[311], was explored.

PAm supplies a wide range of reproducible mechanical properties, topographical uniformity, long-term stability, and optical transparency, making it highly suitable for *in vitro* studies. However, PAm is also known for its limited interaction with proteins, acting as a biologically inert material. Hence, chemical modification is needed to immobilise biological adhesive molecules, thereby promoting healthy cellular activity. Three chemical modifications tested here are sulfo-SANPAH, hydrazine hydrate and addition of carboxylic groups. These three methods rendered the hydrogel cell culture-compliant when adhesive ligands were conjugated. However, the addition of carboxylic group by substituting acrylamide monomer with acrylic acid visually showed better and more uniform adhesion, with higher cell density after 24 h in culture. Theoretically, addition of acrylic acid might be able to provide more protein conjugation sites than sulfo-SANPAH and hydrazine hydrate, hence the better attachment and growth. Therefore, BSA-AF680 was used as a model protein to relatively quantify the amount of conjugated protein on the different PAm variants. Acrylic acid substitution showed the highest amount of BSA-AF680 bound on the PAAm surface. Additionally, the addition of 0.4% w/w acrylic acid has been shown to provide carboxylic functional groups without altering mechanical properties[314]. Therefore, PAAm offers a superior modification of PAm since it can provide stable mechanical properties, a larger quantity of proteins covalently linked to the surface and reduced variability of conjugation[369].

Micropatterns are one of the physical cues that will be studied later this project. Microfabrication is used to form 3D micropatterns due to its high precision with micro scale resolution. Amongst the various techniques involved in 3D micropatterning on hydrogel surface, soft lithography was chosen due to its simplicity in implementation. Soft lithography allows the liquid solution of a polymer to polymerise on the surface, while simultaneously moulding the polymer to form 3D micropatterns. As silicon masters tends to form a strong adhesion to the polymer, it results in the deterioration of the micro features on the master and a non-uniform pattern on PAAm hydrogels. Therefore, a hydrophobic coating was implemented to prevent the

polymer from sticking. Chemical vapor deposition of silane was achieved to aid the polymer removal, while maintaining the surface of silicon master intact. Although this chemical coating acts as a sacrificial layer, it might lead to a reduction of cytocompatibility. However, the result demonstrates that the metabolic activity of CMs cultured on PAAm substrate with or without silane coating remained unchanged. Therefore, chemical coating for hydrophobic surface does not have any detrimental effect on cells. This allows a 3D micropattern to be created on the PAAm with a reusable silicon master.

The interest of using hiPSCs in this project is highlighted by their capacity to dependably recapitulate development and cardiogenesis. Regulating hiPSCs *in vitro* demands a platform that promotes healthy cell behaviours, particularly adhesion, proliferation and differentiation. However, a common limitation of these experiments is weak cell-surface adhesion. This problem can be overcome by conjugating the surface with various ECM proteins. Matrigel is the optimal choice for culturing hiPSCs on TCP. However, the change on matrix substrate could have detrimental effect on cell adhesion. Therefore, conjugation of laminin, Matrigel, poly-d-lysine, fibronectin and poly-d-lysine with Matrigel were tested. hiPSCs showed good adhesion and growth on a combination of high molecular weight poly-d-lysine and Matrigel coating. The high molecular weight poly-d-lysine (70,000 – 150,000 kDa) gives higher and longer positive chains on the surface of PAAm than the 30,000 – 70,000 kDa poly-d-lysine. This charge allows proteins to statically bind to the surface. Therefore, double coating PAAm could provide bioactive molecules from Matrigel on its surface to culture hiPSC *in vitro*.

Different tissues have their unique cellular microenvironments which can be characterised by protein composition, protein-protein interactions and the collective biomechanical properties (e.g. local elasticity and structure), which is what PAAm substrates aims to reproduce. MSCs have been shown to sense underlying stiffness of about 10 - 20 μm from the surface[350]. Here, the depth of the Matrigel coating layer was quantified, showing it was less than 5 μm. Further assessment was conducted to determine cellular response to stiffness changes. MSCs were used as an established mechanosensitive model. MSCs can be modulated by the changes of substrate stiffness. Rigid stiffness substrate, which showed an elevated YAP/TAZ gene expression, drives them toward bone differentiation. Soft environments gradually disable YAP/TAZ expression, allowing MSC to differentiate into other cell types, such as adipocytes[147,148]. PAAm coated with Matrigel demonstrated its capability to manipulate YAP localisation on MSCs, proving that the Matrigel coating layer did not affect the way cell sense the underlying substrate. Next, hiPSCs were seeded and YAP/TAZ localisation studied. The localisation pattern of hiPSCs differentiated

them from MSCs, however, presents as a protein marker for mechanosensitive indicator in both stem cell line. In hiPSCs, YAP downstream genes SCARA3 and RHOF showed similar trend to YAP proteins. The upregulation of these genes showed a higher level of activation, hence higher YAP protein transcription (transcriptionally active). YAP/TAZ are the two major downstream effectors of the Hippo pathway. This pathway plays an essential role in self-renewal and CM differentiation including OCT4. Therefore, the OCT4 protein was quantified, showing that hiPSCs cultured on 560 Pa expressed higher levels of OCT4. During hiPSC-CM culture, mechanoresponsive protein translocations (e.g. class II HDACs and JP2NT) could be further analysed to observe the effect of substrate stiffness on the molecular level. Next, a human phosphorylation proteomic profiler™ array was used to detect phosphorylation changes induced on hiPSC by culture on our platform. Analysis showed significant differences in pathways which have been known to play a role in cardiogenesis, such as Src, β-catenin, GSK3 and FAK. The result showed that these phosphorylation changes can be clustered into two groups correlated with the ErbB pathway. Activation and deactivation of ErbB has been directly linked to improvement and/or incomplete development of heart[370–373]. Another key change, the β-catenin pathway (a mediator in Wnt pathway) was also identified. The significant increase of β-catenin on 9.67 kPa has been previously correlated to an increased efficiency in mesoderm differentiation[215]. The increase of β-catenin induces activation of Wnt pathway. This activation in turn represses OCT4 expression, which was indeed observed on the aforementioned 9.67 kPa hydrogels. This OCT4 pluripotent protein reduction is shown to promote differentiation. This supports a dominant role for Wnt/β-catenin signalling in inducing the differentiation rather than the self-renewal of hiPSC, as previously shown in hESC[374]. Additionally, this signalling pathway has been modulated in chemically defined CM differentiation, so a spontaneous recapitulating of Wnt/β-catenin is likely to positively impacts the differentiation protocol. Therefore, the increase in β-catenin found in this study points towards an increased differentiation capacity towards mesoderm and CM, as well as promoting CM proliferation[375].

Next, given that phosphorylation changes point towards and increased mesodermal differentiation capacity of hiPSCs, the influence of substrate rigidity on the cardiac differentiation of hiPSCs was verified. A robust and reproducible small molecule-based protocol[87,352] was chosen to test if, as predicted, substrate tension directs stem cell fate, thus integrating influences from substrate mechanics with soluble signalling to regulate embryonic specification and direct the functions of the differentiated CMs. Therefore, it is worth noting that the involvement of Wnt/β-catenin signalling modulation by small molecules during CM differentiation may influence cell-cell and cell-matrix contacts, Therefore, they could affect cellular response to differentiation signals

and regulate developmental behaviours. The cardiac structural gene expression analysis showed an upregulation of *MYH6, MYH7, TNNI1 (> 10-fold increase) and TNNI3* after day 7, indicating successful differentiation of hiPSCs into CMs. Next, flow cytometry was used to quantify the efficiency of the differentiation, demonstrating 60 - 80% CMs, similar to recent studies[87,352]. Interestingly, the level of cTnT+ per cell was elevated in lower stiffness compared to pathological stiffness although further experiments on knockout or overexpression are needed to confirm this finding. Changes in the MYL2a and MYL2v expression prevalence were observed. MYL2a decreased its expression while MYL2v increased its percentage of expression. Further analysis could be taken into account, distinct from isoform switching in the cells, such as the alternative that proliferation rates of ventricular-like and atrial-like cardiomyocytes might be different. A recent publication from Przybyla *et al.* showed that substrate stiffness of 600 Pa increases mesoderm differentiation lineage, which could be an underlying mechanism that supports our finding on increasing cTnT+ cells percentage. Macrı´-Pellizzeri *et al.* demonstrated that on EB differentiation, the population of cTnT+ cells increased on a 600 Pa substrate compared to tissue culture plastic vessel. To date, no study has investigated the significance of elevated or reduced cTnT levels in hiPSC-CM function[376–378] and maturation. Next, the study explored how the tuning of the mechanical environment affected hiPSC-CM membrane stiffness. Results showed that there was a concomitant increase in cell membrane stiffness as hiPSC-CMs sense the stiffer underlying substrate, which has been linked to cytoskeletal remodelling in response to environmental stiffness[379]. This previously observed effect has been shown to modulate ion channels[380], leading to the speculation of functional alteration and development. Therefore, optical mapping was performed to study the cycling of intracellular calcium inside hiPSC-CMs. Regarding the kinetics, the biphasic relationship, where the shortest kinetics have been observed at 9.6 kPa, suggests that the calcium handing was improved at 9.67 kPa, and that this is an 'optimal spot'. This faster Tp indicates better coupling of to the RyR in the SR, a key component that is lacking in hiPSC-CM calcium handling[98]. Faster T50 and T80 suggested more efficient decay mechanisms. Improvement in kinetics has been previously reported as a key characteristic of maturation indicator in hiPSC-CMs[70,158,381,382]. Therefore, hiPSC-CMs cultured on 9.67 kPa demonstrate a better coupling of low type calcium channels (LTCC) to RyR in the SR, a key element that is lacking in hiPSC-CM calcium handling. The reduction in amplitude at 9.67 kPa and 114 kPa as compared to 560 Pa. Whilst there are differences, a ratio-metric calcium dye should be implemented to confirm the observation, and hence baseline changes in calcium concentration could contribute to changes in amplitude[383,384]. Additionally, calcium handling showed no significant difference for the percentage of calcium release. This means they are

equally good at calcium regulation and utilisation. Calcium amplitude have been used to predict force generation[94]. However, force generation could be affected by many factors, such as soluble signals[98,107]. Therefore, traction force microscopy was initially optimised. The result showed that single hiPSC-CMs replated and cultured on 9.67 kPa demonstrated the highest force exerted on to the substrate surface. This has been previously reported as the optimal stiffness that similar to physiological stiffness in healthy heart[118]. Given these points, the effect of substrate stiffness on hiPSC fate reveals that stiffness is an essential key regulating hiPSC lineage commitment and function in a time dependent manner. Early on, the embryonic-like environment promotes CM differentiation efficiency, resulting in both increase of hiPSC-CM number and percentage of total population. Further, hiPSC-CMs cultured on native myocardium-like stiffness develop the best functionality (i.e. calcium handling and force production). The study highlights that by modulating the substrate's mechanical properties, one can enhance differentiation of hiPSC toward CM function..

Further optimisation on the maturation level of hiPSC-CMs on each biomedical application is needed. Engraftment survival capacity should be considered as an important factor as well as the consequence of the complex, beating, native environment.

In conclusion, this chapter demonstrated that influences from substrate mechanics can integrate with biochemical signalling to dictate embryonic specification and improve the function of the differentiated hiPSC-CMs. Further experiment to confirm whether β-catenin signalling could be a key modulator, affecting functional changes, is needed. This leads to the next chapter where a modulation substrate physical property will be studied as the function and structure of hiPSC-CMs change.

Chapter 4

CardioArrays: A Novel Platform for The Multidimensional In Vitro Manipulation of Myocyte Niche

4.1 Abstract

The discovery of hiPSCs has fundamentally shifted the model for pharmaceutical screening, disease modelling, and precision medicine. These cells can be generated from human somatic cells. They can be maintained in *vitro* for extended periods and can be potentially differentiated into every cell type in the body. Despite these advantages, concerns persist over the extent to which hiPSC-CM expression develop CM structural and functional properties. This drawback has been partially addressed by the recent studies of hiPSC-CMs, which successfully established the genetically inherited cardiac diseases, including long QT, and Timothy syndromes[272,302–306], ARVD[293], DCM[276] and HCM[294]. These studies provide new biological insights into fundamental mechanisms of health and disease states and possible pharmacologic therapies.

It has been widely accepted that the dynamic interplay between the biophysical and biochemical cues present in the native myocardial environments are essential during cardiogenesis and the maintenance of the adult CM phenotype in both health and disease. Importantly, hiPSC-CMs have standardised the way to study human cardiac development using human origin cells. However, the traditional approach of using hiPSC-CMs (whereby only individual cue is manipulated one at a time) is highly inefficient, falling short when recapitulating the dynamic complexity of the myocardium environment. Therefore, there is an urgent need to create a platform that can manipulate the function, structure and gene expression of hiPSC-CMs to characterise their molecular, structural and functional properties of these cells.

Here, the design and fabrication of a novel and versatile 3D cell culture platform was shown- CardioArrays, which allows the concomitant manipulation of microscopic 3D topography and substrate stiffness, and its employment to direct hiPSC-CM function, structure and gene expression. hiPSC-CMs were generated from hiPSCs using a/the monolayer technique before seeding to CardioArrays for further experiments. The results show the specific contribution of stiffness and a 3D shape on α-sarcomeric structure, cell membrane stiffness, single cell protein/gene expression and intracellular calcium cycling. This demonstrates that supplying the physiological or pathological microenvironment to hiPSC-CMs in 3D leads to a significantly different set of features, thus presenting a differential phenotype, which has the potential to produce more fit-to-application hiPSC-CMs. In combination, this chapter has enhanced the understanding of the mechanisms in health and disease at the single CM level, not previously possible using human adult CMs. In conclusion, this is the first demonstration of a platform capable of simultaneously manipulating cell shape and substrate stiffness within a

biomechanically-relevant environment. The significant changes exerted upon in a single hiPSC-CM demonstrate the importance of multiple, complex stimulations in order to produce relevant and specific phenotypes and functionalities to each application, thereby opening the way for furthering our understanding human cardiac development.

4.2 Introduction

Cardiac contraction is the culmination of a very finely orchestrated succession of molecular events, where not only the presence, but the location and relative abundance of each component is fundamental. It is their unique shape that allows the adult human CM to adequately distribute and compartmentalize its ultrastructural domains[21]. This allows the heart to synchronously beat and generate enough force to pump blood throughout the body. MI is the main cause of death worldwide, causing unrepairable damage to CMs in the affected myocardium. Though CM regeneration occurs in the postnatal human heart, the capacity for renewal is physiologically insignificant[385]. Therefore, there is a need to improve the function and structure of hiPSC-CMs *in vitro* in order to create clinically relevant hiPSC-CMs. Recent studies have shown profound evidences on the roles of ECM and its components to CMs as well as neighbouring cells in regulating cardiac development. Interdisciplinary studies have shed the light on the biophysical influences of the ECM (e.g. elasticity and propagation of biomechanical cues) on cellular compartments, such as the membrane and the nucleus. It has been shown that matrix elasticity and cell niche can promote or demote the transition from an immature to an adult-like phenotype and vice versa, hence resulting in functional and structural changes[212,386–390]. However, there is a lack of the evidence in the relationship between extracellular forces and intracellular signals in directing tissue-specific morphogenesis, development and functionality.

Although much is known about the role of morphogens and transcription factors in CM specification[391,392], how 3D physical cues modulate their behaviour is still obscure. Initially, genetic and biochemical signals have been effortlessly studied to determine the molecular mechanism of CM fate. The mechanical properties of the substrate or ECM consists of two main factors- physical tension and shape. This effect and the underlying mechanisms can be studied using engineered matrices of tuneable stiffness. Studies employing functionalised polyacrylamide substrates have shown to be able to modulate MSC differentiation preferences towards neurogenic, myogenic, or osteogenic, by controlling ECM stiffness [119,311,393]. Additionally, alignment of CMs *in vitro* has been made possible by using a continuous surface. This increased anisotropic contractility is more resembling that of the native myocardium[394,395]. However, the modulation of the role of individual CMs to desirable fates cannot be achieved by applying this technique. Recently, researchers have implemented 3D constructs that has features mimicking the physiological shape and surface features of adult[396]. However, PDMS, the substrate of choice in this work, has been shown to demote hiPSC-CMs to express a disease-like phenotype[71,397], due to the pathological stiffness of the material. Although communication between neighbouring cells undoubtedly plays a role, a

physiological response of single hiPSC-CMs to concomitant changes in substrate mechanical and topographical stimulus has not yet been demonstrated. To be able to fully realise the potential of hiPSC-CMs, the interaction between stem cells and the microenvironment that recapitulate the complexity of native organs must be thoroughly studied. Therefore, a system capable of simultaneously providing a 3D pattern that mimics natural role features with physiologically/pathologically relevant stiffness is needed to improve our understanding of these changes.

In this thesis, the aim is to develop a novel platform capable of simultaneously providing physical and mechanical stimuli using microfabrication-based, stiffness-tuneable, biomaterials. The production of a platform supplying 3D features that mimic the physiological or pathological 3D environment of single adult CMs in the myocardium, named CardioArrays, is presented. Additionally, influence of the novel platform on cardiac development is explored. This highlights the vital factors necessary to imprint desired features onto hiPSC-CMs to serve the needs of cardiac regeneration and drug discovery.

4.3 Results

The ability to finely regulate tissue architecture via modulating substrate stiffness could create the increased homogeneity in phenotypes that cannot be offered using conventional culture dishes or EBs for *in vitro* studies, while providing controllable parameters for directing hiPSC-CM niche features. As previously shown in ***Chapter 3***, PAAm substrates was fabricated to function as scaffolds capable of simultaneously providing multiple biophysical cues in order to guide hiPSC-CM development *in vitro*. Via photolithography, shown in ***Figure 17***, an array of 3D microwells was created resembling the physiological dimensions of adult human CMs (CardioArrays). The micropatterns were designed to mimic adult CM dimensions quoted in previous studies as shown in ***Table 8***. Briefly, the Si master was coated with Trichloro(1H,1H,2H,2H-perfluorooctyl)silane to provide a hydrophobic surface, preventing polymer adhesion and allowing the reuse of the Si masters. Degassed polyacrylamide-*co*-acrylic mixture was casted on the surface to form the 3D micropatterned scaffold. The substrate was then cross-linked via EDC-NHS coupling to collagen I, in order to mimic the collagen-rich ECM found in the myocardium. This demonstrated a capability of the platform, enabling a tuneable 3D dimension on the CardioArrays.

Table 8: Adult cardiomyocytes' dimensions reported in various studies.

No of sample studied	Aetiology	Length (μm)	Diameter (μm)	Reference
9	Healthy isolated CM	141	19	[329]
11	Healthy isolated CM	134	23	[327]
67	Stem cell derived CM	44.2 ± 10.9	16.0 ± 4.6	[328]

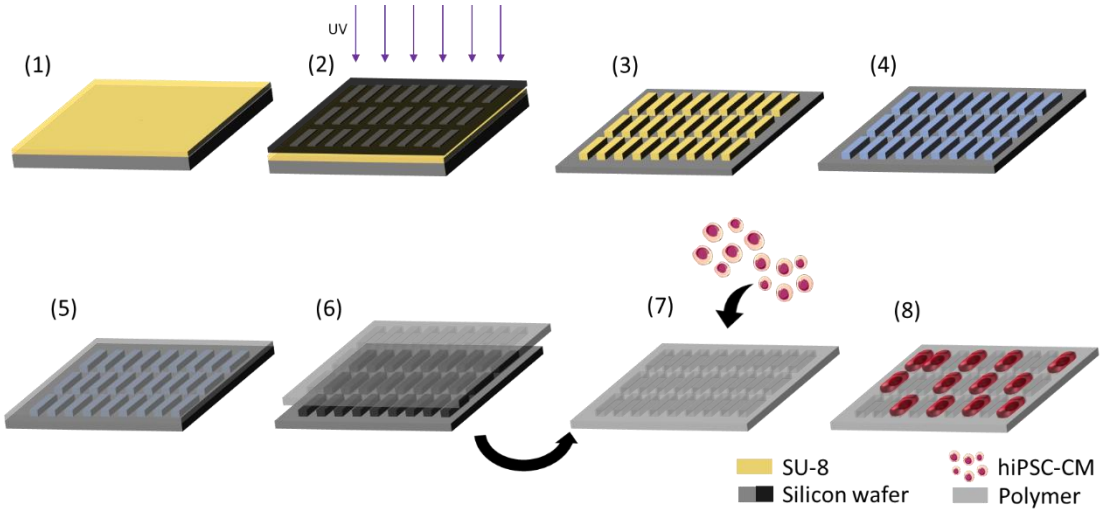

***Figure 17**: **Microfabrication of substrate and cell seeding.** Schematic representation of the microfabrication and cell-seeding process: (1) Deposition of photoresist (SU-8), (2) SU-8 exposure during photolithography patterning of the photoresist, (3) Outcome of the photolithography: adult CM-like-shape arrays of pillars, (4) fluorination of surface (5) Polyacrylamide-co-acrylic acid polymer coating of the hard mould by drop-casting, (6) Removal of PAAm and ECM conjugation, (7) hiPSC-CM seeding on the 3D micropatterned PAAm substrate, (8) hiPSC-CM culture on micropatterned PAAM substrate. The fabrication was carried out by Mr Michele Becce and Dr Ciro Chiappini.*

Figure 18 shows** different representative bright-field images* of 3D micropatterns on PAAm. The micropattern of various sizes (98:14, 56:8, 70:14 and 40:8 μm) was transferred using soft-lithography. The presence of acrylic acid also makes the hydrogel pH responsive, causing it to swell and shrink, depending on the pH of the solution[369]. Therefore, HEPES buffer was added to control these effects. As the potential swelling of the 3D microwell arrays during cell culture can significantly change the design dimensions, the width and length of 3D microwells were measured after a 7-day incubation in the cell culture medium and compared to day 0 (immediately after polymerisation). As shown on ***Figure 18b, no significant change in dimensions was found for any of the PAAm mixtures between acrylamide/bis/acrylic acid.

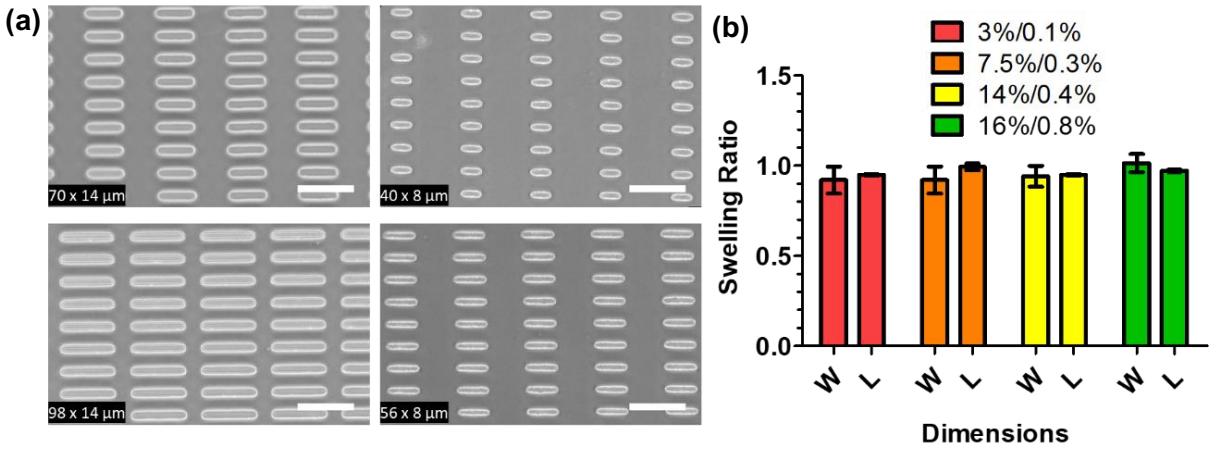

Figure 18 *:* ***CardioArray array characterisation.*** *a) Representative brightfield images of CardioArray. b) Swelling ratio: Width (W) and length (L) of 3D microwell on the hydrogel were measured to compare the size after casting and after 7 days incubation. The result is expressed as a ratio between the size after casting and after 7 days incubation. Data represent mean values determined in three independent experiments ± SEM. N = 3. Scale bars: 50 µm.*

To understand the molecular basis of hiPSC-CMs' responses, a quantitative and reliable method to track hiPSC-CM development is lacking, as many potential cardiac markers of the adult mature CM revert to a foetal state under pathological conditions. As a consequence, a multifactorial characterisation of structural, genetic and functional changes of hiPSC-CMs onto the 3D micropatterned and stiffness-tuneable substrates CardioArray were employed. hiPSC-CMs were differentiated by small molecule-based biphasic modulation of Wnt signalling, dissociated from tissue culture polystyrene (TCP) and seeded onto collagen I-coated 3D micropatterns of four different sizes (***Figure 19 (a)*** 98:14, ***(b)*** 56:8, ***(c)*** 70:14 and ***(d)*** 40:8 µm), while flat surfaces of the same substrates served as controls. To evaluate the effect of the 3D micropatterned PAAm substrates on single hiPSC-CMs, cells were cultured for 7 days at either physiological or pathological stiffness CardioArrays. Each single hiPSC-CM must be able to accommodate the full volume of 3D micropattern. Therefore, two stiffnesses were selected as representative for physiological (9.67 kPa, 7.5%/0.3%) and pathological stiffness (112 kPa, 16%,0.8%) with rectangular box dimension of 8 x 40 x 20 µm for width, length, and depth, respectively for the remainder of the study. ***Figure 19e*** shows a single hiPSC-CM cultured on CardioArray for 7 days. Single hiPSC-CMs were assigned to each condition group as (a) 3D microwell and (b) Flat control for further experiments.

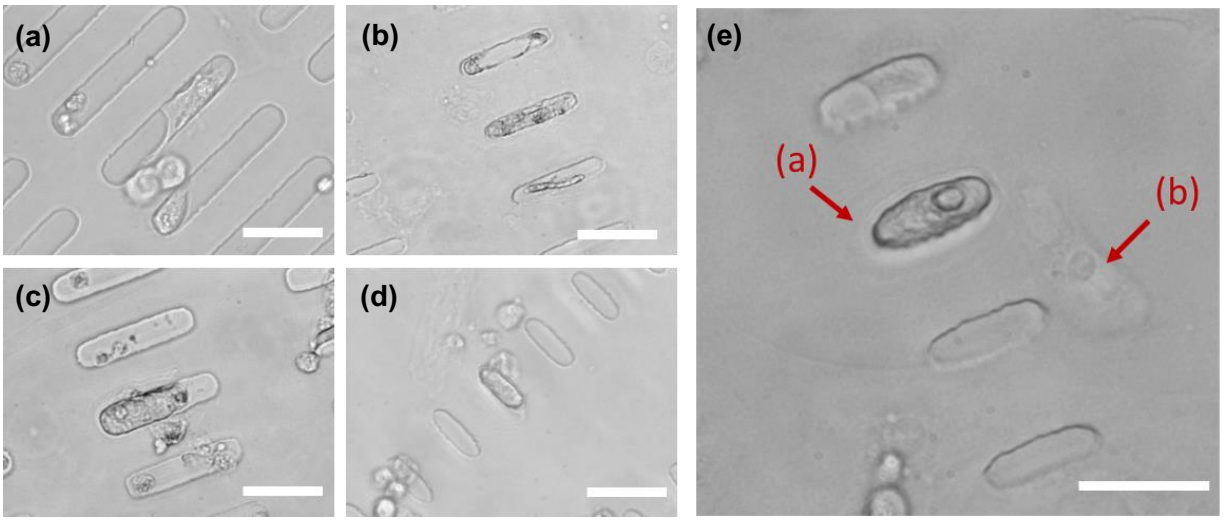

Figure 19: Representative brightfield images of single hiPSC-CMs *seeded onto collagen I coated PAAm. The hydrogel was moulded to form 3D micropattern with dimension of a) 98:14, b) 56:8, c) 70:14 and d) 40:8 µm. e) A single hiPSC-CM on CardioArray (Arrow: hiPSC-CM reside a) Inside 3D microwell, b) Flat control surface). Scale bars: 50 µm.*

Structural characterisation, as another factor in the multifactorial panel, was conducted to observe key structural proteins found in CMs including cardiac protein (cTnT), filament (sarcomere) and connexin gap junctions (connexins). There are three main connexins expressed in mammalian CMs: Cx-40, Cx-43, and Cx-45. While Cx-40 and Cx-45 have dominantly been detected in the conductive tissue of developing mammalian hearts, Cx-43 is abundantly expressed in adult working myocardium (atrial and ventricular). A reduced expression (number and location) of connexin have been reported in MI and heart failure[398]. In order to visualise the ultrastructure and cell orientation, single hiPSC-CMs grown in CardioArrays were fixed and stained for sarcomeric-α-actinin, Cx-40, Cx-43, Cx-45 and cTnT and labelled with DAPI for visualisation, showed in following ***Figure 20*** and ***Figure 21***.

In ***Figure 20a***, flat controls presented higher anisotropy, compared to single hiPSC-CMs cultured on 3D microwells (***Figure 20b***), where cells perfectly adapted to the predesigned shapes. Indeed, a significant increase in sarcomeric alignment was demonstrated in cells residing in the microwells, with hiPSC-CMs demonstrating these contractile structures following the long axis of the patterns (***Figure 20c***). Staining for α-actinin of single hiPSC-CMs cultured on PAAm substrates revealed extensive cell remodelling with reorganisation of the sarcomeric structure, showing a shorter spacing of Z-lines from 1.77 µm to 1.62 µm in the pathological stiffness substrate (112 kPa), compared to physiological stiffness (9.64 kPa), independent of the presence

of the 3D confinement (***Figure 20d***)**.** As shown in ***Figure 20a-b***, Cx-43 expression was detected proximally to the 3D microwell's wall, but was found to be scattered throughout the cell and its membrane in flat control surfaces, demonstrating the capacity of the platform to affect connexin subcellular localization. Additionally, the area of positive staining for Cx-43 in hiPSC-CMs inside the 3D microwell was significantly greater compared to that of the flat control (***Figure 20e***).

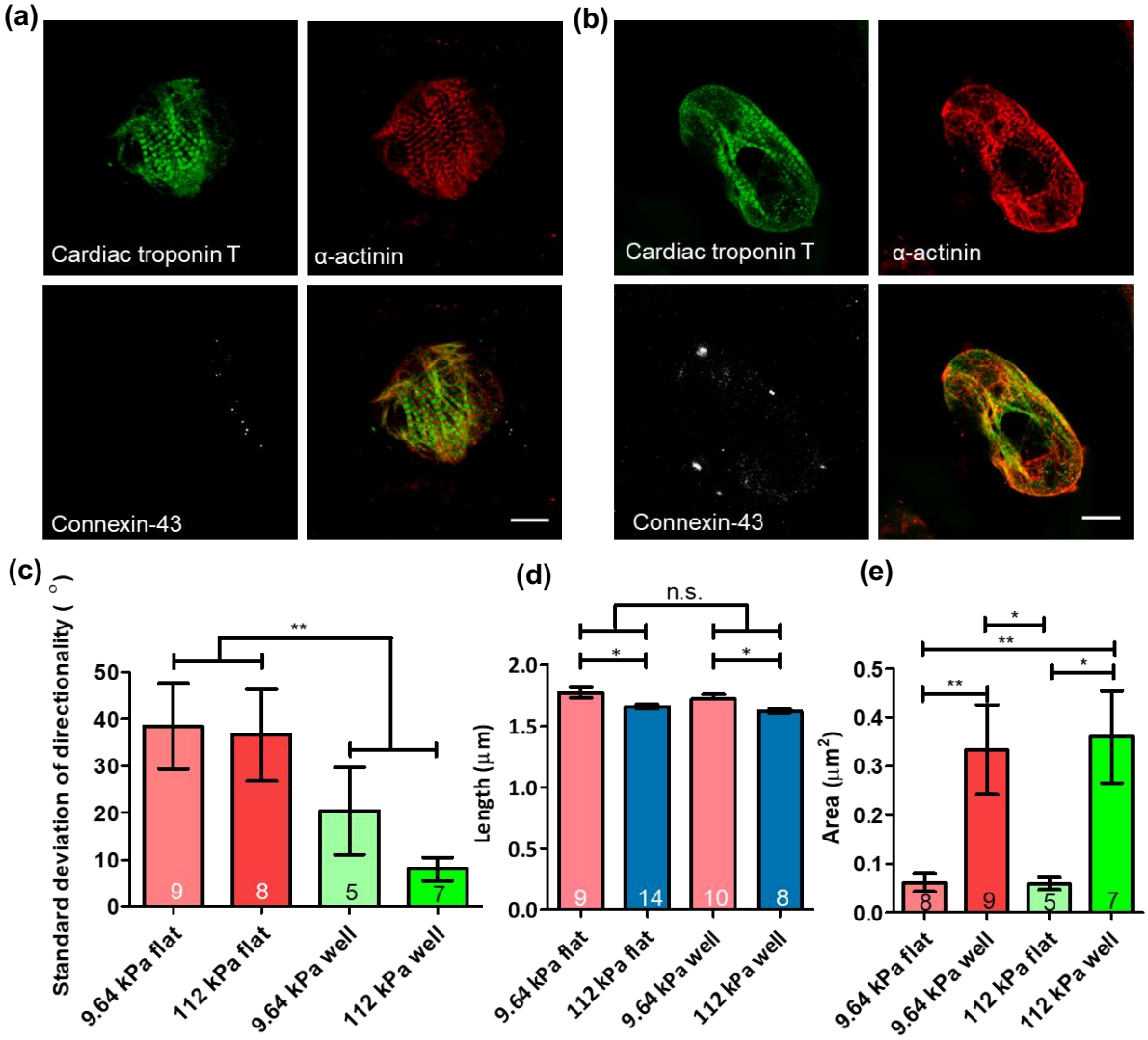

Figure 20: CardioArray directs the structure of hiPSC-CM. *a) Representative images of hiPSC-CMs on a) control flat surface and b) inside the 3D micropatterned substrate on physiological stiffness (9.67 kPa). c) Analysis of CM directionality of single hiPSC-CMs on PAAm demonstrates the capacity of the microwell inducing cell alignment. (2-way ANOVA, ** p< 0.01) d) The sarcomere length measurement of hiPSC-CMs showed a significantly higher spacing inside the 3D micropatterned substrate than on control flat surface. (2-way ANOVA, *p < 0.05) e)*

*Quantification of area occupied by Cx43 within single hiPSC-CMs cultured on 3D microwell and flat control surface. (2-way ANOVA, **p < 0.01) Data represent mean values determined in three independent experiments ± SEM. N = 3. Scale bar = 10 µm. Number indicates on the bar graph show individual sample number in each group.*

As mentioned previously, in the mammalian heart, 3 Cxs have specific expression patterns that display varying levels of co-expressions. This demonstrates different ratios of Cx-40:Cx-45 in the healthy and disease heart during the embryonic stage. As shown in **Figure 21a-b,** hiPSC-CMs cultured in both conditions highly expressed Cx-40, whereas Cx-45 was absent. Therefore, the ratio of Cx-40:Cx-45 was not calculated. Cell membrane stiffness was obtained from force-distance curves of the stress relaxation tests performed with AFM. Analysis demonstrated a significant increase in cellular stiffness (Young's modulus) when single hiPSC-CMs resided in the 3D microwell regardless of substrate stiffness (***Figure 21c***).

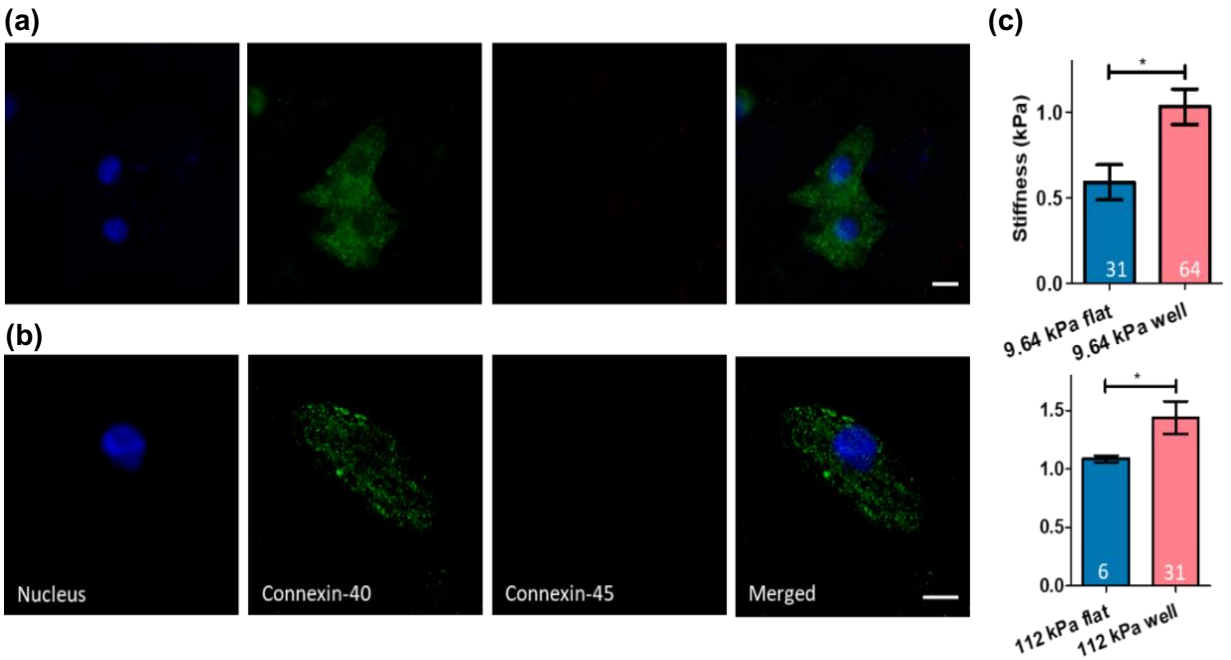

Figure 21: Cx-40, Cx-45 and membrane stiffness affected by different CardioArray condition. *Representative images of Cx-40 and -45 staining on cells cultured on a) 3D micropatterned substrate, b) Flat control surface. c) Cell membrane stiffness measured using atomic force microscopy. (Student t-Test, *p < 0.05) The experiments were conducted with a 20 µm spherical probe and analysed using the Hertz's model. hiPSC-CMs inside the 3D micropatterned substrate showed significantly higher membrane stiffness than those cultured on control flat surface. All scale bars shown are 10 µm. Data represent mean values determined in three independent experiments ± SEM. N = 3. Number indicates on the bar graph show individual sample number in each group.*

CM subtypes (atrial, ventricular or conduction amongst others) display considerable differences at the gene, protein and functional levels, as well as in size and shape. Importantly, it is worth noting that a multifactorial panel is needed to assign chamber-specific CMs. In this study, one of the common panels used to describe chamber-specific CM is the protein expression of MYL-2, -7. Therefore, structural cardiac protein markers – MYL2 and MYL7 proteins were stained to identify any influence of the 3D patterns on the expression of these markers (***Figure 22a***). They have been shown to be preferentially associated with ventricular (MYL2 and MYL7) and atrial (MYL7) CM. As for myosin light chains, the presence of 3D micropatterns and a differential stiffness strongly affected their expression as shown in ***Figure 22b***. Results showed that single hiPSC-CM on flat control surfaces (***Figure 22c***) in both stiffnesses only expressed MYL2. However, in the 3D micropatterned substrate, co-expression of MYL2 and MYL7 was observed.

The proportion of this co-expression was quantified to be higher in pathological stiffness (112 kPa), compared to physiological stiffness (9.67 kPa). Therefore, hiPSC-CM confinement in the 3D microwell arrays significantly affect the expression of CM subtype-specific proteins.

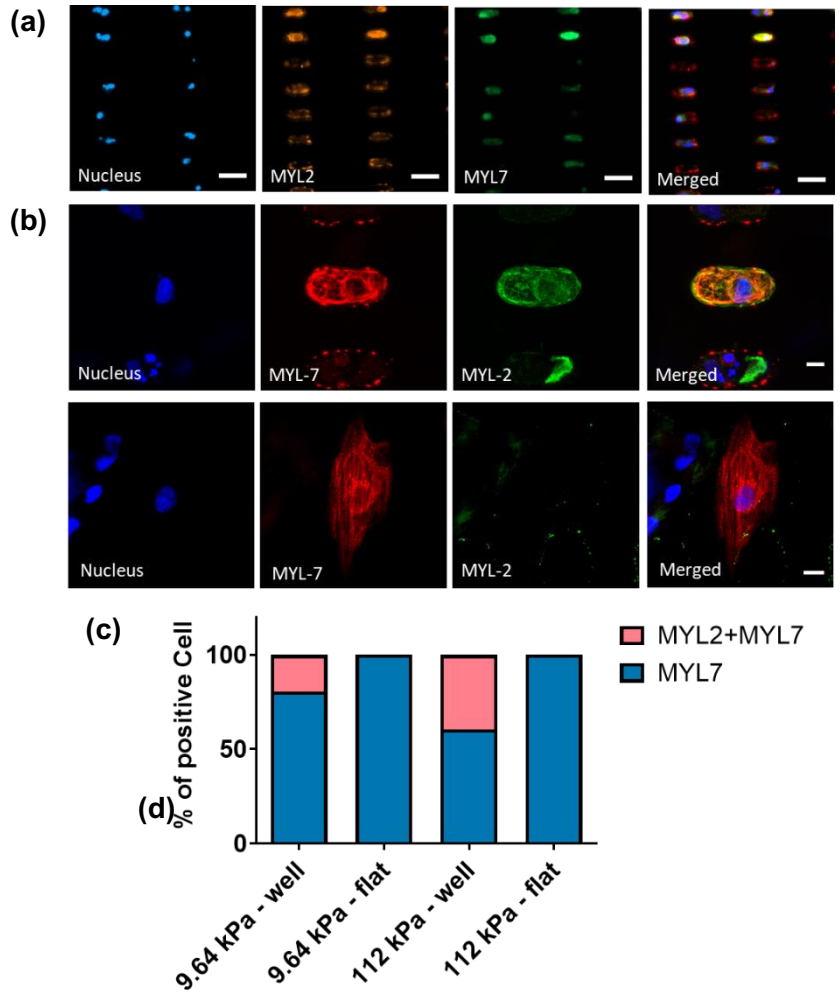

Figure 22: MYL-2 and MYL7 protein expression of single hiPSC-CMs on CardioArray. *a) Immunostaining of hiPSC-CMs for Myosin Light Chain-2 and -7. Single hiPSC-CMs residing in b) 3D microwell and c) Flat control. Cells were co-stained with DAPI to visualise nuclei. d) Bar graph showing the proportion of MYL2 and co-expression of MYL2 and MYL7 cultured on different conditions. Scale bars: 10 µm.*

Given the strong influence the 3D patterns showed on protein expression, gene expression would be similarly modulated. A panel of markers were chosen based on previous reports on human cardiac development and maturation, where MYL2, MYL7, MYH6, MYH7, TNNI1 and TNNI3, were quantified using single cell qRT-PCR (normalised to hiPSC-CMs at day 0). In ***Figure 23a***, the heatmap shows the actual number of hiPSC-CMs cultured in each category , compared to the predicted numbers using multivariate analysis (GLM and PCA). The analysis showed that selected genes were differentially expressed between single hiPSC-CMs residing inside the 3D microwell and flat control surfaces, with MYL7, TNNI3 and shape as key markers in PC2. ***Figure 23b*** shows Spearman's correlation of each gene to another. MYL2, MYL7, MYH6, MYH7, TNNI1, TNNI3, MYL2/MYL7 and MYH7/MYH6 demonstrated a positive correlation to one another. However, TNNI3/TNNI1 showed an inverse proportion to the rest of the gene panel.

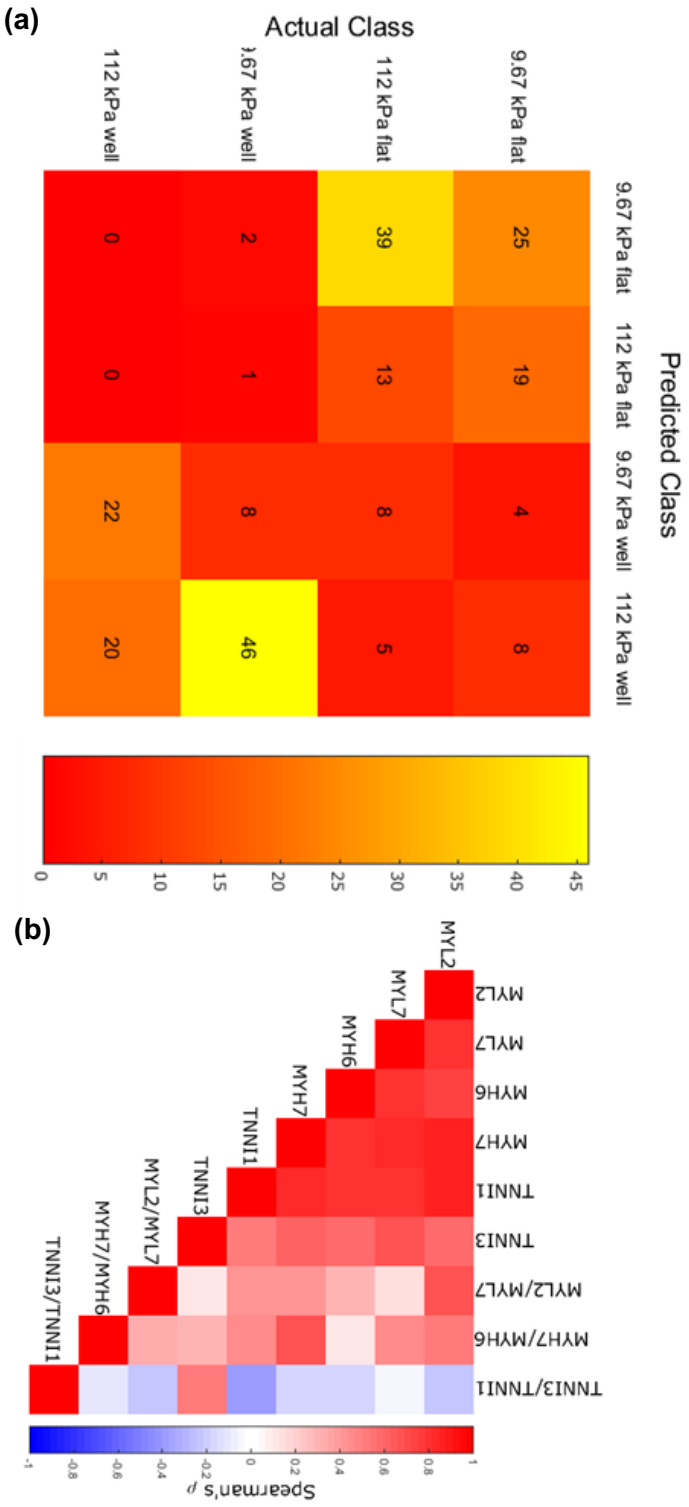

Figure 23: Multivariate analysis using GLM and PCA *demonstrated a correlation between individual gene expression of single hiPSC-CMs cultured on PAAm substrate using a) prediction heatmap and b) Spearman's correlation. N = 4, n = 220.*

The panel of cardiac structural markers showed upregulation during culture in all conditions (as shown in ***Figure 24a***). Individual gene expression of MYL2, MYL7, MYH6, MYH7, TNNI1 and TNNI3 were significantly upregulated in single hiPSC-CMs cultured on a flat control substrate, compared to the 3D micropatterned substrate. The ratio between titin isoforms (TNNI3/TNNI1), known as a robust maturation marker[142], showed a 4-fold and 3-fold upregulation (physiological and pathological stiffnesses, respectively) in the 3D microwell, compared to its respective stiffness in flat control surface (***Figure 24b***), while MYL2/MYL7 and MYH7/MYH6 showed an opposite trend, with downregulation in the 3D microwell, compared to its respective stiffness flat control surfaces.

Therefore, hiPSC-CM confinement in CardioArrays significantly affects the expression of CM subtype-specific proteins, with a higher TNNI3/TNNI1-maturation ratio in hiPSC-CMs residing inside the 3D microwell, and a differential modulation of subtype population-related gene ratio (MYL2/MYL7) with both shape and stiffness. The higher MYH7/MYH6 ratio observed in single hiPSC-CMs cultured on nonconfined topography (flat control) could be correlated to hypertrophic behaviour, diseases and human ventricles. To be able to confirm this finding, other markers are needed to diagnose hypertrophy (e.g. ANP and BNP).

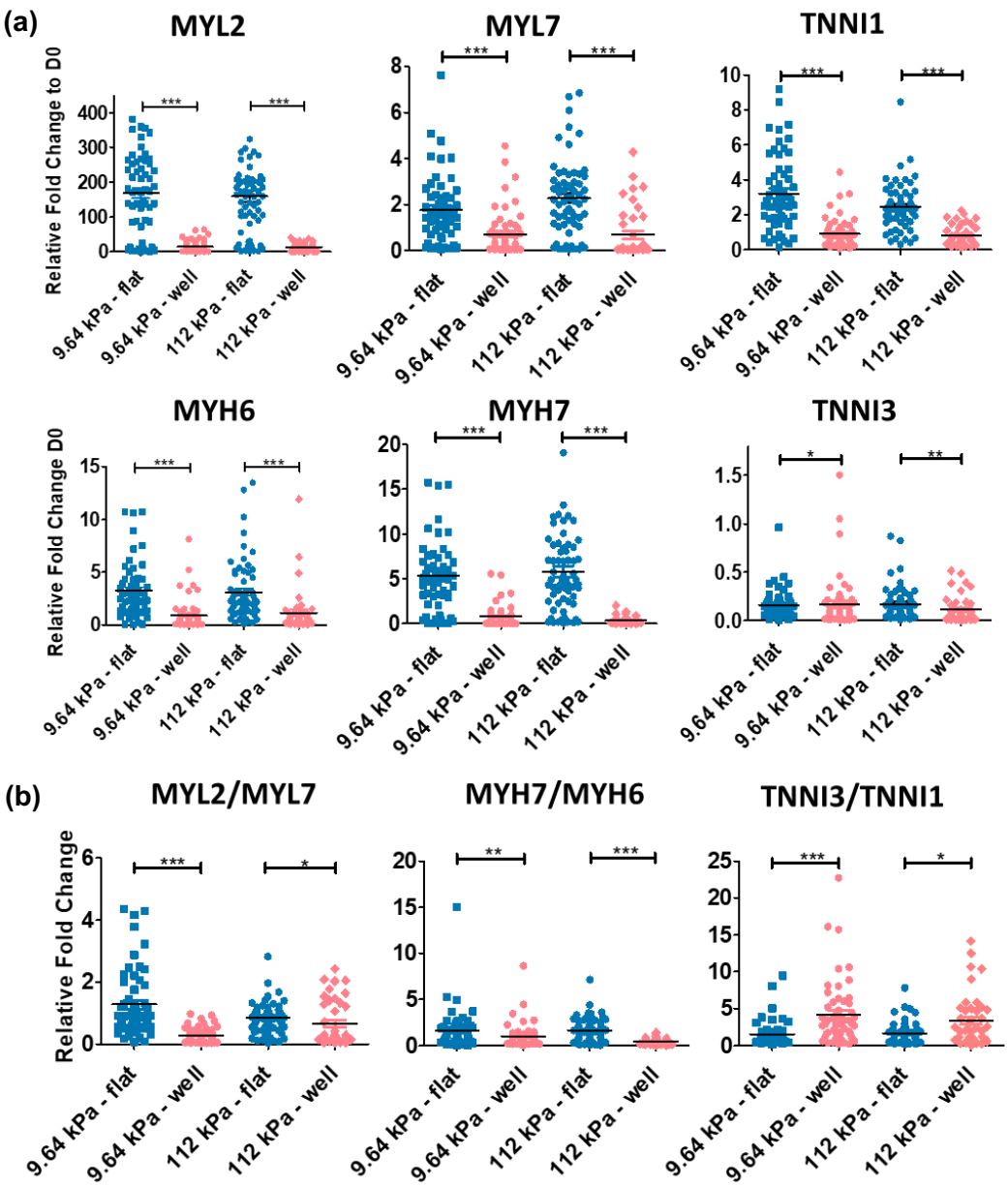

Figure 24: qRT-PCR analysis of the expression levels of cardiogenic markers *showing a) Upregulated levels of MYL2, MYL7, MYH6, MYH7, TNNI1 and downregulated expression of TNNI3 in control flat surface and 3D micropatterned substrate with different substrate stiffness. (2-way ANOVA, *p < 0.05, **p < 0.01, ***p < 0.001), b) Ratios of cardiogenic markers related to cardiac development. Values were normalised to day 0 hiPSC-CMs before plating. (2-way ANOVA, *p < 0.05, **p < 0.01, ***p < 0.001) Data represent mean ± SEM. N = 4 n = 220.*

Finally, in order to investigate the function of single hiPSC-CMs cultured in 3D microwells and flat control surfaces, calcium handling was characterised using optical mapping with a GCamP6f-transgenic hiPSC-line[399]. The shift in calcium transient observed was due to Fluo-4AM compromising the health of single hiPSC-CMs. Fluorescence profiles were recorded from single hiPSC-CMs under electrical field stimulation at 1 Hz. In ***Figure 25a***, analysis revealed that pathological stiffness (112 kPa) significantly abbreviated calcium kinetics (time-to-Peak (146.7, 138.6 ms), time-to-50%-decay (214.1, 215.8 ms) and time-to-80%-decay (404.4, 412.9 ms) as compared to physiological stiffness (time-to-peak (162.8, 164.0 ms), time-to-50%-decay (244.0, 232.0 ms) and time-to-80%-decay (443.0, 431.2 ms)), respectively, shown as hiPSC-CMs cultured on 3D microwell and flat control surface. Additionally, the calcium magnitude of cells cultured on the 112kPa substrate was significantly reduced, when compared to physiological stiffness (9.67 kPa). The 3D microwell in both physiological and pathological conditions did not affect the calcium cycling compared to its flat control surface. The rate of Ca^{2+} decay showed no significant difference between single hiPSC-CMs when cultured on the flat control surface as compared to 3D microwell (***Figure 25b***). This revealed the stiffness of the matrix affected the change in calcium handling with little effect from 3D micropatterns.

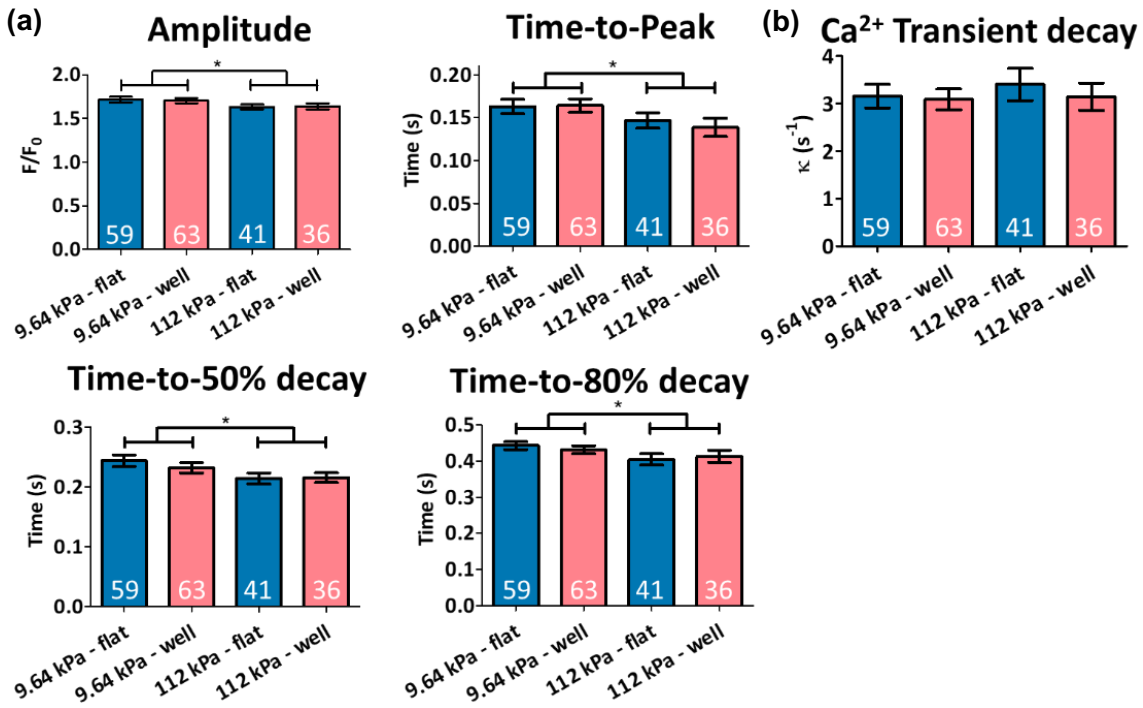

Figure 25: Ca^{2+} handling of hiPSC-CMs *was assessed by using isogenic hiPSC line harbouring a genetically encoded calcium indicator, GCaMP6f, and performing optical mapping field stimulated at 1 Hz. a) Ca^{2+} transient parameters were as follows: amplitude, time to peak, time to 50% decay and time to 80% decay, b) Ca^{2+} Transient decay. Data represent mean values determined in four independent experiments ± SEM. N = 4, n = 199. Number indicates on the bar graph show individual sample number in each group. (2-way ANOVA, *p < 0.05)*

4.4 Discussion and conclusion

ECM influences are essential in directing a cell niche. Two main physical components derived from the ECM´s properties and structure have individually been shown to affect cell fate: topography and stiffness[118,196,213,389,394,400]. Culturing cells on patterned surfaces is widely accepted to dictate both cell behaviours. Natural or engineered substrates have biomechanical cues that can be sensed and translated into cellular signals that control cell fate[185,202,388,401]. Therefore, the cellular shape variations administrated by such confinement constitute a strong physical cue to control cellular behaviour, including gene, protein expression and functional responses. Substrate rigidity is the other side of the coin, with a paramount influence in almost all cell types in living organisms. CMs show a strong dependence on substrate stiffness[71,397,402]. In CMs, biomechanical stimuli alone can modulate force generation, tissue elasticity, cytoskeletal organisation and CM size. However, in spite of the wealth of experimental evidence regarding the influence of topography and stiffness on hiPSC-CMs, their conjunction in an experimental system to assess the combined influence on myocytes has not yet been demonstrated.

The microfabricated 3D micropatterns combined with a substrate with physiological stiffness provides a holistic platform to manipulate single hiPSC-CMs that can be monitored for studying single hiPSC-CMs. There are potential applications for other cell types such fibroblasts, skeletal muscle, chondrocytes or adipocytes amongst others, where there is a strong relationship between shape and function.

hiPSC-CMs have great plasticity, since it has been showed to mimic developing CMs and their ability to respond to their microenvironment[94,107,280,403,404]. hiPSC-CMs show less organised sarcomeres, softer membrane stiffness[183], shorter calcium kinetics with lower amplitude, and differential expression of cardiac-genes[405], compared to human adult CMs. The effects of individual stimuli of stiffness[93,406,407] or shape[70,401] have been previously reported. However, this chapter demonstrated that stiffness and shape regulated different functions and structures, except for changes in cell membrane stiffness, to which both factors contribute. The recent work from Abadi *et al.* demonstrated a 3D micropatterned PDMS using adult CMs as a pattern. Although the fabrication technique has been thoroughly described, functional and structural changes were limited. Quantification of biological responses from hiPSC-CMs must be further carried out. Also, the percentage of single hiPSC-CMs observed on the system was small. In contrast, this study shows for the first time that a 3D micropattern is able to constrain single hiPSC-CMs to adopt the dimensions of an adult CMs, contributing as hypothesised, to directing the cytoskeleton and, in consequence, the cell, as shown by the change in anisotropy and orientation. hiPSC-CMs within

the 3D micropatterns displayed a closer match to adult CMs in sarcomeric length, subcellular localization and connexin expression (presence of Cx-43/Cx-40 and absence of Cx-45, both characteristic of adult working CMs). Since these are isolated hiPSC-CMs, formation of functional gap junctions has not been studied. The sarcomere length closely reached 1.8 μm when experiencing physiological (9.67 kPa) stiffness, a similar value to that of unloaded adult human ventricular CMs, as compared to pathological stiffness (>50 kPa), where the length decreases to 1.6 μm[92]. The sarcomeric length-tension relationship is the crucial factor of the Frank–Starling relationship in cardiac muscle contractility[408]. The highest force and tension generated from CMs is found to be around the optimal resting sarcomeric α-actinin length of 1.8 μm[409] when unloaded, whereas hiPSC-CMs have a sarcomere length of ≈ 1.65 μm[153]. The effect of stiffness on sarcomere and force generation has been described previously on a 2D culture system[93]. However, Hersch *et al.* reported that force generation increased with stiffness, in contrast to the Frank-Starling mechanism[120]. This could be explained by intermediate filaments, linking between substrate and α-actinin (Z-Disk)[410].Therefore, although it has not been measured in this work, this recapitulation of physiological sarcomeric length shown in this platform may result in a higher force production[93]. In addition to the structural benefit imparted by the microwells, the membrane stiffness of hiPSC-CMs cultured on the 3D micropatterns was shown to be higher when compared to flat controls, in line with the reported increase over time taking place during cardiac development (9.67 kPa)[183].

Single cell gene expression analysis revealed the significant influence of the physical extracellular milieu of CardioArrays. In particular, the TNNI3/TNNI1 and MYL7/MYL2 ratios were significantly lower in single hiPSC-CMs cultured on flat control surfaces of both pathological (112 kPa) and physiological (9.67 kPa) conditions than the 3D microwell, implying the capacity of a 3D shape in the platform to modulate cardiomyocyte maturation marker and phenotype associated proteins[411]. The close link of the MYH7/MYH6 ratio with the development of hypertrophy[412,413], diseases and ventricular myocayte[143] that can be modulated by CardioArray, adds to the capacity of the extracellular 3D environment to model both healthy state (on 3D microwell) and a diseased state (flat surface on 112kPa stiffness substrate)[143,414,415]. Single hiPSC-CMs cultured on this platform demonstrated that the MYH7/MYH6 ratio is significantly higher, which points to an increased maturation of cells within the microwells, as also confirmed by individual cardiac genes. Cell stiffness within 3D micropatterns was also increased, again supporting an improved maturation level[183,411]. Moreover, shape-confinement of hiPSC-CMs in this 3D microwells is able to influence the differential expression of markers involved in CM identity, like MYL2, MYL7, Cx40, Cx43 and Cx45, thereby pointing towards the capacity to influence CM phenotype solely by

applying physical stimuli. This provides an extra, useful dimension to the present methodology regarding the biological induction of different populations of CMs[280,359,416–419]. All in all, the upregulation in gene expression versus the starting population, which alongside the increased TNNI3/TNNI1 and cellular stiffness compared to single hiPSC-CMs on flat controls, and the decrease in the hypertrophic ratio MYH7/MYH6, emphasizes the unique capacity of the CardioArray alone. This manipulation of the extracellular physical milieu increases the degree of maturity of single hiPSC-CMs, while at the same time manipulating myocyte phenotype (MYL2 and MYL7 expression). This demonstrated for the first time that a 3D shape strongly directs gene expression on single hiPSC-CMs regardless of stiffness. Comparison to adult CM gene expression would further elucidate the relevance of gene expression to adult human CM.

Although EC-coupling associated proteins have not been studied in this work due to the limit of RNA content acquired, calcium transient modulation from the platform could be analysed. Of note, no substantial effect of single-cell 3D shape confinement on calcium cycling was found, while substrate stiffness was found to be an influential factor. Single hiPSC-CM on physiological stiffness (9.67kPa) displayed increased amplitude and prolonged calcium transients due to an increase in time-to-peak and time-to-decay, compared to pathological stiffness (as previously reported)[213,400]. These differences are similar to the response of adult cardiac tissue in disease, whereby an increase in stiffness due to fibrotic remodelling (> 50 kPa) causes the inversion of the force-frequency relationship in calcium cycling, triggering an increase in heart rate to balance the decrease in ejection fraction as a decompensation mechanism, requiring a shortening of calcium transients as found in single hiPSC-CMs cultured on pathological stiffness. However, it is possible that the induction of changes by the confinement in the 3D micropatterned substrates requires longer times than the 7-day period employed in this work.

In summary, this chapter demonstrated that single hiPSC-CM function, gene expression and structural organisation can be modulated with CardioArrays, combined with physiological and pathological stiffness in *in vitro* culture. Shape-confinement of hiPSC-CMs in the 3D microwells is able to influence the differential expression of markers involved in CM identity, such as MYL2, MYL7, Cx40, Cx43 and Cx45, while stiffness directly influences calcium cycling of hiPSC-CMs. The results indicate that by solely manipulating the biomechanical properties of the extracellular substrate, single hiPSC-CMs can be directed, and a multifactorial characterisation of structural, genetic and functional changes can be studied and potentiated to dictate cellular specification, behaviour and development. Together, this chapter improves the understanding of the interaction between external biomechanical cues provided by CardioArrays with cells via interactions with

topographical features of the microenvironment at the single-cell level. Furthermore, this system is expected to apply to other cell types, where maturity and shape are similarly related and translate to multicellularity *in vitro* models for developmental and clinical studies[39].

Chapter 5

Conductive Collagen–mimetic Foams for Cardiac Tissue Regeneration

5.1 Abstract

MI, initiated by a block of the coronary artery, accounts for at least a third of deaths worldwide. This event reflects a lack of an effective intrinsic mechanism for CM regeneration, leading to an irreparable disruption of the electrical signal, non-synchronous contraction and eventually, HF. Conductive polymers (CPs) are promising materials that can beneficially affect electroresponsive organs like the heart. However, their cardiac application has been hampered by unstable conductivity, toxicity and unmatched mechanical properties. Therefore, cardiac tissue engineering aimsto recreate physiological relevant environment provided to the cells using a biocompatible biomaterials.

Here, a composite biomaterial from Scl2 and polyaniline (PANI) was fabricated, namely Scl2-PANI, which was doped and crosslinked using phytic acid. The strong interaction between PANI, Scl2 and phytic acid led to a cardiac conductive foam with low resistivity (218.6 ± 2.02 kiloohm per square centimetre) that remained relatively low resistivity after a week of incubation in a physiological medium. The dynamic mechanical Young's modulus demonstrated at ~41 ± 3.1 kPa at 1 Hz, closely resembling the physiological stiffness of myocardium. The cardiac conductive foam is conductive and cytocompatible with hiPSC-CMs *in vitro*. After a week, hiPSC-CMs expressed their sarcomeric length at 2.16 µm with significant upregulation of KNCJ2, HCN4, MYL2, MYL7, MYH6 and MYH7 mRNA expression compared to their non-conductive counterpart, cultured on Scl2. Intracellular calcium cycling showed an increase in amplitude of the calcium transient with time-to-90% decay at 243.3 ± 9.517 ms. A preliminary *in vitro* study with acellular PANI-Scl2 and Scl2 demonstrated no acute detrimental effect on healthy ventricular murine ultrathin slices. Interestingly, the Scl2-PANI cardiac foam had an immediate, positive effect on the cryoinjury cardiac slice measured using multielectrode array. The effect showed that conduction velocity (CV) had been regained to more than 80%, compared to healthy conduction velocity of the ventricular ultrathin slice. This robust platform could be utilised as a cardiac biomaterial, representing a promising treatment for MI.

The findings in this chapter established the basis for the design and development of a cardiac conductive composite construct. This provides a robust conductive biomaterial system with physiologically relevant mechanical properties that could be interfaced with the myocardium, to elucidate the communication and consequences of these materials with the myocardium. The findings will also advance the progression of the next-generation cardiac therapies using cell-CP-based strategy.

5.2 Introduction

Chapter 3 and **4** demonstrated the importance of biophysical cues on the structural and functional properties of hiPSC-CMs *in vitro*. This knowledge can be integrated to design a novel biomaterial. Additionally, the contraction and relaxation of the heart also depends on the transmission of electric impulses through cardiac specialised tissue that is interrupted during MI. This causes a reduction in conduction velocity and a delay in repolarisation across the infarct region. This issue cannot be overcome by simply using a natural biomaterial. One of the currently anticipated techniques is the development of conductive biomaterials. This could potentially regain electrical communication between cells separated by a damaged area, and mechanically support the myocardial wall. Since the discovery of hiPSC-CMs, researchers and clinicians have attempted to realise their potential in cardiac applications with much attention over the recent years on conductive materials.

Recently, the Stevens' group demonstrated the beneficial effects of first-generation and second-generation conductive polymers *in vivo* and *ex vivo*. Firstly, Mawad *et al.* performed an *ex vivo* experiment to study acellular PANI-chitosan conductive patch on myocardial ultrathin slice and rat models. The conductive patch demonstrated no effect on healthy myocardial slices' contractility but causing a reduction in CV. Interestingly, the conductive patch increased the conduction velocity in the damaged heart[420]. Later, Kapnisi *et al.* used an advanced fabrication technique called 'excimer laser microablation' to create a honeycomb design on the PANI-chitosan conductive patch. This allowed the patch to obtain finely-tuned mechanical properties that match those of native myocardia. They found no detrimental effects on both healthy and myocardial infarcted heart *in vivo* (specifically, negligible fibrotic response and no improvement in conduction velocity)[231]. Therefore, previous studies indicated that the PANI-chitosan conductive patch may positively affect the reparation process of the heart albeit the underlying mechanism has not been investigated yet. This conductive property could improve the synchronous contraction of cardiac muscle that is damaged after MI while supporting hiPSC-CM integration to the native tissue. However, hiPSC-CM interaction on conductive polymers have not yet been reported. Studies on the interaction with myocardium especially on re-entrant arrhtyhmias must be carried out.

Building on previous knowledge gained in this thesis and work completed in the Stevens group, this chapter aims to study hiPSC-CM interactions *in vitro* on a novel conductive biomaterial that provides physiologically relevant mechanical cues. Here, a composite blending technique was used to produce a composite of synthetic conductive collagen that has physiologically

relevant cues and structure. Ultimately, this chapter demonstrated an improvement on conduction velocity in an *in vitro* MI model .

5.3 Results

In ***Figure 26a***(i), the diagram shows the structure of Scl2 protein. ***Figure 26a***(ii) illustrates the experimental setup of hiPSC-CMs cultured on Scl2 and PANI-Scl2 and then characterised at day 7. The Scl2 protein was crosslinked with polyaniline (PANI) by introducing phytic acid as a crosslinker and dopant. This was done by initiating the polymerisation of aniline and phytic acid (Solution A) using APS (Solution B) (***Figure 26b***(i)), before drop casting a polymer mixture or distilled water on the freeze dried Scl2 (***Figure 26b***(ii)). The freeze dry step was implemented to allow the full absorption of solution throughout the blank Scl2, resulting in PANI-Scl2 and Scl2 control, respectively. Macroscopic photographs of PANI-Scl2 and Scl2 shown in ***Figure 26c***, depicting the change in colour, from yellow to dark green upon crosslinking with emeraldine PANI. The chemical structures of PANI, phytic acid and Scl2 are shown in ***Figure 26d***. Therefore, this constituted the experimental setup for studying conductive polymer interactions with hiPSC-CMs *in vitro*.

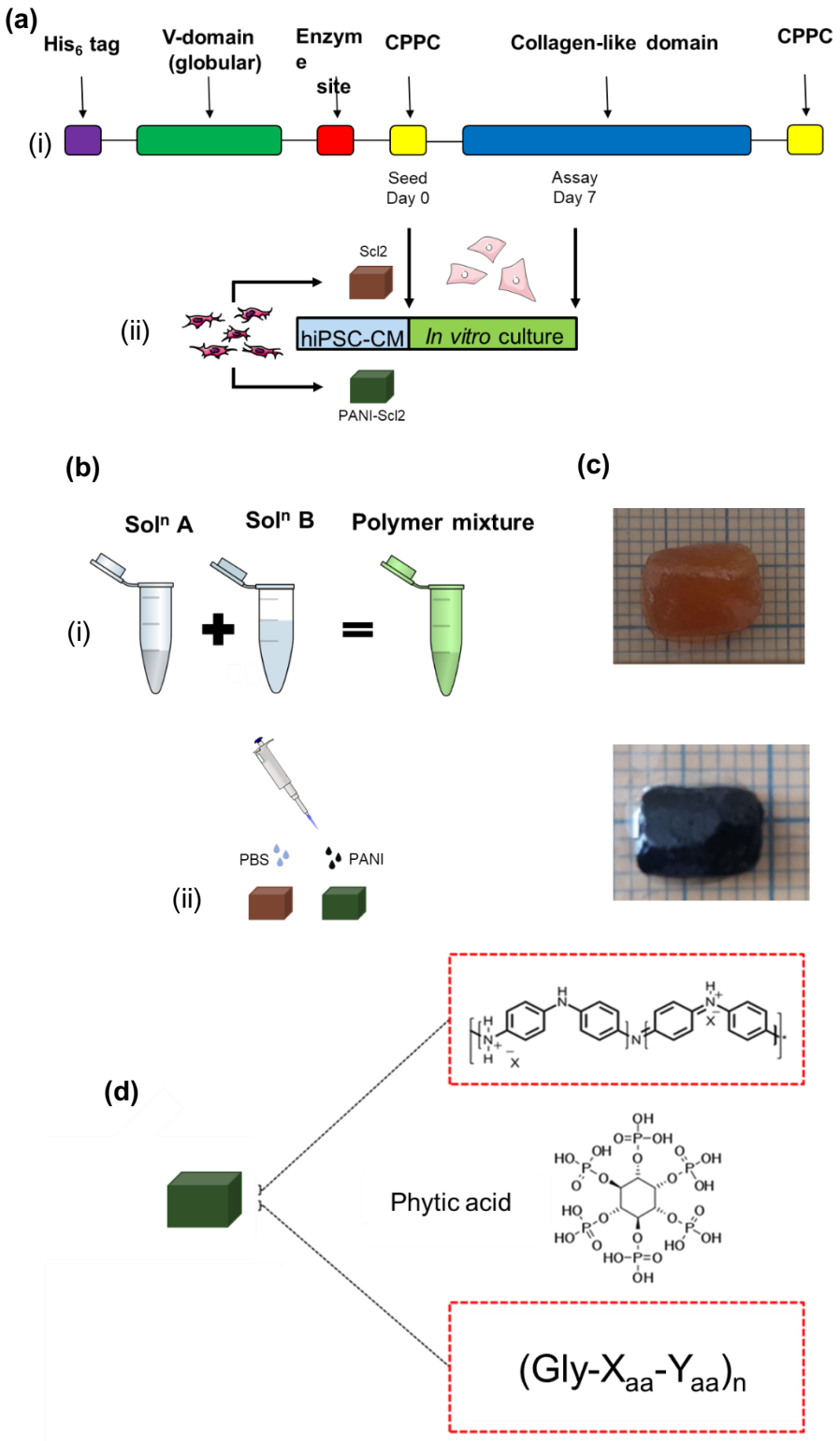

Figure 26: Experimental setup, Scl2 structure and PANI-Scl2 fabrication. *a) Schematic diagram of (i) Scl2 protein (ii) experimental setup for hiPSC-CM study, b) synthesis workflow of PANI-Scl2 and Scl2 fabrication: (i) solution A (aniline and phytic acid) was mixed with solution B*

(28.4% APS) and (ii) Scl2 was drop casted with polymer solution or distilled water (control) to obtain PANI-Scl2 and Scl2 (control), respectively, c) photographs of (i) Scl2 (control) and (ii) PANI-Scl2 hydrogel on 1mm grid, d) chemical structure of PANI, phytic acid and Scl2.

The PANI-Scl2 was mechanically preconditioned by 1,000 cycles of 10% strain dynamic compression to eliminate the transient effect caused by un-crosslinked PANI. To characterise the Scl2 collagen mimetic foam, Fourier Transform Infrared (FTIR) spectroscopy was conducted to identify distinct differences between the two foam formulations. As shown in ***Figure 27a****,* a characteristic infrared transmittance peak at 1630 cm^{-1} (amide C=O) was present in both types of foams. However, the PANI-Scl2 foams had an additional infrared transmittance peaks at 1132 cm^{-1} (in-plane bending of aromatic C-H), a band located at 1653 cm^{-1} related to the NH_2 bending vibration, while the peak at 684 cm^{-1} is attributed to NH_2 wagging and 824 cm^{-1} (out-plane bending of C-H) indicative of the presence of PANI and phytic acid on blank Scl2 foams. The presence of these 3 bands indicates the addition of PANI on Scl2 foam. In addition, the conductive form of PANI demonstrated the peak at 1580 cm^{-1} (a protonated imine group) and 1242 cm^{-1} (the characteristic band of conductive form).

To test the surface resistivity of PANI-Scl2 *in vitro* as a function of time (every 24 h for 7 days), Scl2 conductivity was measured as a control on day 0 and dry PANI-Scl2 I-V traces were recorded. After fabrication, the surface resistivity showed at 0.218 ± 0.020 kiloohms per square centimetre. Following the incubation with cell culture media, the representative I-V characteristic curve is shown in ***Figure 27b***. After 1 day of incubation, the surface resistivity increased by 54% to 0.337 ± 0.064 kiloohms per square centimetre (***Figure 27b***). A further increase was recorded at day 7 (1.045 ± 0.167 kiloohms per square centimetre). After 7 days of incubation in physiological conditions, the PANI-Scl2 hydrogel showed a decrease in its electrical conductivity (as a conductive polymer). This may have resulted from further removal of unbound PANI on Scl-2 hydrogel and a reduction of oxidised state PANI.

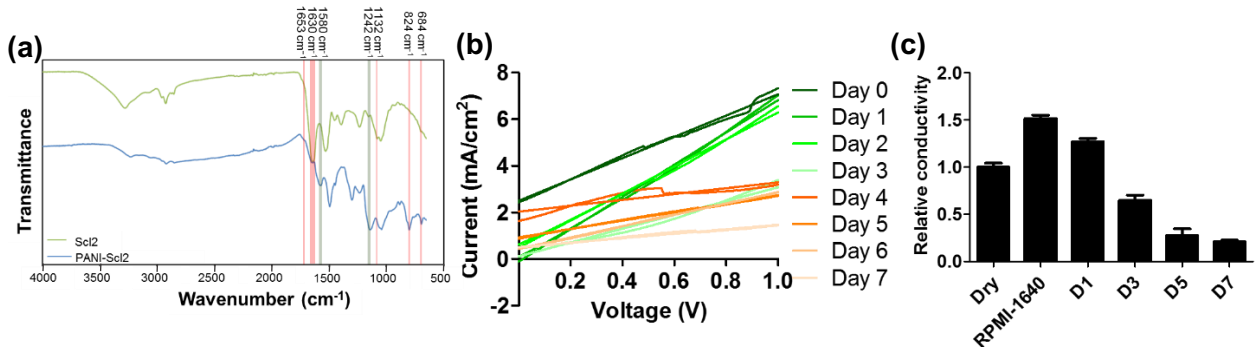

Figure 27: PANI-Scl2's electronic stability under in vitro condition over 7 days. *a) Comparison of the FTIR spectra of Scl2 and PANI-Scl2. The spectra normalised at their absorption maxima and vertically shifted for clarity. This experiment was performed by Dr Paresh Parmar. b) Representative IV cyclic voltammograms (25 mV·s^{-1}) in distilled water reveal the stable electrochemistry, c) surface resistivity of PANI-Scl2. (N = 5).*

XPS characterisation was performed to monitor the oxidation state and doping level of PANI-Scl2 as a function of incubation time in buffer. This quantified the conductive form (emeraldine form) of PANI on the foam surface. Some contaminant elements could be found, such as F 1s, Si 2p and Na 1s. These contaminants' photoelectron signals are suspected to arise during sample preparation. Further investigation has been conducted on the main elements found on PANI and Scl2 at higher energy resolution. The C 1s, O 1s, N 1s, and P 2p core-level spectra were analysed at fabrication (day 0) and after 7 days of *in vitro* condition incubation. In PANI-Scl2, C 1s region is essential for the XPS analysis of polymeric materials. After peak fitting, the result showed three main chemical bonding in the C 1s region (***Figure 28c***). Each of these components, C-C, C-N, C=N shows different binding energies (BE). In this study, C-C component was found at ~284.6 eV of BE, previously showed by Golczak *et al*[421]. A C-N was found at ~285.5 eV and could be assigned to either C=NH or C=NH^{+}. These peaks are attributed to the carbon bonded to the neutral nitrogen atoms. After 7 days, the same peaks of C 1s, P 2p and N 1s region remained. The relative chemical composition of the hydrogel surfaces is shown in ***Figure 28c***. These elemental compositions were calculated based on the main spectra that conducted at high resolution. The area under the curve was normalised to the atomic sensitivity factor 77, thus the total percentage of element is obtained. In the table, the percentage of individual element were tabulated at fabrication (day 0) and post-incubation day 7 in physiological conditions. The result clearly shows a reduction of protonated imine that contribute to reduce in resistivity showed in ***Figure 27b***.

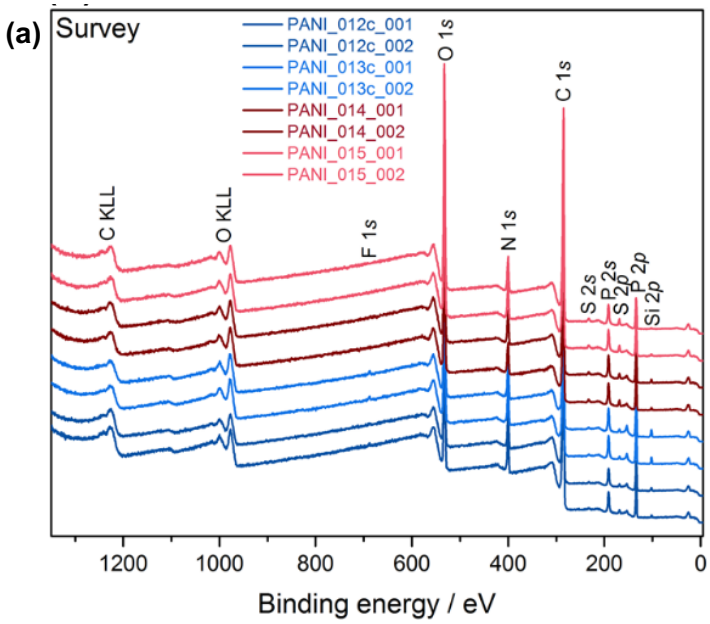

(b)

Sample	Incubation time	=N- (imine)	-NH (amine)	$-NH_2^+$ (ox. amine)	$=NH^+$ (prot imine)
PANI-Scl2	0	n.d.	54.9	0.0	68.7
	7	n.d.	31.3	28.1	17.0

(c)

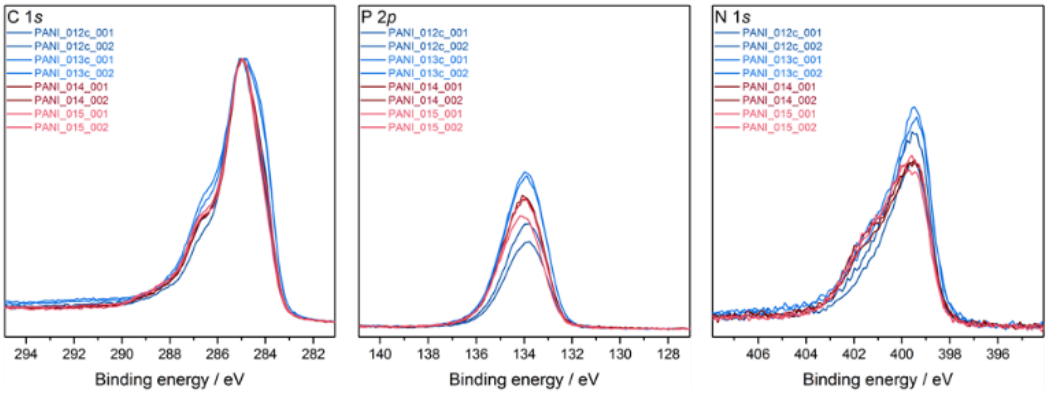

Figure 28: Detection of protonated species using XPS. *a) A representative survey scan of PANI-Scl2 hydrogel. b) High-resolution narrow scans of C 1s, P 2p and N 1s spectra of the PANI patch at day 0. c) The elemental composition of PANI-Scl2 at day 0 and day 7 in physiological conditions.*

To visualise the ultrastructure and morphology of the manufactured scaffolds, Scl2 and PANI-Scl2, scanning electron microscopy (SEM) and multi-photon second harmonic generation (MP-SHG), were used, as shown in ***Figure 29***. Due to the intrinsic light absorbance properties of PANI, the laser cannot pass through the material; hence, no second-harmonic light was collected.

As the MP-SHG image shows, Scl2 collagen mimetic scaffold was visualised from the autofluorescence of endogenous fluorophores, due to the presence of a long, stiff, triple-stranded helical structure[422]. MP-SHG shows the highly porous structure displayed as a darker area on the image, while the Scl2 itself appears as a bright, red region. SEM micrographs confirmed the high porosity of Scl2 foam. PANI-Scl2 showed a less uniform surface due to a deposition of PANI on the Scl2 foam. This deposition changed the surface roughness to be visually higher than blank Scl2. Therefore, clear differences in morphology were observed between the two different types of foams. It is likely that phytic acid, the crosslinker between Scl2 and PANI, contributed towards the differences observed in their respective morphologies, by retaining high amount of PANI on the surface of Scl2.

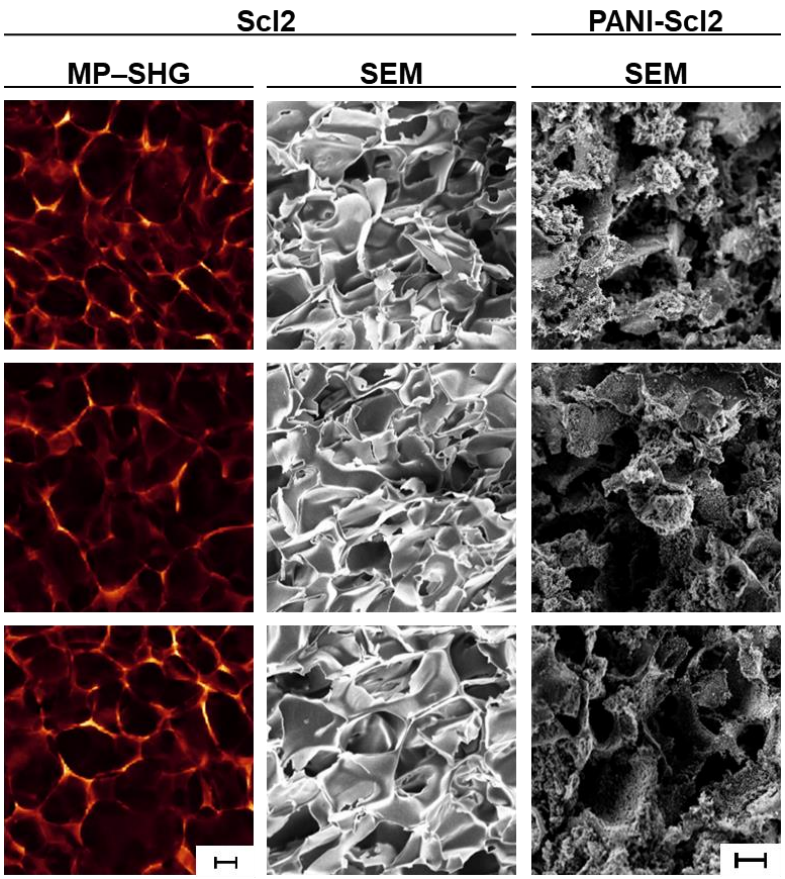

Figure 29: Structural characterisation of Scl2 and PANI-Scl2: *Surface topography of Scl2 hydrogel using MP-SHG imaging and SEM micrograph of PANI-Scl2 and Scl2 hydrogels. Scale bar: SEM image - 100 µm, MP-SHG image - 200 µm.*

The heart is a highly dynamic organ, pumping the blood through the organism every second and capable of more than 2 billion beats in an average life time. With every heartbeat (1 - 1.5 Hz), the myocardium contracts about 10 - 15% strain. A scaffold employed to deliver hiPSC-CMs must be able to withstand this dynamic environment and maintain its properties throughout until full integration occurs. In ***Figure 30***, to investigate these mechanical properties, dynamic mechanical analysis (DMA) was performed using a Bose Electroforce with a 250 g load cell. All the samples underwent preconditioning before being tested at 12.5 ± 7.5% strain, at a fixed random frequency order (0.1, 0.5, 1, 1.5, 2, 3, 5, 10, 1, 0.1, 3, 0.5, 2, 5, 1.5 and 10 Hz), which include the physiological heart frequency of 1.5 Hz discussed here, while using other frequencies as a history dependency indicator. At this frequency for complex modulus, Scl2 hydrogel exhibited 2 kPa, compared to 48 kPa in PANI-Scl2. The foam demonstrated frequency dependence in complex modulus, whereas storage modulus was independent, indicating an insignificant difference in storage modulus regardless of frequency. Storage moduli were 1.38 kPa and 71.16

kPa for Scl2 and PANI-Scl2 respectively, while loss moduli were calculated as 0.7 kPa and 10 kPa. The foams showed viscoelastic properties as in the frequency-dependent increase in loss modulus. Tangent delta and phase shift showed a stronger frequency dependence compared to loss modulus in Scl2 at 0.387 and 0.367 Rad, respectively, while for PANI-Scl2, these values demonstrated at 0.206 (Tangent delta) and 0.203 Rad (Phase shift). Therefore, Scl2 and PANI-Scl2 demonstrated a physiological relevant dynamic stiffness with frequency dependency. In current literature, this is the first report showing a conductive collagen mimetic scaffold that can support the relevant physiological stiffness of the native myocardium.

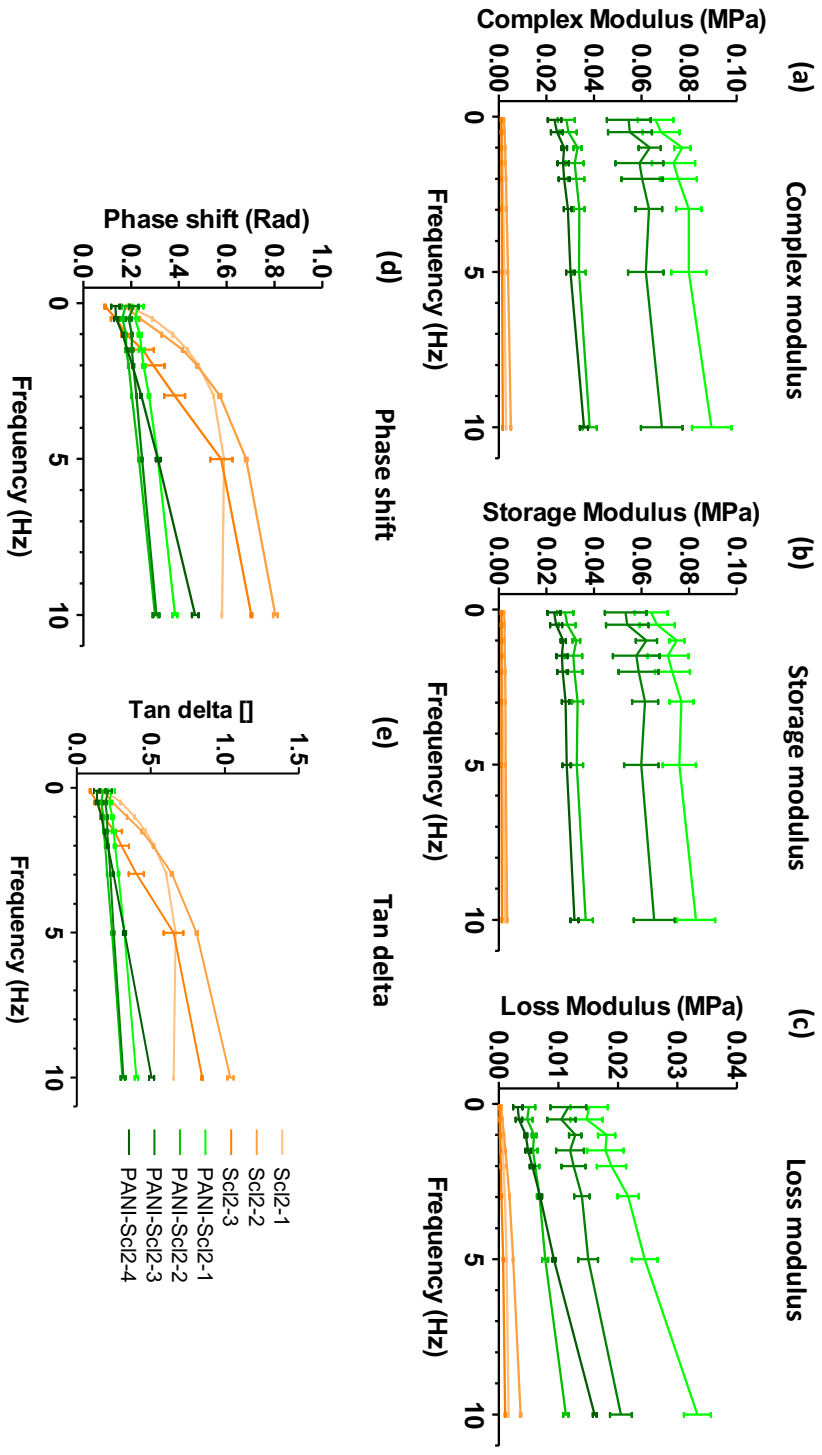

Figure 30: Mechanical properties of hydrogel characterised using DMA *as a function of frequency for N = 4 PANI-Scl2 and N = 3 Scl2 foam. a) complex modulus, b) storage modulus, c) loss modulus, d) tangent delta and e) phase shift. Performed with the assistance of Dr Axel Moore.*

Next, hiPSC-CMs were used as a model to study biological effects, because of their high plasticity and potential maturation during *in vitro* culture. Firstly, LIVE/DEAD™-staining was performed to determine cell survival on the foams after 7 days in culture. The images showed indistinguishable amounts of live cell in Scl2 or PANI-Scl2 as well as dead cells, which were low on both foams. However, as shown in ***Figure 31a***, on day 7 hiPSC-CMs cultured on PANI-Scl2 morphologically tended to form clusters, compared to Scl2, where the cells were more uniformly distributed. This might be due to the difference in scaffold morphology, as previously mentioned. To provide quantitative insight of cell number, DNA content was quantified using a PicoGreen™ assay, while the metabolic activity was determined with alamarBlue™ assay. The amount of DNA on both Scl2 and PANI-Scl2 was not significantly different (***Figure 31b***(i)). However, there is a significant reduction on metabolic activity of hiPSC-CMs cultured on PANI-Scl2, compared to those cultured on Scl2 (***Figure 31b***(ii)). This reduction may be the result of a trace of phytic acid. Conclusively, the reduction in metabolic activity without change in DNA content could have arisen from the dead cells retaining on the scaffold. Absolute count on live cells could be further validated using FACS. However, further exploration to elucidate this finding is needed to fully understand this phenomenon. Indeed, this demonstrates that the foams do not induce any detrimental effect in cell engraftment, although it impacts their metabolic activity.

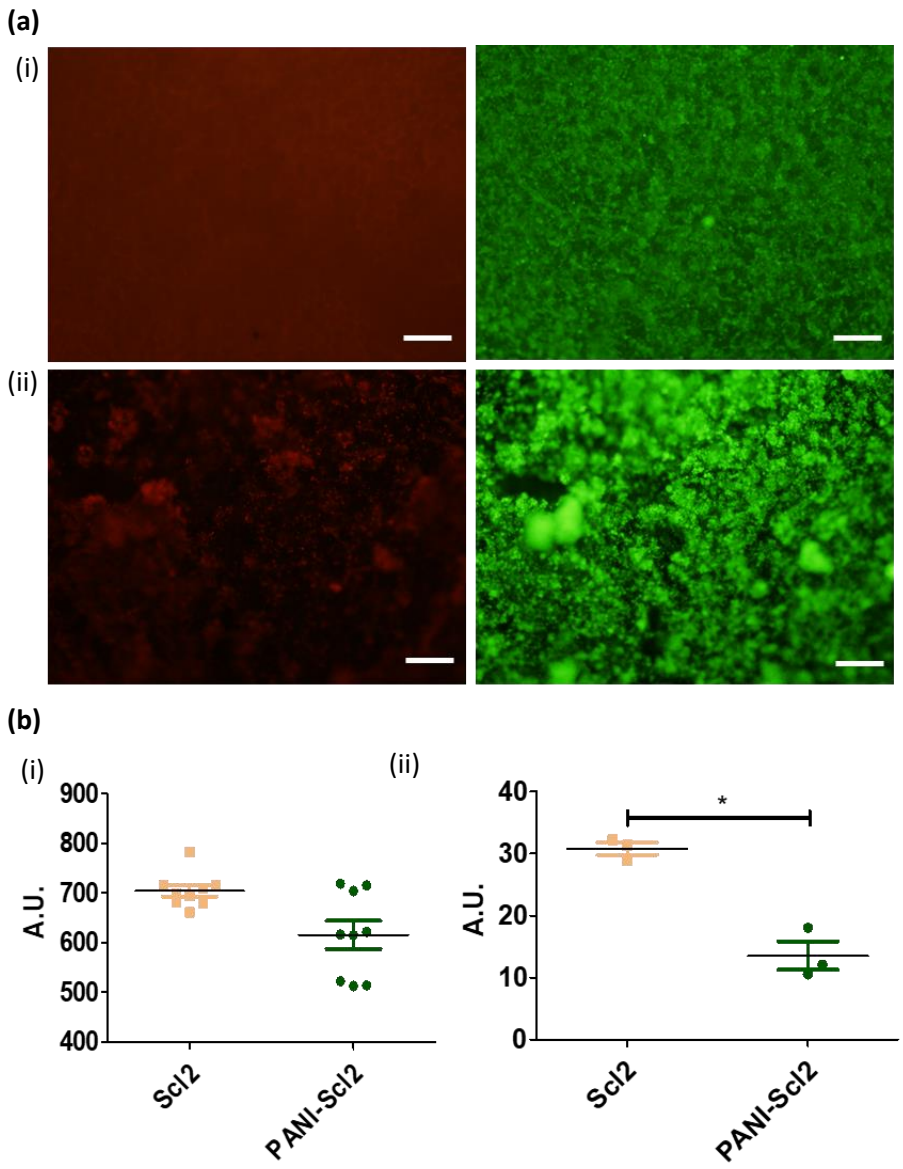

Figure 31: hiPSC-CM viability on hydrogels after 7 days in vitro culture. *a) Representative LIVE/DEAD™ images using calcein (Live - green) and EthD-1 (Dead - red) of hiPSC-CMs cultured on (i) Scl2 and (ii) PANI-Scl2, b) (i) DNA content per construct in each foam quantified using a PicoGreen™ Kit (N = 9), (ii) metabolic activity per construct in each foam measured using alamarBlue™. (N = 3) All data normalised to day 0. (Student t-Test, *p < 0.05). Scale bars: 100 µm*

Next, immunofluorescent staining was performed to visualise hiPSC-CMs morphology on Scl2 and PANI-Scl2 constructs. For this, samples were fixed and stained for two of the main sarcomeric components, cTnT and α-actinin. In ***Figure 32a-b***, cTnT staining confirmed the presence of hiPSC-CMs on both scaffolds after 7 days, showing elongation and striation of cTnT structure. α-actinin also showed striation on both types of foams. These two-staining assays confirmed the healthy status of the hiPSC-CMs on both foams, which displayed no evident differences in structure (i.e. striation and elongated morphology), supporting the healthy status of the hiPSC-CMs. This may indicate that after the cell initially adhered, differences in surface topography and stiffness of Scl2 and PANI-Scl2 may have had little effect on the hiPSC-CM morphology. The structure of the sarcomeric apparatus was assessed with α-actinin staining, showing no significant difference in sarcomeric length (2.14 ± 0.27 μm and 2.33 ± 0.18 μm on Slc2 and PANI-Scl2 foams, respectively). This length is essential for CMs contraction, isometric tension and force generation, where the optimal for human CMs is approximately 2.2 μm[92,409]. Although the contractile force was not measured directly, the matching of the observed values with respect to the native human standard, points towards optimal force generation of the seeded hiPSC-CMs. Therefore, immunostaining demonstrated a healthy morphology of hiPSC-CMs cultured on Scl2 and PANI-Scl2, which were able to form a 3D engineered tissue.

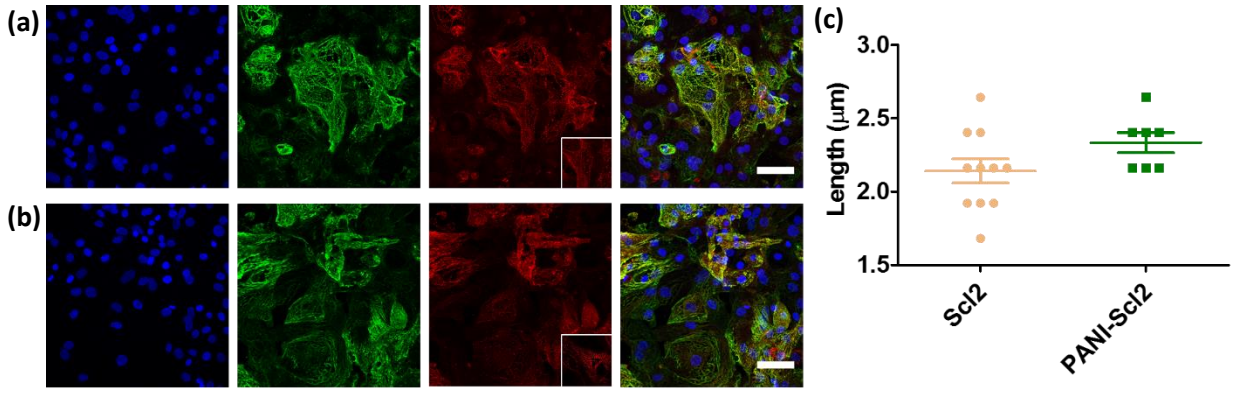

Figure 32: Immunostaining for cardiac structural proteins. *Photomicrograph showing immunostaining of hiPSC-CMs against cardiac troponin T (cTnT - green), alpha-actinin (red) and visualised using DAPI for representative images of hiPSC-CM a) on Scl2 hydrogel. b) on PANI-Scl2. (Scale bar: 10 μm). Inset image: cropped and zoomed from photomicrograph of alpha-actinin stained against hiPSC-CMs culture on PANI-Scl2. c) The sarcomere length of hiPSC-CMs on the PANI-Scl2 (N = 12) showed no significant differences between hiPSC-CMs cultured on Scl2 and PANI-Scl2 (N = 9). Data represents mean ± SEM determined in three independent experiments. (Student t-Test, *p < 0.05)*

To further investigate how culture on the foams affected hiPSC-CMs gene expression, a panel of cardiac genes was selected and determined by RT-qPCR (as shown in ***Figure 33***). KCNJ2, encodes the potassium voltage-gated channel subfamily J member 2, showed an upregulation in hiPSC-CMs cultured on PANI-Scl2 as compared to Scl2. hiPSC-CMs cultured on PANI-Scl2 showed significantly higher expression of KCNJ2, compared to hiPSC-CMs cultured on Scl2, which demonstrated more than a 70% reduction in KCNJ2 expression compared to day 0. RYR, which encodes ryanodine receptor protein, showed insignificant differences in expression between hiPSC-CMs cultured on both foams. HCN4 is prominently expressed in the pacemaker regions of the mammalian heart. It showed a significant upregulation on Scl2-PANI, compared to Scl2.

Next, structural cardiac markers were relatively quantified. MYL2 and MYH6 showed significantly upregulation for hiPSC-CMs cultured on PANI-Scl2 compared to those cultured on Scl2. Additionally, MYL7 and MYH7 showed no significant difference between the two culture conditions. Finally, the MYL2/MYL7 ratio was calculated, showing an insignificant difference between hiPSC-CMs cultured on both foams. This showed no difference in hiPSC-CMs' sub-population. Similarly, MYH6/MYH7 also showed no significant differences. Therefore, the culture on PANI-Scl2 was able to induce significant changes in the gene expression profile of hiPSC-CMs. The increase in KCNJ2 was previously reported to improve ion channel maturity level, which reduces fluctuation of I_f[100]. The significant increase in HCN4 has been associated to pacemaker population in the heart although further validation is required[101,423]. Finally, of the structural protein (MYL2, MYH6)-related markers, MYL2 showed significant upregulation. Some studies reported that MYL2 expression can be used to categorisedchamber specific hiPSC-CMs[418,424]. MYH6 (also known as α-MHC) demonstrated a significant increase in hiPSC-CMs cultured on PANI-Scl2 scaffold. Although the MYH6/MYH7 ratio did not change significantly, this increase in MYH6 could indicate higher maturation in the hiPSC-CMs cultured on PANI-Scl2[425].

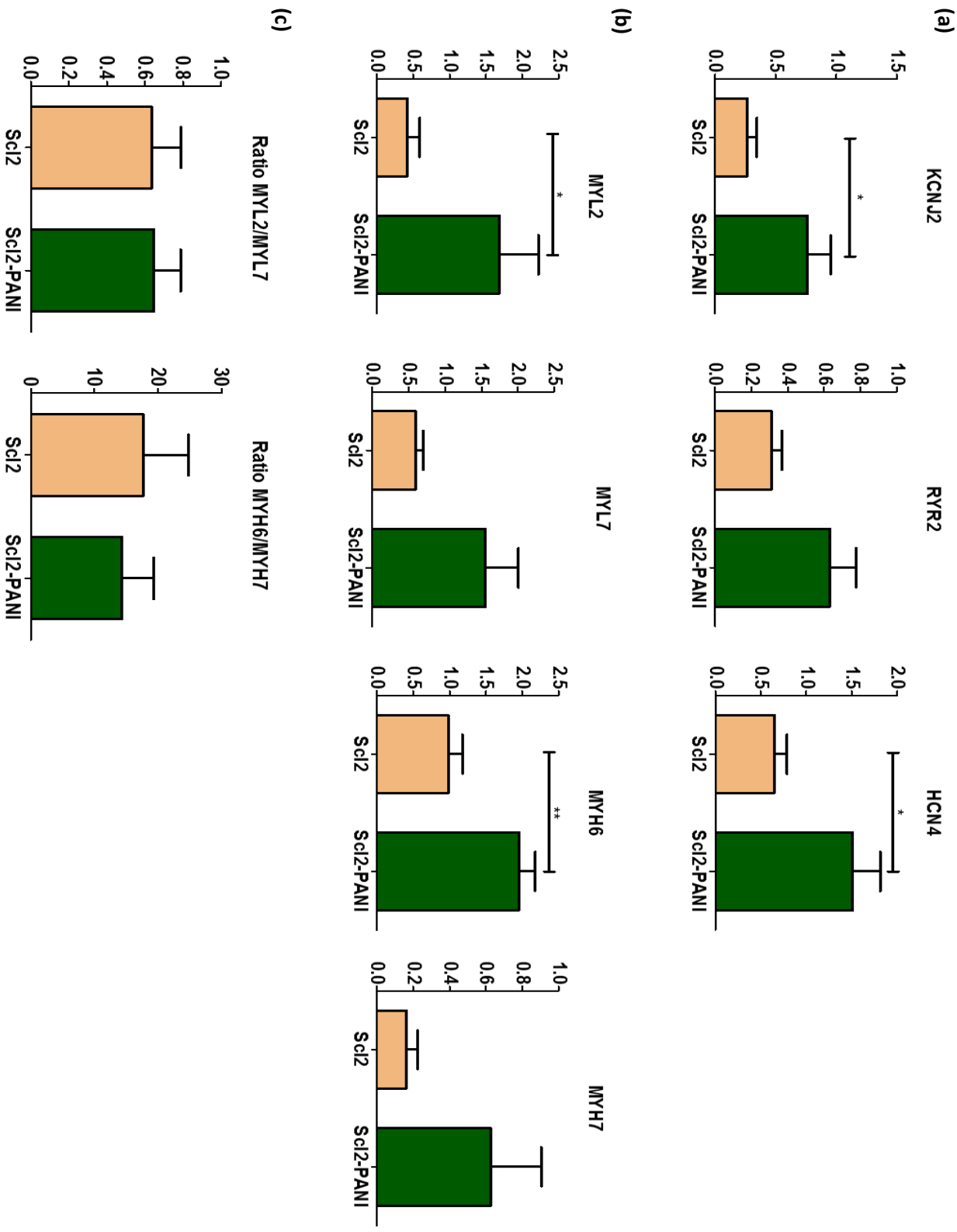

Figure 33: Gene expression profile analysis by RT-qPCR *showing a) upregulated level of KCNJ2, RYR2 and HCN4 of hiPSC-CMs cultured on PANI-Scl2 compared to Scl2, b) upregulated*

*expression of MYL2, MYL7, MYH6, MYH7 in PANI-Scl2 compared to Scl2. c) Ratio of cardiogenic markers related to cardiac development markers. All analyses were conducted after 7 days of in vitro culture. Values were normalised to day 0 before plating. Data represents mean values determined in three independent experiments ± SEM. N = 8. (Student t-Test, *p < 0.05)*

An increase of KNCJ2 and RYR2 was observed, which may point to a modulation of calcium homeostasis. To delve deeper in this matter, calcium handling was determined using optical mapping. Calcium handling has previously shown a direct link to contraction and force generation[34,35]. Therefore, hiPSC-CMs were loaded with an intracellular calcium sensitive dye, fluo4-AM, to visualise the changes in cytosolic calcium under electrical field stimulation at 1 Hz, and fluorescence profiles recorded. All traces were analysed with a custom MatLab® code. A representative trace is shown in ***Figure 34a***. As depicted on ***Figure 34b***, analysis showed no significant difference in amplitude (F/F_0) between hiPSC-CMs cultured on Scl2 and PANI-Scl2 at day 7. For calcium transient kinetics, hiPSC-CMs cultured on PANI-Scl2 for 7 days showed a significant increase in Tp, T_{50}, T_{90}. hiPSC-CMs cultured on Scl2 exhibited Tp = 29.50 ± 3.3 ms, T_{50} = 68 ± 8.9 ms, T_{90} = 110 ± 16.72 ms, while those cultured on PANI-Scl2 demonstrated Tp = 35.5 ± 5.2 ms, T_{50} = 110 ± 8.1 ms, T_{90} = 190.5 ± 9.5 ms, giving a proof of a longer calcium cycling, compared to hiPSC-CMs cultured on Scl2. This demonstrates development of the calcium transient towards that resembling adult CMs. This is the first time an electrophysiological change of hiPSC-CMs cultured on a conductive polymer is shown and consequently, requires further mechanistic studies.

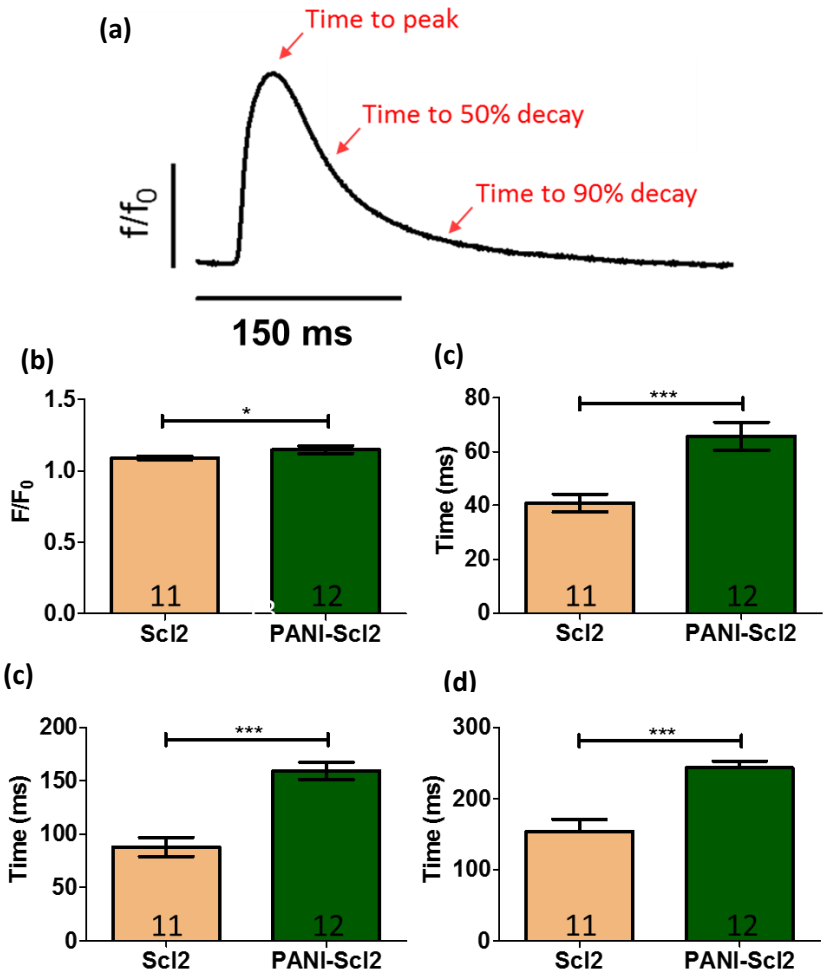

Figure 34: Optical mapping of intracellular Ca^{2+} cycling in hiPSC-CMs loaded with calcium sensitive dye Fluo4-AM. *a) Representative trace of Ca^{2+} transient. Ca^{2+} transient parameters were as follows: b) Ca^{2+} transient amplitude, c) time to Ca^{2+} transient peak, d) time to 50% decay and e) time to 90% decay. All data were analysed using a custom MatLab® code. Data represents mean values determined in independent experiments ± SEM. Number indicated on the bar graph shows number of independent experiments.* (Student t-Test, *p < 0.05)

To further assess the electrophysiological function of the foams on myocardium, a multi electrode array (MEA) was set up, validated and performed using a myocardial slice model of healthy and diseased tissue. The setup, on 64 (8x8) arrays with 100 µm resolution and 700 µm spacing, allowed the measurement of conduction velocity (CV). Viable rat myocardium slices were prepared according to Watson *et al*[332]. Next, optimisation of diseased myocardial slice was initiated by preparing a healthy rat myocardial slice and then cryoinjured using a dry ice-cold metal spatula. The representative recording screen is shown in ***Figure 35a.*** Representative images of the MEA setup, shown in ***Figure 35b***, with viable healthy rat myocardium slice (i) and cryo injury

rat myocardial slice (ii) were taken using a digital camera. ***Figure 35a***(iii) shows a red dotted line demonstrating an area of dead tissue induced by the cryo-injury, which visually confirmed the presence of the injury. Next, CV was measured by MEA on the healthy slice under point stimulation at 1 Hz. The heatmap was produced using a custom MatLab® code (***Figure 35c)*** for longitudinal and transverse electrical propagation, relative to myocardial fibre direction. To confirm the viability of the cardiac injury model, CV was measured on the cryoinjured myocardial slice. The heatmap demonstrated a significant difference from the healthy myocardial slice (***Figure 35c),*** where the electrical propagation was observed in a full area of the MEA dish as compared to half area on the cryoinjured myocardial slice (***Figure 35d***). Therefore, this indicates the electrical propagation was blocked by the cryo-induced injury and proves the success of this technique. There is a limitation posed by the analysis of the cryo-injured samples, due to the electrical signal propagation which observed only half of the MEA dish. To further validate this calculation method, the same analysis was repeated to calculate the healthy rat myocardial slice's CV to observe if there is a difference arising from the calculation method. As shown in ***Figure 35e***, the CV was calculated on healthy myocardial rat slices with two different methods; full area and half area, demonstrating no significant difference on both (i) longitudinal and (ii) transverse electrical propagation relative to myocardial fibre direction. Therefore, this validates that cryo-injury technique resulted in a dead area tissue that can be visually observed, and the analysis technique of MEA is valid for both healthy and cryoinjured ventricular myocardial slices.

(a)

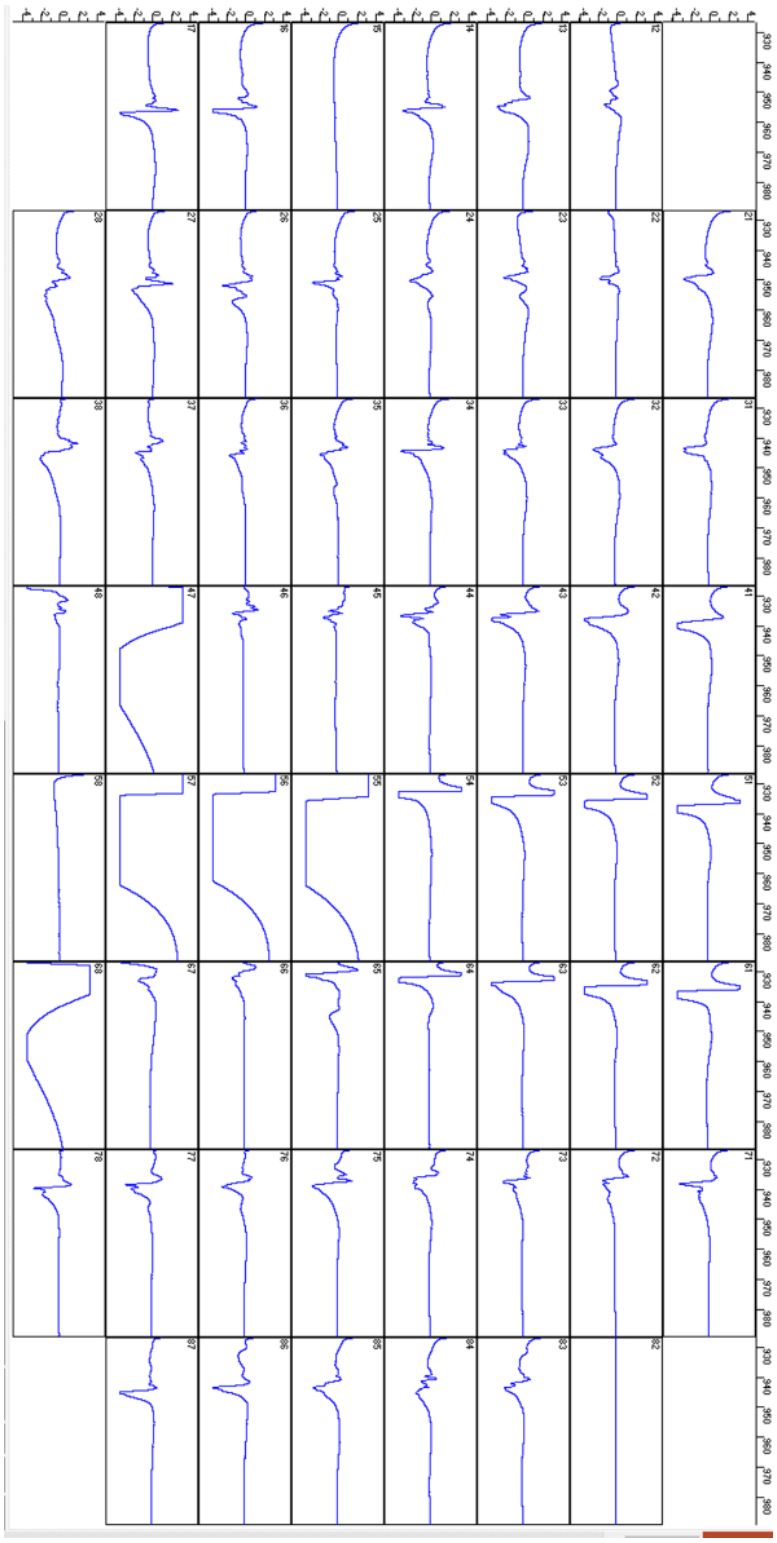

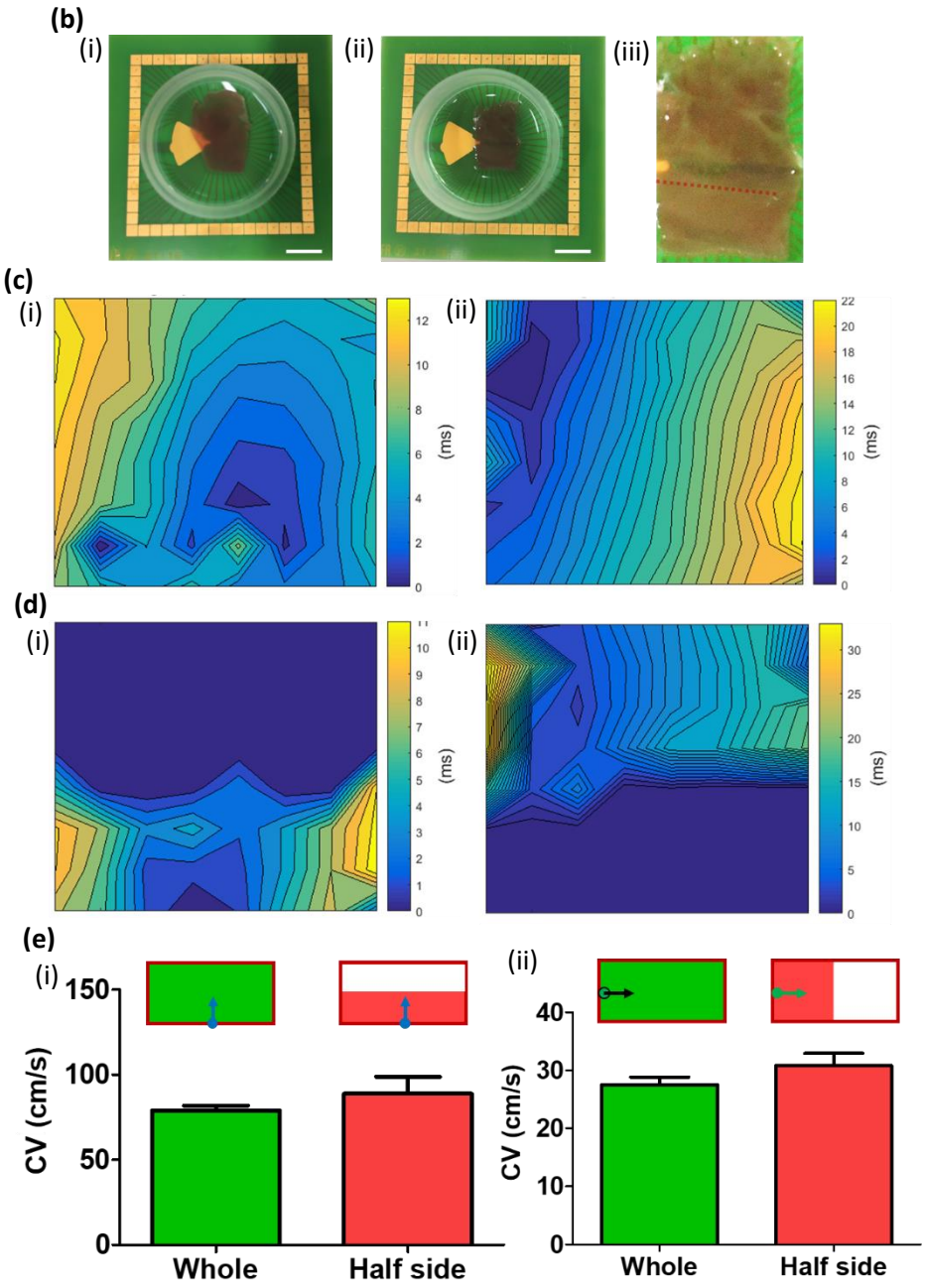

Figure 35: Validation of multiarray electrode array (MEA) on healthy and cryo-injury model in viable rat ventricular myocardium slice. *All work was carried out in accordance to the Animals (Scientific Procedures) Act 1986 and the EU Directive 2010/63/EU. a) Representative image of multielectrode array recording screen using MC_Rack software. b) Representative images of (i) healthy rat myocardial slice and (ii) injured rat myocardial slice on an MEA dish (Scale bar: 0.75 cm). (iii) zoom-in image of cryoinjured rat myocardial slice (Scale bar: 0.1875 cm). All visualised using a camera. c) Representative conduction velocity heatmaps from healthy rat*

*myocardial slices (control), with electrical propagation longitudinal (i) and transverse (ii) relative to myocardial fibre direction. d) Representative conduction velocity heatmaps from cryo-induced injury rat myocardial slices, with electrical propagation longitudinal (i) and transverse (ii) relative to myocardial fibre direction. e) Bar graph shows a conduction velocity of healthy rat myocardial slice with two different analysed areas on electrical propagation (i) longitudinal and (ii) transverse relative to myocardial fibre direction. The illustration indicates the analysis area. (n = 15, N = biological preparation = 4). (Student t-Test, *p < 0.05)*

Once the method had been set up, the effect of the conductive PANI-Scl2 foam on the CV of the myocardial slice was assessed. To further investigate acute biocompatibility of the foams on the myocardium, Scl2 and PANI-Scl2 were applied onto healthy rat myocardial slice. This result showed no detrimental effect in conduction velocity of healthy rat myocardial slice in both longitudinal and transverse conduction velocity relative to myocardial fibre as expected (***Figure 36a***), demonstrating optimal biocompatibility of both polymer foams on healthy myocardial slice.

The assessment continued to determine the effect of each collagen mimetic foam (non-conductive and conductive form) under pathological conditions. Cryoinjured myocardial rat slices were assessed with an application of both foams. As shown in ***Figure 36b-c***, the cryoinjured slices showed around 40% reduction in CV, on both longitudinal and transverse electrical propagation. Scl2 foam was initially applied as a control condition, and no further detrimental change in CV was detected. Next, PANI-Scl2 was immediately applied, revealing a significant increase of 33%, compared to cryo-injury model on longitudinal CV, where the increase in transversal conduction was observed at 42%, compared to cryo-injury model. PANI-Scl2 application induced a recovery of cryoinjured rat myocardial slice's CV to 78% and 90% (longitudinal and transverse CV), compared to healthy rat myocardium slice's CV as shown in ***Figure 36b***. Therefore, attaching the PANI-Scl2 on injured myocardial slices has an effect on CV, whereas the Scl2, an insulating material, did not interfere with the cardiac electrical activity. Currently, the underlying mechanism involved in this improvement is not known but this result demonstrates the exciting finding that electroactive property of the scaffold alone is the key contributor to the observed changes.

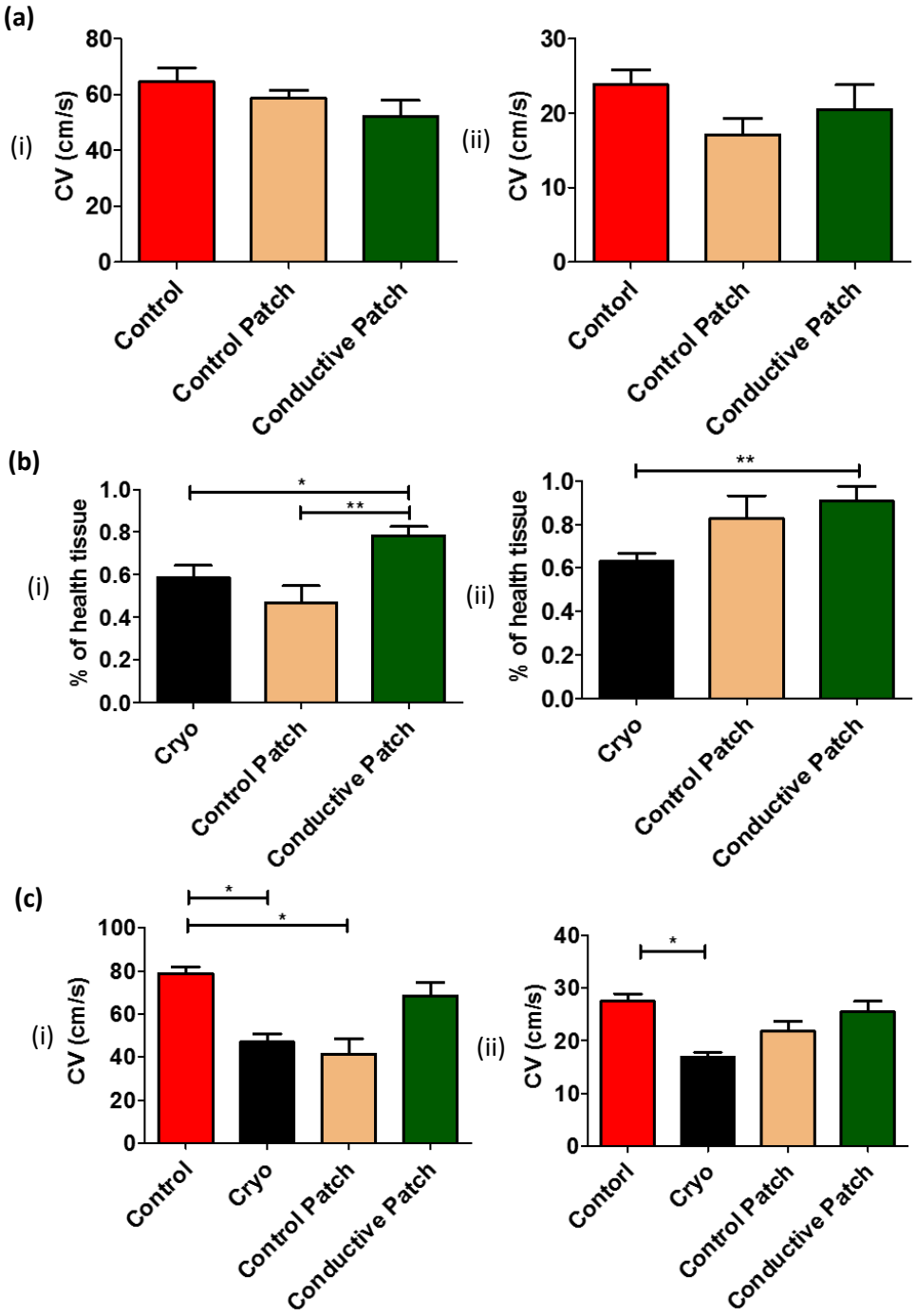

Figure 36: In vitro rat myocardial slice evaluation of the PANI-Scl2 and Scl2 foams. Electrophysiological properties of cardiac slices measured by MEA system. *Conduction velocity (CV) in healthy and cryo induced injury rat myocardial slice. a) CV of healthy rat myocardial slice and application of Scl2 and PANI-Scl2 foams. b) Normalised CV to healthy rat myocardial slice of cryo injury rat myocardial slice before and after foams application, showed as a percentage of healthy control. c) CV to healthy rat myocardial slice of cryo injury rat myocardial*

*slice before and after foams application, showed as a percentage of healthy control. a-c data shows the value respect to electrical propagation longitudinal (i) and transverse (ii) relative to myocardial fibre direction. n = number of slices ≤ 8 N = biological preparations = 4. (one-way ANOVA, *p < 0.05)*

5.4 Discussion and conclusion

After MI onset, a loss of CM results in a fibrotic scar which creates a noncontractile and alters conduction properties, including complete blockage of electrical signal propagation within the scar region and/or delayed impulse propagation across the scar[398]. Stiffening of the scarred area occurs, decreasing contraction efficiency and increasing the preload to the heart. The loss of mechanically dynamic contractility and electrical conduction contributes to ventricular dysfunction and arrhythmias. Ventricular dysfunction and arrhythmias after cardiovascular diseases including MI commonly develop HF, which is the largest cause of mortality worldwide despite the advancements in clinical treatment and management[426]. Adult CMs lack of meaningful natural capacity to regenerate dead cardiac muscle[427], therefore, new treatment strategies are needed to prevent and/or slow down adverse remodelling and to preserve heart function. The basic requirement for a cardiac tissue construct to able to form a hospitable integration to the native tissue is to possess similar anisotropic mechanical properties – especially stiffness and flexibility – to myocardium, to contain high densities of cells, be electrically conductive – to modulate conduction velocity, thereby increasing myocardium synchrony, and have the ability to chemically tether bioactive molecules for clinical application. These basic requirements were all attempted. To date, there is no such biomaterials that can deliver these properties simultaneously.

Previously, Stevens group developed a conductive cardiac patch, PANI-chitosan with stable electronic properties. It was shown to partially improve the CV across the infarct region in an MI rat model[230]. However, the mechanical mismatch between the materials (6.73 ±1.1 MPa) and the native human myocardium (0.02–0.50 MPa)[183,428–430] could harmfully affects the harmonious integration. Recent attempt from Stevens group created a next-generation cardiac patch fabricated by using laser ablation. This allowed the ability to control and tune the effective bulk stiffness and anisotropy of auxetic, providing physiologically mechanical support to the myocardium. However, the auxetic conductive patch caused no negative effect or improvement on the healthy and MI hearts electrophysiology.

Here, the cardiac conductive foam was developed that is electrically active and stable with mechanical properties matching those of the native human myocardium. The conductive foam has a triple helical structure mimicking native collagen with physiological relevant mechanical properties and could utilise the native electrical signals to synchronise the rhythm without disrupting the flow[161]. Its electrical properties showed little reduction over a period of 7 days in a physiological buffer, providing a stable electronic property. This stable electrical property may indicate little dopant leakage from the patch (which might increase toxicity). To confirm this, the

application of the conductive collagen mimetic foam, PANI-Scl2, was performed *in vitro,* showing optimal biocompatibility. Long-term culture of hiPSC-CMs on the conductive foams improves their ion channels and cardiac structural genes expression, as well as promotes a development of calcium handling towards that of isolated adult CMs. Further application of the foams in *in vitro* studies improved CV of cryoinjured rat myocardial slices without altering conduction velocity in healthy rat myocardial slice. Therefore, the cardiac conductive foam has the capacity to mechanically and electrically support the integration of hiPSC-CMs onto the myocardium.

Mechanically, the Frank–Starling-mechanism determines the degree of myocardium contraction and stretch, maintaining a natural decompensation mechanism to prevent the heart from nonphysiological stress. PANI-Scl2 showed physiological relevant dynamic stiffness (Storage modulus) at 71.16 kPa, increased from the relatively low Scl2, which has storage modulus similar to that of brain (around 1 kPa)[431]. The increase in stiffness of PANI-Scl2 is due to the blend of relatively low stiffness Scl2 foam to the conductive polymer, PANI, that has high stiffness, on the MPa range[231]. Loss modulus shows that with an increase in frequency, more force is required to deform the construct (frequency dependency), mimicking the behaviour of the native myocardium. Therefore, PANI-Scl2 demonstrates physiological relevant dynamic mechanical properties as well as exhibits frequency dependent modulus in a similar manner as the native tissue, supporting natural beating of the cardiac rhythm.

A lower protonation level of oxidised amine and protonated imine in conjunction with the loss of dopant in PANI-Scl2 contribute to the increase in its resistance. This has been confirmed by XPS, with lower protonated imine and amine peaks, as well as the visual transition of colour from green to black. The result confirms that this system using phytic acid as a crosslinking dopant leads to the PANI-Scl2 foam that has a relatively stable conductive property under *in vitro* conditions over prolonged incubations (7 days vs 1 day[321,432]). The PANI-Scl2 foam showed a superior stability over other PANI-based biomaterials. After exposure to *in vitro* condition, PANI-Scl2 exhibits a large magnitude positive difference in surface resistivity[230,231,321,433]. Biological applications that require prolonged stimulations would benefit from the cells loaded on the foam to have enough integration time[164,165] as a result of the extending lifetime of PANI-Scl2 in the conductive emeraldine form.

Next, biological experiments were conducted using hiPSC-CMs and rat myocardial slices to assess the foams' influence on CM models *in vitro* . hiPSC-CMs are a compelling *in vitro* model of human cardiac regeneration, as they represent an essentially inexhaustible source of committed human CMs and can be potentially patient-specific. Structure and function

characterised on this thesis show an improvement of hiPSC-CMs towards an adult-like phenotype. PANI-Scl2 demonstrated a good biocompatibility with a slight reduction of metabolic activity, but a stable cell number throughout the experiment. This indicates that PANI-Scl2 can be used to maintain and culture a high density of hiPSC-CMs (10 million cells). Structurally, the hiPSC-CMs showed an improvement of α-actinin striations (2.1 – 2.3 μm), developing towards adult CMs sarcomere spacing (2.0 – 2.2 μm), whereas hiPSC-CMs demonstrate a spacing around 1.6 μm[434]. The sarcomere length–tension relationship for cardiac muscle determines tension and force generation from the degree of cross-bridge between thick and think filament. Although hiPSC-CMs cultured on PANI-Scl2 (sarcomere length: 2.33 μm) may have a little reduction in force generation compared to hiPSC-CMs cultured on Scl2 due to the Frank-Starling mechanism, PANI-Scl2 supplies additional benefits derived from its properties, making it more similar to the physiological environment at several levels, including conductivity and mechanics as already outlined[408]. This, therefore, shows a significant improvement from previous reports on hiPSC-CMs, which have reported a sarcomeric length around 1.6 μm[435]. Functionally, calcium handling in hiPSC-CMs exhibit many different characteristics compared to adult human CMs. The most prominent difference lies in the Ca^{2+} recruitment mechanism. Immature CMs rely on trans-sarcolemmal Ca^{2+} influx and IP_3R-mediated Ca^{2+} release, while mature CMs rely on RyR-mediated Ca^{2+} release with well-developed T-tubular system and coupling between RyR and L-type Ca^{2+} channels. hiPSC-CMs cultured on PANI-Scl2 showed a higher expression of RyR compared to hiPSC-CMs cultured on Scl2, which may point towards a more developed Ca-handling machinery. The KCNJ2 ion channel is essential for generation of I_{K1} current and is responsible for stabilising the resting membrane potential. Low expression of this ion channel has been previously linked to the spontaneous beating characteristic of hiPSC-CMs[99]. Upregulation of this RNA expression found in hiPSC-CMs cultured on PANI-Scl2 indicates a higher maturation level of this potassium channel hence hiPSC-CM maturation upon stimulation[436]. Overexpression of this gene resulted in no spontaneous beating characteristic, as found in adult human CMs. On the other hand, upregulation of HCN4 indicates that a higher proportion of hiPSC-CMs could have significantly larger I_f currents, characteristic of cardiac pacemaker regions[100]. This gene expression profile, with greater abundance of working and pacemaker gene expression, is more representative of the native myocardium. The increased expression indicates that the aforementioned currents are increasingly present in the hiPSC-CMs cultured on PANI-Scl2. They would therefore exhibit a electrophysiologically more mature phenotype compared to hiPSC-CMs cultured on Scl2. Next, the PANI-Scl2 prolongs calcium kinetic of hiPSC-CMs by increasing T_p, T_{50} and T_{90} although the underlying mechanism has not been yet elucidated. The prolongation of

calcium kinetics indicates ineffective CICR mechanism. This could be caused by reduced sequestration of intracellular calcium by SR, resulting in less Ca^{2+} SR available for the next contraction. This immature calcium handling characteristic has been observed in early foetal CMs[437] and disease phenotypes[438]. Altogether, the gene expression profile and calcium handling show higher maturation of hiPSC-CMs cultured on PANI-Scl2, compared to its non-conductive counterpart, Scl2. Cardiac structural markers could predict a higher level of these contractile proteins in hiPSC-CMs, which can be linked to force generation - an important function of CMs. Indeed, MYL2 and MYH6 structural cardiac markers showed significantly upregulation for hiPSC-CMs cultured on PANI-Scl2, compared to those cultured on Scl2. This could predict a higher level of these contractile proteins in hiPSC-CMs which can link to force generation. Additionally, MYL7 and MYH7 showed no significant differences between the two culture conditions. Finally, the MYL2/MYL7 ratio calculated showed an insignificant difference between hiPSC-CMs cultured on both foams. This also showed no difference in the hiPSC-CM sub-population. Similarly, MYH6/MYH7 ratio also showed no significant difference on hiPSC-CMs cultured on Scl2 or PANI-Scl2. Altogether, hiPSC-CMs cultured on Scl2 showed a more mature electrophysiological phenotype and a trend toward structural maturation in gene expression. Conclusively, therefore, hiPSC-CMs showed a large improvement in sarcomere length and gene expression towards adult human CMs.

Myocardial slices enable a large-into-small-mammal xenotransplantation model. They are an intermediate model as they retain native structure, physiology and function of the myocardium. They can be produced from various species including human, providing an *in vitro* model for translational cardiovascular research. However, their uses are limited to acute time points since long term studies are debatable, partly due to the non-physiological culture conditions required *in vitro*. The foams in an *in vitro* model were further characterised to explore the effect of the cardiac foams on myocardial ultrathin slices. The foams showed no detrimental effect on healthy rat myocardial slice. This means when the scaffold is implanted, the healthy tissue around scar region would not be affected by the foam. An *in vitro* cardiac injury model was validated by using cryoinjured rat myocardial slices. A complete impediment of electrical propagation was observed in the injury model. This model showed a significant reduction in CV on infarcted border zone (IBZ), as previously reported, due to a injury-induced uncoupling of the gap junction occuring after MI and/or damage onset[22,23]. In an *in vitro* model, the PANI-Scl2 was applied on the healthy, IBZ and scar region. The recovery of CV showed to be more than 80% compared to native healthy slice, demonstrating a significant improvement and a strong acute effect of PANI-Scl2 foam on cryoinjured myocardial slice. The enhancement of CV after MI has been showed to produce more

homogeneous IBZ scarring and reduce arrhythmia susceptibility[398]. This may represent an important tissue-engineering advancement and a novel treatment strategy that could improve myocardial recovery and reduce late post-MI arrhythmic risk, although re-entry arrhythmias induced by the conductive patch need further characterisation. All in all, these findings suggest that this novel conductive polymer, PANI-Scl2, improved coordinated heart beating and can deliver more mature hiPSC-CMs in a clinically large format as well as enhanced conduction velocity in the infarct areas, hence, improving cardiac function.

Conductive biomaterials have been used to repair and/or stabilise the damaged area of the heart. Current techniques used to introduce conductive biomaterials involve the uses of carbon-[440–443,390] and metal-based[444] and conductive polymers[214,215] by co-polymerisation, blending and chemical and physical crosslinking. However, physiological relevant properties have been ignored especially physical cues that have been showed to induce diseased state of the heart[445]. *In vitro* study of stem cells has been limitedly conducted and there is no evidence of clinical improvement to date. Park *et al.* speculated that reactive oxygen species in the MI areas induce the cells to undergo apoptosis. His group introduced graphene oxide-based materials that showed to improve the survival rate of MSCs, demonstrating that conductive materials might have a protective property against reactive oxygen species. Recent study conducted by Tan *et al.* showed a limited improvement of hiPSC-CMs towards adult CMs using electrically conductive silicon nanowires[446].

Although this preliminary study has some limitations, the result showed a successful fabrication of physiologically relevant conductive composite polymer with the capacity to support hiPSC-CMs activities. An *in vitro* model was performed to study acute effects of the conductive PANI-Scl2 foam. This shows a promising initial finding, although how the conductive patch would perform in a long-term *in vivo* model has not been firmly established. The conductive polymer could have increased impulse propagation in the damaged region similarly to the increase found in the *in vitro* model. Importantly, there is a need to study the underlying mechanisms.

In summary, this chapter has shown that the immobilisation of phytic acid in the system enhanced electroactive stability under physiologically relevant environments. The conductive foam maintained its relatively low surface resistivity and electrochemistry over a week of incubation in cell culture media. Dynamic mechanical properties were demonstrated to be similar to the adult heart. *In vitro* biocompatibility with hiPSC-CMs was shown, with an improvement of ion channel and cardiac structural genes expression, sarcomeric length and enhanced calcium handling, towards those of adult CMs. *The in vitro* cardiac model revealed new biological insights

into the interaction between the novel conductive mimetic collagen and myocardial tissue. An interesting observation was the effect of the conductive foam on the CV of the rat myocardial slice, maintaining its CV in healthy myocardium, while improving CV in damaged myocardial slice. The fundamental mechanism that provides these beneficial results found in this chapter must be explored in the future. The stability of this conductive foam in the conductive state, its ability to provide mechanical and physiological support as well as its positive effect on cardiac electrophysiology recreates a new standard for the cardiac patch design. Significantly, this study presents a robust conductive construct that, because of its biocompatibility, its improving hiPSC-CM gene expression *in vitro*, its electronic stability and physiological mechanics, could potentiate their applications in the cell-biomaterial interface to explore the role of conductive biomaterials in electro responsive tissues, leading to novel cardiac regeneration design and development.

Chapter 6

Conclusion and future perspectives

6.1 Highlights

- Compliant substrate stiffness to that of the native environment enhances hiPSC-CM differentiation and function
- A combination of 3D shape and stiffness is able to significantly modulate a set of hiPSC-CMs features, leading to enhanced fit-for-purpose phenotypic control
- Novel composite conductive polymer scaffolds using PANI-Scl2, improve myocardial *in vitro* (hiPSC-CM and tissue slice) functionality

6.2 Conclusion

Cardiovascular diseases often lead to irreversible damage, progressively descending towards heart failure. Therefore, cardiac regenerative medicine aims to repair this damage and efficiently regain cardiac output. The heart is a vastly complex organ and as such, understanding the interactions between physical, biochemical and electrical cues and subsequent stem cell responses is crucial to advance the field of cardiac regenerative medicine. Current cardiac approaches using biomaterials only manipulate a single factor from the complex interplay of those present in the myocardium, hence resulting in an overly simplified system. Development of biomaterials and stem cell-derived cells for cardiac regenerative medicine requires focussed investigation in order to fully realise their translatable potential as a viable therapeutic option. In particular. improvements in biomaterial design are required for better electrophysiological integration with the of the human heart.

Overall this thesis supports the main hypothesis investigated; ‘multiple stimuli of physical cues affect hiPSC-CM function and structure’ and ‘the design and development of a next generation cardiac patch’. This aims to understand the effects of the physical interaction on modulation of hiPSC differentiation and hiPSC-CMs, observing structural and functional changes. This work highlights how stiffness affects differentiation of hiPSCs to CMs and maturation of hiPSC-CMs, both at the single cell and tissue level, and the fabrication of a novel conductive composite platform that can modulate the electrophysiology of the heart. In addition, it demonstrates the capability of different engineered constructs to dictate the properties of developing hiPSC-CMs. These findings greatly contribute to scientific understanding of human pluripotent stem cell and human CM responses to external stimulating factors. This study has opened numerous avenues for further investigation that have been detailed more specifically at the end of each chapter; the main findings will be summarised here.

As illustrated by the outline of this thesis, the work presented here started from a fundamental study aimed towards understanding how stiffness affects the development of hiPSC-CMs. This was demonstrated by improved calcium handling and force generation of hiPSC-CMs, toward adult CMs (for both calcium kinetics and increased generation), in PAAm substrate stiffness conditions similar to that in the physiologically healthy myocardium. This laid the foundational knowledge leading to the multiple-stimuli-study on single hiPSC-CMs, removing confounding cell-cell interactions, which reveals how stiffness and shape can affect the individual hiPSC-CM phenotype at both the functional and structural levels. This could be greatly beneficial for future design and fabrication of cardiac biomaterials to control hiPSC-CM fate and phenotype. Finally, the novel composite conductive biomaterial, PANI-Scl2, was fabricated in order to obtain desirable biophysical features for cardiac application.

Understanding how fundamental developmental processes are governed by biomechanical cues at different levels provides novel biological insights that can be utilised to enhance cardiac disease management. Different tissues each have their unique cellular microenvironment which can be characterised by protein composition, protein-protein interactions and the collective biomechanical properties that can be modelled using PAAm. hiPSCs have been utilised as a pluripotent model of human embryogenesis. The mechanosensitive indicators, proteins and gene expression of YAP/TAZ and POU5F1, successfully demonstrated the capability of the PAAm substrates to modulate their fates. The study highlights that the differentiation of hiPSCs to CMs was successful regardless of the underlying stiffness, however embryonic-like stiffness (560 Pa) resulted in the highest hiPSC-CM population. Nevertheless, functional analysis of hiPSC-CMs calcium handling and contractility revealed the optimum behaviours in the condition which replicate the stiffness of adult myocardium. A recent publication from Przybyla *et al.* reported that substrate stiffness of 600 Pa increases the mesoderm differentiation lineage, which could be an underlying mechanism that corroborates our findings on increasing cTnT+ cells' percentage. Macrı´-Pellizzeri *et al.* demonstrated that during EB differentiation, the population of cTnT+ cells increased on a 600 Pa substrate compared to tissue culture plastic. To date, no study have investigated the significance of elevated or reduced cTnT levels in hiPSC-CM function[376–378] and maturation.Therefore, the study emphasises the importance of stiffness of the extracellular substrate as a modulator of differentiation of hiPSC-CMs, and identifies the relevant molecular signalling pathways involved.

hiPSC-CMs exhibit high degrees of plasticity, as observed by their capacity to respond to external stimulations provided *in vitro*. However, compared with human adult CMs, they show less organized sarcomeres, softer membrane stiffness[183], shorter calcium kinetics with lower amplitude, and differential expression of cardiac-genes[107,280,403–405]. The effect of individual stimuli of stiffness[93,406,407] or shape[70,401] have been previously reported. However, this chapter demonstrated that stiffness and shape regulated different functions and structures, except for changes in cell membrane stiffness, to which both factors contribute. The recent work from Abadi *et al.* demonstrated a 3D micropatterned PDMS using adult CMs as a pattern. Although the fabrication technique has been thoroughly described, functional and structural changes were limited. Quantification of biological responses from hiPSC-CMs must be further carried out. Focusing on cell-cell interactions would provide more robust results on how physical cues affect hiPSC-CMs, especially at the single cell level. Shape has been shown to be crucial for hiPSC-CM maturation[70]. Therefore, building on the previous results in this thesis, multiple stimuli from physical cues, particularly stiffness and 3D shape, was applied using CardioArray. This novel platform is able to constrain the cell to adopt physiological dimensions of an adult CM as shown by the change in anisotropy and orientation. This single hiPSC-CMs constrained on 3D microwell provide an insight on how physical cues interacted with hiPSC-CMs, isolating them from cell-cell contact effects. This fundamental study could provide a better understanding on how shape indirectly in 3D cultures doing active work such as in EHT[447,448]. Single hiPSC-CMs have been affected by the 3D geometrical constraints and stiffness, as shown in **Table 9**. Based on results reported in this thesis, this table summarises the effect of physical cues applied to single hiPSC-CMs on function (i.e. calcium cycling, gene expression, membrane stiffness, protein expression) and structure (i.e. alignment, sarcomere, Cx).

Table 9: Summary of CardioArrays effects on individual hiPSC-CM function and structure. *Positive correlation = increase in stiffness or contrain in microwell increase mentioned function and structure. Negative correlation = increase in stiffness or contrain in microwell decrease mentioned function and structure.*

Function and structure	3D Shape	Stiffness
Directionality	• Aligned along microwell	N/A
Sarcomere	N/A	• Negative correlation
Cx-43	• Positive correlation	N/A
Membrane stiffness	• Positive correlation	• Positive correlation
MYL2-MYL7 protein	• Higher MYL2+MYL7 co-expression	N/A
Gene expression	• Higher TNNI3/TNNI1 ratio • Key component of prediction score	N/A
Calcium handling	N/A	• Amplitude: negative correlation • Kinetics: negative correlation

Together, the results from **Chapter 3** and **4** improve the understanding of how fundamental developmental processes are regulated via mechanical cues at single cell and tissue level. This knowledge provides novel biological insights that can be exploited to enhance therapeutically and clinically relevant hiPSC-CM applications. Furthermore, a natural progression is that this system can be applied to other cell types where maturity and shape are similarly closely related and translate to multicellularity *in vitro* models for developmental and clinical studies[39].

The summation of knowledge gained from **Chapter 3** and **4** in this thesis confirm the importance of stiffness and 3D shape to hiPSC-CM phenotype, making these properties of foundational importance while designing cardiac biomaterials. Importantly, electrical signal have shown a positive impact on the hiPSC-CM's function, structure and gene expression[449]. Altogether, the fabrication of novel composite PANI-Scl2 constitutes a significant advance from previously reported studies given their capacity to match physiological features of the myocardium[230,231]. PANI-Scl2 has superior electronic stability, physiologically relevant stiffness, high porosity, biocompatibility and is structurally similar to native ECM (triple helix). PANI-Scl2 based materials upregulated hiPSC-CM gene expression (MYL2, MYL7, MYH6, MYH7, RyR, KNCJ2 and HCN4) and abbreviated calcium kinetics *in vitro*. Results from the *ex vivo* study on the application of PANI-Scl2 with viable ventricular myocardial slices showed no detrimental effect on healthy tissue. Importantly, after cryo injury, CV of the cardiac slices was reduced to about 50% as compared to that of healthy tissue. The scaffold acutely regained CV to more than 80% compared to native tissue. This may represent an important tissue-engineering advantage and a novel therapeutic strategy that could improve myocardial recovery and reduce late post-MI arrhythmic risk.

Scientific competition is generally healthy in accelerating cardiac regeneration and repair towards clinical uses. Various approaches have attempted to tackle and/or create new clinical therapies for patients. The table below lists some on-going research that shares the same goal as this thesis, that is using conduvtive polymer as a regenerative approach.

Technique	Advantage	Disadvantage	Ref.
Organ transplant	• Gold standard since it regains majority of the circulation function	• Life-long immunosuppressant medication • Limited availability	450,451
LVAD and electromechanical device	• Use as a bridge-to-transplant or destiny therapy to increase blood flow to the body • Short-waiting time • Immediate improvement in quality of life	• Complications includes thrombosis, GI bleeding, infection and right ventricular failures	452,453
Xenotransplant	• Shorter waiting lists • Comparable function organ	• Disease transmission • Risk of shorter life span of the organ • High rejection rate. Potential reduction	454–458

	• Recent research on humanised pig could mitigate current limitation especially rejection rate	with latest research on pig • Ethical issue	
Cell-based therapy	• Autologous therapy • Larger scale treatment • Personalised treatment	• Expensive • Immunological responses • Migration and homing • Risk associated with tumorigenesis	223–225,459–466
Secretory factors	• Activating endogenous cardiac-associated mechanisms of repair and regeneration • Extracellular vesicles contain multiple beneficial components	• Off-target issue • Delivery route could affect efficiency • Intervention efficiency largely varies • Multiple candidates proteins and non-coding RNAs	15,467–473
Cardiac reprogramming	• Endogenous cell sources in situ	• Low reprogramming efficiency (5 to 20%)	474–480

		• Incomplete maturation of the cardiomyocytes – subtype of cardiomyocytes that are generated by direct reprogramming • Possible diffusion of the genetic material after local delivery • Time of intervention is needed to determine	
Biomaterials	• Tuneable properties for biological support • Increase cells retaintion • Malleable into various forms • Easily available	• Risk of leaches • Host integration issues • Could be expensive • Batch to batch variation	94,230,231,245,481–486

Finally, this thesis emphasises the importance of physical cues towards dictating hiPSC-CMs development, phenotype and maturation. This led to a successful fabrication of a conductive cardiac patch for treating MI. The knowledge gained through this thesis would contribute to the future development of hiPSC-CMs, ideal biomaterials for true cardiac regenerative treatments and personalised *in vitro* models.

6.3 Future perspective

The impact of the headways in regenerative medicine is dependent on the understanding of the underlying mechanisms in cardiac development for a better biomaterial design[487]. Although researchers have resolutely attempted to understand the underlying mechanisms of hiPSC-CM maturation and their responses to stimulation, the lack of a full picture of how fundamental processes are regulated via biomechanical, biochemical and electrical cues at both the single cell and tissue level still hinder the development of successful applications. One puzzling observation is that there are conflicting outcomes when stem cells are exposed to a combination of different stimuli (mimicking myocardial physiology) compared to the summation of responses when stem cells are exposed to the same stimuli separately. Thereupon the field of cardiac tissue engineering is still in debate over what the ideal biomaterial properties are.

There are many routes to restore a broken heart. Both biomaterials and stem cells have been partially shown to be capable of stimulating limited cardiac reparation[488]. The ultimate aim to invent the ideal biomaterial with cellular integration will enable the heart to synchronously beat mechanically and electronically. It must be able to withstand the dynamic changes of the heart, preventing further deterioration and promoting cardiac regeneration. Further studies to find an optimised combination of physical tension and electrical stimulation provided by conductive biomaterials in multicellular 3D culture is needed. One goal in the field of biomaterials and their applications in cardiac regeneration is to develop biocompatible materials that can respond to neighbouring environments and to establish an effective and reproducible method to fabricate the constructs[489]. Future work is required to be able to tailor biomechanical, biochemical and electrical milieu in a temporally and spatially precise manner. This should not only allow the biomaterials to form harmonious integration with native tissue but also allow custom tailoring for purposes, such as promoting proliferation, adhesion, differentiation or the ability to degrade. An ideal biomaterial should have the ability to precisely control multiple stimuli at different cellular levels. This would open the door to a thorough mechanistic investigation to determine how stimuli influence cell fate and their ability to integrate onto myocardium. Both individual and combined responses require thorough and well-designed studies. As mentioned previously, it would also be beneficial to combine all the different parameters considered to produce the novel scaffold for maturation of naive hiPSC-CMs. Developing such a biomaterial is challenging especially a design that combines multiple cues. For example, it can perversely influence biological properties if the biomaterial has suboptimal biomechanical and electrical properties. Bioinspired biomaterials that mimic nature can be initially developed to advance the understanding of cardiac development,

leading to unique biological properties. Composite materials of natural and synthetic polymer lend themselves to development of novel biomaterials that display optimal biochemical, mechanical and humoral properties, taking advantage of both materials' properties. Understanding in the interactions would reduce potential complexity in employing the biomaterials in the body. The design process could exploit the current advancement in a predictive manner using computational simulations and machine learning[490,491]. This can reduce development time and increase success rate.

The current status of hiPSC-CMs maturity limits their use in clinical settings[492]. Although the promise of their application to medicine is slowly starting to be fulfilled, and preliminary initiatives are slowly yielding encouraging results, lack of sufficient maturity of hiPSC-derived cells is a severe concern in order to achieve faithful, adult-like functionality. Current isolated cues provided as seen in previous studies were performed in a manner that might be affected by cell-cell interactions. These conventional platforms result in drastic environmental and functional variance, which has been amplified by the absence of essential population-wide organisation found in the myocardium. One of the debatable topics that might explain this functional variance is sub-population of CMs, specific protocol to generate sub-population and *in vitro* environment that, at least, recapitulates myocardium environment. To answer these questions, systematic fundamental experiments will need to be conducted, including a detailed investigation of hiPSC-CMs' responses to cues individually and in combination. This should be done to elucidate how the cells interact with the scaffolds as individual cells and multiple cells, in the forms of 3D co-culture, with non-CMs.

Testing with these different cell types, both individually and combined, would be a natural progression and increase the understanding of the effects of cell-cell interaction within the myocardium. Previous work showed the effect of endothelial cells[425,493], fibroblasts[40], neurons[494] and lymphocytes[53,68] on CM function. Additionally, one of the most relevant areas where little knowledge has been gathered regarding cardiac maturation is epigenetics. One of the most relevant areas where little knowledge has been gathered regarding cardiac maturation is epigenetics. This refers to an overview of changes in gene expression that are not manipulated by a modification of the genomic sequence. Possible techniques could utilise a wealth of gene expression modifiers, ranging from DNA methylation to non-coding RNAs, and histone post-translational modifications. Incorporation of these techniques could disclose the pathway controlling the maturation. Although histone markers (e.g. trimethylation of histone 3 on lysines 4 or 36, H3K4me3 and H3K36me3 respectively, or acetylation of histone on lysine 27, H3K27ac)

and the machinery responsible for their homeostasis have proven their importance in cardiac development and stem cell differentiation, their role in human cardiac maturation has not been explored yet. This will impact not only the capacity to generate adult hiPSC-CMs for therapeutic purposes by shifting the knowledge frontier on how maturation is epigenetically controlled, but also and importantly, to develop a new testbed for the pharmaceutical industry that is fully representative of the human adult physiology, envisioned to improve drug development efficiency and diminish risks. The complete knowledge of ECM- and cell-cell interactions would fully realise the use of hiPSC-CMs and biomaterials for cardiac applications. This, ultimately, allows the field to progress towards a realistic application of hiPSC-CMs, be it as a therapy or as an experimental platform.

It is increasingly clear that despite the significant increase in public and private investment, the number of new drugs that manage to reach the bedside successfully is quite small. This in turn decreases the treatment options for the patient since the funding has been ineficiently used, adding a dramatic personal dimension to the severe economic burden. Therefore, an efficiency boost in the process is clearly a must for the future of both the healthcare system and the pharmaceutical industry. Light has been shed on the failure of conventional models that are currently in place, which do not faithfully recapitulate the features of the mature cardiac tissue. At the *in vitro* level, either animal (HL1 or H9c2) or human cancer cells transfected with HERG potassium channels are usually employed, whereas animal models are the chosen system for in vivo validation. Notwithstanding their capacity to provide a certain amount of information, the above mentioned issues down the development/validation pipeline highlights their unsuitability to attain the efficacy and prediction capabilities that modern drug development requires, including confident replication of the adult cardiac physiology and capacity to perform in high throughput assays. In addition to this, animal research is tainted by ethical and social issues of great impact. Translation of stem cell-derived cardiomyocytes in conjunction with biomaterials to clinical use requires further optimisation of other elements, too, beyond those addressed in this dissertation, such as manufacturing constraints, storage, regulatory concerns, administration routes, and time-dependent deterioration. For example, the freeze thaw cycle has been shown to detrimentally reduce cell survival in cell-based therapy[495].

In any case, this system, presented in this thesis, provides ways for controlling the generation of clinically relevant hiPSC-CMs and may contribute to the future design of a clinically workable treatment for cardiovascular diseases.

Chapter 7

Publications and awards

List updated as of January 2019

7.1 Publications

W. Kit-Anan, M. Mazo, B. X. Wang, V. Leonardo, I. J. Pence, S. Gopal, A. Gelmi, A. Nagelkerke, M. Becce, C. Chiappini, S. E. Harding, C. M. Terracciano, M. M. Stevens. **"CardioArrays: A novel platform for the multidimensional *in vitro* manipulation of the myocyte niche"**, In preparation.

W. Kit–Anan, P.A. Parmar, I. Bardi, A. C. Moore, A. Regoutz, M.M. Mahat, M. Mazo, S.A. Watson, D.J. Payne, V. Stoichevska, Y.Y. Peng, J.A. Werkmeister, J.A.M. Ramshaw, S.E. Harding, C.M. Terracciano, M.M. Stevens. **"Conductive collagen–mimetic foams for cardiac tissue regeneration"**, In preparation.

W. Kit-Anan, V. Leonardo, M. Mazo, S. Gopal, S. E. Harding, C. M. Terracciano, M. M. Stevens. **"The role of matrix stiffness in modulating cardiac specification of human pluripotent stem cells"**, In preparation.

C. Li, J. PK Armstrong, **W. Kit-Anan**, I. J. Pence, J. L. Puetzer, S. Carreira, W. Schwarzacher, M. M. Stevens. **"Glycosylated Superparamagnetic Nanoparticle Gradients for Osteochondral Tissue Engineering"**, Biomaterials, Vol. 3, p. 24-33. 2018

A. YF. You, Mads S. Bergholt, JP. St-Pierre, **W. Kit-Anan**, I. J. Pence, A. H. Chester, M. H. Yacoub, S. Bertazzo, M. M. Stevens. **"Raman spectroscopy imaging reveals interplay between atherosclerosis and medial calcification in the human aorta"** Sci. Adv., Vol. 3, No 12, e1701156. 2017

7.2 Conferences

ISSCR 2018, Melbourne, Australia
W. Kit-Anan, M. Mazo, B. X. Wang, V. Leonardo, I. J. Pence, S. Gopal, A. Gelmi, A. Nagelkerke, M. Becce, C. Chiappini, S. E. Harding, C. M. Terracciano, M. M. Stevens.
"CardioArrays: A novel platform for the multidimensional *in vitro* manipulation of the myocyte niche." June 2018

MRS Fall Meeting 2017, Boston, USA

W. Kit–Anan, P.A. Parmar, I. Bardi, A. C. Moore, A. Regoutz, M.M. Mahat, M. Mazo, S.A. Watson, D.J. Payne, V. Stoichevska, Y.Y. Peng, J.A. Werkmeister, J.A.M. Ramshaw, S.E. Harding, C.M. Terracciano, M.M. Stevens.

"Conductive Collagen—Mimetic Foams for Cardiac Tissue Regeneration." November 2017

The 5th BHF Fellows Meeting, Queens' College, University of Cambridge, Cambridge, UK

W. Kit-Anan, V. Leonardo, M. Mazo, S. Gopal, S. E. Harding, C. M. Terracciano, M. M. Stevens.

"The Role of Matrix Stiffness in Modulating Cardiac Specification of Human Pluripotent Stem Cells." September 2017

2017 Joint Symposium BHF Centre of Research Excellence and EPSRC Centre for Mathematics-of Precision Healthcare the Heart – Models, Measurements, Medicine, Imperial College London, UK

W. Kit-Anan, V. Leonardo, M. Mazo, S. Gopal, S. E. Harding, C. M. Terracciano, M. M. Stevens.

"The Role of Matrix Stiffness in Modulating Cardiac Specification of Human Stem Cells." June 2017

The Biology of Regenerative Medicine, Wellcome Genome Campus, UK

W. Kit-Anan, V. Leonardo, M. Mazo, S. Gopal, S. E. Harding, C. M. Terracciano, M. M. Stevens.

"The Role of Matrix Stiffness in Modulating Cardiac Specification of Human Stem Cells." April 2017

Postgraduate Research Day 2017, Imperial College London, UK

W. Kit-Anan, M. Mazo, V. Leonardo, A. Gelmi, A. Nagelkerke, C. Chiappini, S. E. Harding, C. M. Terracciano, M. M. Stevens.

"Materials to mimic nature: a novel platform to manipulate the stem cell niche." March 2017

7.3 Awards & Grants

Centre of Research Excellence, The British Heart Foundation, Imperial College London and Rosetree Trust – Awarded a scholarship towards 4 years PhD programme

Travel Grant, Imperial College Trust – Awarded to assist in the cost of attending the MRS Fall Meeting 2017, Boston, USA

Armourers and Brasiers, UK – Awarded to assist in the cost of attending the MRS Fall Meeting 2017, Boston, USA and ISSCR 2018, Melbourne, Australia

TCES, UK – Awarded to assist in the cost of attending the ISSCR 2018, Melbourne, Australia

British Society for Cardiovascular Research, UK – Awarded to assist in the cost of attending the ISSCR 2018, Melbourne, Australia

City and Guilds, Imperial College London – Awarded to assist in the cost of attending the MRS Fall Meeting 2017, Boston, USA and ISSCR 2018, Melbourne, Australia

References

1. Mozaffarian, D. *et al.* Heart Disease and Stroke Statistics—2016 Update. *Circulation* **133,** 1–324 (2016).
2. Media Centre. The top 10 causes of death. *Organ. World Heal.* (2012). doi:http://www.who.int/mediacentre/factsheets/fs310/en/
3. Bergmann, O. *et al.* Evidence for cardiomyocyte renewal in humans. *Science* **324,** 98–102 (2009).
4. Buikema, J. W., Van Der Meer, P., Sluijter, J. P. G. & Domian, I. J. Concise review: Engineering myocardial tissue: the convergence of stem cells biology and tissue engineering technology. *Stem Cells* **31,** 2587–98 (2013).
5. Oyama, K., El-Nachef, D. & MacLellan, W. R. Regeneration potential of adult cardiac myocytes. *Cell Res.* **23,** 978–9 (2013).
6. Haubner, B. J. *et al.* Functional Recovery of a Human Neonatal Heart After Severe Myocardial Infarction. *Circ. Res.* **118,** 216–21 (2016).
7. Kajstura, J., Rota, M., Hosoda, T., Anversa, P. & Leri, A. Response to Bergmann et al: Carbon 14 Birth Dating of Human Cardiomyocytes. *Circ. Res.* **110,** 1–8 (2012).
8. World Health Organization. *World Health Statistic 2018*. (World Health Organization, 2018).
9. Rana, M. S., Christoffels, V. M. & Moorman, A. F. M. A molecular and genetic outline of cardiac morphogenesis. *Acta Physiol.* **207,** 588–615 (2013).
10. Huang, J. *et al.* Myocardin regulates BMP10 expression and is required for heart development. *J. Clin. Invest.* **122,** 3678–91 (2012).
11. Cambier, L., Plate, M., Sucov, H. M. & Pashmforoush, M. Nkx2-5 regulates cardiac growth through modulation of Wnt signaling by R-spondin3. *Development* **141,** 2959–71 (2014).
12. Moorman et al. Development of the heart (1) formation of the cardiac chambers and arterial trunks. *Heart* **89,** 806–14 (2003).
13. Noseda, M., Peterkin, T., Simões, F. C., Patient, R. & Schneider, M. D. Cardiopoietic Factors. *Circ. Res.* **108,** 129–152 (2011).
14. Engels, M. C. *et al.* Insulin-like growth factor promotes cardiac lineage induction in vitro by selective expansion of early mesoderm. *Stem Cells* **32,** 1493–1502 (2014).
15. Xin, M. *et al.* Hippo pathway effector Yap promotes cardiac regeneration. *Proc. Natl. Acad. Sci. U. S. A.* **110,** 13839–44 (2013).

16. Roche, C. *et al.* Tarsal Shape, Size, and Articulating Surface Morphology in Adolescent Surgically Treated Clubfoot and Their Contralateral Normal Foot. *J. Pediatr. Orthop.* **26,** 329–335 (2006).
17. Jacot, J. G., Martin, J. C. & Hunt, D. L. Mechanobiology of cardiomyocyte development. *J. Biomech.* **43,** 93–98 (2010).
18. Prakash, Y. S., Cody, M. J., Housmans, P. R., Hannon, J. D. & Sieck, G. C. Comparison of cross-bridge cycling kinetics in neonatal vs. adult rat ventricular muscle. *J. Muscle Res. Cell Motil.* **20,** 717–723 (1999).
19. Krieg, M. *et al.* Tensile forces govern germ-layer organization in zebrafish. *Nat. Cell Biol.* **10,** 429–36 (2008).
20. Kane, C. & Terracciano, C. M. N. Concise Review: Criteria for Chamber-Specific Categorization of Human Cardiac Myocytes Derived from Pluripotent Stem Cells. *Stem Cells* **35,** 1881–1897 (2017).
21. Peter, A. K., Bjerke, M. A. & Leinwand, L. A. Biology of the cardiac myocyte in heart disease. *Mol. Biol. Cell* **27,** 2149–2160 (2016).
22. Lockhart, M., Wirrig, E., Phelps, A. & Wessels, A. Extracellular matrix and heart development. *Birth Defects Res. Part A - Clin. Mol. Teratol.* **91,** 535–550 (2011).
23. Fan, D., Takawale, A., Lee, J. & Kassiri, Z. Cardiac fibroblasts, fibrosis and extracellular matrix remodeling in heart disease. *Fibrogenesis Tissue Repair* **5,** 15 (2012).
24. Kong, P., Christia, P. & Frangogiannis, N. G. The pathogenesis of cardiac fibrosis. *Cell. Mol. Life Sci.* **71,** 549–574 (2014).
25. Howard, C. M. & Baudino, T. a. Dynamic cell-cell and cell-ECM interactions in the heart. *J. Mol. Cell. Cardiol.* **70,** 19–26 (2014).
26. Kaprielian, R. R. & Severs, N. J. Dystrophin and the cardiomyocyte membrane cytoskeleton in the healthy and failing heart. *Heart Fail. Rev.* **5,** 221–38 (2000).
27. Wheeler, M. T. & McNally, E. M. Sarcoglycans in vascular smooth and striated muscle. *Trends Cardiovasc. Med.* **13,** 238–43 (2003).
28. Wang, N., Tytell, J. D. & Ingber, D. E. Mechanotransduction at a distance: Mechanically coupling the extracellular matrix with the nucleus. *Nat. Rev. Mol. Cell Biol.* **10,** 75–82 (2009).
29. Chen, C., Li, R., Ross, R. S. & Manso, A. M. Integrins and integrin-related proteins in cardiac fibrosis. *J. Mol. Cell. Cardiol.* **93,** 162–174 (2016).
30. Humphrey, J. D., Dufresne, E. R. & Schwartz, M. A. Mechanotransduction and extracellular matrix homeostasis. *Nat. Rev. Mol. Cell Biol.* **15,** 802–812 (2014).

31. Simpson, D. G., Majeski, M., Borg, T. K. & Terracio, L. Regulation of cardiac myocyte protein turnover and myofibrillar structure in vitro by specific directions of stretch. *Circ. Res.* **85,** e59–e69 (1999).
32. Ingber, D. Integrins as mechanochemical transducers. *Curr. Opin. Cell Biol.* **3,** 841–848 (1991).
33. Brancaccio, M. *et al.* Integrin signalling: The tug-of-war in heart hypertrophy. *Cardiovasc. Res.* **70,** 422–433 (2006).
34. de Tombe, P. P. *et al.* Myofilament length dependent activation. *J. Mol. Cell. Cardiol.* **48,** 851–858 (2010).
35. ALLEN, D. & KENTISH, J. The cellular basis of the length-tension relation in cardiac muscle. *J. Mol. Cell. Cardiol.* **17,** 821–840 (1985).
36. Fuchs, F. & Smith, S. H. Calcium, cross-bridges, and the Frank-Starling relationship. *News Physiol. Sci.* **16,** 5–10 (2001).
37. Tobacman, L. S. *et al.* The troponin tail domain promotes a conformational state of the thin filament that suppresses myosin activity. *J. Biol. Chem.* **277,** 27636–27642 (2002).
38. Zhou, P. & Pu, W. T. Recounting Cardiac Cellular Composition. *Circ. Res.* **118,** 368–370 (2016).
39. Wang, B., Kit-Anan, W. & Terracciano, C. Many Cells Make Life Work—Multicellularity in Stem Cell-Based Cardiac Disease Modelling. *Int. J. Mol. Sci.* **19,** 3361 (2018).
40. Cartledge, J. E. *et al.* Functional crosstalk between cardiac fibroblasts and adult cardiomyocytes by soluble mediators. *Cardiovasc. Res.* **105,** 260–70 (2015).
41. Doppler, S. A. *et al.* Cardiac fibroblasts: more than mechanical support. *J. Thorac. Dis.* **9,** S36–S51 (2017).
42. Nakaya, M. *et al.* Cardiac myofibroblast engulfment of dead cells facilitates recovery after myocardial infarction. *J. Clin. Invest.* **127,** 383–401 (2017).
43. Snider, P. *et al.* Origin of Cardiac Fibroblasts and the Role of Periostin. *Circ. Res.* **105,** 934–947 (2009).
44. Jourdan-LeSaux, C., Zhang, J. & Lindsey, M. L. Extracellular matrix roles during cardiac repair. *Life Sci.* **87,** 391–400 (2010).
45. Rajendran, P. *et al.* The vascular endothelium and human diseases. *Int. J. Biol. Sci.* **9,** 1057–1069 (2013).
46. He, L. *et al.* Preexisting endothelial cells mediate cardiac neovascularization after injury. *J. Clin. Invest.* **127,** 2968–2981 (2017).
47. Chen, Q. *et al.* Endothelial cells are progenitors of cardiac pericytes and vascular smooth

muscle cells. *Nat. Commun.* **7,** 1–13 (2016).

48. Cheung, C., Bernardo, A. S., Trotter, M. W. B., Pedersen, R. A. & Sinha, S. Generation of human vascular smooth muscle subtypes provides insight into embryological origin–dependent disease susceptibility. *Nat. Biotechnol.* **30,** 165–173 (2012).
49. White, C. I. *et al.* Cardiomyocyte and vascular smooth muscle-independent 11β-hydroxysteroid dehydrogenase 1 amplifies infarct expansion, hypertrophy, and the development of heart failure after myocardial infarction in male mice. *Endocrinology* **157,** 346–357 (2016).
50. Ardell, J. L. *et al.* Translational neurocardiology: preclinical models and cardioneural integrative aspects. *J. Physiol.* **594,** 3877–3909 (2016).
51. Gilbert, R. E., Connelly, K., Kelly, D. J., Pollock, C. A. & Krum, H. Heart failure and nephropathy: catastrophic and interrelated complications of diabetes. *Clin. J. Am. Soc. Nephrol.* **1,** 193–208 (2006).
52. Margariti, A. Peripheral neuropathy may be a potential risk of cardiovascular disease in diabetes mellitus. *Heart* **100,** 1823–1824 (2014).
53. Akar, F. G. *et al.* Dynamic changes in conduction velocity and gap junction properties during development of pacing-induced heart failure. *Am. J. Physiol. Heart Circ. Physiol.* **293,** H1223–H1230 (2007).
54. Hofmann, U. & Frantz, S. Role of lymphocytes in myocardial injury, healing, and remodeling after myocardial infarction. *Circ. Res.* **116,** 354–367 (2015).
55. Tejada, T. *et al.* IGF-1 degradation by mouse mast cell protease 4 promotes cell death and adverse cardiac remodeling days after a myocardial infarction. *Proc. Natl. Acad. Sci.* **113,** 6949–6954 (2016).
56. Marino, A. *et al.* The novel H2S donor 4-carboxy-phenyl isothiocyanate inhibits mast cell degranulation and renin release by decreasing intracellular calcium. *Br. J. Pharmacol.* **173,** 3222–3234 (2016).
57. Hulsmans, M. *et al.* Macrophages Facilitate Electrical Conduction in the Heart. *Cell* **169,** 510–522.e20 (2017).
58. Pinto, A. R. *et al.* Revisiting cardiac cellular composition. *Circ. Res.* **118,** 400–409 (2016).
59. Kume, T. Specification of arterial, venous, and lymphatic endothelial cells during embryonic development. *Histol. Histopathol.* **25,** 637–46 (2010).
60. AIRD, W. C. Spatial and temporal dynamics of the endothelium. *J. Thromb. Haemost.* **3,** 1392–1406 (2005).
61. Guerrero-Juarez, C. F. *et al.* Single-cell analysis reveals fibroblast heterogeneity and

myeloid-derived adipocyte progenitors in murine skin wounds. *Nat. Commun.* **10,** 1–17 (2019).

62. DeLaughter, D. M. *et al.* Single-Cell Resolution of Temporal Gene Expression during Heart Development. *Dev. Cell* **39,** 480–490 (2016).
63. Skelly, D. A. *et al.* Single-Cell Transcriptional Profiling Reveals Cellular Diversity and Intercommunication in the Mouse Heart. *Cell Rep.* **22,** 600–610 (2018).
64. Tourki, B. & Halade, G. Leukocyte diversity in resolving and nonresolving mechanisms of cardiac remodeling. *FASEB J.* **31,** 4226–4239 (2017).
65. Dobaczewski, M., Xia, Y., Bujak, M., Gonzalez-Quesada, C. & Frangogiannis, N. G. CCR5 Signaling Suppresses Inflammation and Reduces Adverse Remodeling of the Infarcted Heart, Mediating Recruitment of Regulatory T Cells. *Am. J. Pathol.* **176,** 2177–2187 (2010).
66. Yan, X. *et al.* Temporal dynamics of cardiac immune cell accumulation following acute myocardial infarction. *J. Mol. Cell. Cardiol.* **62,** 24–35 (2013).
67. Oh, Y. *et al.* Functional Coupling with Cardiac Muscle Promotes Maturation of hPSC-Derived Sympathetic Neurons. *Cell Stem Cell* **19,** 95–106 (2016).
68. Triposkiadis, F. *et al.* The Sympathetic Nervous System in Heart Failure. Physiology, Pathophysiology, and Clinical Implications. *J. Am. Coll. Cardiol.* **54,** 1747–1762 (2009).
69. McCain, M. L. & Parker, K. K. Mechanotransduction: the role of mechanical stress, myocyte shape, and cytoskeletal architecture on cardiac function. *Pflügers Arch. - Eur. J. Physiol.* **462,** 89–104 (2011).
70. Rao, C. *et al.* The effect of microgrooved culture substrates on calcium cycling of cardiac myocytes derived from human induced pluripotent stem cells. *Biomaterials* **34,** 2399–2411 (2013).
71. McCain, M. L., Yuan, H., Pasqualini, F. S., Campbell, P. H. & Parker, K. K. Matrix elasticity regulates the optimal cardiac myocyte shape for contractility. *Am. J. Physiol. Circ. Physiol.* **306,** H1525–H1539 (2014).
72. Geisse, N. A., Sheehy, S. P., Parker, K. K. & Geisse NA, Sheehy SP, P. K. Control of myocyte remodeling in vitro with engineered substrates. *In Vitro Cell. Dev. Biol. Anim.* **45,** 343–350 (2009).
73. Nishimura, S. *et al.* Microtubules Modulate the Stiffness of Cardiomyocytes Against Shear Stress. *Circ. Res.* **98,** 81–87 (2006).
74. Prabhu, S. D. Cytokine-Induced Modulation of Cardiac Function. *Circ. Res.* **95,** 1140–1153 (2004).

75. Israeli-Rosenberg, S., Manso, A. M., Okada, H. & Ross, R. S. Integrins and integrin-associated proteins in the cardiac myocyte. *Circ. Res.* **114,** 572–586 (2014).
76. Alibhai, F. J., Tobin, S. W., Yeganeh, A., Weisel, R. D. & Li, R.-K. Emerging roles of extracellular vesicles in cardiac repair and rejuvenation. *Am. J. Physiol. Circ. Physiol.* **315,** H733–H744 (2018).
77. Hochedlinger, K. & Plath, K. Epigenetic reprogramming and induced pluripotency. *Development* **136,** 509–523 (2009).
78. Moran, M. M. *et al. Reviews of Physiology, Biochemistry and Pharmacology, Vol. 163*. *Nat Rev Drug Discov* **10,** (Springer Berlin Heidelberg, 2012).
79. Takahashi, K. *et al.* Induction of Pluripotent Stem Cells from Adult Human Fibroblasts by Defined Factors. *Cell* **131,** 861–872 (2007).
80. Thomson, J. A. *et al.* Embryonic stem cell lines derived from human blastocysts. *Science (80-.).* **282,** 1145–1147 (1998).
81. Passier, R. *et al.* Increased cardiomyocyte differentiation from human embryonic stem cells in serum-free cultures. *Stem Cells* **23,** 772–80 (2005).
82. Ohno, Y. *et al.* Distinct iPS Cells Show Different Cardiac Differentiation Efficiency. *Stem Cells Int.* **2013,** 1–11 (2013).
83. Singh, V. K., Kalsan, M., Kumar, N., Saini, A. & Chandra, R. Induced pluripotent stem cells: applications in regenerative medicine, disease modeling, and drug discovery. *Front. Cell Dev. Biol.* **3,** 1–18 (2015).
84. Zhang, J. H. *et al.* Functional cardiomyocytes derived from human induced pluripotent stem cells. *Circ. Res.* **104,** 30–41 (2009).
85. Zwi, L. *et al.* Cardiomyocyte differentiation of human induced pluripotent stem cells. *Circulation* **120,** 1513–1523 (2009).
86. Burridge, P. W. *et al.* A universal system for highly efficient cardiac differentiation of human induced pluripotent stem cells that eliminates interline variability. *PLoS One* **6,** e18293 (2011).
87. Lian, X. *et al.* PNAS Plus: Robust cardiomyocyte differentiation from human pluripotent stem cells via temporal modulation of canonical Wnt signaling. *Proc. Natl. Acad. Sci.* **109,** E1848–E1857 (2012).
88. Du, D. T. M., Hellen, N., Kane, C. & Terracciano, C. M. N. Action potential morphology of human induced pluripotent stem cell-derived cardiomyocytes does not predict cardiac chamber specificity and is dependent on cell density. *Biophys. J.* **108,** 1–4 (2015).
89. Dias, T. P. *et al.* Biophysical study of human induced Pluripotent Stem Cell-Derived

cardiomyocyte structural maturation during long-term culture. *Biochem. Biophys. Res. Commun.* **499,** 611–617 (2018).

90. Dai, D.-F., Danoviz, M. E., Wiczer, B., Laflamme, M. A. & Tian, R. Mitochondrial Maturation in Human Pluripotent Stem Cell Derived Cardiomyocytes. *Stem Cells Int.* **2017,** 1–10 (2017).
91. Lopaschuk, G. D., Spafford, M. A. & Marsh, D. R. Glycolysis is predominant source of myocardial ATP production immediately after birth. *Am. J. Physiol. Circ. Physiol.* **261,** H1698–H1705 (1991).
92. Hanft, L. M. & McDonald, K. S. Length dependence of force generation exhibit similarities between rat cardiac myocytes and skeletal muscle fibres. *J. Physiol.* **588,** 2891–2903 (2010).
93. Wheelwright, M. *et al.* Investigation of human iPSC-derived cardiac myocyte functional maturation by single cell traction force microscopy. *PLoS One* **13,** 1–17 (2018).
94. Ronaldson-Bouchard, K. *et al.* Advanced maturation of human cardiac tissue grown from pluripotent stem cells. *Nature* **556,** 239–243 (2018).
95. Pioner, J. M. *et al.* Isolation and mechanical measurements of myofibrils from human induced pluripotent stem cell-derived cardiomyocytes. *Stem Cell Reports* **6,** 885–896 (2016).
96. Poindexter, B. J., Smith, J. R., Buja, L. M. & Bick, R. J. Calcium signaling mechanisms in dedifferentiated cardiac myocytes: Comparison with neonatal and adult cardiomyocytes. *Cell Calcium* **30,** 373–382 (2001).
97. Gros, D. B. & Jongsma, H. J. Connexins in mammalian heart function. *Bioessays* **18,** 719–730 (1996).
98. Kane, C., Couch, L., M. N. Terracciano, C. & Terracciano, C. M. N. Excitation–contraction coupling of human induced pluripotent stem cell-derived cardiomyocytes. *Front. Cell Dev. Biol.* **3,** 1–8 (2015).
99. Gélinas, R. *et al.* Characterization of a Human Induced Pluripotent Stem Cell-Derived Cardiomyocyte Model for the Study of Variant Pathogenicity: Validation of a KCNJ2 Mutation. *Circ. Cardiovasc. Genet.* **10,** 1–11 (2017).
100. Saito, Y. *et al.* Enhancement of spontaneous activity by hcn4 overexpression in mouse embryonic stem cell-derived cardiomyocytes - a possible biological pacemaker. *PLoS One* **10,** 1–16 (2015).
101. Liang, X. *et al.* HCN4 dynamically marks the first heart field and conduction system precursors. *Circ. Res.* **113,** 399–407 (2013).

102. Verkerk, A. & Wilders, R. Pacemaker Activity of the Human Sinoatrial Node: An Update on the Effects of Mutations in HCN4 on the Hyperpolarization-Activated Current. *Int. J. Mol. Sci.* **16,** 3071–3094 (2015).
103. Itzhaki, I. *et al.* Calcium handling in human induced pluripotent stem cell derived cardiomyocytes. *PLoS One* **6,** (2011).
104. Kim, H. S. *et al.* Functional expression and pharmaceutical efficacy of cardiac-specific ion channels in human embryonic stem cell-derived cardiomyocytes. *Sci. Rep.* **7,** 1–11 (2017).
105. Otsuji, T. G. *et al.* Progressive maturation in contracting cardiomyocytes derived from human embryonic stem cells: Qualitative effects on electrophysiological responses to drugs. *Stem Cell Res.* **4,** 201–213 (2010).
106. Blinova, K. *et al.* International Multisite Study of Human-Induced Pluripotent Stem Cell-Derived Cardiomyocytes for Drug Proarrhythmic Potential Assessment. *Cell Rep.* **24,** 3582–3592 (2018).
107. Hwang, H. S. *et al.* Comparable calcium handling of human iPSC-derived cardiomyocytes generated by multiple laboratories. *J. Mol. Cell. Cardiol.* **85,** 79–88 (2015).
108. Zhang, X. H. *et al.* Ca2+signaling in human induced pluripotent stem cell-derived cardiomyocytes (iPS-CM) from normal and catecholaminergic polymorphic ventricular tachycardia (CPVT)-afflicted subjects. *Cell Calcium* **54,** 57–70 (2013).
109. Kang, J., Chen, X.-L., Ji, J., Lei, Q. & Rampe, D. Ca2+ Channel Activators Reveal Differential L-Type Ca2+ Channel Pharmacology between Native and Stem Cell-Derived Cardiomyocytes. *J. Pharmacol. Exp. Ther.* **341,** 510–517 (2012).
110. Bers, D. M. Cardiac excitation-contraction coupling. *Nature* **415,** 198–205 (2002).
111. Zhang, X.-H. H. *et al.* Regionally diverse mitochondrial calcium signaling regulates spontaneous pacing in developing cardiomyocytes. *Cell Calcium* **57,** 321–336 (2015).
112. Frank, K. & Kranias, E. G. Phospholamban and cardiac contractility. *Ann. Med.* **32,** 572–578 (2000).
113. Dar, A. *et al.* Multipotent Vasculogenic Pericytes From Human Pluripotent Stem Cells Promote Recovery of Murine Ischemic Limb. *Circulation* **125,** 87–99 (2012).
114. Yokoo, N. *et al.* The effects of cardioactive drugs on cardiomyocytes derived from human induced pluripotent stem cells. *Biochem. Biophys. Res. Commun.* **387,** 482–488 (2009).
115. Signore, S. *et al.* Inositol 1, 4, 5-Trisphosphate Receptors and Human Left Ventricular Myocytes. *Circulation* **128,** 1286–1297 (2013).
116. MacMillan, D. & McCarron, J. G. The phospholipase C inhibitor U-73122 inhibits Ca2+

release from the intracellular sarcoplasmic reticulum Ca2+ store by inhibiting Ca2+ pumps in smooth muscle. *Br. J. Pharmacol.* **160,** 1295–1301 (2010).

117. Fine, M. *et al.* Human-induced pluripotent stem cell-derived cardiomyocytes for studies of cardiac ion transporters. *Am. J. Physiol. Cell Physiol.* **305,** C481-91 (2013).
118. Jacot, J. G. *et al.* Cardiac myocyte force development during differentiation and maturation. *Ann. N. Y. Acad. Sci.* **1188,** 121–7 (2010).
119. Engler, A. J. *et al.* Embryonic cardiomyocytes beat best on a matrix with heart-like elasticity: scar-like rigidity inhibits beating. *J. Cell Sci.* **121,** 3794–3802 (2008).
120. Hersch, N. *et al.* The constant beat: cardiomyocytes adapt their forces by equal contraction upon environmental stiffening. *Biol. Open* **2,** 351–361 (2013).
121. Glower, D. D. *et al.* Linearity of the Frank-Starling relationship in the intact heart: the concept of preload recruitable stroke work. *Circulation* **71,** 994–1009 (1985).
122. Rodriguez, M. L. *et al.* Measuring the Contractile Forces of Human Induced Pluripotent Stem Cell-Derived Cardiomyocytes With Arrays of Microposts. *J. Biomech. Eng.* **136,** 510051–5100510 (2014).
123. Tan, J. L. *et al.* Cells lying on a bed of microneedles: An approach to isolate mechanical force. *Proc. Natl. Acad. Sci.* **100,** 1484–1489 (2003).
124. Kita-Matsuo, H. *et al.* Lentiviral Vectors and Protocols for Creation of Stable hESC Lines for Fluorescent Tracking and Drug Resistance Selection of Cardiomyocytes. *PLoS One* **4,** e5046 (2009).
125. Brito-Martins, M., Harding, S. E. & Ali, N. N. β 1- and β 2-adrenoceptor responses in cardiomyocytes derived from human embryonic stem cells: Comparison with failing and non-failing adult human heart. *Br. J. Pharmacol.* **153,** 751–759 (2008).
126. Norstrom, A. *et al.* Molecular and pharmacological properties of human embryonic stem cell-derived cardiomyocytes. *Exp Biol Med* **231,** 1753–1762 (2006).
127. Xu, C. H., Police, S., Rao, N. & Carpenter, M. K. Characterization and enrichment of cardiomyocytes derived from human embryonic stem cells. *Circ. Res.* **91,** 501–508 (2002).
128. Pillekamp, F. *et al.* Contractile Properties of Early Human Embryonic Stem Cell-Derived Cardiomyocytes: Beta-Adrenergic Stimulation Induces Positive Chronotropy and Lusitropy but Not Inotropy. *Stem Cells Dev.* **21,** 2111–2121 (2012).
129. Reppel, M., Boettinger, C. & Hescheler, J. Cellular Physiology and Biochemistr y Biochemistry Beta-adrenergic and Muscarinic Modulation of Human Embryonic Stem Cell-derived Cardio- myocytes. (2004).

130. Mehta, A. *et al.* Pharmacological response of human cardiomyocytes derived from virus-free induced pluripotent stem cells. *Cardiovasc. Res.* **91,** 577–586 (2011).
131. Slotkin, T. A., Lau, C. & Seidler, F. J. β-Adrenergic Receptor Overexpression in the Fetal Rat: Distribution, Receptor Subtypes, and Coupling to Adenylate Cyclase Activity via G-Proteins. *Toxicol. Appl. Pharmacol.* **129,** 223–234 (1994).
132. Kehat, I. & Kenyagin-Karsenti, D. Human embryonic stem cells can differentiate into myocytes with structural and functional properties of cardiomyocytes. *J. Clin. …* **108,** 363–364 (2001).
133. Duncan, S. a *et al.* Mechanisms of Protection from Oxidative Stress in Cardiomyocytes Derived from Human Embryonic Stem. *Anesthesiology* (2010).
134. Kim, J. H. *et al.* Isoflurane decreases death of human embryonic stem cell-derived, transcriptional marker Nkx2.5 + cardiac progenitor cells. *Acta Anaesthesiol. Scand.* **55,** 1124–1131 (2011).
135. Ferdinandy, P., Schulz, R. & Baxter, G. F. Interaction of Cardiovascular Risk Factors with Myocardial Ischemia/Reperfusion Injury, Preconditioning, and Postconditioning. *Pharmacol. Rev.* **59,** 418–458 (2007).
136. Burridge, P. W. *et al.* Human induced pluripotent stem cell-derived cardiomyocytes recapitulate the predilection of breast cancer patients to doxorubicin-induced cardiotoxicity. *Nat. Med.* **22,** 547–556 (2016).
137. Cohen, J. D. *et al.* Use of human stem cell derived cardiomyocytes to examine sunitinib mediated cardiotoxicity and electrophysiological alterations. *Toxicol. Appl. Pharmacol.* **257,** 74–83 (2011).
138. Rana, P., Anson, B., Engle, S. & Will, Y. Characterization of Human-Induced Pluripotent Stem Cell-Derived Cardiomyocytes: Bioenergetics and Utilization in Safety Screening. *Toxicol. Sci.* **130,** 117–131 (2012).
139. Hidalgo, A. *et al.* Modelling ischemia-reperfusion injury (IRI) *in vitro* using metabolically matured induced pluripotent stem cell-derived cardiomyocytes. *APL Bioeng.* **2,** 026102 (2018).
140. Lim, C. C. & Sawyer, D. B. Modulation of Cardiac Function: Titin Springs into Action. *J. Gen. Physiol.* **125,** 249–252 (2005).
141. Lahmers, S., Wu, Y., Call, D. R., Labeit, S. & Granzier, H. Developmental Control of Titin Isoform Expression and Passive Stiffness in Fetal and Neonatal Myocardium. *Circ. Res.* **94,** 505–513 (2004).
142. Sheng, J.-J. & Jin, J.-P. TNNI1, TNNI2 and TNNI3: Evolution, regulation, and protein

structure–function relationships. *Gene* **576,** 385–394 (2016).

143. Warkman, A. S. *et al.* Developmental expression and cardiac transcriptional regulation of Myh7b, a third myosin heavy chain in the vertebrate heart. *Cytoskeleton* **69,** 324–335 (2012).
144. Piccini, I., Rao, J., Seebohm, G. & Greber, B. Human pluripotent stem cell-derived cardiomyocytes: Genome-wide expression profiling of long-term in vitro maturation in comparison to human heart tissue. *Genomics Data* **4,** 69–72 (2015).
145. Cox, E. J. & Marsh, S. A. A systematic review of fetal genes as biomarkers of cardiac hypertrophy in rodent models of diabetes. *PLoS One* **9,** 1–11 (2014).
146. Denning, C. *et al.* Cardiomyocytes from human pluripotent stem cells: From laboratory curiosity to industrial biomedical platform. *Biochim. Biophys. Acta - Mol. Cell Res.* **1863,** 1728–1748 (2016).
147. Piccolo, S., Dupont, S. & Cordenonsi, M. The biology of YAP/TAZ: hippo signaling and beyond. *Physiol. Rev.* **94,** 1287–312 (2014).
148. Dupont, S. *et al.* Role of YAP/TAZ in mechanotransduction. *Nature* **474,** 179–183 (2011).
149. Ieda, M. *et al.* Cardiac Fibroblasts Regulate Myocardial Proliferation through β1 Integrin Signaling. *Dev. Cell* **16,** 233–244 (2009).
150. Godier-Furnémont, A. F. G. *et al.* Physiologic force-frequency response in engineered heart muscle by electromechanical stimulation. *Biomaterials* **60,** 82–91 (2015).
151. Jackman, C. P., Carlson, A. L. & Bursac, N. Dynamic culture yields engineered myocardium with near-adult functional output. *Biomaterials* **111,** 66–79 (2016).
152. Kamakura, T. *et al.* Ultrastructural Maturation of Human-Induced Pluripotent Stem Cell-Derived Cardiomyocytes in a Long-Term Culture. *Circ. J.* **77,** 1307–1314 (2013).
153. Lundy, S. D., Zhu, W.-Z., Regnier, M. & Laflamme, M. A. Structural and Functional Maturation of Cardiomyocytes Derived from Human Pluripotent Stem Cells. *Stem Cells Dev.* **22,** 1991–2002 (2013).
154. Kadota, S., Pabon, L., Reinecke, H. & Murry, C. E. E. In Vivo Maturation of Human Induced Pluripotent Stem Cell-Derived Cardiomyocytes in Neonatal and Adult Rat Hearts. *Stem Cell Reports* **7,** 278–289 (2017).
155. Chng, S. C., Ho, L., Tian, J. & Reversade, B. ELABELA: A hormone essential for heart development signals via the apelin receptor. *Dev. Cell* **27,** 672–680 (2013).
156. Mai, W. *et al.* Thyroid hormone receptor alpha is a molecular switch of cardiac function between fetal and postnatal life. *Proc. Natl. Acad. Sci. U. S. A.* **101,** 10332–7 (2004).
157. Chattergoon, N. N. *et al.* Thyroid hormone drives fetal cardiomyocyte maturation. *FASEB*

J. **26,** 397–408 (2012).

158. Yang, X. *et al.* Tri-iodo-l-thyronine promotes the maturation of human cardiomyocytes-derived from induced pluripotent stem cells. *J. Mol. Cell. Cardiol.* **72,** 296–304 (2014).
159. Ribeiro, M. C. *et al.* Functional maturation of human pluripotent stem cell derived cardiomyocytes in vitro – Correlation between contraction force and electrophysiology. *Biomaterials* **51,** 138–150 (2015).
160. Birket, M. J. *et al.* Contractile Defect Caused by Mutation in MYBPC3 Revealed under Conditions Optimized for Human PSC-Cardiomyocyte Function. *Cell Rep.* **13,** 733–745 (2015).
161. Radisic, M. *et al.* Functional assembly of engineered myocardium by electrical stimulation of cardiac myocytes cultured on scaffolds. *Proc. Natl. Acad. Sci. U. S. A.* **101,** 18129–34 (2004).
162. Hardy, J. G., Lee, J. Y. & Schmidt, C. E. Biomimetic conducting polymer-based tissue scaffolds. *Curr. Opin. Biotechnol.* **24,** 847–854 (2013).
163. Chan, Y.-C. *et al.* Electrical Stimulation Promotes Maturation of Cardiomyocytes Derived from Human Embryonic Stem Cells. *J. Cardiovasc. Transl. Res.* **6,** 989–999 (2013).
164. Nunes, S. S. *et al.* Biowire: a platform for maturation of human pluripotent stem cell-derived cardiomyocytes. *Nat Meth* **10,** 781–787 (2013).
165. Tandon, N. *et al.* Electrical stimulation systems for cardiac tissue engineering. *Nat. Protoc.* **4,** 155–173 (2009).
166. Baumgartner, S. *et al.* Electrophysiological and morphological maturation of murine fetal cardiomyocytes during electrical stimulation in vitro. *J. Cardiovasc. Pharmacol. Ther.* **20,** 104–112 (2015).
167. Wan, A. M. D. *et al.* Electrical control of protein conformation. *Adv. Mater.* **24,** 2501–2505 (2012).
168. Borriello, A., Guarino, V., Schiavo, L., Alvarez-Perez, M. A. & Ambrosio, L. Optimizing PANi doped electroactive substrates as patches for the regeneration of cardiac muscle. *J. Mater. Sci. Mater. Med.* **22,** 1053–1062 (2011).
169. Hsiao, C. W. *et al.* Electrical coupling of isolated cardiomyocyte clusters grown on aligned conductive nanofibrous meshes for their synchronized beating. *Biomaterials* **34,** 1063–1072 (2013).
170. Cui, Z. *et al.* Polypyrrole-chitosan conductive biomaterial synchronizes cardiomyocyte contraction and improves myocardial electrical impulse propagation. *Theranostics* **8,** 2752–2764 (2018).

171. Gelmi, A., Ljunggren, M. K., Rafat, M. & Jager, E. W. H. Influence of conductive polymer doping on the viability of cardiac progenitor cells. *J. Mater. Chem. B* **2,** 3860–3867 (2014).
172. Spearman, B. S. *et al.* Conductive interpenetrating networks of polypyrrole and polycaprolactone encourage electrophysiological development of cardiac cells. *Acta Biomater.* **28,** 109–120 (2015).
173. Goenezen, S., Rennie, M. Y. & Rugonyi, S. Biomechanics of early cardiac development. *Biomech. Model. Mechanobiol.* **11,** 1187–1204 (2012).
174. Chaui-Berlinck, J. G. & Monteiro, L. H. A. Frank-Starling mechanism and short-term adjustment of cardiac flow. *J. Exp. Biol.* jeb.167106 (2017). doi:10.1242/jeb.167106
175. Lucitti, J. L. *et al.* Vascular remodeling of the mouse yolk sac requires hemodynamic force. *Development* **134,** 3317–3326 (2007).
176. Andrés-Delgado, L. & Mercader, N. Interplay between cardiac function and heart development. *Biochim. Biophys. Acta - Mol. Cell Res.* **1863,** 1707–1716 (2016).
177. Tulloch, N. L. *et al.* Growth of engineered human myocardium with mechanical loading and vascular coculture. *Circ. Res.* **109,** 47–59 (2011).
178. Mihic, A. *et al.* The effect of cyclic stretch on maturation and 3D tissue formation of human embryonic stem cell-derived cardiomyocytes. *Biomaterials* **35,** 2798–2808 (2014).
179. Tzatzalos, E., Abilez, O. J., Shukla, P. & Wu, J. C. Engineered heart tissues and induced pluripotent stem cells: macro-and microstructures for disease modeling, drug screening, and translational studies. *Adv. Drug Deliv. Rev.* **96,** 234–244 (2016).
180. Zuppinger, C. 3D culture for cardiac cells. *Biochim. Biophys. Acta - Mol. Cell Res.* **1863,** 1873–1881 (2016).
181. Tiburcy, M. *et al.* Defined Engineered Human Myocardium With Advanced Maturation for Applications in Heart Failure Modeling and Repair. *Circulation* **135,** 1832–1847 (2017).
182. Noshadi, I. *et al.* Engineering Biodegradable and Biocompatible Bio-ionic Liquid Conjugated Hydrogels with Tunable Conductivity and Mechanical Properties. *Sci. Rep.* **7,** 4345 (2017).
183. Young, J. L. & Engler, A. J. Hydrogels with time-dependent material properties enhance cardiomyocyte differentiation in vitro. *Biomaterials* **32,** 1002–1009 (2011).
184. Van Heerebeek, L. *et al.* Diastolic stiffness of the failing diabetic heart importance of fibrosis, advanced glycation end products, and myocyte resting tension. *Circulation* **117,** 43–51 (2008).
185. Engler, A. J., Sen, S., Sweeney, H. L. & Discher, D. E. Matrix elasticity directs stem cell

lineage specification. *Cell* **126,** 677–689 (2006).

186. Tseng, Q. *et al.* A new micropatterning method of soft substrates reveals that different tumorigenic signals can promote or reduce cell contraction levels. *Lab Chip* **11,** 2231–2240 (2011).
187. McCain, M. L., Lee, H., Aratyn-Schaus, Y., Kleber, a. G. & Parker, K. K. Cooperative coupling of cell-matrix and cell-cell adhesions in cardiac muscle. *Proc. Natl. Acad. Sci.* **109,** 9881–9886 (2012).
188. Radisic, M. *et al.* Pre-treatment of synthetic elastomeric scaffolds by cardiac fibroblasts improves engineered heart tissue. *J. Biomed. Mater. Res. - Part A* **86,** 713–724 (2008).
189. Liau, B., Christoforou, N., Leong, K. W. & Bursac, N. Pluripotent stem cell-derived cardiac tissue patch with advanced structure and function. *Biomaterials* **32,** 9180–9187 (2011).
190. Curtis, a S. & Varde, M. Control of Cell Behavior: Topological Factors. *J. Natl. Cancer Inst.* **33,** 15–26 (1964).
191. Kulangara, K. & Leong, K. W. Substrate topography shapes cell function. *Soft Matter* **5,** 4072–4076 (2009).
192. Yang, Y. & Leong, K. W. Nanoscale surfacing for regenerative medicine. *Wiley Interdiscip. Rev. Nanomedicine Nanobiotechnology* **2,** 478–495 (2010).
193. Lord, M. S., Foss, M. & Besenbacher, F. Influence of nanoscale surface topography on protein adsorption and cellular response. *Nano Today* **5,** 66–78 (2010).
194. Parker, K. K., Tan, J., Chen, C. S. & Tung, L. Myofibrillar Architecture in Engineered Cardiac Myocytes. *Circ. Res.* **103,** 340–342 (2008).
195. Kim, J. *et al.* Quantitative evaluation of cardiomyocyte contractility in a 3D microenvironment. *J. Biomech.* **41,** 2396–2401 (2008).
196. Yin, L. Scaffold topography alters intracellular calcium dynamics in cultured cardiomyocyte networks. *AJP Hear. Circ. Physiol.* **287,** H1276–H1285 (2004).
197. Entcheva, E. & Bien, H. Tension development and nuclear eccentricity in topographically controlled cardiac syncytium. *Biomed. Microdevices* **5,** 163–168 (2003).
198. Motlagh, D., Senyo, S. E., Desai, T. A. & Russell, B. Microtextured substrata alter gene expression, protein localization and the shape of cardiac myocytes. *Biomaterials* **24,** 2463–2476 (2003).
199. Dalby, M. J., Riehle, M. O., Yarwood, S. J., Wilkinson, C. D. W. & Curtis, A. S. G. Nucleus alignment and cell signaling in fibroblasts: Response to a micro-grooved topography. *Exp. Cell Res.* **284,** 274–282 (2003).
200. Trantidou, T., Terracciano, C. M., Kontziampasis, D., Humphrey, E. J. & Prodromakis, T.

Biorealistic cardiac cell culture platforms with integrated monitoring of extracellular action potentials. *Sci. Rep.* **5,** 11067 (2015).

201. Zimmermann, W. H. *et al.* Tissue engineering of a differentiated cardiac muscle construct. *Circ. Res.* **90,** 223–230 (2002).
202. Lu, T.-Y. *et al.* Repopulation of decellularized mouse heart with human induced pluripotent stem cell-derived cardiovascular progenitor cells. *Nat. Commun.* **4,** 1–11 (2013).
203. Kochupura, P. V. *et al.* Tissue-engineered myocardial patch derived from extracellular matrix provides regional mechanical function. *Circulation* **112,** (2005).
204. Wainwright, J. M. *et al.* Preparation of cardiac extracellular matrix from an intact porcine heart. *Tissue Eng. Part C. Methods* **16,** 525–532 (2010).
205. Guyette, J. P. *et al.* Bioengineering Human Myocardium on Native Extracellular Matrix. *Circ. Res.* (2015). doi:10.1161/CIRCRESAHA.115.306874
206. Thavandiran, N. *et al.* Design and formulation of functional pluripotent stem cell-derived cardiac microtissues. *Proc. Natl. Acad. Sci.* **110,** E4698–E4707 (2013).
207. Suhaeri, M. *et al.* Novel Platform of Cardiomyocyte Culture and Coculture via Fibroblast-Derived Matrix-Coupled Aligned Electrospun Nanofiber. *ACS Appl. Mater. Interfaces* **9,** 224–235 (2017).
208. Rother, J. *et al.* Crosstalk of cardiomyocytes and fibroblasts in co-cultures. *Open Biol.* **5,** (2015).
209. Valarmathi, M. T., Fuseler, J. W., Davis, J. M. & Price, R. L. A Novel Human Tissue-Engineered 3-D Functional Vascularized Cardiac Muscle Construct. *Front. Cell Dev. Biol.* **5,** 1–24 (2017).
210. Takeuchi, A. *et al.* Device for co-culture of sympathetic neurons and cardiomyocytes using microfabrication. *Lab Chip* **11,** 2268–2275 (2011).
211. Matsa, E., Burridge, P. W. & Wu, J. C. Human stem cells for modeling heart disease and for drug discovery. *Sci Transl Med* **6,** 239ps6 (2014).
212. Bray, M. A., Sheehy, S. P. & Parker, K. K. Sarcomere alignment is regulated by myocyte shape. *Cell Motil. Cytoskeleton* **65,** 641–651 (2008).
213. Jacot, J. G., McCulloch, A. D. & Omens, J. H. Substrate Stiffness Affects the Functional Maturation of Neonatal Rat Ventricular Myocytes. *Biophys. J.* **95,** 3479–3487 (2008).
214. Kuo, P. L. *et al.* Myocyte Shape Regulates Lateral Registry of Sarcomeres and Contractility. *Am. J. Pathol.* **181,** 2030–2037 (2012).
215. Przybyla, L., Lakins, J. N. & Weaver, V. M. Tissue Mechanics Orchestrate Wnt-

Dependent Human Embryonic Stem Cell Differentiation. *Cell Stem Cell* **19,** 462–475 (2016).

216. Dado-Rosenfeld, D., Tzchori, I., Fine, A., Chen-Konak, L. & Levenberg, S. Tensile Forces Applied on a Cell-Embedded Three-Dimensional Scaffold Can Direct Early Differentiation of Embryonic Stem Cells Toward the Mesoderm Germ Layer. *Tissue Eng. Part A* **00,** 1–10 (2014).
217. Mannhardt, I. *et al.* Human Engineered Heart Tissue: Analysis of Contractile Force. *Stem Cell Reports* **7,** 29–42 (2016).
218. Kumar, A., Placone, J. K. & Engler, A. J. Understanding the extracellular forces that determine cell fate and maintenance. *Development* **144,** 4261–4270 (2017).
219. Marelli, D., Desrosiers, C., El-Alfy, M., Kao, R. L. & Chiu, R. C. Cell transplantation for myocardial repair: an experimental approach. *Cell Transplant.* **1,** 383–90 (1992).
220. Menasché, P. *et al.* The myoblast autologous grafting in ischemic cardiomyopathy (MAGIC) trial: First randomized placebo-controlled study of myoblast transplantation. *Circulation* **117,** 1189–1200 (2008).
221. Menasche, P. *et al.* Towards a clinical use of human embryonic stem cell-derived cardiac progenitors: a translational experience. *Eur. Heart J.* **36,** 743–750 (2015).
222. Menasché, P. *et al.* Human embryonic stem cell-derived cardiac progenitors for severe heart failure treatment: First clinical case report. *Eur. Heart J.* **36,** 2011–2017 (2015).
223. Burridge, P. W. *et al.* Chemically defined generation of human cardiomyocytes. *Nat. Methods* **11,** 855–60 (2014).
224. Liu, Y.-W. W. *et al.* Human embryonic stem cell-derived cardiomyocytes restore function in infarcted hearts of non-human primates. *Nat. Biotechnol.* **36,** 597–605 (2018).
225. Tabei, R. *et al.* Development of a transplant injection device for optimal distribution and retention of human induced pluripotent stem cell–derived cardiomyocytes. *J. Hear. Lung Transplant.* **38,** 203–214 (2019).
226. Akhyari, P. *et al.* Mechanical Stretch Regimen Enhances the Formation of Bioengineered Autologous Cardiac Muscle Grafts. *Circulation* **106,** I-137 LP-I-142 (2002).
227. Zimmermann, W. H., Melnychenko, I. & Eschenhagen, T. Engineered heart tissue for regeneration of diseased hearts. *Biomaterials* **25,** 1639–1647 (2004).
228. Landa, N. *et al.* Effect of injectable alginate implant on cardiac remodeling and function after recent and old infarcts in rat. *Circulation* **117,** 1388–1396 (2008).
229. Ruvinov, E. & Cohen, S. Alginate biomaterial for the treatment of myocardial infarction: Progress, translational strategies, and clinical outlook. From ocean algae to patient

bedside. *Adv. Drug Deliv. Rev.* **96,** 54–76 (2016).

230. Mawad, D. *et al.* A conducting polymer with enhanced electronic stability applied in cardiac models. *Sci. Adv.* **2,** 1–13 (2016).
231. Kapnisi, M. *et al.* Auxetic Cardiac Patches with Tunable Mechanical and Conductive Properties toward Treating Myocardial Infarction. *Adv. Funct. Mater.* **28,** (2018).
232. Liu, Z. *et al.* The influence of chitosan hydrogel on stem cell engraftment, survival and homing in the ischemic myocardial microenvironment. *Biomaterials* **33,** 3093–3106 (2012).
233. Chang, M. Y. *et al.* Functionalized nanoparticles provide early cardioprotection after acute myocardial infarction. *J. Control. Release* **170,** 287–294 (2013).
234. Meng, X. *et al.* Novel injectable biomimetic hydrogels with carbon nanofibers and self assembled rosette nanotubes for myocardial applications. *J. Biomed. Mater. Res. - Part A* **101 A,** 1095–1102 (2013).
235. Lakshmanan, R., Krishnan, U. M. & Sethuraman, S. Polymeric scaffold aided stem cell therapeutics for cardiac muscle repair and regeneration. *Macromol. Biosci.* **13,** 1119–1134 (2013).
236. Zammaretti, P. & Jaconi, M. Cardiac tissue engineering: Regeneration of the wounded heart. *Curr. Opin. Biotechnol.* **15,** 430–434 (2004).
237. Carver, W., Terracio, L. & Borg, T. K. Expression and accumulation of interstitial collagen in the neonatal rat heart. *Anat. Rec.* **236,** 511–520 (1993).
238. Weber, K. T. Cardiac interstitium in health and disease: The fibrillar collagen network. *J. Am. Coll. Cardiol.* **13,** 1637–1652 (1989).
239. Miyagi, Y. *et al.* Biodegradable collagen patch with covalently immobilized VEGF for myocardial repair. *Biomaterials* **32,** 1280–1290 (2011).
240. Rosca, A.-M. *et al.* Collagen regulates the ability of endothelial progenitor cells to protect hypoxic myocardium through a mechanism involving miR-377/VE-PTP axis. *J. Cell. Mol. Med.* **22,** 4700–4708 (2018).
241. Christman, K. L., Fok, H. H., Sievers, R. E., Fang, Q. & Lee, R. J. Fibrin Glue Alone and Skeletal Myoblasts in a Fibrin Scaffold Preserve Cardiac Function after Myocardial Infarction. *Tissue Eng.* **10,** 403–409 (2004).
242. Deng, B. *et al.* Delivery of alginate-chitosan hydrogel promotes endogenous repair and preserves cardiac function in rats with myocardial infarction. *J. Biomed. Mater. Res. - Part A* **103,** 907–918 (2015).
243. Leor, J. *et al.* Intracoronary Injection of In Situ Forming Alginate Hydrogel Reverses Left

Ventricular Remodeling After Myocardial Infarction in Swine. *J. Am. Coll. Cardiol.* **54,** 1014–1023 (2009).

244. Anker, S. D. *et al.* A prospective comparison of alginate-hydrogel with standard medical therapy to determine impact on functional capacity and clinical outcomes in patients with advanced heart failure (AUGMENT-HF trial). *Eur. Heart J.* **36,** 2297–2309 (2015).
245. Mann, D. L. *et al.* One-year follow-up results from AUGMENT-HF : a multicentre randomized controlled clinical trial of the efficacy of left ventricular augmentation with Algisyl in the treatment of heart failure. *Eur. J. Heart Fail.* **18,** 314–25 (2015).
246. Suarez, S. L. *et al.* Intramyocardial injection of hydrogel with high interstitial spread does not impact action potential propagation. *Acta Biomater.* **26,** 13–22 (2015).
247. Onakpoya, I. J., Heneghan, C. J. & Aronson, J. K. Post-marketing withdrawal of 462 medicinal products because of adverse drug reactions: A systematic review of the world literature. *BMC Med.* **14,** 1–11 (2016).
248. Sun, W. Cardiotoxicity Testing in Drug Development. *SM J. Cardiovasc. Disord.* **1,** 18–21 (2016).
249. Laverty, H. *et al.* How can we improve our understanding of cardiovascular safety liabilities to develop safer medicines? *Br. J. Pharmacol.* **163,** 675–693 (2011).
250. Engle, S. J. & Vincent, F. Small molecule screening in human induced pluripotent stem cell-derived terminal cell types. *J. Biol. Chem.* **289,** 4562–4570 (2014).
251. Kannankeril, P., Roden, D. M. & Darbar, D. Drug-Induced Long QT Syndrome. *Pharmacol. Rev.* **62,** 760–781 (2010).
252. Henrique Franco, N. Animal experiments in biomedical research: A historical perspective. *Animals* **3,** 238–273 (2013).
253. Ericsson, A. C., Crim, M. J. & Franklin, C. L. A brief history of animal modeling. *Mo. Med.* **110,** 201–5 (2008).
254. Guénet, J.-L. Animal models of human genetic diseases: do they need to be faithful to be useful? *Mol. Genet. Genomics* **286,** 1–20 (2011).
255. Smithies, O. Animal models of human genetic diseases. *Trends Genet.* **9,** 112–116 (1993).
256. Erickson, R. P. Minireview: Creating Animal Models of Genetic Disease. *Am. J. Hum. Genet* **43,** 582–586 (1988).
257. Whitelaw, C. B. A., Sheets, T. P., Lillico, S. G. & Telugu, B. P. Engineering large animal models of human disease. *J. Pathol.* **238,** 247–256 (2016).
258. Olson, H. *et al.* Concordance of the toxicity of pharmaceuticals in humans and in animals.

Regul. Toxicol. Pharmacol. **32,** 56–67 (2000).

259. Jones, D. K. *et al.* hERG 1b is critical for human cardiac repolarization. *Proc. Natl. Acad. Sci. U. S. A.* **2014,** 1–5 (2014).
260. Physiol, C. Ion Channels in the Heart. **5,** 1423–1464 (2016).
261. Zhang, Y. *et al.* Dedifferentiation and proliferation of mammalian cardiomyocytes. *PLoS One* **5,** 1–13 (2010).
262. Wang, W. E. *et al.* Dedifferentiation, proliferation, and redifferentiation of adult mammalian cardiomyocytes after ischemic injury. *Circulation* **136,** 834–848 (2017).
263. Dispersyn, G. D., Geuens, E., Ver Donck, L., Ramaekers, F. C. S. & Borgers, M. Adult rabbit cardiomyocytes undergo hibernation-like dedifferentiation when co-cultured with cardiac fibroblasts. *Cardiovasc. Res.* **51,** 230–240 (2001).
264. Pinz, I., Zhu, M., Mende, U. & Ingwall, J. S. An Improved Isolation Procedure for Adult Mouse Cardiomyocytes. *Cell Biochem. Biophys.* **61,** 93–101 (2011).
265. Dutta, D., Heo, I. & Clevers, H. Disease Modeling in Stem Cell-Derived 3D Organoid Systems. *Trends Mol. Med.* **23,** 393–410 (2017).
266. Ho, B., Pek, N. & Soh, B.-S. Disease Modeling Using 3D Organoids Derived from Human Induced Pluripotent Stem Cells. *Int. J. Mol. Sci.* **19,** 936 (2018).
267. Ryan, A. J., Brougham, C. M., Garciarena, C. D., Kerrigan, S. W. & O'Brien, F. J. Towards 3D in vitro models for the study of cardiovascular tissues and disease. *Drug Discov. Today* **21,** 1437–1445 (2016).
268. Mathur, A., Ma, Z., Loskill, P., Jeeawoody, S. & Healy, K. E. In vitro cardiac tissue models: Current status and future prospects. *Adv. Drug Deliv. Rev.* **96,** 203–213 (2016).
269. Takahashi, K. & Yamanaka, S. Induction of Pluripotent Stem Cells from Mouse Embryonic and Adult Fibroblast Cultures by Defined Factors. *Cell* **126,** 663–676 (2006).
270. Mordwinkin, N. M., Burridge, P. W. & Wu, J. C. A review of human pluripotent stem cell-derived cardiomyocytes for high-throughput drug discovery, cardiotoxicity screening, and publication standards. *J. Cardiovasc. Transl. Res.* **6,** 22–30 (2013).
271. Dick, E., Rajamohan, D., Ronksley, J. & Denning, C. Evaluating the utility of cardiomyocytes from human pluripotent stem cells for drug screening. *Biochem. Soc. Trans.* **38,** 1037–1045 (2010).
272. Rocchetti, M. *et al.* Elucidating arrhythmogenic mechanisms of long-QT syndrome CALM1-F142L mutation in patient-specific induced pluripotent stem cell-derived cardiomyocytes. *Cardiovasc. Res.* **113,** 531–541 (2017).
273. Kadota, S. *et al.* Development of a reentrant arrhythmia model in human pluripotent stem

cell-derived cardiac cell sheets. *Eur. Heart J.* **34,** 1147–1156 (2013).

274. Shaheen, N. *et al.* Human Induced Pluripotent Stem Cell-Derived Cardiac Cell Sheets Expressing Genetically Encoded Voltage Indicator for Pharmacological and Arrhythmia Studies. *Stem Cell Reports* **10,** 1879–1894 (2018).
275. Novak, A. *et al.* Functional abnormalities in iPSC-derived cardiomyocytes generated from CPVT1 and CPVT2 patients carrying ryanodine or calsequestrin mutations. *J. Cell. Mol. Med.* **19,** 2006–2018 (2015).
276. Tse, H.-F. *et al.* Patient-specific Induced Pluripotent Stem Cells Derived Cardiomycoytes Recapitulates the Pathogenic Phenotypes of Dilated Cardiomyopathy due to a Novel DES Mutation Identified by Whole Exome Sequencing. *Hum. Mol. Genet.* 1–28 (2013).
277. Veerman, C. C. *et al.* HiPSC-derived cardiomyocytes from Brugada Syndrome patients without identified mutations do not exhibit clear cellular electrophysiological abnormalities. *Sci. Rep.* **6,** 1–10 (2016).
278. Kehl, D., Weber, B. & Hoerstrup, S. P. Bioengineered living cardiac and venous valve replacements: current status and future prospects. *Cardiovasc. Pathol.* (2016). doi:10.1016/j.carpath.2016.03.001
279. Wen, J.-Y. *et al.* Maturation-Based Model of Arrhythmogenic Right Ventricular Dysplasia Using Patient-Specific Induced Pluripotent Stem Cells. *Circ. J.* **79,** 1402–1408 (2015).
280. Karakikes, I., Ameen, M., Termglinchan, V. & Wu, J. C. Human Induced Pluripotent Stem Cell-Derived Cardiomyocytes: Insights into Molecular, Cellular, and Functional Phenotypes. **117,** 80–88 (2016).
281. Adams, W. J. *et al.* Functional Vascular Endothelium Derived from Human Induced Pluripotent Stem Cells. *Stem Cell Reports* **1,** 105–113 (2013).
282. Zhang, J. *et al.* A human iPSC model of hutchinson gilford progeria reveals vascular smooth muscle and mesenchymal stem cell defects. *Cell Stem Cell* **8,** 31–45 (2011).
283. Ge, X. *et al.* Modeling supravalvular aortic stenosis syndrome with human induced pluripotent stem cells. *Circulation* **126,** 1695–1704 (2012).
284. Granata, A. *et al.* An iPSC-derived vascular model of Marfan syndrome identifies key mediators of smooth muscle cell death. *Nat. Genet.* **49,** 97–109 (2017).
285. French, A., Yang, C.-T., Taylor, S., Watt, S. M. & Carpenter, L. Human Induced Pluripotent Stem Cell-Derived B Lymphocytes Express sIgM and Can Be Generated via a Hemogenic Endothelium Intermediate. *Stem Cells Dev.* **24,** 1082–1095 (2015).
286. Fan, F. *et al.* Induction of Pluripotent Stem Cell-Derived Cardiomyocyte Toxicity by Supernatant of Long Term-Stored Red Blood Cells in Vitro. *Cell. Physiol. Biochem.* **46,**

1230–1240 (2018).

287. Myocytes, H. C. E MBRYONIC S TEM C ELLS / I NDUCED P LURIPOTENT S TEM (I PS) C ELLS An Induced Pluripotent Stem Cell Model of Hypoplastic Left Heart Syndrome (HLHS) Reveals Multiple Expression and Functional Differences in. 416–423 (2014).
288. Jung, G. & Bernstein, D. hiPSC MODELING OF INHERITED CARDIOMYOPATHIES Opinion Statement. **16,** 1–15 (2015).
289. Abilez, O. J. *et al.* Patient-Specific Induced Pluripotent Stem Cell as a Model for Familial Dilated Cardiomyopathy. *Sci. Transl. Med.* **4,** (2013).
290. Streckfuss-Bömeke, K. *et al.* Severe DCM phenotype of patient harboring RBM20 mutation S635A can be modeled by patient-specific induced pluripotent stem cell-derived cardiomyocytes. *J. Mol. Cell. Cardiol.* **113,** 9–21 (2017).
291. Schick, R. *et al.* Functional abnormalities in induced pluripotent stem cell-derived cardiomyocytes generated from titin-mutated dilated cardiomyopathy patients. *Eur. Heart J.* **38,** 1–25 (2017).
292. Wyles, S. P. *et al.* Modeling structural and functional deficiencies of RBM20 familial dilated cardiomyopathy using human induced pluripotent stem cells. *Hum. Mol. Genet.* **25,** 254–265 (2016).
293. Kim, C. *et al.* Studying arrhythmogenic right ventricular dysplasia with patient-specific iPSCs. *Nature* **494,** 105–110 (2013).
294. Lan, F. *et al.* Abnormal Calcium Handling Properties Underlie Familial Hypertrophic Cardiomyopathy Pathology in Patient-Specific Induced Pluripotent Stem Cells. *Cell Stem Cell* **12,** 101–113 (2013).
295. Ben Jehuda, R. *et al.* CRISPR correction of the PRKAG2 gene mutation in the patient's induced pluripotent stem cell-derived cardiomyocytes eliminates electrophysiological and structural abnormalities. *Hear. Rhythm* **15,** 267–276 (2018).
296. Smith, J. G. W. *et al.* Isogenic Pairs of hiPSC-CMs with Hypertrophic Cardiomyopathy/LVNC-Associated ACTC1 E99K Mutation Unveil Differential Functional Deficits. *Stem Cell Reports* **11,** 1226–1243 (2018).
297. Han, L. *et al.* Study familial hypertrophic cardiomyopathy using patient-specific induced pluripotent stem cells. *Cardiovasc. Res.* **104,** 258–269 (2014).
298. Carvajal-Vergara, X. *et al.* Patient-specific induced pluripotent stem-cell-derived models of LEOPARD syndrome. *Nature* **465,** 808–812 (2010).
299. Hick, A. *et al.* Neurons and cardiomyocytes derived from induced pluripotent stem cells

as a model for mitochondrial defects in Friedreich's ataxia. *Dis. Model. Mech.* **6,** 608–621 (2013).

300. Biochemistr, and *et al.* Cellular Physiology Cellular Physiology Cellular Physiology Cellular Physiology Cellular Physiology In vitro Modeling of Ryanodine Receptor 2 Dysfunction Using Human Induced Pluripotent Stem Cells. *Orig. Pap. Cell Physiol Biochem* **28,** 579–592 (2011).
301. Novak, A. *et al.* Cardiomyocytes generated from CPVT D307H patients are arrhythmogenic in response to β-adrenergic stimulation. *J. Cell. Mol. Med.* **16,** 468–482 (2012).
302. Lahti, A. L. *et al.* Model for long QT syndrome type 2 using human iPS cells demonstrates arrhythmogenic characteristics in cell culture. *Dis. Model. Mech.* **5,** 220–230 (2012).
303. Davis, R. P. *et al.* Cardiomyocytes derived from pluripotent stem cells recapitulate electrophysiological characteristics of an overlap syndrome of cardiac sodium channel disease. *Circulation* **125,** 3079–3091 (2012).
304. Moretti, A. *et al.* Patient-Specific Induced Pluripotent Stem-Cell Models for Long-QT Syndrome. *N. Engl. J. Med.* **363,** 1397–1409 (2010).
305. Yazawa, M. *et al.* Using induced pluripotent stem cells to investigate cardiac phenotypes in Timothy syndrome. *Nature* **471,** 230–236 (2011).
306. Limpitikul, W. B. *et al.* A Precision Medicine Approach to the Rescue of Function on Malignant Calmodulinopathic Long-QT Syndrome. *Circ. Res.* **120,** 39–48 (2017).
307. Wang, G. *et al.* Modeling the mitochondrial cardiomyopathy of Barth syndrome with induced pluripotent stem cell and heart-on-chip technologies. *Nat. Med.* **20,** 616–623 (2014).
308. Ebert, A. D. *et al.* Characterization of the molecular mechanisms underlying increased ischemic damage in the aldehyde dehydrogenase 2 genetic polymorphism using a human induced pluripotent stem cell model system. *Sci. Transl. Med.* **6,** 255ra130-255ra130 (2014).
309. Crowder, S. W., Leonardo, V., Whittaker, T., Papathanasiou, P. & Stevens, M. M. Material Cues as Potent Regulators of Epigenetics and Stem Cell Function. *Cell Stem Cell* **18,** 39–52 (2016).
310. Boudou, T., Ohayon, J., Picart, C. & Tracqui, P. An extended relationship for the characterization of Young's modulus and Poisson's ratio of tunable polyacrylamide gels. *Biorheology* **43,** 721–728 (2006).
311. Tse, J. R. & Engler, A. J. Preparation of hydrogel substrates with tunable mechanical

properties. *Curr Protoc Cell Biol* **Chapter 10,** Unit 10 16 (2010).

312. Aratyn-Schaus, Y., Oakes, P. W., Stricker, J., Winter, S. P. & Gardel, M. L. Preparation of Complaint Matrices for Quantifying Cellular Contraction. *J. Vis. Exp.* e2173 (2010). doi:10.3791/2173
313. Poellmann, M. J. FABRICATION OF TOPOGRAPHICALLY PATTERNED HYDROGEL SUBSTRATES AND THEIR INFLUENCE ON CELL MORPHOLOGY. (University of Illinois at Urbana-Champaign, 2010).
314. Poellmann, M. J. & Johnson, A. J. W. Multimaterial polyacrylamide: fabrication with electrohydrodynamic jet printing, applications, and modeling. *Biofabrication* **6,** 35018 (2014).
315. Xu, C., Yu, Z., Inouye, M., Brodsky, B. & Mirochnitchenko, O. Expanding the Family of Collagen Proteins: Recombinant Bacterial Collagens of Varying Composition Form Triple-Helices of Similar Stability. *Biomacromolecules* **11,** 348–356 (2010).
316. Peng, Y. Y. *et al.* A Streptococcus pyogenes derived collagen-like protein as a non-cytotoxic and non-immunogenic cross-linkable biomaterial. *Biomaterials* **31,** 2755–2761 (2010).
317. Wong, J. Y., Langer, R. & Ingber, D. E. Electrically conducting polymers can noninvasively control the shape and growth of mammalian cells. *Proc. Natl. Acad. Sci.* **91,** 3201–3204 (1994).
318. [a]bert[o] Groenendaal, L., Jonas, F., Freitag, D., Pielartzik, H. & Reynolds, J. R. Poly(3,4-ethylenedioxythiophene) and Its Derivatives: Past, Present, and Future. 481–494 (2000). doi:10.1144/GSL.SP.2000.173.01.01
319. Peramo, A. *et al. In Situ* Polymerization of a Conductive Polymer in Acellular Muscle Tissue Constructs. *Tissue Eng. Part A* **14,** 423–432 (2008).
320. Ravichandran, R., Sundarrajan, S., Venugopal, J. R., Mukherjee, S. & Ramakrishna, S. Applications of conducting polymers and their issues in biomedical engineering. *J. R. Soc. Interface* **7,** S559–S579 (2010).
321. Jaymand, M. Recent progress in chemical modification of polyaniline. *Prog. Polym. Sci.* **38,** 1287–1306 (2013).
322. Wang, H., Ji, L., Li, D. & Wang, J.-Y. Characterization of Nanostructure and Cell Compatibility of Polyaniline Films with Different Dopant Acids. *J. Phys. Chem. B* **112,** 2671–2677 (2008).
323. Wang, C. H., Dong, Y. Q., Sengothi, K., Tan, K. L. & Kang, E. T. In-vivo tissue response to polyaniline. *Synth. Met.* **102,** 1313–1314 (1999).

324. Silvestri, A., Boffito, M., Sartori, S. & Ciardelli, G. Biomimetic Materials and Scaffolds for Myocardial Tissue Regeneration. *Macromol. Biosci.* **13,** 984–1019 (2013).
325. Park, J. *et al.* Electromechanical cardioplasty using a wrapped elasto-conductive epicardial mesh. *Sci. Transl. Med.* **8,** 1–12 (2016).
326. Engelmayr, G. C. *et al.* Accordion-like honeycombs for tissue engineering of cardiac anisotropy. *Nat. Mater.* **7,** 1003–1010 (2008).
327. Gerdes, A. M., Kellerman, S. E., Malec, K. B. & Schocken, D. D. Transverse shape characteristics of cardiac myocytes from rats and humans. *Cardioscience* **5,** 31–6 (1994).
328. Kehat, I., Gepstein, A., Spira, A., Itskovitz-Eldor, J. & Gepstein, L. High-Resolution Electrophysiological Assessment of Human Embryonic Stem Cell-Derived Cardiomyocytes: A Novel In Vitro Model for the Study of Conduction. *Circ. Res.* **91,** 659–661 (2002).
329. Gerdes, A. M. *et al.* Structural remodeling of cardiac myocytes in patients with ischemic cardiomyopathy. *Circulation* **86,** 426–430 (1992).
330. Potse, M., Dubé, B. & Vinet, A. Cardiac anisotropy in boundary-element models for the electrocardiogram. *Med. Biol. Eng. Comput.* **47,** 719–729 (2009).
331. Roth, B. J. Electrical conductivity values used with the bidomain nodel of cardiac tissue. *IEEE Trans. Biomed. Eng.* **44,** 326–328 (1997).
332. Watson, S. A. *et al.* Preparation of viable adult ventricular myocardial slices from large and small mammals. *Nat. Protoc.* **12,** 2623–2639 (2017).
333. King, J. H., Huang, C. L. H. & Fraser, J. A. Determinants of myocardial conduction velocity: Implications for arrhythmogenesis. *Front. Physiol.* **4 JUN,** 1–14 (2013).
334. Sun, X. R. *et al.* Fast GCaMPs for improved tracking of neuronal activity. *Nat. Commun.* **4,** 1199–1216 (2013).
335. Metsalu, T. & Vilo, J. ClustVis: A web tool for visualizing clustering of multivariate data using Principal Component Analysis and heatmap. *Nucleic Acids Res.* **43,** W566–W570 (2015).
336. Parmar, P. A. *et al.* Collagen-mimetic peptide-modifiable hydrogels for articular cartilage regeneration. *Biomaterials* **54,** 213–225 (2015).
337. Peng, Y. Y. *et al.* Towards scalable production of a collagen-like protein from Streptococcus pyogenes for biomedical applications. *Microb. Cell Fact.* **11,** 146 (2012).
338. Xu, Y., Keene, D. R., Bujnicki, J. M., Höök, M. & Lukomski, S. Streptococcal Scl1 and Scl2 Proteins Form Collagen-like Triple Helices. *J. Biol. Chem.* **277,** 27312–27318 (2002).

339. Yoshizumi, A. *et al.* Self-association of streptococcus pyogenes collagen-like constructs into higher order structures. *Protein Sci.* **18,** 1241–1251 (2009).
340. Cosgriff-Hernandez, E. *et al.* Bioactive hydrogels based on Designer Collagens. *Acta Biomater.* **6,** 3969–3977 (2010).
341. Hermanowicz, P., Sarna, M., Burda, K. & Gabryś, H. AtomicJ: An open source software for analysis of force curves. *Rev. Sci. Instrum.* **85,** 063703 (2014).
342. Seah, M. P. The quantitative analysis of surfaces by XPS: A review. *Surf. Interface Anal.* **2,** 222–239 (1980).
343. Clarke, R. W. *et al.* Low Stress Ion Conductance Microscopy of Sub-Cellular Stiffness. *Soft Matter* **12,** 7953–7958 (2016).
344. Yang, X., Pabon, L. & Murry, C. E. Engineering Adolescence: Maturation of Human Pluripotent Stem Cell-Derived Cardiomyocytes. *Circ. Res.* **114,** 511–523 (2014).
345. Hazeltine, L. B. *et al.* Temporal impact of substrate mechanics on differentiation of human embryonic stem cells to cardiomyocytes. *Acta Biomater.* **10,** 604–12 (2014).
346. Ribeiro, A. J. S. *et al.* Contractility of single cardiomyocytes differentiated from pluripotent stem cells depends on physiological shape and substrate stiffness. *Proc. Natl. Acad. Sci.* **112,** 201508073 (2015).
347. Macrí-Pellizzeri, L. *et al.* Substrate Stiffness and Composition Specifically Direct Differentiation of Induced Pluripotent Stem Cells. *Tissue Eng. Part A* **21,** 1633–1641 (2015).
348. Rani, G. U., Mishra, S., Pathak, G., Jha, U. & Sen, G. Synthesis and applications of poly(2-hydroxyethylmethacrylate) grafted agar: A microwave based approach. *Int. J. Biol. Macromol.* **61,** 276–284 (2013).
349. Damljanovic, V. *et al.* Bulk and micropatterned conjugation of extracellular matrix proteins to characterized polyacrylamide substrates for cell mechanotransduction assays. *Biotechniques* **39,** 847 (2005).
350. Buxboim, A., Rajagopal, K., Brown, A. E. X. A. E. X. & Discher, D. E. How deeply cells feel: methods for thin gels. *J. Phys. Condens. Matter* **22,** 194116 (2010).
351. Subramony, S. D. *et al.* The guidance of stem cell differentiation by substrate alignment and mechanical stimulation. *Biomaterials* **34,** 1942–1953 (2013).
352. Burridge, P. W., Holmström, A. & Wu, J. C. Chemically Defined Culture and Cardiomyocyte Differentiation of Human Pluripotent Stem Cells. in *Current Protocols in Human Genetics* 21.3.1-21.3.15 (John Wiley & Sons, Inc., 2015). doi:10.1002/0471142905.hg2103s87

353. Bajaj, P., Tang, X., Saif, T. a. & Bashir, R. Stiffness of the substrate influences the phenotype of embryonic chicken cardiac myocytes. *J. Biomed. Mater. Res. Part A* **95,** 1261–1269 (2010).
354. Laco, F. *et al.* Unraveling the Inconsistencies of Cardiac Differentiation Efficiency Induced by the GSK3β Inhibitor CHIR99021 in Human Pluripotent Stem Cells. *Stem Cell Reports* **10,** 1851–1866 (2018).
355. Sato, N., Meijer, L., Skaltsounis, L., Greengard, P. & Brivanlou, A. H. Maintenance of pluripotency in human and mouse embryonic stem cells through activation of Wnt signaling by a pharmacological GSK-3-specific inhibitor. *Nat. Med.* **10,** 55–63 (2004).
356. McCubrey, J. A. *et al.* GSK-3 as potential target for therapeutic intervention in cancer. *Oncotarget* **5,** 2881–911 (2014).
357. John Solaro, R. Mechanisms of the Frank-Starling Law of the Heart: The Beat Goes On. *Biophys. J.* **93,** 4095–4096 (2007).
358. Argenziano, M. *et al.* Electrophysiologic Characterization of Calcium Handling in Human Induced Pluripotent Stem Cell-Derived Atrial Cardiomyocytes. *Stem Cell Reports* **10,** 1867–1878 (2018).
359. Devalla, H. D. *et al.* Atrial-like cardiomyocytes from human pluripotent stem cells are a robust preclinical model for assessing atrial-selective pharmacology. *EMBO Mol. Med.* **7,** 394–410 (2015).
360. Lv, H. *et al.* Mechanism of regulation of stem cell differentiation by matrix stiffness. *Stem Cell Res. Ther.* **6,** 103 (2015).
361. Lampi, M. C. & Reinhart-King, C. A. Targeting extracellular matrix stiffness to attenuate disease: From molecular mechanisms to clinical trials. *Sci. Transl. Med* **10,** 475 (2018).
362. Shevchuk, A. I. *et al.* Imaging proteins in membranes of living cells by high-resolution scanning ion conductance microscopy. *Angew. Chemie - Int. Ed.* **45,** 2212–2216 (2006).
363. Korchev, Y. E., Bashford, C. L., Milovanovic, M., Vodyanoy, I. & Lab, M. J. Scanning ion conductance microscopy of living cells. *Biophys. J.* **73,** 653–658 (1997).
364. Beningo, K. A., Dembo, M. & Wang, Y. Responses of fibroblasts to anchorage of dorsal extracellular matrix receptors. *Proc. Natl. Acad. Sci. U. S. A.* **101,** 18024–9 (2004).
365. Han, S. J., Oak, Y., Groisman, A. & Danuser, G. Traction microscopy to identify force modulation in subresolution adhesions. *Nat. Methods* **12,** 653–656 (2015).
366. Pourjavadi, A., Sadat Afjeh, S., Seidi, F. & Salimi, H. Preparation of acrylated agarose-based hydrogels and investigation of their application as fertilizing systems. *J. Appl. Polym. Sci.* **122,** 2424–2432 (2011).

367. De Paepe, I., Declercq, H., Cornelissen, M. & Schacht, E. Novel hydrogels based on methacrylate-modified agarose. *Polym. Int.* **51,** 867–870 (2002).
368. Borbely, A. Cardiomyocyte Stiffness in Diastolic Heart Failure. *Circulation* **111,** 774–781 (2005).
369. Poellmann, M. J. & Johnson, A. J. W. Characterizing and patterning polyacrylamide substrates functionalized with n-hydroxysuccinimide. *Cell. Mol. Bioeng.* **6,** 299–309 (2013).
370. Tenin, G. *et al.* Erbb2 is required for cardiac atrial electrical activity during development. *PLoS One* **9,** e107041 (2014).
371. Hao, J., Galindo, C. L., Tran, T.-L. & Sawyer, D. B. Neuregulin-1β induces embryonic stem cell cardiomyogenesis via ErbB3/ErbB2 receptors. *Biochem. J.* **458,** 335–41 (2014).
372. Sanchez-Soria P, C. T. ErbB signaling in cardiac development and disease. *Semin Cell Dev Biol.* **21,** 929–935 (2010).
373. Ozcelik, C. *et al.* Conditional mutation of the ErbB2 (HER2) receptor in cardiomyocytes leads to dilated cardiomyopathy. *Proc. Natl. Acad. Sci.* **99,** 8880–8885 (2002).
374. Davidson, K. C. *et al.* Wnt/ -catenin signaling promotes differentiation, not self-renewal, of human embryonic stem cells and is repressed by Oct4. *Proc. Natl. Acad. Sci.* **109,** 4485–4490 (2012).
375. Ozhan, G. & Weidinger, G. Wnt/β-catenin signaling in heart regeneration. *Cell Regen.* **4,** 4:3 (2015).
376. Beatty, A. L. *et al.* High-sensitivity cardiac troponin t levels and secondary events in outpatients with coronary heart disease from the heart and soul study. *JAMA Intern. Med.* **173,** 763–769 (2013).
377. Tarkowska, A. & Furmaga-Jabłońska, W. The evaluation of diagnostic role of cardiac troponin T (cTnT) in newborns with heart defects. *Sci. World J.* **2012,** 7–11 (2012).
378. Wettersten, N. & Maisel, A. Role of Cardiac Troponin Levels in Acute Heart Failure. *Card. Fail. Rev.* **1,** 102–106 (2015).
379. Banerjee, S., Sknepnek, R. & Marchetti, M. C. Optimal shapes and stresses of adherent cells on patterned substrates. *Soft Matter* **10,** 2424–2430 (2014).
380. Uesugi, M., Ojima, A., Taniguchi, T., Miyamoto, N. & Sawada, K. Low-density plating is sufficient to induce cardiac hypertrophy and electrical remodeling in highly purified human iPS cell-derived cardiomyocytes. *J. Pharmacol. Toxicol. Methods* **69,** 177–88 (2014).
381. Herron, T. J. *et al.* Extracellular Matrix–Mediated Maturation of Human Pluripotent Stem Cell–Derived Cardiac Monolayer Structure and Electrophysiological Function. *Circ.*

Arrhythmia Electrophysiol. **9,** 6 (2016).

382. Hirt, M. N. *et al.* Functional improvement and maturation of rat and human engineered heart tissue by chronic electrical stimulation. *J. Mol. Cell. Cardiol.* **74,** 151–61 (2014).
383. Rohrbach, P. *et al.* Quantitative Calcium Measurements in Subcellular Compartments of Plasmodium falciparum -infected Erythrocytes. *J. Biol. Chem.* **280,** 27960–27969 (2005).
384. Paredes, R. M., Etzler, J. C., Watts, L. T., Zheng, W. & Lechleiter, J. D. Chemical calcium indicators. *Methods* **46,** 143–151 (2008).
385. Kikuchi, K. & Poss, K. D. Cardiac Regenerative Capacity and Mechanisms. *Annu. Rev. Cell Dev. Biol.* **28,** 719–741 (2012).
386. Sheehy, S. P., Grosberg, A. & Parker, K. K. The contribution of cellular mechanotransduction to cardiomyocyte form and function. *Biomech. Model. Mechanobiol.* **11,** 1227–1239 (2012).
387. McCain, M. L., Sheehy, S. P., Grosberg, A., Goss, J. A. & Parker, K. K. Recapitulating maladaptive, multiscale remodeling of failing myocardium on a chip. *Proc. Natl. Acad. Sci.* **110,** 9770–9775 (2013).
388. Aratyn-Schaus, Y. *et al.* Coupling primary and stem cell–derived cardiomyocytes in an in vitro model of cardiac cell therapy. *J. Cell Biol.* **212,** 389–397 (2016).
389. McCain, M. L., Lee, H., Aratyn-Schaus, Y., Kléber, A. G. & Parker, K. K. Cooperative coupling of cell-matrix and cell–cell adhesions in cardiac muscle. *Proc. Natl. Acad. Sci.* **109,** 9881–9886 (2012).
390. Pasqualini, F. S. S., Sheehy, S. P. P., Agarwal, A., Aratyn-Schaus, Y. & Parker, K. K. K. Structural Phenotyping of Stem Cell-Derived Cardiomyocytes. *Stem Cell Reports* **4,** 340–347 (2015).
391. Josowitz, R. *et al.* Identification and Purification of Human Induced Pluripotent Stem Cell-Derived Atrial-Like Cardiomyocytes Based on Sarcolipin Expression. *PLoS One* **9,** e101316 (2014).
392. Miquerol, L. *et al.* Resolving cell lineage contributions to the ventricular conduction system with a Cx40-GFP allele: A dual contribution of the first and second heart fields. *Dev. Dyn.* **242,** 665–677 (2013).
393. Gobaa, S., Hoehnel, S. & Lutolf, M. P. Substrate elasticity modulates the responsiveness of mesenchymal stem cells to commitment cues. *Integr. Biol. (United Kingdom)* **7,** 1135–1142 (2015).
394. Trantidou, T. *et al.* Surface Chemistry and Microtopography of Parylene C Films Control the Morphology and Microtubule Density of Cardiac Myocytes. *Tissue Eng. Part C*

Methods **22,** 464–472 (2016).

395. You, J. *et al.* Cardiomyocyte sensor responsive to changes in physical and chemical environments. *J. Biomech.* **47,** 400–409 (2014).
396. Abadi, P. P. S. S. *et al.* Engineering of Mature Human Induced Pluripotent Stem Cell-Derived Cardiomyocytes Using Substrates with Multiscale Topography. *Adv. Funct. Mater.* **28,** 1707378 (2018).
397. Pandey, P. *et al.* Cardiomyocytes Sense Matrix Rigidity through a Combination of Muscle and Non-muscle Myosin Contractions. *Dev. Cell* **44,** 326–336.e3 (2018).
398. Ng, F. S. *et al.* Enhancement of Gap Junction Function During Acute Myocardial Infarction Modifies Healing and Reduces Late Ventricular Arrhythmia Susceptibility. *JACC. Clin. Electrophysiol.* **2,** 574–582 (2016).
399. Mandegar, M. A. *et al.* CRISPR Interference Efficiently Induces Specific and Reversible Gene Silencing in Human iPSCs. *Cell Stem Cell* **18,** 541–553 (2016).
400. Callaghan, N. I. & Lee, X. A. Extracellular matrix stiffness affects contractility in adult rat cardiomyocytes: implications for dynamic nitric oxide signalling and calcium handling. *J. Physiol.* **595,** 5759–5760 (2017).
401. Agarwal, A. *et al.* Micropatterning Alginate Substrates for In Vitro Cardiovascular Muscle on a Chip. *Adv. Funct. Mater.* **23,** 3738–3746 (2013).
402. Berk, B. C., Fujiwara, K. & Lehoux, S. Review series ECM remodeling in hypertensive heart disease. *J. Clin. Invest.* **117,** 568–575 (2007).
403. Koivumäki, J. T. *et al.* Structural immaturity of human iPSC-derived cardiomyocytes: In silico investigation of effects on function and disease modeling. *Front. Physiol.* **9,** 1–17 (2018).
404. Bedada, F. B., Wheelwright, M. & Metzger, J. M. Maturation status of sarcomere structure and function in human iPSC-derived cardiac myocytes. *Biochim. Biophys. Acta - Mol. Cell Res.* **1863,** 1829–1838 (2015).
405. Zhou, Y. *et al.* Comparative Gene Expression Analyses Reveal Distinct Molecular Signatures between Differentially Reprogrammed Cardiomyocytes. *Cell Rep.* **20,** 3014–3024 (2017).
406. Pasqualini, F. S. *et al.* Traction force microscopy of engineered cardiac tissues. *PLoS One* **13,** 1–14 (2018).
407. Biendarra-Tiegs, S. M. *et al.* Single-cell RNA-seq and optical electrophysiology of human induced pluripotent stem cell-derived cardiomyocytes reveal discordance between cardiac subtype-associated gene expression patterns and electrophysiological

phenotypes. *Stem Cells Dev.* doi:10.1089/scd.2019.0030

408. Shiels, H. A. & White, E. The Frank-Starling mechanism in vertebrate cardiac myocytes. *J. Exp. Biol.* **211,** 2005–2013 (2008).
409. Bird, S. D. *et al.* The human adult cardiomyocyte phenotype. *Cardiovasc. Res.* **58,** 423–34 (2003).
410. Konieczny, P. *et al.* Myofiber integrity depends on desmin network targeting to Z-disks and costameres via distinct plectin isoforms. *J. Cell Biol.* **181,** 667–681 (2008).
411. Bedada, F. B. *et al.* Acquisition of a Quantitative, Stoichiometrically Conserved Ratiometric Marker of Maturation Status in Stem Cell-Derived Cardiac Myocytes. *Stem Cell Reports* **3,** 594–605 (2014).
412. Farrell, E. T., Grimes, A. C., de Lange, W. J., Armstrong, A. E. & Ralphe, J. C. Increased postnatal cardiac hyperplasia precedes cardiomyocyte hypertrophy in a model of hypertrophic cardiomyopathy. *Front. Physiol.* **8,** 1–13 (2017).
413. England, J. & Loughna, S. Heavy and light roles: Myosin in the morphogenesis of the heart. *Cell. Mol. Life Sci.* **70,** 1221–1239 (2013).
414. Chien, K. R., Knowlton, K. U., Zhu, H. & Chien, S. Regulation of cardiac gene expression during myocardial growth and hypertrophy: molecular studies of an adaptive physiologic response. *FASEB J.* **5,** 3037–46 (1991).
415. Nadal-Ginard, B. & Mahdavi, V. Molecular basis of cardiac performance. Plasticity of the myocardium generated through protein isoform switches. *J. Clin. Invest.* **84,** 1693–1700 (1989).
416. Bizy, A. *et al.* Myosin light chain 2-based selection of human iPSC-derived early ventricular cardiac myocytes. *Stem Cell Res.* **11,** 1335–1347 (2013).
417. Lee, J. H., Protze, S. I., Laksman, Z., Backx, P. H. & Keller, G. M. Human Pluripotent Stem Cell-Derived Atrial and Ventricular Cardiomyocytes Develop from Distinct Mesoderm Populations. *Cell Stem Cell* **21,** 179–194.e4 (2017).
418. Chen, Z. *et al.* Subtype-specific promoter-driven action potential imaging for precise disease modelling and drug testing in hiPSC-derived cardiomyocytes. *Eur. Heart J.* **38,** 292–301 (2017).
419. Marczenke, M. *et al.* Cardiac subtype-specific modeling of Kv1.5 ion channel deficiency using human pluripotent stem cells. *Front. Physiol.* **8,** 1–11 (2017).
420. Mawad, D. *et al.* A Single Component Conducting Polymer Hydrogel as a Scaffold for Tissue Engineering. *Adv. Funct. Mater.* **22,** 2692–2699 (2012).
421. GOLCZAK, S., KANCIURZEWSKA, A., FAHLMAN, M., LANGER, K. & LANGER, J.

Comparative XPS surface study of polyaniline thin films. *Solid State Ionics* **179,** 2234–2239 (2008).

422. Chen, X., Nadiarynkh, O., Plotnikov, S. & Campagnola, P. J. Second harmonic generation microscopy for quantitative analysis of collagen fibrillar structure. *Nat. Protoc.* **7,** 654–669 (2012).
423. Später, D. *et al.* A HCN4+ cardiomyogenic progenitor derived from the first heart field and human pluripotent stem cells. *Nat. Cell Biol.* **15,** 1098–1106 (2013).
424. Bizy, A. *et al.* Myosin light chain 2-based selection of human iPSC-derived early ventricular cardiac myocytes. *Stem Cell Res.* **11,** 1335–47 (2013).
425. Yoshida, S. *et al.* Maturation of Human Induced Pluripotent Stem Cell-Derived Cardiomyocytes by Soluble Factors from Human Mesenchymal Stem Cells. *Mol. Ther.* **26,** 2681–2695 (2018).
426. Mosterd, A. Prevalence of heart failure and left ventricular dysfunction in the general population; The Rotterdam Study. *Eur. Heart J.* **20,** 447–455 (1999).
427. Rosenthal, N. & Harvey, R. P. *Heart Development and Regeneration, Volume 1*. (Academic Press, 2010).
428. Park, H., Larson, B. L., Kolewe, M. E., Vunjak-Novakovic, G. & Freed, L. E. Biomimetic scaffold combined with electrical stimulation and growth factor promotes tissue engineered cardiac development. *Exp. Cell Res.* **321,** 297–306 (2014).
429. Zhao, Y., Feric, N. T., Thavandiran, N., Nunes, S. S. & Radisic, M. The Role of Tissue Engineering and Biomaterials in Cardiac Regenerative Medicine. *Can. J. Cardiol.* **30,** 1307–1322 (2014).
430. Reis, L. A., Chiu, L. L. Y., Feric, N., Fu, L. & Radisic, M. Biomaterials in myocardial tissue engineering. *J. Tissue Eng. Regen. Med.* **10,** 11–28 (2016).
431. Weickenmeier, J. *et al.* Brain stiffness increases with myelin content. *Acta Biomater.* **42,** 265–272 (2016).
432. Bober, P., Lindfors, T., Pesonen, M. & Stejskal, J. Enhanced pH stability of conducting polyaniline by reprotonation with perfluorooctanesulfonic acid. *Synth. Met.* **178,** 52–55 (2013).
433. Bidez, P. R. *et al.* Polyaniline, an electroactive polymer, supports adhesion and proliferation of cardiac myoblasts. *J. Biomater. Sci. Polym. Ed.* **17,** 199–212 (2006).
434. Lian, X. *et al.* Directed cardiomyocyte differentiation from human pluripotent stem cells by modulating Wnt/β-catenin signaling under fully defined conditions. *Nat. Protoc.* **8,** 162–175 (2013).

435. Zuppinger, C. *et al.* Characterization of cytoskeleton features and maturation status of cultured human iPSC-derived cardiomyocytes. *Eur. J. Histochem.* **61,** 135–143 (2017).
436. Sartiani, L. *et al.* Developmental Changes in Cardiomyocytes Differentiated from Human Embryonic Stem Cells: A Molecular and Electrophysiological Approach. *Stem Cells* **25,** 1136–1144 (2007).
437. Scuderi, G. J. & Butcher, J. Naturally Engineered Maturation of Cardiomyocytes. *Front. Cell Dev. Biol.* **5,** 1–28 (2017).
438. Høydal, M. A. *et al.* Human cardiomyocyte calcium handling and transverse tubules in mid-stage of post-myocardial-infarction heart failure. *ESC Hear. Fail.* 332–342 (2018). doi:10.1002/ehf2.12271
439. Ashikaga, H. *et al.* Electromechanical analysis of infarct border zone in chronic myocardial infarction. *Am. J. Physiol. Circ. Physiol.* **289,** H1099–H1105 (2005).
440. Dvir, T. *et al.* Nanowired three-dimensional cardiac patches. *Nat Nano* **6,** 720–725 (2011).
441. Martinelli, V. *et al.* Carbon nanotubes promote growth and spontaneous electrical activity in cultured cardiac myocytes. *Nano Lett.* **12,** 1831–8 (2012).
442. Sun, H. *et al.* Carbon nanotubes enhance intercalated disc assembly in cardiac myocytes via the β1-integrin-mediated signaling pathway. *Biomaterials* **55,** 84–95 (2015).
443. Shin, S. R. *et al.* Carbon-nanotube-embedded hydrogel sheets for engineering cardiac constructs and bioactuators. *ACS Nano* **7,** 2369–2380 (2013).
444. Baei, P. *et al.* Electrically conductive gold nanoparticle-chitosan thermosensitive hydrogels for cardiac tissue engineering. *Mater. Sci. Eng. C* **63,** 131–141 (2016).
445. Røe, Å. T. *et al.* Increased passive stiffness promotes diastolic dysfunction despite improved Ca2+handling during left ventricular concentric hypertrophy. *Cardiovasc. Res.* **113,** 1161–1172 (2017).
446. Tan, Y. *et al.* Cell number per spheroid and electrical conductivity of nanowires influence the function of silicon nanowired human cardiac spheroids. *Acta Biomater.* **51,** 495–504 (2017).
447. Eschenhagen, T., Didié, M., Heubach, J. & Somers, P. *Cardiac Tissue Engineering*. *Transplant …* **1181,** (Springer New York, 2014).
448. Weinberger, F., Mannhardt, I. & Eschenhagen, T. Engineering Cardiac Muscle Tissue: A Maturating Field of Research. *Circ. Res.* **120,** 1487–1500 (2017).
449. Nunes, S. S. *et al.* Biowire: a platform for maturation of human pluripotent stem cell–derived cardiomyocytes. *Nat. Methods* **10,** 781–787 (2013).

450. Watson, C. J. E. & Dark, J. H. Organ transplantation: historical perspective and current practice. *Br. J. Anaesth.* **108,** i29–i42 (2012).
451. Shafran, D., Kodish, E. & Tzakis, A. Organ Shortage: The Greatest Challenge Facing Transplant Medicine. *World J. Surg.* **38,** 1650–1657 (2014).
452. McLarty, A. Mechanical Circulatory Support and the Role of LVADs in Heart Failure Therapy. *Clin. Med. Insights. Cardiol.* **9,** 1–5 (2015).
453. Kozik, D. J. & Plunkett, M. D. Mechanical circulatoary support. *Organogenesis* **7,** 50–63
454. Niu, D. *et al.* Inactivation of porcine endogenous retrovirus in pigs using CRISPR-Cas9. *Science (80-.).* **357,** 1303–1307 (2017).
455. Deschamps, J.-Y., Roux, F. A., Sai, P. & Gouin, E. History of xenotransplantation. *Xenotransplantation* **12,** 91–109 (2005).
456. Patience, C., Takeuchi, Y. & Weiss, R. A. Infection of human cells by an endogenous retrovirus of pigs. *Nat. Med.* **3,** 282–6 (1997).
457. Fernández-Ruiz, I. Breakthrough in heart xenotransplantation. *Nat. Rev. Cardiol.* **16,** 69–69 (2019).
458. Längin, M. *et al.* Consistent success in life-supporting porcine cardiac xenotransplantation. *Nature* **564,** 430–433 (2018).
459. Makkar, R. R. *et al.* Intracoronary cardiosphere-derived cells for heart regeneration after myocardial infarction (CADUCEUS): a prospective, randomised phase 1 trial. *Lancet* **379,** 895–904 (2012).
460. Shiba, Y. *et al.* Allogeneic transplantation of iPS cell-derived cardiomyocytes regenerates primate hearts. *Nature* **538,** 388–391 (2016).
461. Chong, J. J. H. *et al.* Human embryonic-stem-cell-derived cardiomyocytes regenerate non-human primate hearts. *Nature* **510,** 273–277 (2014).
462. Kawamura, M. *et al.* Feasibility, Safety, and Therapeutic Efficacy of Human Induced Pluripotent Stem Cell-Derived Cardiomyocyte Sheets in a Porcine Ischemic Cardiomyopathy Model. *Circulation* **126,** S29–S37 (2012).
463. Kawamura, M. *et al.* Enhanced Therapeutic Effects of Human iPS Cell Derived-Cardiomyocyte by Combined Cell-Sheets with Omental Flap Technique in Porcine Ischemic Cardiomyopathy Model. *Sci. Rep.* **7,** 8824 (2017).
464. Chow, A. *et al.* Human Induced Pluripotent Stem Cell-Derived Cardiomyocyte Encapsulating Bioactive Hydrogels Improve Rat Heart Function Post Myocardial Infarction. *Stem Cell Reports* **9,** 1415–1422 (2017).
465. Tohyama, S. *et al.* Efficient Large-Scale 2D Culture System for Human Induced

Pluripotent Stem Cells and Differentiated Cardiomyocytes. *Stem Cell Reports* **9,** 1406–1414 (2017).

466. Sougawa, N. *et al.* Immunologic targeting of CD30 eliminates tumourigenic human pluripotent stem cells, allowing safer clinical application of hiPSC-based cell therapy. *Sci. Rep.* **8,** 3726 (2018).
467. Fiedler, L. R. *et al.* MAP4K4 Inhibition Promotes Survival of Human Stem Cell-Derived Cardiomyocytes and Reduces Infarct Size In Vivo. *Cell Stem Cell* (2019). doi:10.1016/j.stem.2019.01.013
468. Mathiyalagan, P. & Sahoo, S. Cardiac Gene Therapy. **1521,** 139–152 (2017).
469. Barile, L. *et al.* Extracellular vesicles from human cardiac progenitor cells inhibit cardiomyocyte apoptosis and improve cardiac function after myocardial infarction. *Cardiovasc. Res.* **103,** 530–541 (2014).
470. Garbayo, E. *et al.* Catheter-based Intramyocardial Injection of FGF1 or NRG1-loaded MPs Improves Cardiac Function in a Preclinical Model of Ischemia-Reperfusion. *Sci. Rep.* **6,** 25932 (2016).
471. Eulalio, A. *et al.* Functional screening identifies miRNAs inducing cardiac regeneration. *Nature* **492,** 376–381 (2012).
472. Gallet, R. *et al.* Exosomes secreted by cardiosphere-derived cells reduce scarring, attenuate adverse remodelling, and improve function in acute and chronic porcine myocardial infarction. *Eur. Heart J.* ehw240 (2016). doi:10.1093/eurheartj/ehw240
473. D'Uva, G. *et al.* ERBB2 triggers mammalian heart regeneration by promoting cardiomyocyte dedifferentiation and proliferation. *Nat. Cell Biol.* **17,** 627–638 (2015).
474. Li, J. *et al.* Conversion of human fibroblasts to functional endothelial cells by defined factors. *Arterioscler. Thromb. Vasc. Biol.* **33,** 1366–1375 (2013).
475. Inagawa, K. & Ieda, M. Direct reprogramming of mouse fibroblasts into cardiac myocytes. *J. Cardiovasc. Transl. Res.* **6,** 37–45 (2013).
476. Nam, Y.-J. *et al.* Reprogramming of human fibroblasts toward a cardiac fate. *Proc. Natl. Acad. Sci. U. S. A.* **110,** 5588–93 (2013).
477. Addis, R. C. & Epstein, J. a. Induced regeneration--the progress and promise of direct reprogramming for heart repair. *Nat. Med.* **19,** 829–36 (2013).
478. Song, K. *et al.* Heart repair by reprogramming non-myocytes with cardiac transcription factors. *Nature* **485,** 599–604 (2012).
479. Qian, L. *et al.* In vivo reprogramming of murine cardiac fibroblasts into induced cardiomyocytes. *Nature* **485,** 593–598 (2012).

480. Lalit, P. A. *et al.* Lineage Reprogramming of Fibroblasts into Proliferative Induced Cardiac Progenitor Cells by Defined Factors. *Cell Stem Cell* **18,** 354–367 (2016).
481. Zhang, D. *et al.* Tissue-engineered cardiac patch for advanced functional maturation of human ESC-derived cardiomyocytes. *Biomaterials* **34,** 5813–5820 (2013).
482. Vunjak-Novakovic, G., Lui, K. O., Tandon, N. & Chien, K. R. Bioengineering Heart Muscle: A Paradigm for Regenerative Medicine. *Annu. Rev. Biomed. Eng.* **13,** 245–267 (2011).
483. Eschenhagen, T., Eder, A., Vollert, I. & Hansen, A. Physiological aspects of cardiac tissue engineering. *Am. J. Physiol. Circ. Physiol.* **303,** H133–H143 (2012).
484. Zimmermann, W.-H. *et al.* Engineered heart tissue grafts improve systolic and diastolic function in infarcted rat hearts. *Nat. Med.* **12,** 452–8 (2006).
485. Radisic, M. *et al.* Functional assembly of engineered myocardium by electrical stimulation of cardiac myocytes cultured on scaffolds. *Proc. Natl. Acad. Sci. U. S. A.* **101,** 18129–34 (2004).
486. Zimmermann, W.-H. *et al.* Tissue engineering of a differentiated cardiac muscle construct. *Circ. Res.* **90,** 223–30 (2002).
487. Sun, X. & Nunes, S. S. Bioengineering Approaches to Mature Human Pluripotent Stem Cell-Derived Cardiomyocytes. *Front. cell Dev. Biol.* **5,** 19 (2017).
488. Radisic, M. & Christman, K. L. Materials science and tissue engineering: repairing the heart. *Mayo Clin. Proc.* **88,** 884–98 (2013).
489. Ye, G. & Qiu, X. Conductive biomaterials in cardiac tissue engineering. *Biotarget* **1,** 9–9 (2017).
490. Karanasiou, G. S. *et al.* Stents: Biomechanics, Biomaterials, and Insights from Computational Modeling. *Ann. Biomed. Eng.* **45,** 853–872 (2017).
491. Hutmacher, D. W., Little, J. P., Pettet, G. J. & Loessner, D. Biomaterial science meets computational biology. *J. Mater. Sci. Mater. Med.* **26,** 185 (2015).
492. Kolanowski, T. J., Antos, C. L. & Guan, K. Making human cardiomyocytes up to date: Derivation, maturation state and perspectives. *Int. J. Cardiol.* **241,** 379–386 (2017).
493. Berecz, T. *et al.* Generation and Analysis of Pluripotent Stem Cell-Derived Cardiomyocytes and Endothelial Cells for High Content Screening Purposes. in (2019). doi:10.1007/7651_2019_222
494. Joki, Y. *et al.* Neuron-derived neurotrophic factor ameliorates adverse cardiac remodeling after experimental myocardial infarction. *Circ. Hear. Fail.* **8,** 342–351 (2015).
495. Lee, A. S. *et al.* Prolonged survival of transplanted stem cells after ischaemic injury via

the slow release of pro-survival peptides from a collagen matrix. *Nat. Biomed. Eng.* **2,** 104–113 (2018).

Appendices

Table 10: *Table shows membrane coordinates and target on Proteome Profiler™ Array (ARY003B).*

Membrane coordinate	Target/Control	Phosphorylation site
A-A1, A2	Reference spot	-
A-A3, A4	p38α	T180/Y182
A-A5, A6	ERK1/2	T202/Y204, T185/ Y187
A-A7, A8	JNK 1/2/3	T183/Y185, T221/ Y223
A-A9, A10	GSK-3α/β	S21/S9
B-A13, A14	p53	S392
B-A17, A18	Reference spot	-
A-B3, B4	EGF R	Y1086
A-B5, B6	MSK1/2	S376/S360
A-B7, B8	AMPKα1	T183
A-B9, B10	Akt 1/2/3	S473
B-B11, B12	Akt 1/2/3	T308
B-B13, B14	p53	S46
A-C1, C2	TOR	S2448
A-C3, C4	CREB	S133
A-C5, C6	HSP27	S78/S82
A-C7, C8	AMPKα2	T172
A-C9, C10	β-Catenin	-
B-C11, C12	P70 S6 Kinase	T389
B-C13, C14	P53	S15
B-C15, C16	C-Jun	S63
A-D1, D2	Src	Y419
A-D3, D4	Lyn	Y397
A-D5, D6	Lck	Y394
A-D7, D8	STAT2	Y689
A-D9, D10	STAT5a	Y694
B-D11, D12	P70 S6 Kinase	T421/S424

B-D13, D14	RSK1/2/3	S380/S386/S377
B-D15, D16	eNOS	S1177
A-E1, E2	Fyn	Y420
A-E3, E4	Yes	Y426
A-E5, E6	Fgr	Y412
A-E7, E8	STAT6	Y641
A-E9, E10	STAT5b	Y699
B-E11, E12	STAT3	Y705
B-E13, E14	P27	T198
B-E15, E16	PLC-γ1	Y783
A-F1, F2	Hck	Y411
A-F3, F4	Chk-2	T68
A-F5, F6	FAK	Y397
A-F7, F8	PDGF Rβ	Y751
A-F9, F10	STAT5a/b/	Y694/Y699
B-F11, F12	STAT3	S727
B-F13, F14	WNK1	T60
B-F15, F16	PYK2	Y402
A-G1, G2	Reference spot	-
A-G3, G4	PRAS40	T246
A-G9, G10	PBS (Negative control)	-
B-G11, G12	HSP60	-
B-G17, G18	PBS (Negative control)	-

Copyright permission

Thesis	Ref	Name of work	Copyright holder	Detail
Figure 1	2	Figure 1: Estimates of mortality from WHO Global Health Estimates (GHE)	World Health Organisation	Permission not required for educational and non-commercial purposes
Figure 2	22	Figure 2: Transmembrane receptor interactions to the extracellular environment	Nature publishing	Written permission received 18th January 2019
Figure 4	88	Figure 4: Visual comparison of early hiPSC-CM, late hiPSC-CM and adult CM phenotype	John Wiley and Sons	Written permission received 17th January 2019
Figure 6	201	Figure 6: The stem cell as a mathematical integrator	Company of Biologists	Written permission received 17th January 2019
Figure 7	282	Figure 7: Biomaterials and their cues for stem cell fates.	Elsevier	Written permission received 17th January 2019

Table 1		Table 1: Summary of non-cardiomyocyte roles in healthy and diseased myocardium	MDPI	Licensed with a Creative Commons Attribution License (CC BY 4.0)
Table 3		Table 3: Status of physiological and pathological modelling.	MDPI	Licensed with a Creative Commons Attribution License (CC BY 4.0)
Table 4		Table 4: Summary of main available hiPSC derived cells used in disease modelling	MDPI	Licensed with a Creative Commons Attribution License (CC BY 4.0)